In vivo arterial geometry

In vivo state Ω_2

Prediction of the arterial zero-stress state Ω_0

Strojniški vestnik – Journal of Mechanical Engineering (SV-JME)

Aim and Scope

The international journal publishes original and (mini)review articles covering the concepts of materials science, mechanics, kinematics, thermodynamics, energy and environment, mechatronics and robotics, fluid mechanics, tribology, cybernetics, industrial engineering and structural analysis.

The journal follows new trends and progress proven practice in the mechanical engineering and also in the closely related sciences as are electrical, civil and process engineering, medicine, microbiology, ecology, agriculture, transport systems, aviation, and others, thus creating a unique forum for interdisciplinary or multidisciplinary dialogue.

The international conferences selected papers are welcome for publishing as a special issue of SV-JME with invited co-editor(s).

Cover:
The prediction of the arterial zero-stress state (or, alternatively, the corresponding residual stress state) is as of yet an unresolved problem in the field of modelling the mechanical response of patient-specific arteries. To tackle this problem, a methodology has been developed with which the arterial residual stresses are predicted using a thermomechanical analogy.

Courtesy:
University of Ljubljana, Faculty of Mechanical Engineering, Laboratory for Numerical Modelling and Simulations

ISSN 0039-2480

Contents

Editorial

International Editorial Board Acknowledgement

As Editor of *Strojniški vestnik – Journal of Mechanical Engineering* I would like to thank our colleagues who will be finishing their work as Editorial Board members in 2014 for their hard work throughout the years in reviewing articles and providing important feedback to authors:

Koshi Adachi, Graduate School of Engineering,Tohoku University, Japan
Bikramjit Basu, Indian Institute of Technology, Kanpur, India
Narendra B. Dahotre, University of Tennessee, USA
Matija Fajdiga, University of Ljubljana, Faculty of Mechanical Engineering, Slovenia
Jože Flašker, University of Maribor, Faculty of Mechanical Engineering, Slovenia
Bernard Franković, Faculty of Engineering Rijeka, Croatia
Janez Kopač, University of Ljubljana, Faculty of Mechanical Engineering, Slovenia
Franc Kosel, University of Ljubljana, Faculty of Mechanical Engineering, Slovenia
Brian Prasad, California Institute of Technology, Pasadena, USA
Brane Širok, University of Ljubljana, Faculty of Mechanical Engineering, Slovenia
Leopold Škerget, University of Maribor, Faculty of Mechanical Engineering, Slovenia
George E. Totten, Portland State University, USA
Nikos C. Tsourveloudis, Technical University of Crete, Greece
Toma Udiljak, University of Zagreb, Croatia

I would also like to welcome the following new Editorial Board members to *Strojniški vestnik – Journal of Mechanical Engineering*:

Kamil Arslan, Karabuk University, Turkey
Josep M. Bergada, Politechnical University of Catalonia, Spain
Miha Boltežar, University of Ljubljana, Faculty of Mechanical Engineering, Slovenia
Anselmo Eduardo Diniz, State University of Campinas, Brazil
Igor Emri, University of Ljubljana, Faculty of Mechanical Engineering, Slovenia
Aleš Hribernik, University of Maribor, Faculty of Mechanical Engineering, Slovenia
Iyas Khader, Fraunhofer Institute for Mechanics of Materials, Germany
Jernej Klemenc, University of Ljubljana, Faculty of Mechanical Engineering, Slovenia
Janez Kušar, University of Ljubljana, Faculty of Mechanical Engineering, Slovenia
Gorazd Lojen, University of Maribor, Faculty of Mechanical Engineering, Slovenia
George K. Nikas, KADMOS Engineering, UK
José L. Ocaňa, Technical University of Madrid, Spain
Vladimir Popovič, University of Belgrade, Faculty of Mechanical Engineering, Serbia
Franci Pušavec, University of Ljubljana, Faculty of Mechanical Engineering, Slovenia
Rudolph J. Scavuzzo, University of Akron, USA

Vincenc Butala
Editor-in-chief

Applying Thermomechanical Analogy to Predict the Arterial Residual Stress State

Janez Urevc[1,*] – Milan Brumen[2,3] – Vojko Flis[4] – Boris Štok[1]

[1]University of Ljubljana, Faculty of Mechanical Engineering, Slovenia
[2]University of Maribor, Faculty of Medicine, Slovenia
[3]Jožef Stefan Institute, Slovenia
[4]University Medical Centre Maribor, Department of Vascular Surgery, Slovenia

The prediction of the arterial zero-stress state is as of yet an unresolved problem in the field of modelling the mechanical response of patient-specific arteries. This is because the configuration associated with arterial zero-stress state is impossible to obtain experimentally. However, the zero-stress configuration (or, equivalently, the residual stresses related to this configuration) represents the crucial data of any numerical analysis.

In this study, the mechanical response of a pre-stressed, pressurised, hyperelastic tube (representing the artery) is determined without knowing the initial zero-stress configuration of the artery. Instead, to predict the arterial residual (bending and stretching) stresses, a corresponding thermomechanical analogy is used. As shown in the paper, the arterial residual stress state can equally be obtained by thermally loading a properly defined closed tube. Thus, based on the loaded state of the corresponding thermomechanical model, the arterial residual stress sate is constructed, from where the arterial loaded state can be obtained. The initial configuration of the thermomechanical model is defined on the basis of the arterial loaded configuration. The methodology is validated by predicting the zero-stress state of the artery. The predicted equilibrium state of the artery, when cut longitudinally and transversally, has the form of an opened-up tube with a relatively low stress state in comparison to the arterial residual stresses. The results thus demonstrate that arterial residual stresses that are predicted with the corresponding thermomechanical model exhibited the bending distribution, which proves the methodology to be adequate.
Keywords: residual stresses, zero-stress state of arteries, finite element method, thermomechanics

Highlights
- *Predicting the arterial mechanical response based on the* in vivo *arterial data.*
- *Proposed methodology for predicting the arterial mechanical response.*
- *Using thermomechanical analogy for predicting the arterial residual stress state.*
- *Predicting the arterial zero-stress state based on the* in vivo *arterial data.*
- *Determination of bending stresses by means of thermomechanical analogy.*

0 INTRODUCTION

The progress of medical imaging has enabled the increasingly accurate acquisition of patient-specific arterial geometries. This, in turn, allows for the study of arterial response under various conditions, giving additional insight into human physiology that cannot be experimentally obtained. Medical imaging is most often performed *in vivo*, thus providing the arterial geometry that corresponds to the arterial loaded (i.e., physiological) state. To numerically model the arterial mechanical response, however, either the arterial zero-stress configuration or the arterial residual stress state is needed. This study addresses the problem of modelling the arterial response in cases when the arterial zero-stress configuration is not given whereas the arterial loaded configuration is known. The artery is treated as a hyperelastic, residually pre-stressed and pressurised tube.

The arterial *unloaded state* represents a part of the artery removed from the surrounding tissue, freed of intraluminal pressure, and removed from the body. In this state, the artery is free of external loads but is still subject to some amount of stresses, referred to as *the residual stresses*. These stresses are relieved by cutting the artery longitudinally. The artery then springs open and assumes a sector-like shape in which the size of this opening quantifies the magnitude of the relieved residual stresses. Because of their transmural distribution, with compressive stresses on the arterial inside and tensile stresses on the outside [1], the residual stresses are normally associated with pure bending stresses [2]. Although some residual stresses exist in the arterial longitudinal direction [3] and [4], we will assume that only one longitudinal cut is sufficient to release almost all residual stresses [5] and [6]. In this work, the artery is treated as single-layered structure. Even though this is a rough approximation of the complex structure of an artery, it is able to provide a reasonable assessment of the arterial physiological response [7].

Residual stress produces a favourable (physiological) environment for cell functions [8], which is created by lowering the gradient of the transmural stresses [9] and [10]. According to the so-called *uniform strain hypothesis* [11], the distribution and magnitude of the residual stresses cause the physiological intraluminal distribution of the *circumferential strain* $\lambda_\phi(r)$ to be uniform ($\lambda_\phi(r)$ = const), which implies a low gradient of transmural stresses. Furthermore, it has been experimentally observed that the distribution of the residual stresses in the vessel wall is three dimensional, meaning that they depend on both the radial position and on the axial position [5], [12] and [13].

A crucial datum needed for any numerical prediction of the arterial response, as already mentioned, is the zero-stress configuration of the artery. To the knowledge of the authors, the only methodology that allows the inclusion of residual stresses in a patient-specific arterial geometry is presented in the study performed by Alastrué et al. [2]. There, the residual stresses are accounted for by applying a simplified initial strain field that is obtained from a computation of the residual stress field in a circular arterial segment. The drawback of this approach is that the zero-stress configuration of the circular segment, which must be adopted from the literature, does not correspond with a patient-specific artery. Furthermore, due to the complexity of the problem, various simplifications have been made in the literature in order to obtain the patient-specific arterial zero-stress configuration. The most general approach is to take the loaded configuration of the artery for the arterial initial stress-free state. This approach leads to unphysically large arterial deformations [14] where, subsequently, the predicted arterial configuration obtained by pressurising the artery with intraluminal pressure strongly differs from the one observed *in vivo*. Another approach is to neglect the arterial residual stresses and assume the arterial *unloaded configuration* for the arterial initial *zero-stress configuration*. For example, in the study conducted by Gee et al. [14], two such methods are presented that enable a prediction of the pre-stress state of a patient-specific geometries under *in vivo* loads. The first is the inverse design (ID) analysis. In this approach, which is also used in [15] and [16], the zero-stress configuration is computed and then used to compute a (non-unique) strain and stress state that satisfied equilibrium with respect to the known spatial configuration. The second method is based on a modified updated Lagrangian formulation (MULF), in which a multiplicative split of the deformation

gradient is used to produce a displacement-free pre-strained/pre-stressed state. Despite the widespread use of the first method in particular, the drawback of such an approach is that it neglects the residual stresses. On the other hand, progress has been made in obtaining the arterial unloaded state starting from the opened-up configuration (see for instance [12], [17] and [18]). In this case, however, the arterial opened-up configuration needed to be provided (i.e., given).

In this paper, a new methodology is presented that predicts the mechanical response of a hyperelastic, residually pre-stressed and pressurised tube (representing an artery). The loaded configuration of the artery is assumed known whereas the arterial opened-up zero-stress configuration is unknown. The methodology for predicting the arterial residual (i.e., bending and stretching) stresses is based on an equivalent approach where a corresponding thermomechanical problem of an associated closed tube is defined. In Section 1, a case study is presented and the assumptions of the considered mechanical problem are specified. Section 2 gives a theoretical background on (i) the characterisation of the circular arterial segment, (ii) the thermomechanical analogy for obtaining the arterial residual stresses, and (iii) the use of the thermomechanical analogy to predict the mechanical response of a realistic arterial segment. The methodology presented for the arterial segment is then generalised to treat a real artery in Section 3. The analysis results obtained by applying the developed methodology to the case study are given in Section 4 together with a corresponding validation of the methodology. Finally, in Section 5, the conclusions are given along with some guidelines for future research.

1 PROBLEM DEFINITION

The methodology for predicting the arterial residual stress state is demonstrated using a case study analysis considering an analytically defined, hyperelastic tube. The tube, here referred to as the *arterial model* (AM), is defined so as to resemble the *in vivo* observed artery. The inner, i.e., the luminal surface of the AM (Γ_i^{AM}, Fig. 1a) is defined as a straight tube of an elliptical cross section having respective principal directions coincident with the x and y axis along the entire AM. The assumed variation of the elliptical semi-minor and semi-major axis ($a(z)$ and $b(z)$), specifying the surface Γ_i^{AM}, is shown in Fig. 1b. Based on this variation, the AM luminal cross-sectional area $A(z)$ variation is computed as show in Fig. 1b. Furthermore, the thickness t of the AM is assumed to be constant along the whole section, its
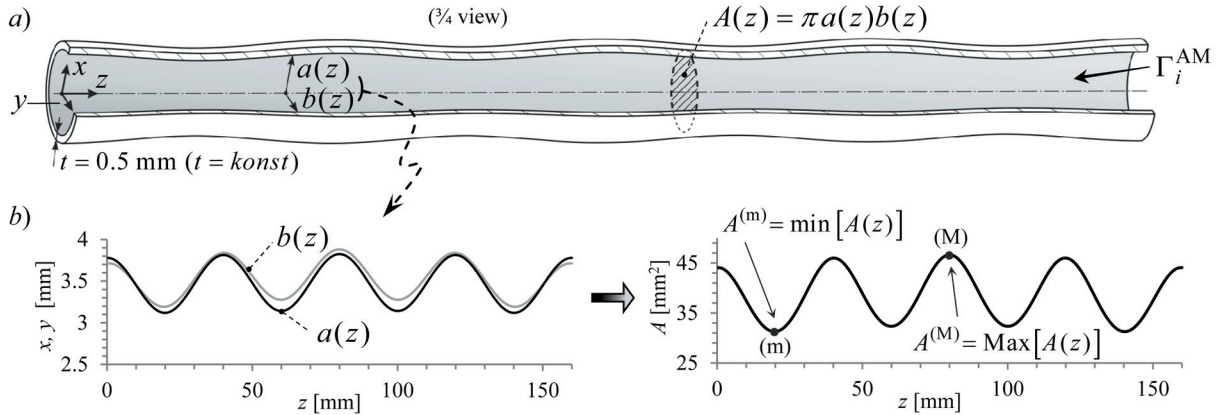
Fig. 1. *Presentation of the case-study: a) Three-dimensional representation of the arterial model (AM); b) the inner, i.e., the luminal surface of the AM (Γ_i^{AM}) represents a straight tube of an elliptical cross section which is defined by the ellipse semi-axes a(z) and b(z)*

value being $t = 0.5$ mm. The length of the model is 160 mm.

Let us assume that the AM geometry is obtained from medical imaging and that the configuration presented in Fig. 1a corresponds to the AM diastolic state with an intraluminal pressure of $P = 70$ mmHg. For the material behaviour of the AM, an isotropic hyperelastic material model is assumed, described by a strain energy density function W [17]:

$$W = \frac{c_a}{c_b}\left[\exp\left[\frac{c_b}{2}(I_1 - 3)\right] - 1\right], \qquad (1)$$

where I_1 is the first invariant of the strain tensor and c_a and c_b are the constitutive parameters. In [17], their values were experimentally determined to be $c_a = 44.2$ kPa and $c_b = 16.7$.

Remark: The artery is treated as a single-layered tube with isotropic properties. This is an oversimplification because it is well known that arteries are composed of three distinct layers (intima, media and adventitia), which have, in general, anisotropic properties [19]. Nevertheless, as discussed in the introduction, the considered AM is still able to provide a reasonable approximation of the arterial response. In this regard, when taking into consideration that the primary goal of this paper is to give a presentation of the new developed methodology, the adopted model approximation may be considered acceptable and justified for the given purpose. Additionally, the effect of the tissue surrounding the artery, which acts as a pressure load on the arterial outer surface, is neglected in this study.

1.1 Arterial Configurations

The arterial configurations are denoted by the symbol Ω. The subscript supplementing Ω specifies the corresponding arterial loading state whereas the superscript of Ω indicates the corresponding model. The superscript "AM" will refer to the *arterial model* and "C" to the configurations of the *circular arterial segments*. The following arterial configurations are considered (Fig. 2):

Loaded state (Ω_2): In its *loaded state* the artery is subject to intraluminal pressure P and longitudinal (axial) as well as circumferential pre-stretch.

Stretched state ($\Omega_{1\lambda}$): The arterial stretched state is obtained by removing the pressure P from Ω_2. (Note that the term *arterial stretched state* is not common in the literature; it is defined here because it offers a good targeting state for the methodology presented in the following sections.)

Unloaded state (Ω_1): The unloaded state is obtained by releasing the axial pre-stretch from $\Omega_{1\lambda}$. The associated axial contraction is described by the axial stretch λ. Since the *in vivo* data is insufficient to determine λ [20], we have adopted here the data of Delfino et al. [17], where λ is set to 10% ($\lambda = 1.1$).

Zero-stress state (Ω_0): Once the artery in its unloaded state is cut open, it is assumed that the stresses in the artery are close to zero. The obtained state is taken as the arterial zero-stress state. The axial contraction Λ, that is associated with the longitudinal cut is normally neglected, therefore $\Lambda = 1$ [17].

2 MECHANICAL RESPONSE OF A CIRCULAR ARTERIAL SEGMENT

The subsequent subsections begin with some theoretical background on the characterisation of the circular arterial segment, and are followed by a presentation on an analogical approach aimed to obtain the stretched state of a circular arterial segment. The latter is achieved by defining a corresponding thermomechanical problem of a closed circular tube. Finally, the application of this analogy to predict the stretched state of a realistic arterial segment is schematically presented.

2.1 Stress Analysis of a Circular Arterial Segment

The mechanical response of an arterial segment (i.e., a slice of the artery) can be characterised by simplifying the segment geometry to a straight circular tube [20] to [23]. The *zero-stress state* configuration of the open circular segment Ω_0^C (Fig. 2) is thus defined with the radii R_i and R_o and the opening angle Θ_0. The *unloaded state* configuration Ω_1^C is then obtained by bending (closing) the segment from its zero-stress state configuration Ω_0^C. By further applying the axial stretch λ and the inner pressure P to the unloaded state configuration Ω_1^C, the *stretched state* configuration $\Omega_{1\lambda}^C$ and the *loaded state* configuration Ω_2^C of the segment are obtained, respectively.

The deformation gradient tensor $\mathbf{F}$ associated with the loaded state configuration Ω_2^C accounts for all three successive motions of material particles, displayed in Fig. 2. A material particle ($r_i \leq r \leq r_o$) can be represented in terms of the principal stretches as:

$$\mathbf{F} = \mathrm{diag}\left[\frac{\mathrm{d}r}{\mathrm{d}R}, \frac{\pi r}{\Theta_0 R}, \lambda\Lambda\right] = \mathrm{diag}\left[\lambda_r, \lambda_\phi, \lambda_z\right], \quad (2)$$

where λ_r, λ_ϕ, λ_z are, respectively, the principal stretches in the radial, circumferential, and axial directions. The right Cauchy-Green tensor is defined as $\mathbf{C} = \mathbf{F}^T\mathbf{F}$, where $\mathbf{F}^T$ is the transpose of $\mathbf{F}$. The reference radius $R(r)$ of the material particle in the zero-stress state configuration Ω_0^C is determined by imposing the incompressibility condition $J = \det\mathbf{F} = \lambda_r\lambda_\phi\lambda_z = 1$ and considering the functional expressions for the principal stretches given in Eq. (2):

$$R = \left(R_o^2 - \frac{\pi\lambda\Lambda}{\Theta_0}\left(r_o^2 - r^2\right)\right)^{1/2}. \quad (3)$$

In addition, the radial stretch is written as:

$$\lambda_r = 1\big/\lambda_\phi\lambda_z = \frac{\Theta_0 R}{\pi r \lambda \Lambda}, \quad (4)$$

which also comes from the incompressibility condition.

Considering the strain energy density function W the Cauchy stress tensor σ is obtained as:

$$\boldsymbol{\sigma} = -p\mathbf{I} + \bar{\boldsymbol{\sigma}} = -p\mathbf{I} + 2\mathbf{F}\frac{\partial W}{\partial\mathbf{C}}\mathbf{F}^T, \quad (5)$$

where p is the Langrange multiplier, which enforces the incompressibility constraint $\det\mathbf{F} = 1$, and $\mathbf{I}$ is the identity tensor. Using Eqs. (1) and (5) the non-zero components of the stress tensor are written as:

$$\sigma_{kk} = -p + \bar{\sigma}_{kk} = -p + \lambda_k^2 c_a \cdot$$
$$\cdot \exp\left[\frac{c_b}{2}\left(\lambda_r^2 + \lambda_\phi^2 + \lambda_z^2 - 3\right)\right]; \; k = r, \phi, z. \quad (6)$$

Because the considered problem is a radial one, all the quantities in the above equation depend only on the radial direction. In the absence of the body forces the equilibrium equations reduce to:
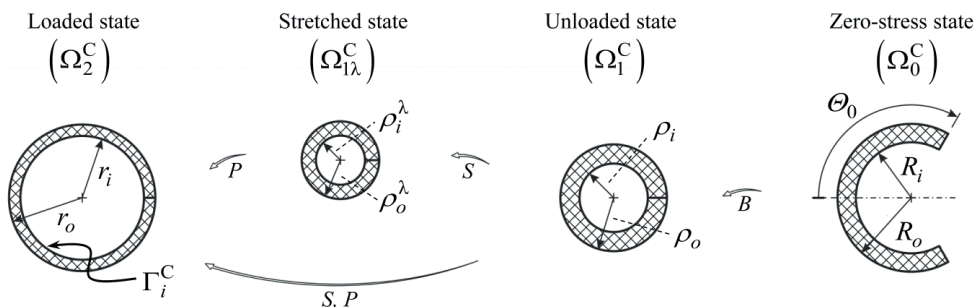
Fig. 2. *Configurations of the circular arterial segment: loaded Ω_2^C, stretched $\Omega_{1\lambda}^C$, unloaded Ω_1^C and zero-stress state Ω_0^C; the symbols B, S, and P represent bending, axial stretching and pressurising; Γ_i^C represents the inner (luminal) surface of the loaded state configuration Ω_2^C of the segment*

$$\frac{d\sigma_{rr}}{dr} + \frac{\sigma_{rr} - \sigma_{\phi\phi}}{r} = 0. \qquad (7)$$

The natural boundary conditions, Eq. (8), are applied both to the inner and outer surface of the segment. The inner surface is subject to the intraluminal pressure P, whereas the outer surface is considered traction-free:

$$\sigma_{rr}(r_i) = -P, \quad \sigma_{rr}(r_o) = 0. \qquad (8)$$

In addition, fulfilment of the equilibrium of the *in vivo* configuration yields the following expression for the Lagrange multiplier p [24]:

$$p(r) = P + \bar{\sigma}_{rr}(r) - \int_{r_i}^{r} \left(\sigma_{\phi\phi}(r) - \sigma_{rr}(r)\right)\frac{dr}{r}, \quad (9)$$

and an integral constraint on the stress distribution:

$$\int_{r_i}^{r_o} \left(\sigma_{\phi\phi}(r) - \sigma_{rr}(r)\right)\frac{dr}{r} = P. \qquad (10)$$

By knowing the zero-stress configuration Ω_0^C and the material properties of the segment, the stress state of the segment for a given loaded configuration Ω_2^C is obtained from Eq. (6), after having solved Eq. (9). The stretched state of the segment $\Omega_{1\lambda}^C$ with the material particles positioned in the interval $\rho_i^\lambda \le \rho \le \rho_o^\lambda$ (Fig. 2) is obtained from the above equations, if we consider the traction-free boundary condition on both the inner and outer surface of the segment (which means setting P to zero) and the substitution of the integral limits r_i, r, r_o, in Eqs. (9) and (10) with ρ_i^λ, ρ, ρ_o^λ. In the computation of stresses, the principal stretches computed in accordance with Eqs. (2) to (4) and considering the mapping of $r_i \le r \le r_o$ to $\rho_i^\lambda \le \rho \le \rho_o^\lambda$ have to be taken into account. The schematic representations of the stresses that occur in the stretched state of the circular arterial segment $\Omega_{1\lambda}^C$ are shown in Fig. 3.

2.1.1 Identification of the Zero-Stress State Configuration

The zero-stress state configuration of the circular arterial segment Ω_0^C is defined by the radius R_o and the opening angle Θ_0 (Fig. 2). Given that the geometry of the loaded state of the segment Ω_2^C is known, the parameters R_o and Θ_0 can be obtained by solving an inverse identification problem. Actually, the problem is considered to be an optimisation problem where the vector of optimisation variables $u = \{R_o, \Theta_0\}$ is supposed to minimise the corresponding objective function $\chi = \chi(u)$, which is defined so as to quantify the established difference between the *desired* and the *computed response* of the arterial segment in its loaded state. The *desired response* denotes the experimentally measured values of the selected quantities whereas the *computed response* refers to the same quantities predicted with the numerical model taking into account the optimisation vector u.

In order to minimise (i) the error between the desired and computed stress state of the loaded configuration Ω_2^C, and (ii) the transmural gradient of the circumferential strain (which takes into account the uniform strain hypothesis), the objective function $\chi = \chi(u)$ is adequately structured, with functions $\chi_P(u)$ and $\chi_\lambda(u)$ taking into account the respective effects:

Fig. 3. *Left-hand side of the figure: schematic representation of the stretched state of the circular arterial segment ($\Omega_{1\lambda}^C$, Fig. 2); the same state (i.e., its geometry and stresses) can be obtained by thermally loading a closed tube (fictitious model), presented in the right-hand side of the figure*
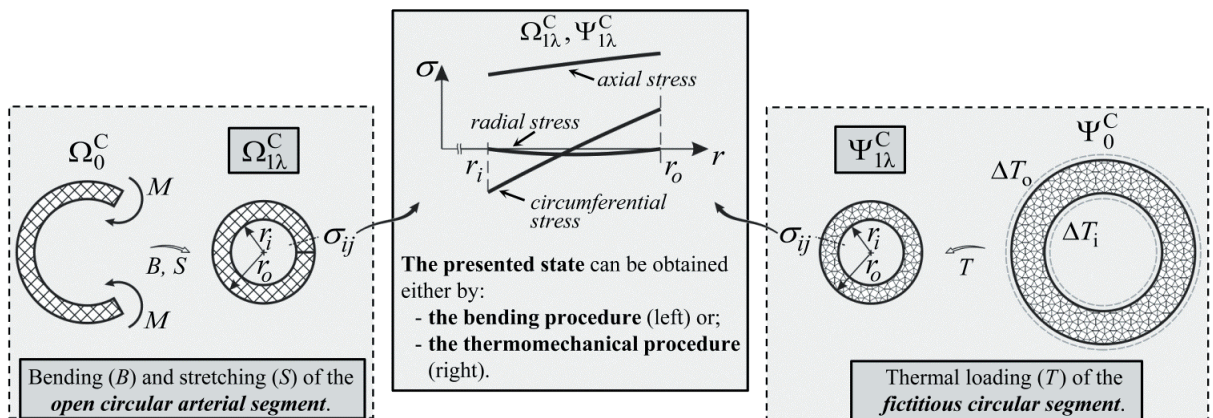
$$\chi(\boldsymbol{u}) = \chi_P(\boldsymbol{u}) + \chi_\lambda(\boldsymbol{u}) =$$
$$= \left(P_c(\boldsymbol{u}) - P\right)^2 + g_\lambda\left(\lambda_\phi^i(\boldsymbol{u}) - \lambda_\phi^o(\boldsymbol{u})\right)^2. \quad (11)$$

Above, P and P_c are respectively the desired and the computed intraluminal pressures; λ_ϕ^i and λ_ϕ^o the circumferential stretches, computed at the inner and outer surface of the segment's wall; and g_λ is the weighting factor.

2.2 Determination of the Arterial Residual Stresses Using the Thermomechanical Analogy

In this subsection, an alternative method for obtaining the stretched state of the circular arterial segment $\Omega_{1\lambda}^C$ (Fig. 3) using an analogy, based on the theory of thermoelasticity, is presented. Namely, from the theory of thermoelasticity it is known that the same deflection of, for instance, a cantilever beam can be obtained either by exposing the beam to an external bending moment at its free end or, alternatively, by adequately thermally loading the beam along its length. If we project this analogy to the modelling of the arterial response, this implies that the *stretched state of the circular arterial segment* $\Omega_{1\lambda}^C$, which is obtained by bending the open circular section Ω_0^C and subsequent axial stretching, can equally be obtained by thermally loading an associated *closed* tube Ψ_0^C. In Fig. 3, this is schematically outlined in the left and right box, respectively. The real significance of introducing the proposed thermomechanical analogy as a means to determine the residual stresses will be put forward in the subsequent sections, where the method will be adequately generalised and applied to a real artery's geometry.

The model considered in the described thermomechanical analogue needs to be properly defined, which is in fact the key step in the procedure of determining residual stresses. This model will be referred to in the sequel as the *fictitious model* because the material properties of the fictitious model, as will be shown, have nothing to do with the physical properties of the artery, and also because the thermal loading is fictitious with respect to the original mechanical model. Also, the boundary conditions have to be adequately changed in order to obtain the expected similarity of the mechanical response. The fictitious model will actually serve only as a mathematical tool to predict the arterial stretched state. The respective configurations of the fictitious model will be denoted with the symbol Ψ. The subscript supplementing Ψ will specify the corresponding loading state of the fictitious model whereas the superscript of Ψ will indicate the considered geometrical model. The superscript 'AM' will refer to the *fictitious arterial model* and 'C' to the configurations of the *fictitious circular segment*.

Now, let us give a definition of the fictitious circular segment and the mathematical framework needed to compute its thermomechanical response. The fictitious circular segment, the role of which in the procedure of predicting the stretched state of a realistic arterial segment is schematically presented in the following subsection (see Fig. 5), is defined in the following way:

Geometry of the fictitious circular model in its zero-stress configuration Ψ_0^C (Fig. 4): The geometry of the fictitious model, which is assumed to be free of stresses, we defined based on the geometry of the corresponding arterial model in its loaded state (configuration Ω_2^C, see Fig. 2), thus: (i) the inner radius of the fictitious circular segment $\mathfrak{R}_i$ equals the inner radius of the corresponding circular arterial segment in its loaded state r_i, $\mathfrak{R}_i = r_i$; and (ii) the length of the fictitious model equals the length of the corresponding arterial model in its loaded state. The thickness of the fictitious model is denoted by δ_f.

Material properties of the fictitious model: For the fictitious model a linearly elastic material is assumed. The material's behaviour needs, however, to be transversely isotropic with respect to the z axis (Fig. 4). (Remark: A transversely isotropic material is characterised by a plane of isotropy at every point in the material.) Thus, in the fictitious model, the circumferential and axial stresses can be tuned independently by changing the material properties. This fact, as will be shown in the following sections, enables us to tune the material properties of the fictitious model in such a way that the stress distribution in the *loaded state of the fictitious model* $\Psi_{1\lambda}^C$ matches the stress distribution in the *stretched state of the arterial segment* $\Omega_{1\lambda}^C$. If the material behaviour of the fictitious model were isotropic this could not be achieved.

In cylindrical coordinates (Fig. 4) an elastic transversely isotropic material is defined by: "in plane" (P) and transverse (T) elastic moduli: $E_r = E_\phi = E_P$ and $E_z = E_T$; Poisson ratios: $v_{zr} = v_{z\phi} = v_{TP}$, $v_{rz} = v_{\phi z} = v_{PT}$; shear moduli: $G_{r\phi} = G_P$, $G_{rz} = G_{\phi z} = G_T$; and coefficients of the thermal expansion: $\alpha_r = \alpha_\phi = \alpha_P$, $\alpha_z = \alpha_T$ [25]. Moreover, the following relations hold: $v_{TP}/E_T = v_{PT}/E_P$ and $G_P = E_P/2(1+v_P)$. The thermal properties of the fictitious model, i.e., the thermal conductivity and specific heat, are considered isotropic.

Mechanical and thermal boundary conditions: Because the length of the fictitious model in the stress-free configuration Ψ_0^C already equals the length of $\Omega_{1\lambda}^C$, the model is prevented from deforming in the longitudinal direction when loaded. Consequently, the front and rear surfaces of the fictitious model are fixed in the axial direction (i.e., in the *z* direction). In addition, the adiabatic boundary conditions are applied to these surfaces.

Thermal loading of the fictitious model: The fictitious model with the uniform initial temperature distribution $T(r)=0$ is exposed to a temperature change ΔT_i and ΔT_o, applied, respectively, to its inner and outer surface (Fig. 4). Considering the given mechanical and thermal boundary conditions the stress distribution, corresponding to the established steady-state temperature field, is obtained.
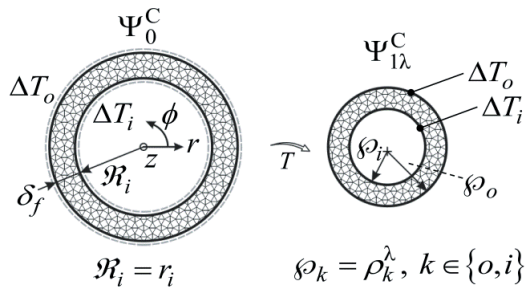
Fig. 4. *Geometry and thermal loading of the fictitious model (Ψ_0^C); radii r_i, ρ_i^λ, and ρ_o^λ are defined in Fig. 2; symbol T represents thermal loading*

Mathematical relations for computing the steady-state thermomechanical response of the fictitious circular segment are outlined next:

Steady-state thermal field: Taking into account the fact that the considered problem is a radial one, the steady-state heat equation, written in the cylindrical coordinates and with the omission of the internal heat generation term, is given as:

$$\frac{1}{r}\frac{d}{dr}\left(r\frac{dT}{dr}\right)=0, \tag{12}$$

where *r* is the radius. Taking the applied temperature changes on the segment's surfaces, $T(\mathcal{R}_i)=\Delta T_i$ and $T(\mathcal{R}_o)=\Delta T_o$, as associate boundary conditions into account the following temperature distribution $T(r)$ is obtained by solving Eq. (12):

$$T(r)=\Delta T_i+\frac{\Delta T_o-\Delta T_i}{\ln\left(\dfrac{\mathcal{R}_o}{\mathcal{R}_i}\right)}\ln\left(\frac{r}{\mathcal{R}_i}\right), \tag{13}$$

where $\mathcal{R}_i=r_i$ and $\mathcal{R}_o=\mathcal{R}_i+\delta_f$ (Fig. 4).

Steady-state thermomechanical response: The stress state associated with the initial temperature distribution $T(r)=T_{amb}=0$ being zero, the thermal stresses caused by the temperature change $T(r)$, Eq. (13), are governed by the generalised Hooke's law considering transversely isotropic material behaviour:

$$\varepsilon_{rr}=\frac{1}{E_P}\sigma_{rr}-\frac{v_P}{E_P}\sigma_{\phi\phi}-\frac{v_{TP}}{E_T}\sigma_{zz}+\alpha_P T,$$

$$\varepsilon_{\phi\phi}=-\frac{v_P}{E_P}\sigma_{rr}+\frac{1}{E_P}\sigma_{\phi\phi}-\frac{v_{TP}}{E_T}\sigma_{zz}+\alpha_P T,$$

$$\varepsilon_{zz}=-\frac{v_{PT}}{E_P}\sigma_{rr}-\frac{v_{PT}}{E_P}\sigma_{\phi\phi}+\frac{1}{E_T}\sigma_{zz}+\alpha_T T,$$

$$\varepsilon_{\phi z}=\frac{1}{G_P}\sigma_{\phi z},\quad \varepsilon_{rz}=\frac{1}{G_T}\sigma_{rz},\quad \varepsilon_{r\phi}=\frac{1}{G_T}\sigma_{r\phi}, \tag{14}$$

where ε_{ij} and σ_{ij} are the strain and the stress tensor. Next, the components of the strain tensor are expressed in terms of the radial and axial displacements $u(r)$ and $w(r)$ [26]:

$$\varepsilon_{rr}=\frac{du}{dr},\quad \varepsilon_{\phi\phi}=\frac{u}{r},$$

$$\varepsilon_{zz}=\frac{dw}{dz}=e=\text{const},$$

$$\varepsilon_{r\phi}=\varepsilon_{rz}=\varepsilon_{\phi z}=0. \tag{15}$$

Using Eqs. (14) and (15), the following relationships between the stress tensor components and radial displacement $u(r)$ are obtained:

$$\sigma_{rr}=A_P\frac{du}{dr}+A_{PT}\frac{u}{r}+A_{TP}e-\beta_P T,$$

$$\sigma_{\phi\phi}=A_{PT}\frac{du}{dr}+A_P\frac{u}{r}+A_{TP}e-\beta_P T,$$

$$\sigma_{zz}=A_{TP}\left(\frac{du}{dr}+\frac{u}{r}\right)+A_T e-\beta_T T,$$

$$\sigma_{r\phi}=\sigma_{rz}=\sigma_{\phi z}=0, \tag{16}$$

where the constants A_P, A_{PT}, A_{TP}, A_T, D, β_P and β_T are defined as:

$$A_P=\frac{E_P(1-v_{TP}v_{PT})}{D},\ A_{PT}=\frac{E_P(v_P+v_{TP}v_{PT})}{D},$$

$$A_{TP}=\frac{E_P(v_{TP}+v_P v_{TP})}{D},\quad A_T=\frac{E_T(1-v_P^2)}{D},$$

$$D=1-2v_P v_{TP}v_{PT}-2v_{TP}v_{PT}-v_P^2,$$

$$\beta_P=A_P\alpha_P+A_{PT}\alpha_P+A_{TP}\alpha_T,$$

$$\beta_T=2A_{TP}\alpha_P+A_T\alpha_T. \tag{17}$$

Next, by considering: (i) the expression for σ_{rr} in (16) and (ii) the substitution of $\sigma_{\phi\phi}$, as specified in Eq. (16), in the equilibrium equation (Eq. (7)), the problem reduces to two first-order differential equations for the variables $u(r)$ and $\sigma_{rr}(r)$ [26], written as:

$$\frac{\mathrm{d}u}{\mathrm{d}r} = -\frac{A_{\mathrm{PT}}}{A_{\mathrm{P}}}\frac{u}{r} + \frac{\sigma_{rr}}{A_{\mathrm{P}}} - \frac{A_{\mathrm{TP}}}{A_{\mathrm{P}}}e + \frac{\beta_{\mathrm{P}}}{A_{\mathrm{P}}}T,$$

$$\frac{\mathrm{d}\sigma_{rr}}{\mathrm{d}r} = \left(A_{\mathrm{P}} - \frac{A_{\mathrm{PT}}^2}{A_{\mathrm{P}}}\right)\frac{u}{r^2} + \left(\frac{A_{\mathrm{PT}}}{A_{\mathrm{P}}} - 1\right)\frac{\sigma_{rr}}{r} +$$

$$+ \left(A_{\mathrm{TP}} - \frac{A_{\mathrm{PT}}A_{\mathrm{TP}}}{A_{\mathrm{P}}}\right)\frac{e}{r} + \left(\frac{A_{\mathrm{PT}}}{A_{\mathrm{P}}} - 1\right)\frac{\beta_{\mathrm{P}}T}{r}. \quad (18)$$

The natural boundary conditions for a traction-free hollow cylinder are: $\sigma_{rr}(\mathfrak{R}_i) = 0$ and $\sigma_{rr}(\mathfrak{R}_o) = 0$. The constant e is zero ($e = 0$) because the segment is axially fixed. Once the system in Eq. (18) is solved taking into account the given boundary conditions, the remaining non-zero components of the stress tensor $\sigma_{\phi\phi}(r)$ and $\sigma_{zz}(r)$ can be obtained from the relations (Eq. (16)). The differential equations (Eq. (18)) were solved numerically using the finite difference method.

2.2.1 Identification of the Unknown Model Parameters

Up to now only a portion of the properties regarding the fictitious circular segment are defined. Actually, only the length and the inner radius $\mathfrak{R}_i$ of the segment's geometry in the zero-stress configuration Ψ_0^{C} have been specified while the thickness δ_f is unknown. Here, let us remember that the principal function of introducing the fictitious modelling is to match, by adequately choosing the respective model parameters, the stress distribution of the loaded state of the fictitious segment $\Psi_{1\lambda}^{\mathrm{C}}$ with the stress distribution of the stretched state of the arterial segment $\Omega_{1\lambda}^{\mathrm{C}}$. From the given theoretical framework, it follows that the mechanical response of the fictitious circular segment depends on: (i) the material properties, and (ii) the applied thermal loads, which may be considered to be unknowns to be determined in accordance with the expected objective.

The desired (targeting) state of the fictitious segment $\Psi_{1\lambda}^{\mathrm{C}}$ is the stretched state of the associated circular arterial segment $\Omega_{1\lambda}^{\mathrm{C}}$, i.e., its geometry and stress state. The parameters of the fictitious segment that need to be identified are: E_P, α_P, E_T, α_T, δ_f, ΔT_i, and ΔT_o. The remaining material properties that also define the fictitious segment, namely the thermal conductivity k, specific heat c, density ρ,

and Poisson's ratios v_P and v_{PT}, either do not affect the steady-state thermomechanical response of the segment (k, c, ρ) or are "interconnected" with some other material variables (v_P, v_{PT}). Their values were therefore arbitrarily pre-set prior to the identification procedure to: $v_P = 0.45$, $v_{PT} = 0.1$, $k = 100$ W/(mK), $c = 100$ J/(kgK) and $\rho = 2200$ kg/m³.

The objective function of the identification problem $\chi = \chi(v)$ is formulated to account for: (i) the relative error between the computed geometry (the fictitious segment) and desired geometry (the arterial segment), and (ii) the relative error between the computed and desired stress states; where v is the vector of optimisation variables $v = \left(E_P,\ \alpha_P,\ E_T,\ \alpha_T,\ \delta_f,\ \Delta T_i,\ \Delta T_o\right)$. The equation reads:

$$\chi(v) = \sum_{m=r,\phi,z}\frac{1}{N_m}\sum_{k=1}^{N_m}\left(\frac{S_{\mathrm{c}k}^m(v) - S_k^m}{S_k^m}\right)^2 +$$

$$+ g_\rho\sum_{k=i,o}\left(\frac{\wp_k(v) - \rho_k^\lambda}{\rho_k^\lambda}\right)^2, \quad (19)$$

where the vectors S_{c}^m and S^m; $m \in \{r,\phi,z\}$ are holding the computed and desired discrete values of the radial, circumferential, and axial stresses, respectively; and N_m; $m \in \{r,\phi,z\}$ is the length of vector S^m. (Note that in S^m, only the non-zero values of the stresses are included.) The quantities $\wp_k$ and ρ_k^λ; $k \in \{i,o\}$ are, respectively, the inner and outer radius of the fictitious (computed) and arterial (desired) segment, while g_ρ is the weighting factor.

2.3 Application of the Thermomechanical Analogy to a Realistic Arterial Segment

Let us assume that the irregularly shaped, straight tube that is presented in the upper left box in Fig. 5 represents an arterial segment (AS) obtained by the medical imaging process. This subsection schematically presents how the thermomechanical analogy can be used to predict the stretched state of the observed AS $\Omega_{1\lambda}^{\mathrm{AS}}$. The initial properties of the AS that have to be known for the procedure are: the AS material properties and the *in vivo* stretches λ and Λ (see Section 1).

First, the *equivalent circular tube* (segment) is defined based on the luminal cross-section area of the AS. The circular segment is then characterised as presented in Section 2.1 to determine its zero-stress configuration Ω_0^{C}. Now that this configuration
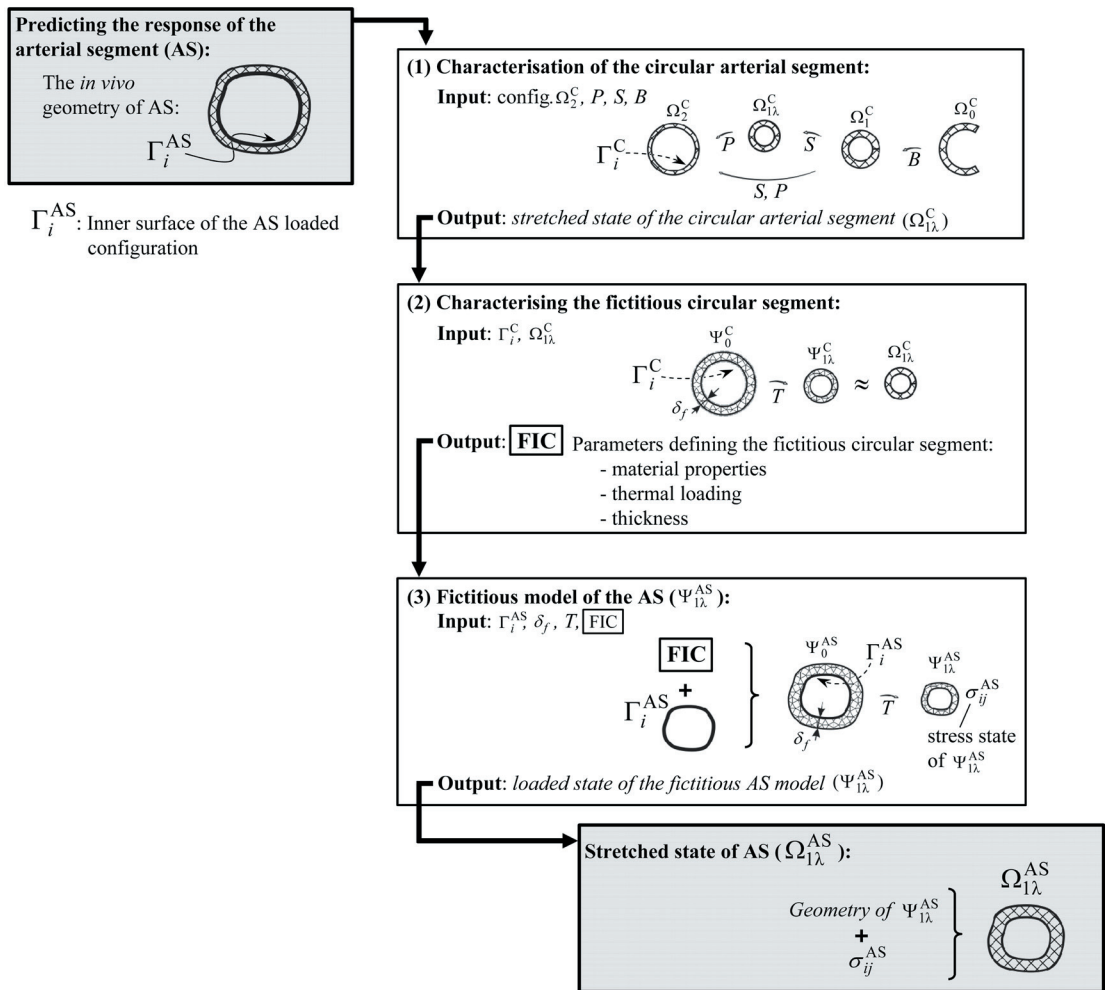
Fig. 5. *Methodology that predicts the stretched state ($\Omega_{1\lambda}^{AS}$) of a realistic arterial segment (AS)*

is known, the stretched state of the circular arterial segment $\Omega_{1\lambda}^{C}$ can be computed.

Next, the thermomechanical analogy to predict the residual stresses is defined on the basis of the obtained $\Omega_{1\lambda}^{C}$ state. This is done by identifying the fictitious circular segment Ψ_0^{C} corresponding to the characterised circular arterial segment. The initial geometry of Ψ_0^{C} is defined based on the surface Γ_i^{C} (see Fig. 5) whereas the thickness and material properties of Ψ_0^{C} should be identified so that the loaded state of the fictitious circular segment $\Psi_{1\lambda}^{C}$ resembles the stretched state of the circular arterial segment $\Omega_{1\lambda}^{C}$.

So far in this subsection, the stretched state of the AS has been quantified on the basis of a simplified AS geometry assumed to have the form of a circular tube. Based on this simplification, the parameters that characterise the fictitious circular segment Ψ_0^{C}

have been obtained. Next, the fictitious AS model Ψ_0^{AS} needs to be defined. This is done by applying the identified parameters of the fictitious circular segment (represented as FIC in Fig. 5) to the luminal surface of the AS, i.e., the surface Γ_i^{AS}. With thus defined Ψ_0^{AS} state, the thermomechanical response of the fictitious AS ($\Psi_{1\lambda}^{AS}$) can be computed. Note that in general this computation, i.e., solving the thermomechanical problem of the fictitious AS model, cannot be performed analytically because of the irregular geometry of the AS model. An approximate method, such as FEM, needs to be considered.

Finally, based on the results of the $\Psi_{1\lambda}^{AS}$ state the AS stretched state $\Omega_{1\lambda}^{AS}$ is approximated – note that $\Omega_{1\lambda}^{AS}$ is just defined based on the state $\Psi_{1\lambda}^{AS}$ and thus $\Omega_{1\lambda}^{AS}$ still includes the nonlinearities of the arterial mechanical response. The geometry of the $\Omega_{1\lambda}^{AS}$ state

equals the geometry of the $\Psi_{1\lambda}^{AS}$ state, and the stresses of the $\Omega_{1\lambda}^{AS}$ state equal the stresses of the $\Psi_{1\lambda}^{AS}$ state.

3 APPLICATION OF THE THERMOMECHANICAL ANALOGY TO THE ARTERIAL MODEL

The methodology for determining the residual stresses in the arterial segment, which were discussed thoroughly in the previous section, is generalised in this section to enable a prediction of the arterial response based on the *in vivo* arterial data. The individual steps of the methodology are demonstrated considering the AM, defined in Section 1 (Fig. 1).

To give an overview of the methodology, let us consider the flowchart presented in Fig. 6: (i) the starting data, needed for a prediction of the AM stretched state $\Omega_{1\lambda}^{AM}$, are the AM loaded geometry, the corresponding intraluminal pressure, the *in vivo* stretch λ, and the material properties of the AM. (ii) The stretched state of the AM is quantified based on characterising the mechanical response of two idealised (circular) arterial segments, corresponding to the arterial smallest (m) and largest (M) luminal cross-sectional area (see Fig. 1). (iii) The *fictitious arterial model* (FAM), i.e., the fictitious model of the AM, is defined next. This is done by defining the *fictitious circular segments* for the aforementioned *circular*

arterial segments. The identified parameters of the fictitious circular segments are then interpolated/extrapolated over the AM luminal cross-sectional area $A(z)$ and applied to the AM luminal surface Γ_i^{AM}. In this way, the FAM in its zero-stress state Ψ_0^{AM} is obtained. Its loaded state $\Psi_{1\lambda}^{AM}$ is then predicted by solving the corresponding steady-state thermomechanical problem. (iv) Finally, the AM stretched state $\Omega_{1\lambda}^{AM}$ is defined based on the obtained FAM $\Psi_{1\lambda}^{AM}$ state (i.e., based on the $\Psi_{1\lambda}^{AM}$ geometry and stress state). Further on, the loaded state of the AM Ω_2^{AM}, as well as the AM zero-stress state Ω_0^{AM}, are predicted. The individual steps of the methodology are presented in more detail in the following subsections.

3.1 Quantification of the AM Stretched State

The quantification of the AM stretched state is performed based on the observation of two idealised (circular) arterial segments that refer to the arterial smallest (m) and largest (M) luminal cross-sectional area, see Fig. 1b. The respective segments' geometry is obtained from the AM cross-sectional area $A(z)$ on the area equivalence basis:

$$A(z) = \pi a(z) b(z) = \pi \left(\tilde{r}_i(z) \right)^2, \qquad (20)$$
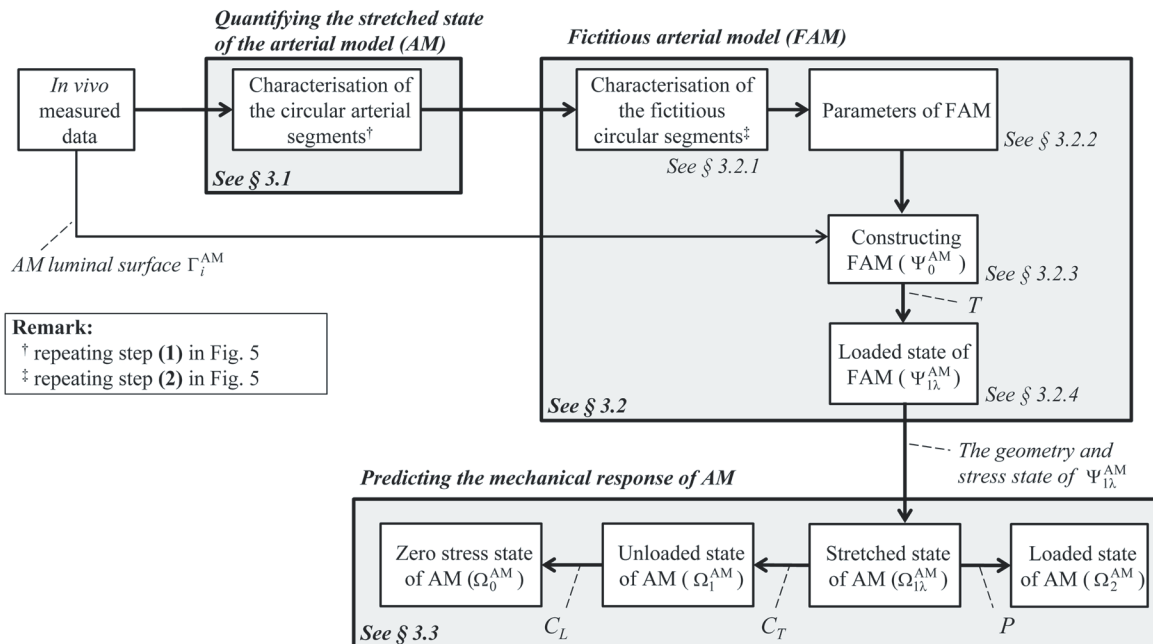
Fig. 6. *The methodology that predicts the mechanical response of the artery based on the arterial* in vivo *geometry (i.e., without the arterial zero-stress state being known); the symbols P, T, C_T, and C_L represent pressurising, thermal loading, transversal cut, and longitudinal cut, respectively*

from where the equivalent radius $\tilde{r}_i(z)$, see r_i Fig. 2, is computed, and in particular, $\tilde{r}_i^{(k)} = \sqrt{A^{(k)}/\pi}$; $k \in \{m, M\}$ for segment (m) and (M), respectively. Next, the zero-stress state configurations of both segments, (m) and (M), are separately identified (see Section 2.1). The identification results are tabulated in Table 1, where $R_o^{(k)}$ and $\Theta_0^{(k)}$; $k \in \{m, M\}$ are respectively the outer radius and the opening angle for the segment (m) and (m).

With the zero-stress state of both segments determined, their stretched states, designated as $\Omega_{1\lambda}^{(m)}$ and $\Omega_{1\lambda}^{(M)}$ for the segment (m) and (M), respectively, can be computed.

Table 1. *The identified properties of the circular arterial segments*

Segment: k	(m)	(M)	($\tilde{m}$)
$R_o^{(k)}$ [mm]	4.45	5.34	4.9
$\Theta_0^{(k)}$ [°]	132.89	129.94	131.34

3.2 Fictitious Arterial Model

As discussed in Section 2.2, the AM stretched state $\Omega_{1\lambda}^{AM}$ can be predicted by defining an associated fictitious arterial model, designated as FAM and solving the corresponding thermomechanical problem. The advantage of this approach is that the arterial response is predicted without the arterial zero-stress state being known. How to define the FAM is discussed in detail in the following subsections.

3.2.1 *Thermomechanical Characterisation of the Fictitious Circular Segments*

The thermomechanical analysis of the FAM is basically defined by the characterisation of the *fictitious circular segments* corresponding to the *circular arterial segments* (m) and (M), as presented in step 2 in Fig. 5. Note that in this way, essentially, the properties of the FAM for its location $A^{(m)}$ and $A^{(M)}$, see Fig. 1, are defined.

The variables that need to be identified in order to characterise both fictitious segments (see Section 2.3) are: the material properties, the thicknesses $\delta_f^{(k)}$, the thermal loadings $\Delta T_i^{(k)}$, and $\Delta T_o^{(k)}$; $k \in \{m, M\}$ for segment (m) and (M), respectively. During the identification of the unknowns, the material properties of both segments were initially assumed to be equal because they represent the material properties of the FAM. However, what was found is that in order for the stresses of both fictitious segments to correspond to the stresses of the associated arterial segments, the coefficient of thermal expansion α_T has to be identified separately for each segment.

Because of a relatively large number of unknowns, the identification procedure was performed in the following way. First, the identification of the parameters defining the fictitious segment (m) (see Section 2.2.1.) is performed. The unknowns to be determined: thickness $\delta_f^{(m)}$, material constants E_P, α_P, E_T and $\alpha_T^{(m)}$, and thermal loadings $\Delta T_i^{(m)}$ and $\Delta T_o^{(m)}$, are identified by targeting the $\Omega_{1\lambda}^{(m)}$ state of the circular arterial segment (m). Next, the identification of the fictitious segment (M) is performed by adopting the material properties identified for the segment (m). The remaining variables to be determined: $\delta_f^{(M)}$, $\Delta T_i^{(M)}$, $\Delta T_o^{(M)}$, and $\alpha_T^{(M)}$, are obtained by targeting the $\Omega_{1\lambda}^{(M)}$ state of the circular arterial segment (M). The result of the identification is given in Table 2.

Table 2. *The identified properties of the fictitious circular segments*

Segment: k		(m)	(M)
$\Delta T_i^{(k)}$	[°]	1.0059	1.069
$\Delta T_o^{(k)}$	[°]	1.255	1.295
$\delta_f^{(k)}$	[mm]	0.6931	0.71
$\alpha_T^{(k)}$	[1/K]	−0.05	−0.048
E_P	[kPa]	299.29	
E_T	[kPa]	299.29	
α_P	[1/K]	−0.1388	

3.2.2 *Thermomechanical Characterisation of the Fictitious Arterial Model*

As mentioned, the parameters of the FAM are defined based on the parameters identified for the *fictitious circular segments* (m) and (M). The parameters that are common to both fictitious segments are also assumed constant in the FAM. These are: E_P, α_P, E_T, G_P, G_T, ν_P, ν_{PT}, k, c and ρ (see Section 2.2). However, some parameters of the fictitious segments, namely their thickness δ_f, thermal loadings ΔT_i and ΔT_o, and the coefficient of thermal expansion α_T, are not the same in both fictitious segments. We will refer to these variables as the *varying variables* because they depend on the cross-sectional area of the fictitious circular segments. Note that the cross-sectional area of the FAM also varies – from $A^{(m)}$ to $A^{(M)}$. Therefore,

in order to apply the *varying variables* to the FAM, their values need to be generalised (interpolated) over the cross-sectional area $A(z)$ of the FAM.

In this paper, a linear interpolation of the *varying variables* across the $A(z)$, i.e., from $A^{(m)}$ to $A^{(M)}$, is adopted. For example, a linear interpolation of the variable α_T^{AM} (where the superscript "AM" refers to the interpolated variable) as a function of $A(z)$ can be written as:

$$\alpha_T^{AM}(A) = \alpha_T^{(m)} \Upsilon_m(A) +$$
$$+ \alpha_T^{(M)} \Upsilon_M(A) = \alpha_T^{AM}(z), \quad (21)$$

where $\alpha_T^{(m)} = \alpha_T\left(A^{(m)}\right)$ and $\alpha_T^{(M)} = \alpha_T\left(A^{(M)}\right)$, and the shape functions $\Upsilon_m(A)$ and $\Upsilon_M(A)$ are defined as: $\Upsilon_m(A) = 1 - \dfrac{A - A^{(m)}}{A^{(M)} - A^{(m)}} = \Upsilon_m(z)$

and $\Upsilon_M(A) = \dfrac{A - A^{(m)}}{A^{(M)} - A^{(m)}} = \Upsilon_M(z)$. Note that

$\alpha_T^{AM}(A)$ (as well as $\Upsilon_m(A)$ and $\Upsilon_M(A)$) is essentially a function of the coordinate z, thus $\alpha_T^{AM}(z)$ because $A = A(z)$ (see Fig. 1). The same interpolation approach is used to define the remaining *varying variables*: $\delta_f^{AM}(z)$, $\Delta T_i^{AM}(z)$ and $\Delta T_o^{AM}(z)$. Their variations as a function of the coordinate z are plotted in Fig. 7.

Remark: For the purpose of defining the properties of the FAM, it would be possible to characterise more than two circular arterial segments. For these segments, the corresponding fictitious segments could be obtained and characterised, thus allowing for a higher-order interpolation used in the

FAM characterisation. However, as shown in Section 4.1.1, the linear interpolation, which is used to define the FAM properties, is sufficient.
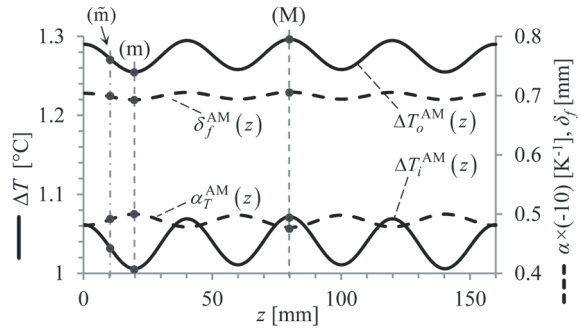
Fig. 7. *Variations of the FAM properties:* $\alpha_T^{AM}(z)$, $\delta_f^{AM}(z)$, $\Delta T_i^{AM}(z)$, *and* $\Delta T_o^{AM}(z)$ *(see Eq. (21)), along the coordinate z*

3.2.3 Construction of the Fictitious Arterial Model (FAM) Considering in vivo Measured Data

Based on the characterisation of the FAM parameters that were determined in previous subsections under the assumption of idealised circular arterial segments, it is now possible to construct a computational model of the FAM taking *in vivo* measured data into account. Accordingly, the geometry of the FAM is constructed based on the inner surface of the AM Γ_i^{AM} (Fig. 1), as shown in Fig. 8, considering its variation Γ_i^{AM} along the z direction. As discussed, we define the inner surface of the FAM to be the same as the inner (luminal) surface of the associated AM, whereas the outer surface of the FAM is obtained by applying the thickness $\delta_f^{AM}(z)$ (Fig. 7) to the surface Γ_i^{AM}.

Fig. 8. *Constructing the fictitious arterial model*

Note that the thickness of the FAM is assumed to be constant in the circumferential direction of the model while changing in the z direction.

As assumed, the material behaviour of the FAM is transversely isotropic with respect to the z axis. Some of the material properties are constant (see Table 2) whereas $\alpha_T^{\mathrm{AM}}(z)$ is given in Fig. 7. The remaining material parameters that are not presented in Table 2 are given in Section 2.2.1.

3.2.4 Loaded State of the Fictitious Arterial Model

In order to evaluate the residual stresses of the AM, the above-defined FAM is thermally loaded by the temperature changes $\Delta T_i^{\mathrm{AM}}(z)$ and $\Delta T_o^{\mathrm{AM}}(z)$ applied respectively on the inner and outer surfaces of the model (Fig. 8). Note that both $\Delta T_i^{\mathrm{AM}}(z)$ and $\Delta T_o^{\mathrm{AM}}(z)$ (Fig. 7) are assumed to be constant in the circumferential direction of the model, while changing in the z direction. The stress distribution in the loaded state of the FAM $\Psi_{1\lambda}^{\mathrm{AM}}$, obtained by solving the given thermomechanical problem with associated mechanical and thermal boundary conditions (see Section 2.2), yields an approximation of the residual stresses distribution in the AM and its configuration.

3.3 Modelling the Mechanical Response of the Arterial Model with Residual Stresses Considered

The geometry and the stresses of the loaded state $\Psi_{1\lambda}^{\mathrm{AM}}$ of the FAM represent an approximation to the geometry and stresses of the arterial model in its stretched state $\Omega_{1\lambda}^{\mathrm{AM}}$. The computational model of the AM stretched state $\Omega_{1\lambda}^{\mathrm{AM}}$ is thus specified by adopting the geometry of the $\Psi_{1\lambda}^{\mathrm{AM}}$ configuration and the given arterial material behaviour. For the initial stress state of the thus-defined model, representing, actually, the residual stresses in the artery, the stresses from $\Psi_{1\lambda}^{\mathrm{AM}}$ are adopted whereas the stretches corresponding to the $\Omega_{1\lambda}^{\mathrm{AM}}$ configuration with the initial stresses considered are obtained by taking into account the arterial material model, Eq. (1).

From the arterial stretched state all the remaining arterial states can be predicted (see the lower grey box in Fig. 6). The *loaded state* Ω_2^{AM} of the AM is obtained by inflating the AM from its stretched state. The AM *unloaded state* $\Omega_{1\lambda}^{\mathrm{AM}}$ is predicted by releasing the axial stretch λ from the AM stretched state, whereas the approximation of the AM *zero-stress state* Ω_0^{AM} is obtained by further releasing the constraints on one of the AM symmetry surfaces (Fig. 2).

Remark: The reason why the arterial stretched state $\Omega_{1\lambda}^{\mathrm{AM}}$ is predicted with the fictitious model, and not, for instance, by considering the arterial unloaded state Ω_1^{AM}, is the following: normally, the goal of the arterial characterisation is to predict the arterial loaded state. Therefore it is more convenient to predict the *arterial loaded state* from the *arterial stretched state* given that in between both states there is only the inflation process (see Fig. 2). For example, by predicting the *arterial loaded state* from the *a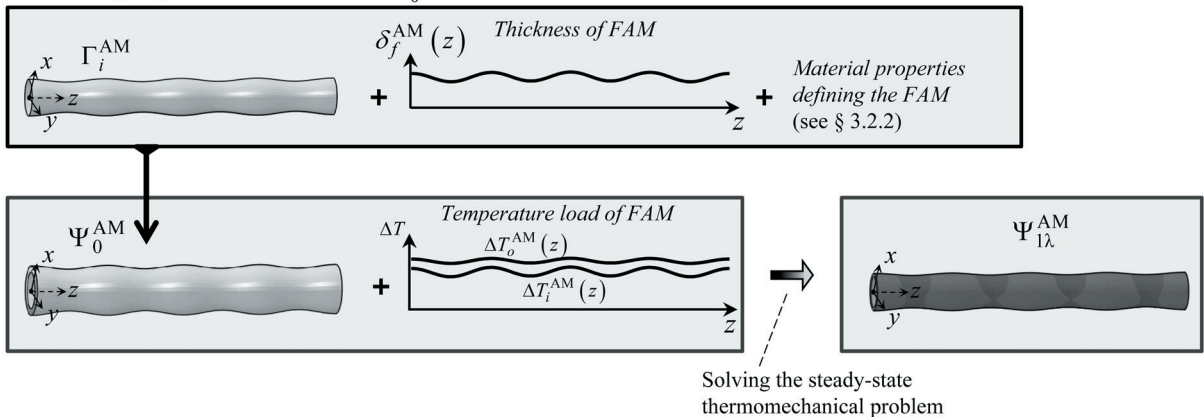rterial unloaded state*, the artery first needs to be stretched for λ in order to obtain its stretched state, and can only later be inflated.

4 RESULTS, VALIDATION OF THE METHODOLOGY AND DISCUSSION

In this section, the developed methodology of determining the arterial response based on the *in vivo* measured arterial data and taking the residual stresses into account is applied in the analysis of the given case study (Fig. 1). In the analysis, regardless of whether the computation applies to the real or the fictitious model, the computations that relate to the *circular* models are performed using the finite difference method while the FEM is used, because of the complexity of respective model geometries, for the computations related to the arterial models.

First, after giving a brief description of the numerical model in Section 4.1, the results for the circular arterial and fictitious segments are presented in Section 4.2. The results regarding the arterial response are presented in Sections 4.3.1 and 4.3.2 for the AM stretched and loaded state, respectively. Finally, at the end of the section, the methodology is validated based on the prediction of the AM zero-stress state.

4.1 FEM Modelling

Taking into consideration that the geometry of the FAM loaded state $\Psi_{1\lambda}^{\mathrm{AM}}$ configuration may be considered to be an approximation to the geometry of the AM stretched state $\Omega_{1\lambda}^{\mathrm{AM}}$ configuration, only one single FEM discretisation is needed for all of the computations regardless of whether the computation applies to the real or the fictitious model.

The FEM model is constructed based on the geometry of the FAM in its stress-free configuration Ψ_0^{AM} (Fig. 8) taking into account the data specified in Section 3.2.3. In principle, because the considered case study (Fig. 1) is symmetric with respect to two perpendicular planes (note that the cross section of the

AM is elliptical), only one quarter of the model could be considered for computations. However, in order for the computation of the AM *zero-stress state* Ω_2^{AM} to also be performed (see Fig. 2), half of the model is considered for the FEM discretisation with the $x-z$ plane being the plane of symmetry. The FEM model is built of 17640 eight-node brick elements with displacement and temperature degrees of freedom.

The conceived FEM model is used first for the computation of the FAM loaded state $\Psi_{1\lambda}^{AM}$. For this purpose, a linearly elastic, transversely isotropic behaviour of the material is assumed taking the data specified in Section 3.2.3 into account. The thermomechanical analysis is performed using the commercial FEM software Abaqus/Standard [27] under prescribed boundary and loading conditions. The front and rear surfaces of the model are fixed in the z direction whereas they are free to move in the $x-y$ plane. On the same surfaces, the adiabatic thermal conditions are applied. Moreover, proper mechanical and thermal conditions are applied on the symmetry surfaces (see Section 3.2.4).

The stresses of the FAM loaded state $\Psi_{1\lambda}^{AM}$ represent an approximation of the residual stresses in the artery. The computational model of the AM stretched state $\Omega_{1\lambda}^{AM}$ is thus specified by adopting the geometry of the $\Psi_{1\lambda}^{AM}$ configuration and related stresses as initial stresses, and, importantly, taking the given arterial material behaviour into account, Eq. (1). Clearly, the stretches corresponding to the $\Omega_{1\lambda}^{AM}$ configuration are readily computed considering the constitutive relations and the initial stresses. When the thus-defined computational model $\Omega_{1\lambda}^{AM}$ is inflated with the intraluminal pressure P, the *loaded state* Ω_2^{AM} is computed. If, on the contrary, the constraints on the axial displacement are removed and the

axial stretch λ is released, the *unloaded state* Ω_1^{AM} can be computed. Finally, by further releasing the constraints on one of the AM symmetry surfaces, the approximation of the zero-stress state Ω_0^{AM} can be attained.

4.2 Arterial and Fictitious Circular Segment

The stretched states of the circular arterial segments (m) $\Omega_{1\lambda}^{C(m)}$ and (M) $\Omega_{1\lambda}^{C(M)}$ are presented in Fig. 9. Both states are computed as presented in Section 2.1 based on the identified data of their zero-stress states (Table 1). As seen in Fig. 9, the stresses predicted for both segments are in the same order of magnitude. The circumferential stresses are somewhat bigger for the segment (m) whereas the axial stresses are higher in the segment (M). The same graphs also represent the stresses predicted for the corresponding fictitious segments $\Psi_{1\lambda}^{C(m)}$ and $\Psi_{1\lambda}^{C(M)}$ as well as for the fictitious circular segments (m) and (M), respectively.

Despite a minimal deviation between the axial stresses (see Fig. 9), an excellent agreement of the stress distributions and geometries between the circular arterial segments ($\Omega_{1\lambda}^{C}$) and the fictitious circular segments ($\Psi_{1\lambda}^{C}$) is obtained. The results presented demonstrate that the thermomechanical state, obtained by thermally loading a fixed, closed (fictitious) tube, is equivalent to the stretched state that is obtained by bending and stretching an open arterial section.

As discussed, the fictitious *circular segments* have essentially been defined in order to characterise the thermomechanical procedure and to apply the determined parameters of fictitious segments to the AM. So far, we have demonstrated that the stretched state of the arterial segments (m) and (M) can be
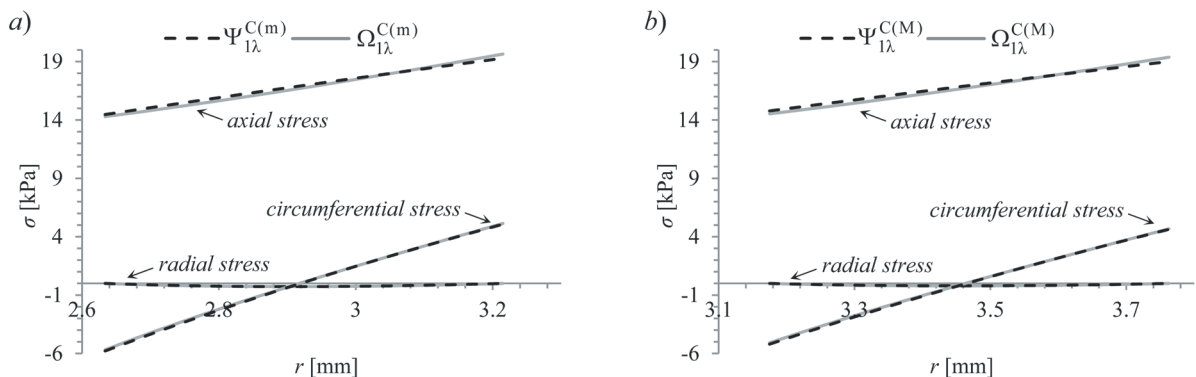
Fig. 9. *Stresses computed for the $\Omega_{1\lambda}^{C(m)}$ and $\Omega_{1\lambda}^{C(M)}$ states of the circular arterial segments (full line), and their comparison with the stresses obtained for the fictitious circular segments $\Psi_{1\lambda}^{C(m)}$ and $\Psi_{1\lambda}^{C(M)}$ (broken line); the results for the segment (m) are given in a) whereas b) shows the results for the segment (M)*

obtained with the fictitious segments (m) and (M), respectively. In the next subsection, we shall assess the used linear interpolation that was applied to interpolate the properties of the fictitious segments with the purpose of defining the FAM (see Section 3.2.2).

4.2.1 The Adequacy of the Considered Interpolation

The variables $\alpha_T^{AM}(z)$, $\delta_f^{AM}(z)$, $\Delta T_i^{AM}(z)$ and $\Delta T_o^{AM}(z)$ were obtained by linearly interpolating the corresponding variables that have been determined for the fictitious segments (m) and (M) (see Section 3.2.2). The adequacy of this approximation is assessed by characterizing an arterial segment, denoted by ($\tilde{m}$), with the equivalent radius $\tilde{r}_i^{(\tilde{m})} = (\tilde{r}_i^{(m)} + \tilde{r}_i^{(M)})/2$. For the segment ($\tilde{m}$), its stretched state $\Omega_{1\lambda}^{C(\tilde{m})}$ is identified and then compared to the stretched state, obtained through defining an associated fictitious segment ($\Psi_{1\lambda}^{C(\tilde{m})}$ state).

The parameters of the fictitious segment ($\tilde{m}$) are obtained by considering the data in Fig. 7 and Table 2. The loaded state of the fictitious segment ($\Psi_{1\lambda}^{C(\tilde{m})}$) is computed as presented in Section 2.2.

To determine the stretched state of the arterial segment ($\tilde{m}$), its zero-stress configuration needs to be identified as presented in Section 2.1. The identified values of the unknowns $R_o^{(\tilde{m})}$ and $\Theta_0^{(\tilde{m})}$ are given in Table 1. The computed stresses of the arterial segment ($\Omega_{1\lambda}^{C(\tilde{m})}$) and the fictitious segment ($\Psi_{1\lambda}^{C(\tilde{m})}$) are presented in Fig. 10.
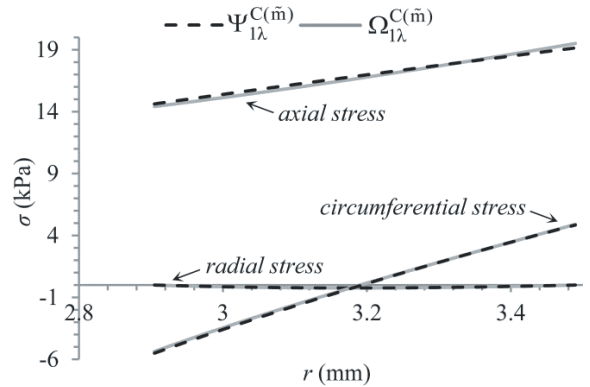
Fig. 10. The calculated stresses of the $\Omega_{1\lambda}^{C(\tilde{m})}$ state of the circular artery segment ($\tilde{m}$) (full line), compared to stresses of the $\Psi_{1\lambda}^{C(\tilde{m})}$ state, computed with the associated fictitious circular segment (broken line)
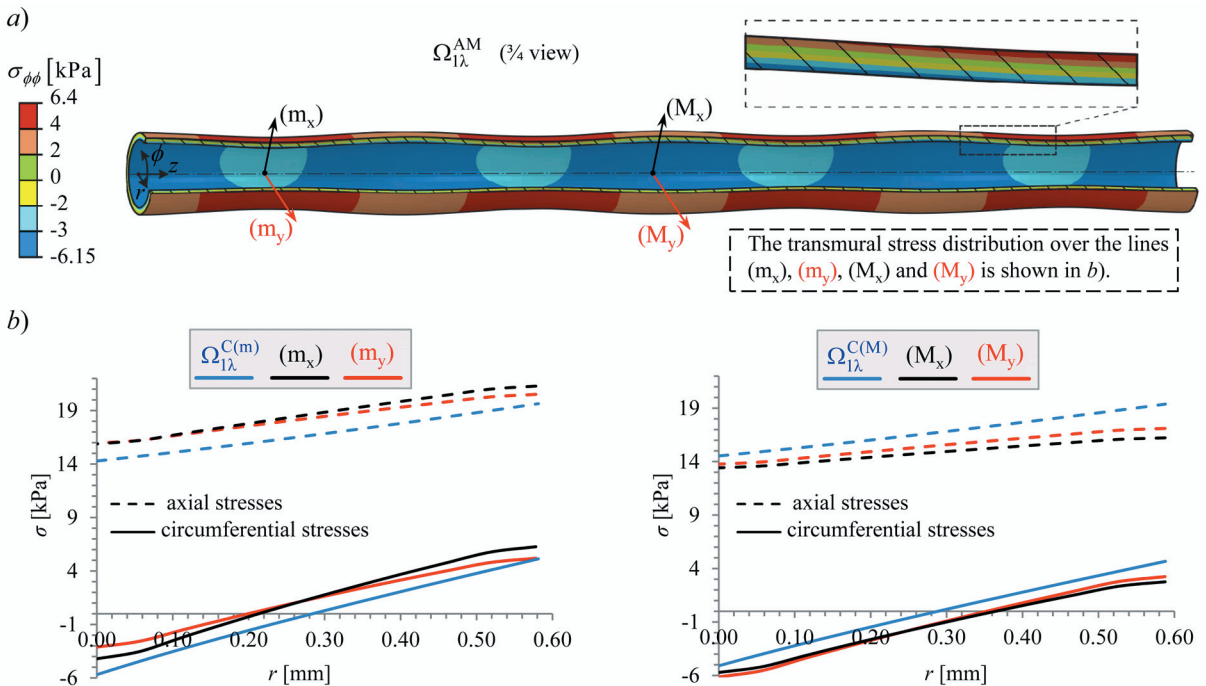
Fig. 11. The predicted AM loaded state (Ω_2^{AM}): a) 3D view and b) the transmural distribution of the circumferential and axial stresses at the AM positions (m_x), (m_y), (M_x), and (M_y); for their location see Fig. 11a

Despite a slight discrepancy between the axial stresses (Fig. 10), the agreement between the obtained arterial and fictitious state of the segment ($\tilde{m}$) is excellent. Based on these results, it is possible to conclude that the first-order interpolation, which is used to interpolate the properties of the fictitious segments, is justified.

4.3 The Predicted Mechanical Response of AM

4.3.1 AM Stretched State

The circumferential stresses $\sigma_{\phi\phi}$ of the predicted AM stretched state ($\Omega_{1\lambda}^{AM}$) are presented in Fig. 11a. The transmural variation of the $\sigma_{\phi\phi}$ shows the bending distribution (see the zoomed-in detail along the wall thickness), as was also observed for the circular arterial segments. In contrast to the straight circular arterial segment, the stresses in the AM vary along the AM length because of the varying AM cross-sectional area. The transmural distribution of the stresses at the AM positions (m) and (M) are shown in Fig. 11b (red and black curves). In the figure, the stresses are presented at the position of the AM cross-sectional x and y axis. Note that the stresses at position (m) are higher on the (m_x) axis compared to the values on the (m_y) axis. At position (M), on the other hand, the opposite is observed. This is interesting because the x axis represents the cross-sectional semi-minor axis at both position (m) as well as at position (M) (see Fig. 1). The reason for this can be probably attributed to the variable cross-sectional area of the AM.

Next, let us compare the transmural distribution of the stresses at the AM locations (m) and (M) with the stresses predicted for the *circular arterial segments* $\Omega_{1\lambda}^{C(m)}$ and $\Omega_{1\lambda}^{C(M)}$. The stress distribution in Fig. 11b that corresponds to the circular arterial segment is shown in blue. At position (m), the stresses predicted for the AM are somewhat higher in comparison to the stresses of $\Omega_{1\lambda}^{C(m)}$, whereas the opposite is true for the position (M). Such an error between the stresses predicted for the AM and for the circular arterial segments is a result of the AM variable cross-sectional area. The behaviour of the individual AM cross sections or segments is limited by the behaviour of the whole AM. Therefore, the individual AM segments cannot extend freely as is the case of the circular arterial segment. The error between the maximal circumferential stresses predicted for circular arterial segments and those predicted for the AM is around 30%.

4.3.2 AM Loaded State

The predicted AM loaded state (Ω_2^{AM}) is presented in Fig. 12a. The stresses, as seen in the figure, are somewhat higher in the areas where the arterial cross-sectional area is larger. The maximal circumferential stress $\sigma_{\phi\phi}$ is 73 kPa, which appears on the outer surface of the AM wall at the AM location (M_y) (see the graphs in Fig. 12b). The range of stresses $\sigma_{\phi\phi}$, as well as their transmural distribution (Fig. 12b), agree with the corresponding data from literature [24] and [28].

Next, let us see the stresses that would be predicted for the AM sections (m) and (M) if they were treated as straight circular segments. The loaded state of the circular arterial segments (m) and (M), presented as $\Omega_2^{C(m)}$ and $\Omega_2^{C(M)}$, respectively, are shown in blue in Fig. 12b. The loaded states of both circular arterial segments (m) and (M) are computed as presented in Section 2.1.

Similar to what has been observed in the previous subsection, the stresses predicted for the AM at the position (m) are somewhat higher in comparison to $\Omega_2^{C(m)}$, whereas the opposite is true for the position (M). The reason for this lies in the AM variable cross section which prevents the individual cross sections of the AM to extend freely. The error between the stresses predicted for the circular arterial segments and for those of the AM can be as high as 15%. Given the size of the error, the suitability of using the circular arterial segments in order to determine the stress states of arteries, as is common in literature, is questionable.

4.3.3 Predictions of the AM Zero-Stress State

A way to partially verify the adequacy of the presented method is to simulate the opening angle experiment. If the stresses predicted for the arterial opened-up configuration are almost null, the method can be considered adequate. The same approach, for instance, can be seen in [2].

The zero-stress state of the AM (Ω_0^{AM}) is predicted based on the AM stretched state ($\Omega_{1\lambda}^{AM}$) in two steps. First, the axial constraint that is applied to the $\Omega_{1\lambda}^{AM}$ state is released. The AM thereby contracts axially and occupies its unloaded state Ω_1^{AM}. In addition, the AM zero-stress state is obtained with a longitudinal cut which is performed in a numerical analysis by releasing the constraint on one of the AM symmetry surfaces (located on the $x-z$ plane, see Fig. 13a). The predicted equilibrium state of the AM opened-up configuration, obtained with a single longitudinal cut is designated as $\Omega_0^{AM\#1}$ and

(a)

(b)
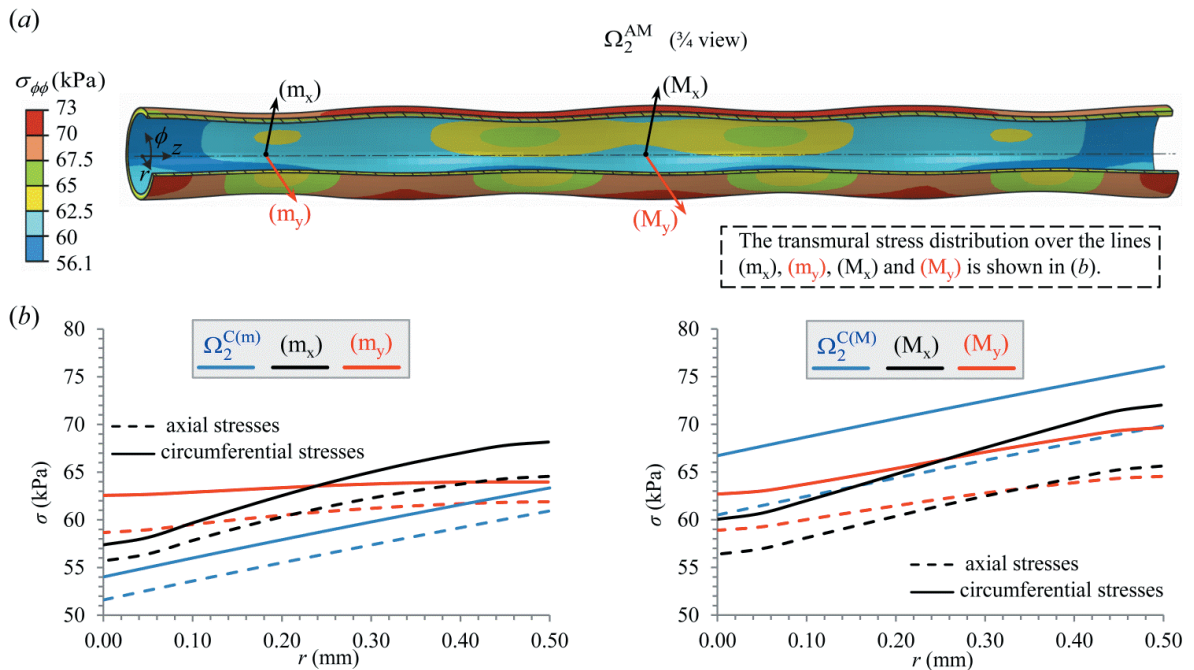
Fig. 12. *The predicted AM stretched state ($\Omega_{1\lambda}^{AM}$): a) 3D view and b) the transmural distribution of the circumferential and axial stresses at positions (m_x), (m_y), (M_x), and (M_y): their location is presented in Fig. 12a*

(a)
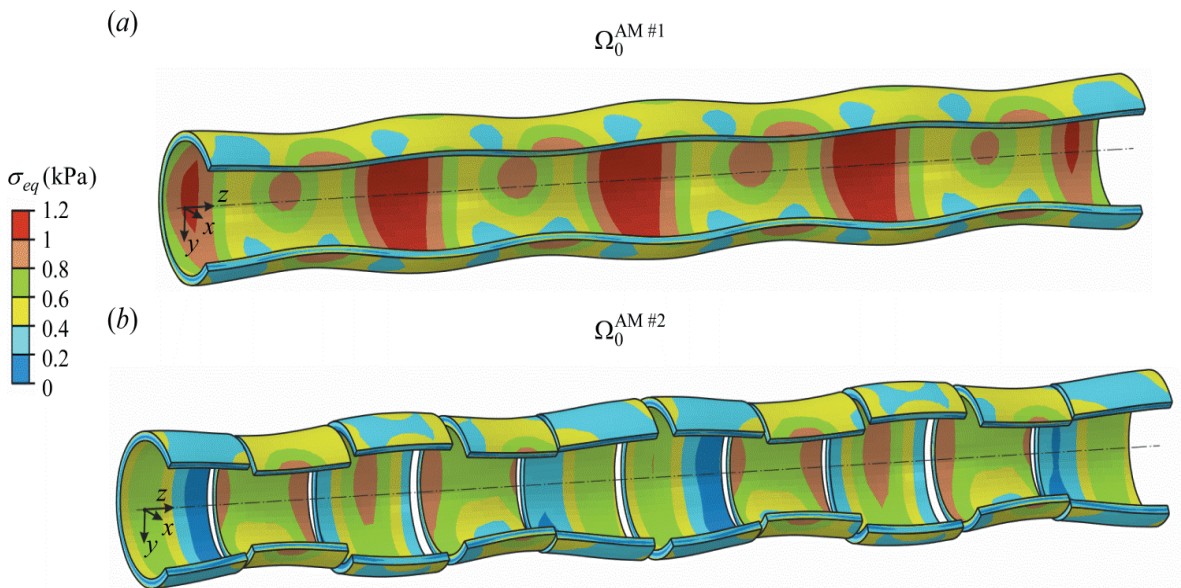
Fig. 13. *Predictions of the AM zero-stress state: a) zero-stress state $\Omega_0^{AM\,\#1}$, obtained by longitudinal cutting of the AM unloaded state, and b) zero-stress state $\Omega_0^{AM\,\#2}$, obtained by transversely cutting the predicted AM $\Omega_0^{AM\,\#1}$ state into smaller segments*

is presented in Fig. 13a. The maximal von Mises equivalent stresses in $\Omega_0^{AM\,\#1}$ are around 1.2 kPa (Fig. 13a). These stresses occur locally in the areas where the AM cross-sectional area is larger. As seen in Fig. 13a, the predicted AM $\Omega_0^{AM\,\#1}$ state is not stress-free. The reason for this is that the AM variable cross-sectional area limits the AM's ability to extend freely, and consequently, it prevents the AM from occupying its *zero-stress* configuration. In order to obtain a better estimation of the AM zero-stress state, the predicted AM $\Omega_0^{AM\,\#1}$ state would have to be cut into smaller segments. This procedure is presented next.

The predicted AM zero-stress state $\Omega_0^{AM\#2}$, which is obtained by cutting the $\Omega_0^{AM\#1}$ state into 10 separate sections, is presented in Fig. 13b. As seen in the figure, the maximal stresses obtained for the individually cut segments ($\Omega_0^{AM\#2}$ state) are less than 1 kPa. These stresses occur in the second, third, and fourth segments (from both ends) whereas the maximal stresses range up to 0.8 kPa in the remaining ones (the first and the fifth segment from both ends). For these segments, the stresses are lower by approximately 30% compared to the AM $\Omega_0^{AM\#1}$ state. Higher stresses that appear in the second, third, and fourth segments are the result of the shape of the segments, which is, if compared to the first segment, somewhat curved in the z direction. Based on the results presented, however, and given that the stresses of the AM $\Omega_0^{AM\#2}$ state are relatively low, it is possible to conclude that the use of the thermomechanical analogy in order to enforce the residual (bending and stretching) stresses into arterial model is justified.

5 CONCLUSION

In this paper, a method is presented which determines the arterial mechanical response without knowing the arterial opened-up zero-stress configuration. The arterial configuration on which the method is based is the arterial loaded configuration. We approach the problem of predicting the arterial residual (bending and stretching) stresses by considering a thermomechanical analogy. These stresses are determined by thermally loading a clamped, closed tube (called a *fictitious model*). The initial geometry of the fictitious model is constructed based on the luminal surface of the observed artery. The consequence of the applied thermal loading is that the fictitious model shrinks and the thermal (residual) stresses occur. In this paper, we have demonstrated that the loaded state of the fictitious model (i.e., its geometry and its stress state) is equivalent to the stretched state of the arterial model (see Section 4.1). However, in order for the presented analogical procedure to be adequate, the parameters of the fictitious model need to be properly defined.

The adequacy of the method has been verified by computing the zero-stress state of the arterial model. As presented in Fig. 13, the equilibrium configurations of the segments that are obtained following a longitudinal and transversal cut of the arterial model have the form of an opened-up tube. Furthermore, the residual stresses remaining in the segments are fairly mild compared to the stresses of the arterial stretched state. The results obtained show that the residual stresses predicted for the arterial stretched state with the thermomechanical analogy exhibit what is known as the bending distribution. This has proved the method to be adequate.

An interesting aspect that aroused in the analysis of the results is suitability of using the *straight circular arterial segment* for the characterisation of the arteries. This is a common approach in the literature **[19]**, **[28]** and **[29]**. The segment is considered straight and stand-alone, meaning that the effect of the remaining artery in the segment's axial direction is not taken into account. Based on our results (see Section 4.2.2), the error between the stresses that are predicted for a straight circular arterial segment, and the stresses predicted for the arterial model, can be as high as 15%. Additionally, the gradient of transmural distribution of the stresses for both cases differs (see Fig. 12). Nevertheless, it has to be said that a realistic artery does not exhibit such a variable cross-sectional area as was considered in this article. In a realistic artery, in fact, the influence of neglecting the effect of the remaining artery is smaller when observing one straight circular segment as a separate unit.

The results of the methodology presented in the paper show a distinction between the mechanical state predicted for a circular segment that is observed as a separate unit and the mechanical state that is predicted when the arterial variable cross-sectional area is taken into account. This topic therefore warrants further research, and presents one of the goals of our further work. Moreover, some of the arterial properties that have been neglected in this work, such as their multi-layered structure or associated longitudinal residual stress, are planned to be implemented further in the methodology.

As for the clinical applicability of the presented methodology, the methodology could – supported by the medical imaging techniques – serve as a useful tool for predicting the patient-specific arterial mechanical response.

6 REFERENCES

[1] Holzapfel, G.A., Sommer, G., Auer, M., Regitnig, P., Ogden, R.W. (2007). Layer-Specific 3D residual deformations of human aortas with non-atherosclerotic intima thickening. *Annals of Biomedical Engineering*, vol. 35, no. 4, p. 530-545, **DOI:10.1007/s10439-006-9252-z.**

[2] Alastrué, V., Pena, E., Martinez, M.A., Doblare, M. (2007). Assessing the use of the "opening angle method" to enforce residual stresses in patient-specific arteries. *Annals of Biomedical Engineering*, vol. 35, no. 10, p. 1821-1837, **DOI:10.1007/s10439-007-9352-4.**

[3] Vossoughi, J. (1992). Longitudinal residual strains in arteries. *Proceedings of the 11th Southern Biomedical Engineering Conference*, Memphis.

[4] Wang, R., Gleason, R.L. (2010). A mechanical analysis of conduit arteries accounting for longitudinal residual strains. *Annals of Biomedical Engineering*, vol. 38, no. 4, p. 1377-1387, **DOI:10.1007/s10439-010-9916-6**.

[5] Fung, Y.C., Liu, S.Q. (1989). Change of residual strains in arteries due to hypertrophy caused by aortic constriction. *Circulation Research*, vol. 65, no. 5, p. 1340-1349, **DOI:10.1161/01.RES.65.5.1340**.

[6] Humphrey, J.D. (2002). *Cardiovascular Solid Mechanics: Cells, Tissues, and Organs*. Springer-Verlag, New York, **DOI:10.1007/978-0-387-21576-1**.

[7] Bazilevs, Y., Hsu, M.C., Zhang, Y., Wang, W., Kvamsdal, T., Hentschel, S. Isaksen, J.G. (2010). Computational vascular fluid-structure interaction: methodology and application to cerebral aneurysms. *Biomechanics and Modeling in Mechanobiology*, vol. 9, no. 4, p. 481-498, **DOI:10.1007/s10237-010-0189-7**.

[8] Fung, Y.C. (1991). What are the residual stresses doing in our blood vessels? *Annals of Biomedical Engineering*, vol. 19, p. 237-249, **DOI:10.1007/BF02584301**.

[9] Chuong, C.J., Fung, Y.C. (1983). Three-dimensional stress distribution in arteries. *Journal of Biomechanical Engineering*, vol. 105, no. 3, p. 268-274, **DOI:10.1115/1.3138417**.

[10] Chuong, C.J., Fung, Y.C. (1986). On residual stresses in arteries. *Journal of Biomechanical Engineering*, vol. 108, no. 2, p. 189-192, **DOI:10.1115/1.3138600**.

[11] Takamizawa, K., Hayashi, K. (1987). Strain energy density function and uniform strain hypothesis for arterial mechanics. *Journal of Biomechanics*, vol. 20, no. 1, p. 7-17, **DOI:10.1016/0021-9290(87)90262-4**.

[12] Bustamante, R., Holzapfel, G.A. (2010). Methods to compute 3D residual stress distributions in hyperelastic tubes with application to arterial walls. *International Journal of Engineering Science*, vol. 48, p. 1066-1082, **DOI:10.1016/j.ijengsci.2010.06.005**.

[13] Greenwald, M., Moore, J., Rachev, A., Kang, T., Meister, J.J. (1997). Experimental investigation of the distribution of residual strains in the artery wall. *Journal of Biomechanical Engineering*, vol. 119, no. 4, p. 438-444, **DOI:10.1115/1.2798291**.

[14] Gee, M.W., Förster, Ch., Wall, W.A. (2010). A computational strategy for prestressing patient-specific biomechanical problems under finite deformation. *International Journal for Numerical Methods in Engineering*, vol. 26, no. 1, p. 52-72, **DOI:10.1002/cnm.1236**.

[15] Govindjee, S., Mihalic, P. (1996). Computational methods for inverse finite elastostatics. *Computer Methods in Applied Mechanics and Engineering*, vol. 136, no. 1-2, p. 47-57, **DOI:10.1016/0045-7825(96)01045-6**.

[16] Lu, J., Zhou, X., Raghavan, M.L. (2008). Inverse method of stress analysis for cerebral aneurysms. *Biomechanics*

[17] *and Modeling in Mechanobiology*, vol. 7, no. 6, p. 477-486, **DOI:10.1007/s10237-007-0110-1**.

[17] Delfino, A., Stergiopulos, N., Moore, J.E.Jr., Meister, J.J. (1997). Residual strain effects on the stress field in a thick wall finite element model of the human carotid bifurcation. *Journal of Biomechanics*, vol. 30, no. 8, p. 777-786, **DOI:10.1016/S0021-9290(97)00025-0**.

[18] Raghavan, M.L., Trivedi, S., Nagaraj, A., McPherson, D.D., Chandran, K.B. (2004). Three-dimensional finite element analysis of residual stress in arteries. *Annals of Biomedical Engineering*, vol. 32, no. 2, p. 257-263.

[19] Holzapfel, G.A., Ogden, R.W. (2010). Modelling the layer-specific three-dimensional residual stresses in arteries, with an application to the human aorta. *Journal of the Royal Society Interface*, vol. 7, no. 46, p. 787-99, **DOI:10.1098/rsif.2009.0357**.

[20] Schulze-Bauer, C.A.J., Holzapfel, G.A. (2003). Determination of constitutive equations for human arteries from clinical data. *Journal of Biomechanics*, vol. 36, no. 2, p. 165-169, **DOI:10.1016/S0021-9290(02)00367-6**.

[21] Masson, I., Boutouyrie, P., Laurent, S., Humphrey, J.D., Zidi, M. (2008). Characterization of arterial wall mechanical behavior and stresses from human clinical data. *Journal of Biomechanics*, vol. 41, no. 12, p. 2618-2627, **DOI:10.1016/j.jbiomech.2008.06.022**.

[22] Stålhand, J., Klarbring, A., Karlsson, M. (2004). Towards in vivo aorta material identification and stress estimation. *Biomechanics and Modeling in Mechanobiology*, vol. 2, no. 3, p. 169-186, **DOI:10.1007/s10237-003-0038-z**.

[23] Stålhand, J. (2009). Determination of human arterial wall parameters from clinical data. *Biomechanics and Modeling in Mechanobiology*, vol. 8, no. 2, p. 141-148, **DOI: 10.1007/s10237-008-0124-3**.

[24] Cardamone, L., Valentin, A., Eberth, J.F., Humphrey, J.D. (2009). Origin of axial prestretch and residual stress in arteries. *Biomechanics and Modeling in Mechanobiology*, vol. 8, no. 6, p. 431-446, **DOI:10.1007/s10237-008-0146-x**.

[25] Abaqus 6.7.1 (2008). *Users Manual.* Simulia, Providence.

[26] Birger, B.I. (1972). Temperature stresses in an anisotropic cylinder, NASA, Washington.

[27] Fonck, E., Prod'hom, G., Ray, S., Augsburger, L., Rüfenacht, D.A., Stergiopulos, N. (2007). Effect of elastin degradation on carotid wall mechanics as assessed by a constituent-based biomechanical model. *American Journal of Physiology - Heart and Circulatory Physiology*, vol. 292, no. 6, p. H2754-H2763, **DOI:10.1152/ajpheart.01108.2006**.

[28] Stålhand, J., Klarbring, A. (2005). Aorta in vivo parameter identification using an axial force constraint. *Biomechanics and Modeling in Mechanobiology*, vol. 3, no. 4, p. 191-199.

[29] Masson, I., Beaussier, H., Boutouyrie, P., Laurent, S., Humphrey, J.D., Zidi, M. (2011). Carotid artery mechanical properties and stresses quantified using in vivo data from normotensive and hypertensive humans. *Biomechanics and Modeling in Mechanobiology*, vol. 10, no. 6, p. 867-882, **DOI:10.1007/s10237-010-0279-6**.

Surface Defect Detection on Optical Devices Based on Microscopic Dark-Field Scattering Imaging

Yingjie Yin – De Xu – Zhengtao Zhang* – Mingran Bai – Feng Zhang – Xian Tao – Xingang Wang
Chinese Academy of Sciences, Institute of Automation, Research Center of Precision Sensing and Control, China

Methods of surface defect detection on optical devices are proposed in this paper. First, a series of microscopic dark-field scattering images were collected with a line-scan camera. Translation transformation between overlaps of adjacent microscopic dark-field scattering images resulted from the line-scan camera's imaging feature. An image mosaic algorithm based on scale invariance feature transform (SIFT) is proposed to stitch dark-field images collected by the line-scan camera. SIFT feature matching point-pairs were extracted from regions of interest in the adjacent microscopic dark-field scattering images. The best set of SIFT feature matching point-pairs was obtained via a parallel clustering algorithm. The transformation matrix of the two images was calculated by the best matching point-pair set, and then image stitching was completed through transformation matrix. Secondly, a sample threshold segmentation method was used to segment dark-field images that were previously stitched together because the image background was very dark. Finally, four different supervised learning classifiers are used to classify the defect represented by a six-dimensional feature vector by shape (point or line), and the performance of linear discriminant function (LDF) classifier is demonstrated to be the best. The experimental results showed that defects on optical devices could be detected efficiently by the proposed methods.
Keywords: scale invariance feature transform, linear discriminant function, cluster algorithm, image segmentation, image mosaic, dark-field imaging, optical devices

Highlights
- Collected microscopic dark-field scattering images with the line-scan camera.
- Proposed an new image mosaic algorithm based on scale invariance feature transform (SIFT) to stitch dark-field images.
- Proposed a parallel clustering algorithm to obtain the best set of SIFT feature matching point-pairs.
- Used a six-dimensional feature vector to describe the defect.
- Classified the defect by shape (point or line) using four different supervised learning classifiers.

0 INTRODUCTION

In the laser system for inertial confinement fusion (ICF) [1] and [2], optical devices are essential parts of the power amplifier and the final optics assembly. Defects, such as point defects and line defects on the surface of optical devices, seriously affect the performance of the laser system for ICF. Image processing and pattern recognition technology is widely used for the detection of defects. In [3], laser profilometry is used to detect defects on the surface of power transmission belts. In [4], a defect detection system based on dark-field optical scattering images is designed and assembled for locating and determining the sizes of crystal-originated "particles" (COPs) on the polished surface of silicon wafers. In [5], a pulsed eddy current (PEC) thermography system is implemented for notch detection in carbon-fibre reinforced plastic (CFRP) samples and the proposed methods allow the user to observe the eddy current distribution in a structure using infrared imaging and to detect defects over a relatively wide area. In [6], a pit-count method based on computer-aided image processing is used for direct measurements of the cavitation erosion by evaluating the damage on the surface of the hydrofoil. In [7], methods based on image processing technology are proposed to detect the defects on the surface of ceramic tiles. In [8], a novel visual system is built to recognize erythema migrans. In the visual system, the GrowCut method improved with the new finger draw marker is used to detect potential erythema migrans skin lesion edge, and several methods are used for the classification of skin lesions into ellipses. In [9], several neural networks are used for the roughness prediction model of the steel surface machined by face milling. In [10], the regression model and the model based on the application of neural networks are used to predict the machined surface roughness in the face milling of aluminium alloy on a low-power cutting machine.

An apparatus for detecting defects on the surface of optical devices was designed and constructed in the lab of the authors. A high-precision motorized linear stage and a high-precision motorized vertical stage are used to control the line-scan camera moving along the planned path. A series of microscopic dark-field scattering images are collected with the line-scan camera. There is translation transformation

*Corr. Author's Address: Institution of Automation Chinese Academy of Sciences, 95 Zhongguancun East Road, Beijing, China, zhengtao.zhang@ia.ac.cn

relationship between the overlaps of adjacent microscopic dark-field scattering images because of the line-scan camera's imaging feature. In order to obtain the transformation matrix of the overlaps of two adjacent dark-field images, an image mosaic algorithm based on SIFT [11] is proposed. In [12], the simple template matching is used to complete image mosaic. However, the template matching method is not stable and is affected easily by noise. SIFT features are local image features, have higher stability, and are widely used in image registration algorithms [13] to [15]. Pixel values of defects are much brighter than pixel values of the background in dark-field images, so a sample threshold segmentation method is used to segment images that have been stitched together by the image mosaic algorithm. Defects on the surface of optical devices can be divided into point defects and line defects. In order to effectively identity the types of defects, the performances of four different classifiers (linear discriminant function (LDF) [16], support vector machine (SVM) [17] to [19], k-nearest neighbour (KNN) [20] and radial basis function (RBF) network [21] and [22]) are compared to select a suitable classifier.

The organization of this paper is as follows. In Section 1, the imaging principle of microscopic dark-field scattering imaging is introduced. The motion path of line-scan camera is also introduced, and the reason for translation transformation relationship between the overlaps of adjacent microscopic dark-field scattering images is explored. In Section 2, the SIFT features is reviewed, and an image mosaic algorithm based on SIFT features is proposed. In Section 3, a sample threshold segmentation method is used to segment images. In Section 4, different classifiers are trained to recognize the types of defects. In Section 5, image stitching experiments and defect classification experiments are carried out, and in Section 6, the ideas discussed throughout the paper are summarized.

1 IMAGING FOR OPTICAL DEVICES' SURFACE

1.1 Microscopic Dark-Field Scattering Imaging

Microscopic dark-field scattering imaging is an ideal means of detecting defects on the surfaces of optical devices. Such surfaces are illuminated by visible light, and some light is scattered by defects on the surface of the optical device. The line-scan camera will receive the scattered light when it collects the images of the surfaces of optical devices, so the defects' pixel values in the images will be much brighter than the pixel values of the background (other parts of the optical devices).
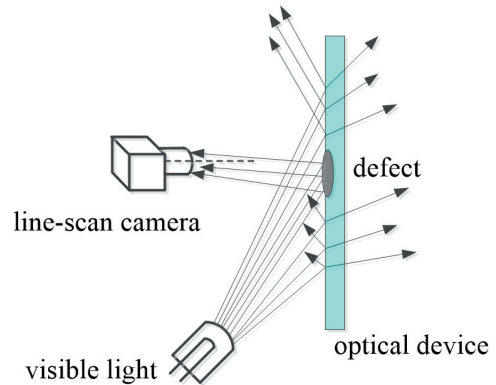
Fig. 1. *The principle of dark-field scattering imaging*

The principle of dark-field scattering imaging is shown in Fig. 1. The geometric-optics model of the dark-field scattering imaging is analysed in [12], and a conclusion that the distribution of the light source need to be circular is given.

1.2 Imaging of the Line-Scan Camera

There are two important reasons for using a line-scan camera rather than a plane array camera. First, only one degree of freedom is adjusted to ensure that the line array CCD is parallel to the surface of the optical device when the line-scan camera is used; however, two degrees of freedom need to be adjusted to ensure that the plane array CCD is parallel to the surface of the optical device when the plane array camera is used. Secondly, a high-resolution image (such as Image I_1 in Fig. 3) containing all parts of the optical device in the Z axis direction can be obtained by the line scan camera; however, if the plane array camera is used, more images need to be taken to contain all parts of the optical device in the Z axis direction, and these images need to be stitched to obtain Image I_1. Therefore, the number of images needing to be stitched is decreased and the running time of the image mosaic is reduced when the line-scan camera is used to acquire the images of the optical devices.

The imaging principle of line-scan camera is shown in Fig. 2. The optical axis of the camera is perpendicular to the surface of optical devices, and AB is the camera's field of view, in Fig. 2. The moving speed of the line-scan camera and the image acquisition speed are synchronized to ensure that the images collected by line-scan camera do not become distorted. The moving speed of the line-scan camera can be calculated by Eq. (1).

$$v_m = \frac{Dl}{f} v_a, \qquad (1)$$

where v_m is the moving speed of the line-scan camera, D is distance between the camera's lens and the surface of optical devices, f is the focal length, l is the pixel size of line-scan camera and v_a is the line-scan speed of the line-scan camera.
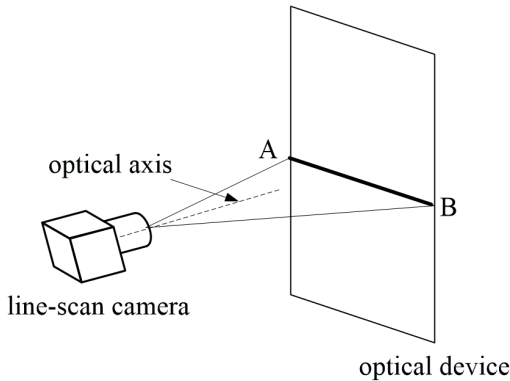
Fig. 2. *The imaging principle of line-scan camera*

A high-precision motorized linear stage and a high-precision motorized vertical stage are used to control the line-scan camera moving along the *X* axis and *Z* axis, shown in Fig. 3, and the surface of optical devices is parallel to the *XZ* plane. The line-scan camera is controlled to move from Point 1 to Point 2 along the opposite direction of the *Z* axis by the high-precision motorized vertical stage and dark-field images are collected by the line-scan camera at the same time. Following that, the line-scan camera is controlled to move from Point 2 to Point 3 along the direction of the *X* axis by the high-precision motorized linear stage and the line-scan camera does not collect images in this process. Next, the line-scan camera is controlled to move from Point 3 to Point 4 along the direction of the *Z* axis by the high-precision motorized vertical stage, and dark-field images are simultaneously collected by the line-scan camera. Next, the line-scan camera is controlled to move from Point 4 to Point 5 along the direction of the *X* axis by the high-precision motorized linear stage, and the line-scan camera does not collect images in this process. The line-scan camera moves according to the above movement rule until the images collected by the camera include the entire surface of the optical device. Finally, dark-field image set *I* shown in Fig. 3 and Eq. (2) is obtained.

$$I = \{I_1, I_2, \cdots, I_n\}. \qquad (2)$$

The conclusion that the relationship between the overlaps of adjacent dark-field images such as image I_1 and image I_2 is the translation transformation *T*, shown in Eq. (3), can be easily drawn from the imaging principle shown in Fig. 2 and the moving path (shown in Fig. 3) of the line-scan camera.

$$T = \begin{bmatrix} 1 & 0 & -\Delta x \\ 0 & 1 & -\Delta y \\ 0 & 0 & 1 \end{bmatrix}. \qquad (3)$$
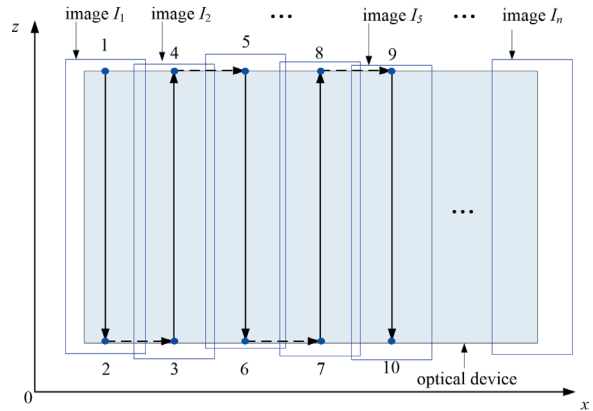
Fig. 3. *The motion path of the line-scan camera*

Δx is the horizontal offset of adjacent dark-field images' overlaps and Δy is the vertical offset of adjacent dark-field images' overlaps. Usually, the vertical offset Δy is caused by kinematic errors of the high-precision motorized vertical stage, and the horizontal offset Δx is mainly caused by the setting value. The horizontal offset Δx usually is set at 300 to 400 pixels in order to balance the number of feature points and the speed of the image mosaic algorithm. Therefore, the value of Δx is much larger than the value of Δy (usually the value of Δy is less than 10 pixels).

2 IMAGE MOSAIC BASED ON SIFT

Feature point matching is widely used to stitch images. SIFT features are invariant to image scale and rotation, and are shown to provide robust matching across a substantial range of affine distortion, change in 3D viewpoint, addition of noise, and change in illumination [11]. An image mosaic algorithm based on SIFT features is proposed in order to solve the problem stemming from the fact that a translation transformation relationship exists in the adjacent dark-field images in Section 1.2.

The image mosaic principle is shown in Fig. 4. SIFT feature matching point-pairs were extracted from regions of interest in the adjacent dark-field images. The best set of SIFT feature matching point-pairs were obtained by parallel clustering algorithms. The transformation matrix of the two images was calculated by the best matching point-pair set and the adjacent dark-field images were stitched by the transformation matrix.
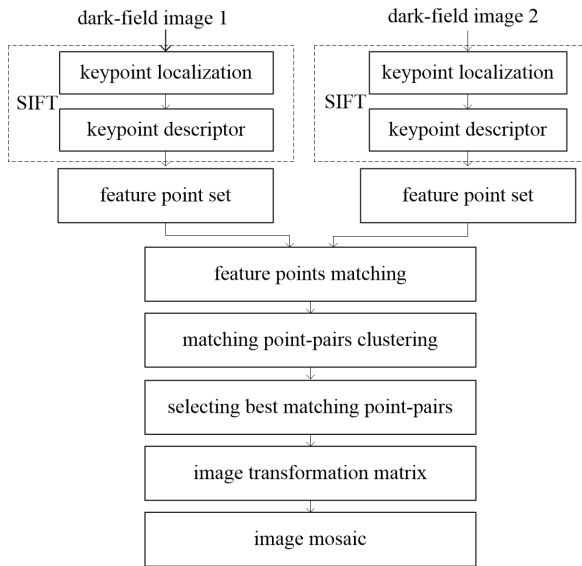
Fig. 4. *The image mosaic principle*

2.1 SIFT Feature

SIFT features proposed by D.G. Lowe are widely used in image mosaic, object recognition, robotic mapping and navigation, gesture recognition and video tracking. The following steps are taken to generate SIFT features [11]:

Step 1: Scale-space extrema detection. The scale space of an image is produced from the convolution of a variable-scale Gaussian with an input image. The difference of Gaussian scale-space is computed from the difference of two nearby scales. Maxima and minima of the difference-of-Gaussian images are detected by comparing a pixel to its 26 neighbours in 3×3 regions at current and adjacent scales.

Step 2: Accurate keypoint localization. A 3D quadratic function to the local sample is fitted to determine the interpolated location of the extremum and unstable extrema with low contrast and a low response along edges are simultaneously rejected.

Step 3: Orientation assignment for keypoints. Local image gradient directions are used to assign one or more directions to each keypoint and the image data is transformed relative to the assigned orientation.

Step 4: Generating SIFT feature vector. At the selected scale in the region around each keypoint, the local image gradients are measured to generate a 128-dimensional vector (SIFT feature vector) for each keypoint.

2.2 Clustering and Screening of Matching Point-Pairs

The Best-Bin-First (BBF) algorithm [23] is used to find the matching point-pairs set S between the adjacent dark-field images.

$$S = \left\{ {}^{1}s, {}^{2}s, \cdots, {}^{k}s, \cdots, {}^{n}s \right\}, \tag{4}$$

and

$$ {}^{k}s = \left\{ {}^{k}p_1, {}^{k}p_2, {}^{k}\theta, {}^{k}L_x, {}^{k}L_y \right\}. \tag{5}$$

where ${}^{k}s$ is a feature representation of the kth matching point-pair, ${}^{k}p_1$ is the position of the matching point in dark-field image 1, ${}^{k}p_2$ is the position of the matching point in dark-field image 2, ${}^{k}\theta$ is the angle between the vector $\overline{{}^{k}p_1 {}^{k}p_2}$ and the X axis, ${}^{k}L_x$ is length of the vector $\overline{{}^{k}p_1 {}^{k}p_2}$'s component along the X axis, ${}^{k}L_y$ is length of the vector $\overline{{}^{k}p_1 {}^{k}p_2}$'s component along the Y axis.
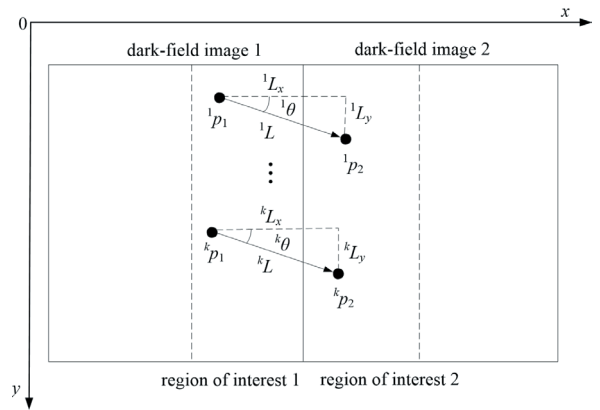
Fig. 5. *The features of matching point-pairs*

There are bad matching point-pairs in the matching point-pairs set S. In order to improve the accuracy of image mosaic, the best matching point-pair set S_{best} must be selected from the set S. In Section 1.2, a conclusion that the horizontal offset Δx is much larger than the value of Δy is drawn, so ${}^{k}L_x$ is much larger than ${}^{k}L_y$. Bad matching point-pairs are removed from the set S to obtain the set S' according to the inequality constraint Eq. (6).

$$\left|{}^{k}\theta\right| > \theta_{T}. \tag{6}$$

where θ_T is an angle threshold. A parallel clustering algorithm, shown in Fig. 6, is designed to obtain the best matching point-pair set S_{best}. In the parallel clustering algorithm, the features ${}^{k}L_x$ and ${}^{k}L_y$ of the matching point-pair are used for clustering of matching point-pairs. The class owning the most matching point-pairs is reserved for generating the set S_x in the process of ${}^{k}L_x$ clustering and the class owning the most matching point-pairs is reserved to generate the set S_y in the process of ${}^{k}L_y$ clustering. The best matching point-pair set S_{best} is the intersection of S_x and S_y.
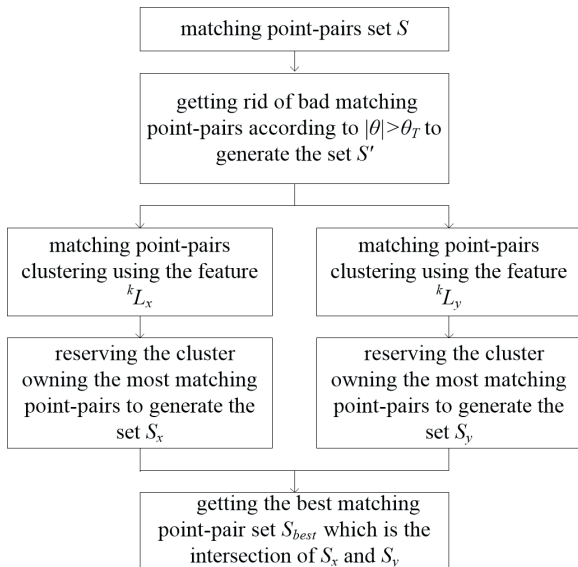
Fig. 6. *The clustering and screening of matching point-pairs*

2.2.1 L_x Clustering Algorithm

One matching point-pair ${}^{m}s'$ ($1 \le m \le n'$) is selected randomly from the set S'.

$$S' = \left\{ {}^{1}s', {}^{2}s', \cdots, {}^{n'}s' \right\}. \tag{7}$$

*M*atching point-pairs satisfying the inequality constraint (Eq. (8)) in the set S' are to generate the set S'_1 as a cluster.

$$\left\| L_x\left({}^{k}s'\right) - L_x\left({}^{m}s'\right) \right\| \le r_x, \tag{8}$$

where k ranges from 1 to n', $L_x({}^{m}s')$ is the L_x feature of the matching point-pair ${}^{m}s'$, $L_x({}^{k}s')$ is the L_x feature of the matching point-pair ${}^{k}s'$ and r_x is a threshold. Next, another matching point-pair is selected randomly from the remaining matching point-pairs of the set S', and

the set S'_2 is generated in the same way. The iterative process above is not stopped until all the matching point-pairs are clustered. The pseudo-code of L_x clustering algorithm is shown in Fig. 7.

L_x **clustering algorithm** *Cluster_L_x( )*

Input: The set $S' = \{{}^{1}s', {}^{2}s', \ldots, {}^{n'}s'\}$.
Output: The set S_x.
1: $i \leftarrow 1$
2: **while** 1 **do**
3:    **if** $S' = \varnothing$ **then**
4:       **if** $i = 1$ **then**
5:          **return** null
6:       **else**
7:          $S_x \leftarrow \underset{S'_j \in \{S'_1, S'_2, \cdots, S'_i\}}{\arg\max}\ size(S'_j)$
8:          **return** S_x
9:       **end if**
10:    **end if**
11:    ${}^{m}s'$ is selected randomly from the set S'
12:    $S'_i \leftarrow \varnothing$
13:    **for** $k \leftarrow 1$ to $size(S')$ **do**
14:       **if** $\| L_x({}^{k}s') - L_x({}^{m}s') \| \le r_x$ **then**
15:          $S'_i \leftarrow S'_i \cup {}^{k}s'$
16:          $S' \leftarrow S' - {}^{k}s'$
17:       **end if**
18:    **end for**
19:    $i \leftarrow i+1$
20: **end while**
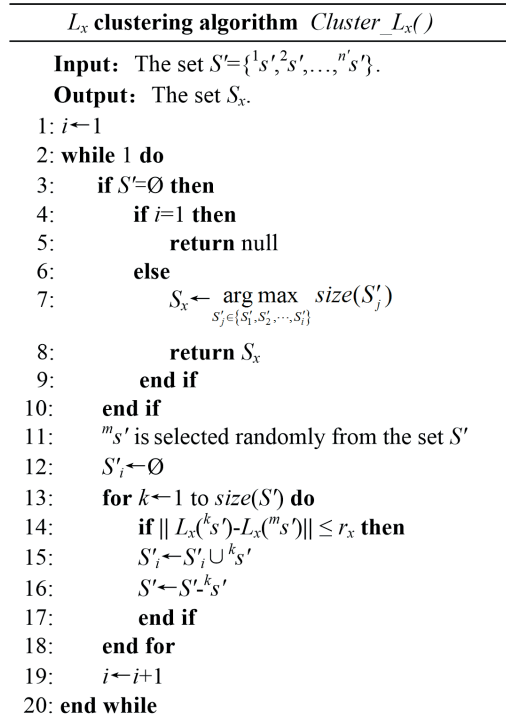
Fig. 7. *L_x clustering algorithm*

The L_y clustering algorithm is generated analogous to the L_x clustering algorithm.

2.2.2 The Best Matching Point-Pair Set

The best matching point-pair set S_{best} shown in Fig. 8 is the intersection of S_x obtained with the L_x clustering algorithm and S_y obtained with the L_y clustering algorithm.

Algorithm of obtaining S_{best}

Input: The set $S' = \{{}^{1}s', {}^{2}s', \ldots, {}^{n'}s'\}$.
Output: The set S_{best}.
1: $S_x \leftarrow Cluster\_L_x( )$
2: $S_y \leftarrow Cluster\_L_y( )$
3: $S_{best} \leftarrow S_x \cap S_y$
4: **return** S_{best}

Fig. 8. *The algorithm of obtaining S_{best}*

2.3 Translation Transformation Matrix

The offsets (Δx, Δy) in Section 1.2 can be calculated by Eq. (9).

$$\Delta x = \frac{\sum_{i=1}^{q} \left(W_1 - {}^{i}p_{1(x)} + {}^{i}p_{2(y)} \right)}{q},$$

$$\Delta y = \frac{\sum_{i=1}^{q} \left({}^{i}p_{2(y)} - {}^{i}p_{1(y)} \right)}{q}, \qquad (9)$$

where W_1 is the width of the dark-field Image 1 shown in Fig. 5, q is the number of elements in S_{best}, ${}^{i}p_{1(x)}$ is the X coordinate of the matching point in image 1, ${}^{i}p_{2(x)}$ is the X coordinate of the matching point in Image 2, ${}^{i}p_{1(y)}$ is the Y coordinate of the matching point in Image 1 and ${}^{i}p_{2(y)}$ is the Y coordinate of the matching point in Image 2.

The coordinates of the pixels in Image 2 are translated by the matrix $\mathbf{T}$ to finish the image mosaic.

$$\begin{bmatrix} u_T \\ v_T \\ 1 \end{bmatrix} = \mathbf{T} \begin{bmatrix} u \\ v \\ 1 \end{bmatrix}. \qquad (10)$$

where (u, v) is the pixel coordinate in Image 2 and (u_T, v_T) is the new pixel coordinate in Image 2.

3 IMAGE SEGMENTATION AND CONTOUR EXTRACTION

A sample threshold segmentation method in Eq. (11) is used to segment images because the pixel values of defects are much brighter than pixel values of the background in dark-field images.

$$f_s(x,y) = \begin{cases} 255 & f(x,y) > T \\ 0 & f(x,y) \le T \end{cases}, \qquad (11)$$

where $f(x,y)$ is the pixel value in the position (x, y), $f_s(x,y)$ is the new pixel value in position (x, y) after segmentation and T is the threshold.

The contours of the defects are extracted from the segmented image by the function *cvFindContours()* in *Opencv* [24].

4 DEFECT CLASSIFICATION

4.1 Feature Vectors of Defects

Supervised learning methods are widely used to infer a prediction function from labelled training data. Given a set of N training examples $T=\{(x_1, y_1), (x_2, y_2), …, (x_N, y_N)\}$ such that x_i is the feature vector of the ith example and y_i is its label, a prediction function $f: X{\to}Y$ (X is the input space and Y is the output space) is obtained by supervised learning algorithms.

$$f(x) = \arg\max_{y \in Y} F(x, y), \qquad (12)$$

where $F: X{\times}Y{\to}R$ is a scoring function.
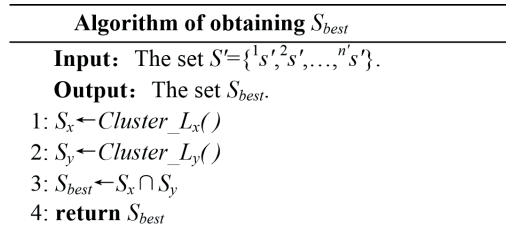
Defects on the surface of optical devices can be divided into line defects (labelled as +1) and point defects (labelled as −1), so supervised learning methods can be used to classify the defects. The six main features of defects shown in Eq. (13) are used to train classifiers.

$$x_i = \left(x_{i1}, x_{i2}, x_{i3}, x_{i4}, x_{i5}, x_{i6} \right), \qquad (13)$$

where x_{i1} is the area of the defect, x_{i2} is the area of the defect's envelope rectangle, x_{i3} is the length of the defect's contour, x_{i4} is the ratio of the length of the defect's contour and the area of the defect, x_{i5} is the ratio of the defect's area and the area of the defect's envelop rectangle and x_{i6} is the aspect ratio of the defect's envelop rectangle.

By using the proposed six-dimensional feature vector, four different supervised learning classifiers (LDF, SVM, KNN and RBF network) are used. The experimental results in Section 5.3 show that the performance of LDF classifier is better than that of the other classifiers.

4.2 LDF Classifier for Two Classes

The LDF classifier approaches the binary classification problems by assuming that the conditional probability density functions $p(x|y=+1)$ and $p(x|y=−1)$ are both normally distributed with mean and covariance parameters (u_{+1}, M_{+1}) and $(u_{−1}, M_{−1})$ and the class co-variances (M_{+1} and $M_{−1}$) are identical.

Based on Bayes decision-making theory, the discriminant rule is: assign x_i to +1 if $g(x_i,+1) \ge g(x_i,-1)$ and assign x_i to −1 if $g(x_i,-1) > g(x_i,+1)$, where $g(x_i,y)$ shown in Eq. (14) is the linear discriminant function.

$$g(x_i, y) = f_1 + f_2,$$
$$f_1 = 2\hat{\mu}_y^{T} \widehat{M}^{-1} x_i, \quad f_2 = 2\ln P(y) - \hat{\mu}_y^{T} \widehat{M}^{-1} \hat{\mu}_y, \quad (14)$$

where $P(y)$ is the prior probability, $\hat{\mu}_y$ is the within-class sample mean, and the co-variance $\widehat{M}$ is the weighted average of the co-variances $\widehat{M}_{+1}$ and $\widehat{M}_{-1}$.

$$\widehat{M} = \frac{n_{+1}}{N} \widehat{M}_{+1} + \frac{n_{-1}}{N} \widehat{M}_{-1}, \qquad (15)$$

where N is the number of training examples. $\widehat{M}_{+1}$ and $\widehat{M}_{-1}$ are the within-class sample covariance matrix. n_{+1} is the number of training samples labelled as +1, n_{-1} is the number of training samples labelled as −1.

5 EXPERIMENTS

5.1 Experimental Equipment

As shown in Fig. 9, the experimental equipment principally consists of the motion module, the vision module and the PC control module. The motion module consists of the motorized vertical stage, the motorized linear stage and the focus movement axis. The resolution of the motorized vertical stage and the motorized linear stage is 1 μm. The vision module consists of the line-scan camera and the light source. The resolution of the line-scan camera is 8192 pixels, the pixel size is 7×7 μm. The line-scan camera is controlled by the motorized vertical stage and motorized linear stage to move along the path shown in Fig. 3. Via camera calibration, the parameter $D/f = 1.357$ is obtained in Eq. (1). The speed of the line-scan camera along the Z axis is 30 mm/s. The line-scan speed is 3158 frames per second. The distance of the two adjacent images is between (8192–400) pixels and (8192–300) pixels, and we can ensure that the distance is in the above range by setting the moving distance of the line-scan camera along the direction of the X axis.
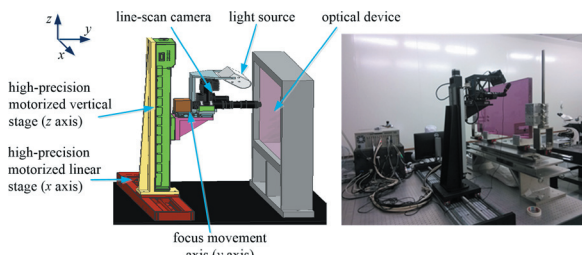
Fig. 9. *Experimental equipment*

5.2 Image Mosaic Experiment

The two adjacent dark-field images (each image is 2048×2048 pixels) collected by the line-scan camera are shown in Fig. 10, and the red line in Fig. 10 is the boundary between the two images.
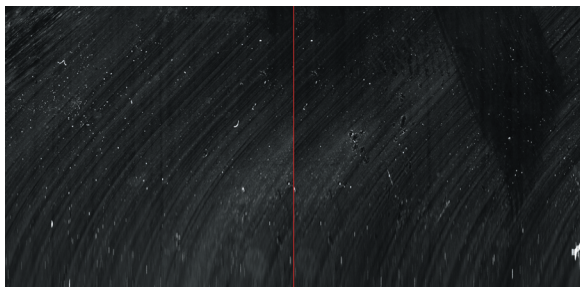
Fig. 10. *Two adjacent dark-field images collected by line-scan camera*
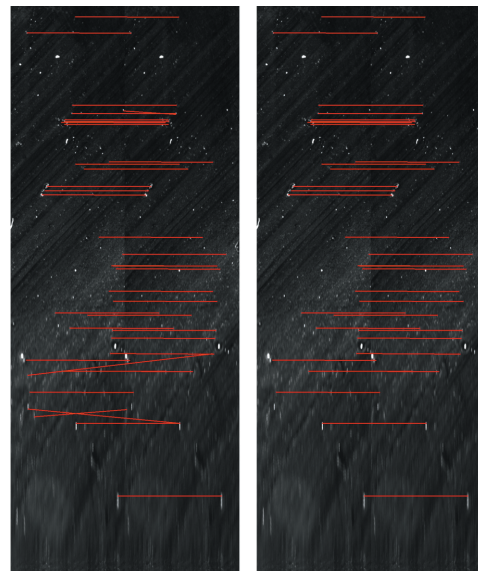
| a) SIFT matching point-pairs | b) The best matching point-pairs |

Fig. 11. *Matching point-pairs of two adjacent dark-field images*
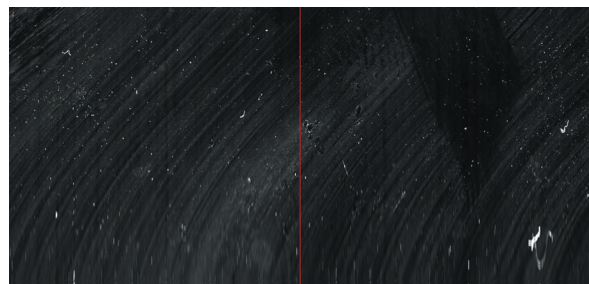
Fig. 12. *The stitching result for the two adjacent dark-field images*
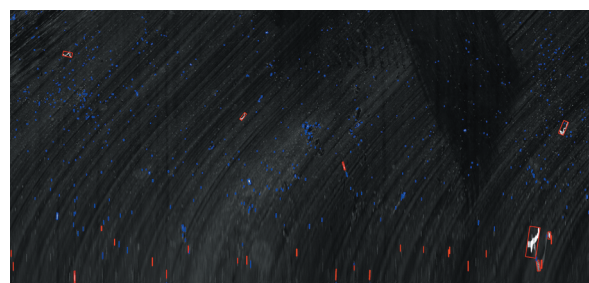
Fig. 13. *The classification results of Fig. 12*

The region R_1 (1648, 0, 2048, 2048) is the region of interest (ROI) in Image 1 (as shown in Fig. 5); (1648, 0) is the coordinate of the ROI's top left corner in Image 1 and (2048, 2048) is the coordinate of the ROI's bottom right corner in Image 1. R_2 (0, 0, 400, 2048) is the ROI in Image 2. SIFT feature points are extracted from the region R_1 and R_2, and the matching point-pair set S shown in Fig. 11a is generated by the BBF algorithm. The best matching point-pair set S_{best}

Table 1. *Results of 15 experiments of image mosaic*

Number	1	2	3	4	5	6	7	8
Ground truth $(\Delta x, \Delta y)$	(366, 0)	(378, 3)	(376, 0)	(372, 0)	(360, 0)	(366, 3)	(369, 0)	(375, 0)
Measured value $(\Delta x, \Delta y)$	(367, 0)	(377, 4)	(375, 0)	(372, 0)	(360, 0)	(366, 2)	(369, 1)	(373, 0)
Measurement error of Δx	1	−1	−1	0	0	0	0	−2
Measurement error of Δy	0	1	0	0	0	−1	1	0
Number	9	10	11	12	13	14	15	
Ground truth $(\Delta x, \Delta y)$	(375, 0)	(373, 4)	(371, 0)	(367, 2)	(366, 4)	(370, 2)	(365, 4)	
Measured value $(\Delta x, \Delta y)$	(372, 0)	(371, 3)	(370, 0)	(367, 1)	(364, 2)	(368, 0)	(363, 2)	
Measurement error of Δx	−3	−2	−1	0	−2	−2	−2	
Measurement error of Δy	0	−1	0	−1	−2	−2	−2	

(shown in Fig. 11b) is generated by the clustering and screening algorithm introduced in Section 2.2.

In the experiment, θ_T is set to 10°, r_x is set to 20 pixels and r_y is set to 20 pixels. The offsets $(\Delta x, \Delta y)$ calculated by Eq. (3) and the set S_{best} is (-367, 0), so the matrix **T** is:

$$\mathbf{T} = \begin{bmatrix} 1 & 0 & -367 \\ 0 & 1 & 0 \\ 0 & 0 & 1 \end{bmatrix}. \qquad (16)$$

The stitching result for the two adjacent dark-field images shown in Fig. 10 is shown in Fig. 12 and the red line in Fig. 12 is the boundary between the two images. The results of 15 experiments of image mosaic are shown in Table 1, and the ground truth is obtained by the manual annotation. The maximum absolute error of Δx is 3 pixels and the maximum absolute error of Δy is 2 pixels in Table 1.

5.3 Defects Detection and Classification Experiment

A set of 269 training samples including 75 line samples labelled as +1 and 194 point samples labelled as −1 are used to train the four classifiers (LDF, SVM, KNN and RBF network), and a set of 300 testing samples including 86 line samples labelled as +1 and 214 point samples labelled as −1 are used to test the performance of the four classifiers. The parameter K of the KNN classifier is set to 1 (a KNN classifier with the parameter $K = 1$ also called the nearest neighbour classifier). The SVM classifier is a Gaussian kernel SVM classifier with penalty parameter $C = 32$. The number of the hidden layers is 50 in the RBF network, and the LDF classifier is trained by Eqs. (14) and (15).

The experimental results of different classifiers are shown in Table 2. The precision of the LDF classifier is higher than the other classifier, so the LDF classifier is more suitable for classifying the defect

represented by a six-dimensional feature vector, shown in Eq. (13).

The classification results of Fig. 12 are shown in Fig. 13. The defects enveloped by red rectangles are labelled as line defects by the LDF classifier and the defects enveloped by blue rectangles are labelled as point defects in Fig. 13.

Table 2. *Test Results of different classifiers; test results of the a) LDF classifier, b) SVM classifier, c) KNN classifier, and d) RBF network*

	Line defects	Point defects	Precision
a) LDF			
Real quantity	86	214	
The number of true positives	65	213	92.7%
The number of false positives	21	1	
b) SVM			
Real quantity	86	214	
The number of true positives	63	197	86.7%
The number of false positives	23	17	
c) KNN			
Real quantity	86	214	
The number of true positives	68	190	86%
The number of false positives	18	24	
d) RBF network			
Real quantity	86	214	
The number of true positives	40	203	81%
The number of false positives	46	11	

6 CONCLUSIONS

Methods of defecting defects on the surface of optical devices are proposed in this paper. Translation transformation between the overlaps of adjacent microscopic dark-field scattering images resulted from the imaging feature and the moving path of the line-scan camera. An image mosaic algorithm-based SIFT feature is proposed to stitch the adjacent dark-field images collected by the line-scan camera. A sample

threshold segmentation method was used to segment dark-field images according to the characteristic of the stitched dark-field images. The LDF classifier is more suitable for classifying the defect represented by the proposed six-dimensional feature vector. The experimental results showed that defects on optical devices could be efficiently detected by the proposed methods.

7 ACKNOWLEDGMENTS

8 REFERENCES

[1] Moses, E.I. (2010). The national ignition facility and the national ignition campaign. *IEEE Transactions on Plasma Science*, vol. 38, no. 4, p. 684-689, **DOI:10.1088/0029-5515/53/10/104020**.

[2] Cuneo, M.E., Herrman, M.C., Sinars, S.A., et al. (2012). Magnetically driven implosions for inertial confinement fusion at Sandia National Laboratories. *IEEE Transactions on Plasma Science*, vol. 40, no. 12, p. 3222-3245, **DOI:10.1109/TPS.2012.2223488**.

[3] Bračun, D., Perdan, B., Diaci, J. (2011). Surface defect detection on power transmission belts using laser profilometry. *Strojniški vestnik - Journal of Mechanical Engineering*, vol. 57, no. 3, p. 257-266, **DOI:10.5545/sv-jme.2010.176**.

[4] Lee, W.P., Yow, H.K., Tou, T.Y. (2004). Efficient detection and size determination of crystal originated "particles" (COPs) on silicon wafer surface using optical scattering technique integrated to an atomic force microscope. *IEEE Transactions on Semiconductor Manufacturing*, vol. 17, no. 3, p. 422-431, **DOI:10.1109/TSM.2004.831531**.

[5] Cheng, L., Tian, G.Y. (2011). Surface crack detection for carbon fiber reinforced plastic (CFRP) materials using pulsed eddy current thermography. *IEEE Sensors Journal*, vol. 11, no. 12, p. 3261-3268, **DOI:10.1109/JSEN.2011.2157492**.

[6] Dular, M., Širok, B., Stoffel, B. (2005). The influence of the gas content of water and the flow velocity on cavitation erosion aggressiveness. *Strojniški vestnik - Journal of Mechanical Engineering*, vol. 51, no. 3, p. 132-145.

[7] Rahaman, G.M.A., Hossain, M.M. (2009). Automatic defect detection and classification technique from image: a special case using ceramic tiles. *International Journal of Computer Science and Information Security*, vol. 1, no. 1, p. 22-30.

[8] Čuk, E., Gams, M., Možek, M., Strle, F., Maraspin Čarman, V., Tasič, J. (2014). Supervised visual system for recognition of erythema migrans, an early skin manifestation of Lyme Borreliosis. *Strojniški vestnik - Journal of Mechanical Engineering*, vol. 60, no. 2, p. 115-123, **DOI:10.5545/sv-jme.2013.1046**.

[9] Saric, T., Simunovic, G., Simunovic, K. (2013). Use of Neural Networks in Prediction and Simulation of Steel Surface Roughness. *International Journal of Simulation Modelling*, vol. 12, no. 4, p. 225-236, **DOI:10.2507/IJSIMM12(4)2.241**.

[10] Simunovic G., Simunovic K., Saric T. (2013). Modelling and Simulation of Surface Roughness in Face Milling. *International Journal of Simulation Modelling*, vol. 12, no. 3, p. 141-153, **DOI:10.2507/IJSIMM12(3)1.219**.

[11] Lowe, D.G. (2004). Distinctive image features from scale-invariant keypoints. *International Journal of Computer Vision*, vol. 60, no. 2, p. 91-110, **DOI:10.1023/B:VISI.0000029664.99615.94**.

[12] Yang, Y., Lu, C., Liang, J., Liu, D., Yang, L., Li R. (2007). Microscopic dark-field scattering imaging and digitalization evaluation system of defects on optical devices precision surface. *Acta Optical Sinica*, vol. 27, no. 6, p. 1031-1038.

[13] Koo, H.I., Cho, N.I. (2011). Feature-based image registration algorithm for image stitching applications on mobile devices. *IEEE Transactions on Consumer Electronics*, vol. 57, no. 3, p. 1303-1310, **DOI:10.1109/TCE.2011.6018888**.

[14] Xu, P., Zhang, L., Yang, K., Yao, H. (2013). Nested-SIFT for efficient image matching and retrieval. *IEEE MultiMedia*, vol. 20, no. 3, p. 34-46, **DOI:10.1109/MMUL.2013.18**.

[15] Fan, B., Huo, C., Pan, C., Kong, Q. (2013). Registration of optical and SAR satellite images by exploring the spatial relationship of the improved SIFT. *IEEE Geoscience and Remote Sensing Letters*, vol. 10, no. 4, p. 657-661, **DOI:10.1109/LGRS.2012.2216500**.

[16] Webb, A.R., Copsey, K.D. (2011). *Statistical Pattern Recognition*. John Wiley & Sons, Hoboken, **DOI:10.1002/9781119952954**.

[17] Lim, C., Lee, S.R., Chang, J.H. (2012). Efficient implementation of an SVM-based speech/music classifier by enhancing temporal locality in support vector references. *IEEE Transactions on Consumer Electronics*, vol. 58, no. 3, p. 898-904, **DOI:10.1109/TCE.2012.6311334**.

[18] Leiva-Murillo, J.M., Gomez-Chova, L., Camps-Valls, G. (2013). Multitask remote sensing data classification. *IEEE Transaction on Geoscience and Remote Sensing*, vol. 51, no. 1, p. 151-161, **DOI:10.1109/TGRS.2012.2200043**.

[19] Qian, H., Mao, Y., Xiang, W., Wang, Z. (2010). Recognition of human activities using SVM multi-class classifier. *Pattern Recognition Letters*, vol. 31, no. 2, p. 100-111, **DOI:10.1016/j.patrec.2009.09.019**.

[20] Tan, S. (2006). An effective refinement strategy for KNN text classifier. *Expert Systems with Applications*, vol. 30, no. 2, p. 290-298, **DOI:10.1016/j.eswa.2005.07.019**.

[21] Gavrila, D.M. (2000). Pedestrian detection from a moving vehicle. *Proceedings of 6th European Conference on Computer Vision*, Dublin.

[22] Jayasree, T., Devaraj, D., Sukanesh, R. (2010). Power quality disturbance classification using Hilbert transform and RBF networks. *Neurocomputing*, vol. 73, no. 7-9, p. 1451-1456, **DOI:10.1016/j.neucom.2009.11.008**.

[23] Beis, J., Lowe, D.G. (1997). Shape indexing using approximate nearest-neighbour search in high-dimensional spaces. *Proceedings of IEEE Computer Society Conference on Computer Vision and Pattern Recognition*, San Juan, **DOI:10.1109/CVPR.1997.609451**.

[24] Bradski, G., Kaehler, A. (2008). *Learning OpenCV: Computer Vision with the OpenCV Library*. O'Reilly, Sebastopol.

Configuring A Mini-Laboratory and Desktop 3-Axis Parallel Kinematic Milling Machine

Sasa Zivanovic* – Milos Glavonjic – Dragan Milutinovic

University of Belgrade, Faculty of Mechanical Engineering, Serbia

Configuring new machine tools is a complex task that involves the use of a large range of conceptions, methods, models, virtual prototypes and simulations. This paper presents a methodology for configuring a new machine tool to the level of a virtual prototype by using CAD configurator Pro/WEB.Link and a top-down approach. This methodology is explained via an example of the development of a mini-laboratory and desktop 3-axis parallel kinematic milling machine (PKMM). The results are two variants of the virtual prototype and one real world prototype. The configured virtual prototypes are used for the verification of the machining program and programming system using machining simulation in the CAD/CAM environment. The mini-laboratory and desktop 3-axis PKMM has been verified by the successful machining of test workpieces.

Keywords: CAD configurator, Pro/Web.Link, top-down, CAD/CAM, configuring, machine tool, machining simulation

Highlights
- *CAD configurators with web interface and Top Down approach.*
- *Configuring and developing the new mini-laboratory and desktop 3-axis PKMM.*
- *Machining simulation in the CAD/CAM system.*
- *Virtual machine is included in the control and programming system.*
- *Mini-laboratory and desktop 3-axis PKMM was verified by simulation and by the machining of standardized test pieces.*

0 INTRODUCTION

Globalization and the shortening of products' life cycles have caused dramatic changes in the configuring and designing of new products. The customization of products has become a trend in recent years [1] to [3]. Consequently, the customization of configuring process represents a critical issue that can be addressed by adapting interfaces to CAD/CAM systems, thereby using the web interface to rapidly configure a new product.

The application of the web interface as a link to the CAD system is currently widely used in the development of various products [4] to [6]. Examples of some of the available CAD configurators of standard components from different manufacturers are shown in Fig. 1. Available CAD configurators can provide standard, but not custom-made components, which are also required for the process of designing the product families. Programming customized configurators for a family of particular components is possible using programmable web interfaces, such as Pro/Web.Link in the Creo CAD/CAM system. This approach is applicable at the component and assembly levels.

The conceptual design of product families has inspired many research efforts [7] to [9]. The state-of-the-art methods can be classified into two main categories: scalable and configurational product family design [10].
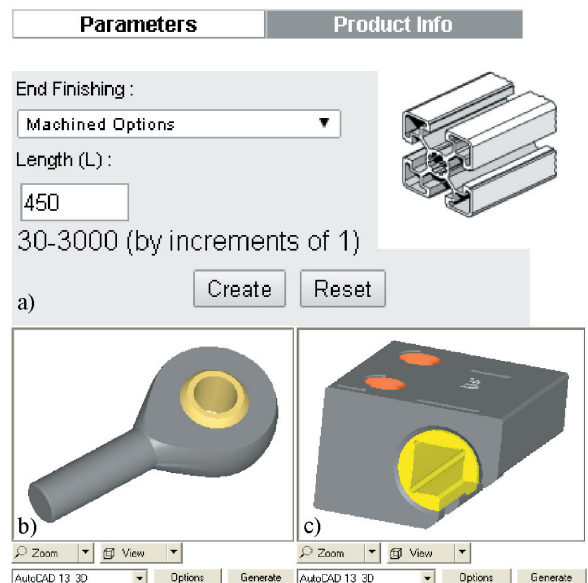
Fig. 1. *The choice of standard components in CAD configurator [4] and [6]*

Scalable product family design refers to the definition of scaling variables (parameters) that are used to scale product components/subassemblies in one or more directions in order to address a variety of customer requests [10] and [11]. The second approach is configurational product family design (also known as module-based product family design) in which the family members are configured by adding, removing

or substituting one or more functional modules from the initially developed modular product [12]. The application of programmable web interfaces in the design of a product family is an emerging field of research.

In [6] the authors use Pro/Web.Link and Pro/Engineer CAD/CAM system for designing a family of trailers. A similar approach presented in [8] investigates configuring a family of products starting from a low-level skeleton model. A lamp and a golf cart were the examples considered.

In this paper, the application of CAD configurators with web interfaces in configuring the components and assemblies of new machine tools are investigated. Compared to the examples presented in [7] and [8], a machine tool is a highly complex product in which the kinematics of the machine is a critical issue. Therefore, the conceptual (skeleton) model of a machine tool should incorporate all the kinematic joints that will enable the kinematic verification of the mechanism.

The main benefits of the web interface application for configuring new machine tools can be expressed as follows:

- Interactive decision-making that is based on the configuration of the machine tool and its settings according to the specific input data based on user requirements, database access, standards, recommendations, functional requirements, etc.;
- Automation of machine tool modelling and configuration, with new input parameters that can be interactively set;
- Use of a large number of standard components and generation of machine configuration that can be easily remodelled;
- Use of CAD configurators with the web interface for unique components;
- Verification of the machine virtual prototypes through simulation of mechanism kinematics during machining according to a control program (this is enabled by incorporation of all kinematic joints into the machine conceptual model);
- Improved efficiency for machine designers, in order to reduce the time required to configure the new product.

Finished solid models of the standard components with the desired dimensions, based on a query filled in by the user, can be downloaded. Downloaded standard components should not be further developed at all, and they are directly built in the main assembly. This approach is applicable in configuring new machine tools [13]. In this paper, the web configurators, web interface, CAD/CAM systems and Pro/Web.Link are

utilized for the development of a mini-laboratory and a desktop 3-axis parallel kinematic milling machine (PKMM).

PKMM is a research-and-development topic in many laboratories [14] and [15], although many of them, unfortunately, in fact, do not have a PKMM. Therefore, the use of a mini-laboratory and desktop educational 3-axis PKMM has been suggested as an aid in the process of acquiring basic experience with a PKMM [16] to [18]. Research works that consider diverse aspects of PKMM have been published [19] and [20].

The simulation of the machining process created in this paper includes the simulation of machine operation based on a generated program in a CAD/CAM system. However, since the mini-laboratory machine is used for the machining of workpieces of soft materials (Styrofoam), the simulation does not include finite element (FE) analysis of cutting forces, as in [21] and [22].

The rest of the paper is organized as follows. In Section 1, a general methodology for application of CAD configurators, Pro/WEB.Link and top-down approach in configuring new products is presented. This methodology was applied for designing mini-laboratory and desktop 3-axis PKMM in Section 2. We have developed two virtual prototypes, one of which was implemented in the real world. In Section 3, the configured virtual prototypes are used for the verification of the machining program and off-line programming system using machining simulation in the CAD/CAM environment, which was possible because the skeleton model of the virtual prototypes had the incorporated all kinematic joints. During the simulation, PKMM tool paths were based on programs that were created using CAM systems [23]. In Section 4, the test workpieces that were used for verifying the control and programming system on a real world laboratory prototype are presented.

1 CONFIGURING BY PRO/WEB.LINK AND TOP-DOWN APPROACH

Pro/Web.Link links the internet to Creo Parametric, enabling the use of web as a tool to automate and streamline parts of the engineering process [24] and [25]. This paper describes the implementation of a simple automation solutions using Pro/Web.Link in configuring the family of parts or assemblies.

Pro/Web.Link is a set of routines, protocols, and tools that can change and adjust parts and assemblies in Creo or Pro/Engineer CAD/CAM systems. An embedded web browser in the Creo CAD/CAM system

improves communication with parts and assemblies in Creo, allowing researchers to concentrate on the process of configuring a new product based on available modules. Pro/Web.Link allows users to rapidly obtain CAD models of components.

The application of Pro/Web.Link provides direct access to information about the model. Moreover, the designer can create, modify, or delete any information regarding the model.

Traditionally, machines have been designed using a classic approach, from smaller to larger (bottom-up), i.e., from the components to the main assembly, Fig. 2a. In this case, the necessary information for the main assembly depends significantly on the selected components.
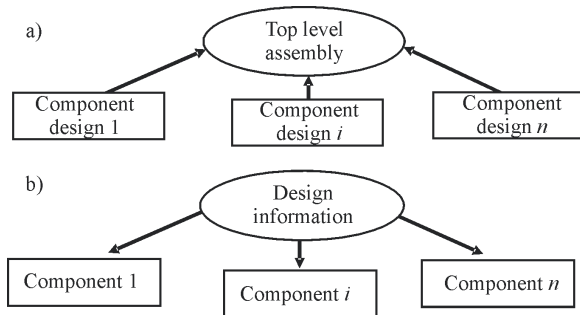

Fig. 2. Different approaches to configuring, a) bottom-up; b) top-down [26]

Opposite to the bottom-up approach, the top-down approach, [26] and [27], uses system analysis as a method for project management. The structure and basic logic of the top-down approach are shown in Fig. 2b. In this approach, all the data are located at the top level and dictate the essential information needed for components. The result is a component that fits perfectly to the main assembly and requires very little modification later.

The essential features of the top-down approach are: (1) a method for placing critical information at a high-level location, (2) communicating that information to the lower levels of the product structure, and (3) capturing the overall design information at one centralized location [26]. The main goals achieved by the top-down approach are: cycle time reduction, increased user satisfaction with software, design efficiency increase, and cost reduction.

The top-down design strategy is the most-common method currently used by industries. This design process is conducted from the system to sub-system, then to the sub-sub-system, and eventually to the part, as shown in Fig. 3. The advantage of the top-

down design approach is that inter-linkages from one sub-system to another can be correlated [8].
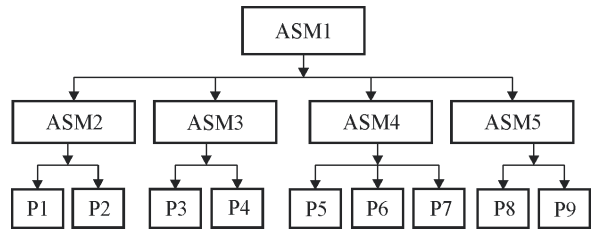
Fig. 3. Top-down design strategy for product development [8]

The main assembly (ASM1) is organized like a tree according to subassemblies (ASM2, ASM3, etc.) and components (P1, P2, P3, etc.), which are allocated to specific project teams and designers who are responsible for their own tasks and who do not and should not view the project as a whole.

The use of a skeleton model is a powerful method for implementing the top-down design. The skeleton model is a simplified assembly, with zero mass and geometry with features such as outer surface contours, parting lines, hole locations, etc. Although it is typically only a non-solid geometry (surfaces, planes, curves, axis, etc.), there is no restriction on what kind of features can be put into a skeleton.

2 DEVELOPMENT OF THE MINI-LABORATORY AND DESKTOP 3-AXIS PKMM

Previous experience in the field of PKMM and a successfully developed first experimental prototype of a vertical milling machine based on newly developed parallel mechanism, [19] and [20], inspired the idea of developing a mini-laboratory and desktop 3-axis PKMM.

The structure of the mechanism, modelling approach, inverse and direct kinematics, workspace and singularity analysis of developed mini-laboratory and desktop 3-axis PKMM, as well as control and programming systems have been described in previous research, [16] to [18].

A representation of the initial model of the developed parallel mechanism and analytically obtained workspace are shown in Fig. 4.

The mechanism consists of the moving platform, three joint parallelograms, c_1, c_2, and c_3, and a stationary base with two parallel guide-ways. Two crossed parallelograms (c_1 and c_2) with spherical and/or universal, i.e. cardan joints, are connected with one of their ends to the mobile platform, and with their other ends to the independent sliders (p_1 and p_2)

which, with a common guideway, make two powered and controlled translatory joints.

Fig. 4. *Parallel mechanism pn101* [13]

The third joint parallelogram (c_3) is connected with one of its ends, through passive translator rotating joints with 2-DOF, to the moving platform. Its other end is connected with rotating joints to the slider p_3, which makes, with the second guideway, the third powered and controlled translatory joint. The actuation of sliders p_1, p_2, and p_3 offers three degrees of freedom to the moving platform, i.e., the tool, so that the platform retains a constant orientation in its motion through the space [16] to [18].
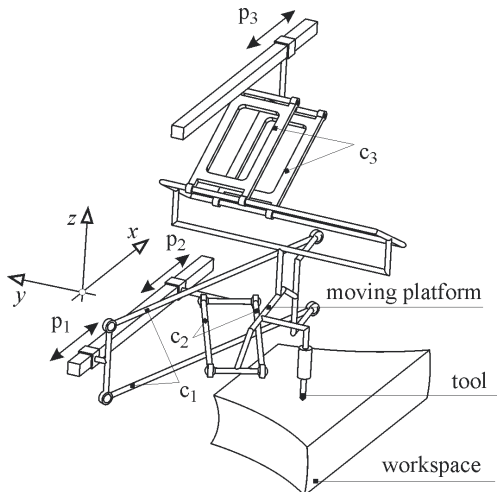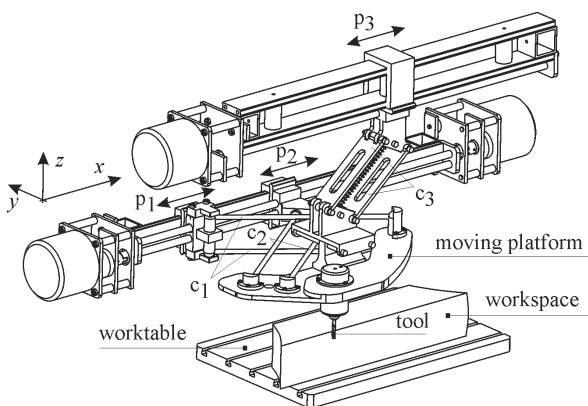

Fig. 5. *CAD model of the parallel mechanism pn101_st* [17]

Since this machine has guideways in a parallel position, the workspace extension is achieved by elongation of one axis (*x*-axis).

Configuring the mini-laboratory and desktop 3-axis PKMM is done in the Creo CAD/CAM system, using the top-down approach, PRO/Web.Link and the web CAD configurator for the standard components.

The CAD model of the developed mini-laboratory and desktop 3-axis PKMM are shown in Fig. 5.

2.1 The Application of Top-Down Approach

Using the top-down approach, all of the crucial information is at the highest level, from where it is forwarded to the lower levels. During configuring, the skeleton model of a parallel mechanism (Fig. 6) is used to define a plan for integration of parts/subassemblies in final assembly of the machine (completing the project of machine).
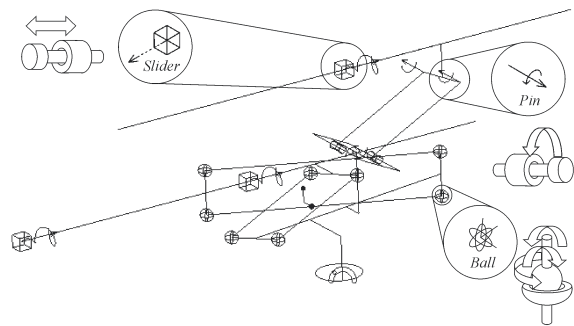
Fig. 6. *A simplified assembly of the skeleton model with constraints*

This is a critical issue when working with large assemblies. Steps to create the skeleton model of the mechanism for the machine are: (1) the analysis and definition of the machine tool configurations; (2) the definition of assembly interfaces in the assembly model with constraints and parameters; (3) the building of a simplified skeleton model with common geometries and constraint interface of the mechanism for 3-axis PKMM.

The skeleton model (Fig. 6) of the parallel mechanism contains all the crucial parameters of the mechanism and the kinematic relations between moving components. The following kinematic relations are used: (1) a slider joint for moving three sliders (p_1, p_2, and p_3) and the passive translational joint, (2) a spherical joint (ball) for coupling two joint parallelograms (c_1 and c_2) with the platform and sliders (p_1 and p_2) and (3) rotary axes (pins) for the passive rotating joint c_3. Illustration of the application of a skeleton model is shown in Fig. 7.

Components and sub-assemblies are integrated into the skeleton model, and, as a result, a parallel mechanism ready for further assembly is obtained. The main machine assembly (ASM0) is organized like a tree, Fig. 8. A large number of standard and

commercially available components (Igus **[4]**, NSK **[5]**, Bosch **[6]**) have been used.
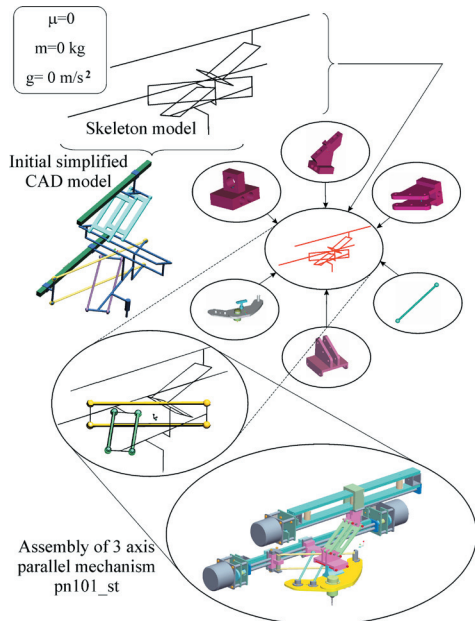
Fig. 7. *The application of a skeleton model in configuring*
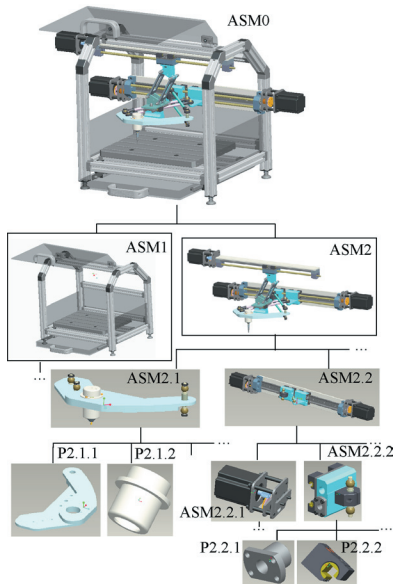
Fig. 8. *Design strategy for the development of mini-laboratory and desktop 3-axis PKMM*

2.2 The Application of Pro/WEB.Link

The dominant axis (*x*-axis) of the parallel mechanism pn101 can be elongated, which makes the mechanism suitable for the design of a family of machines with different lengths of the *x* axis. In this section, how the family of supporting structures and guideways can be easily configured using CAD configurator (Pro/WEB. Link) for design of the family of machines is shown.

Fig. 9a presents the web application interface for the CAD configurator for the example of the supporting structure. The configurator for Igus guideways is shown in Fig. 9b. These guideways are used for lead sliders (p_1, p_2, and p_3) and for the passive translatory joint.
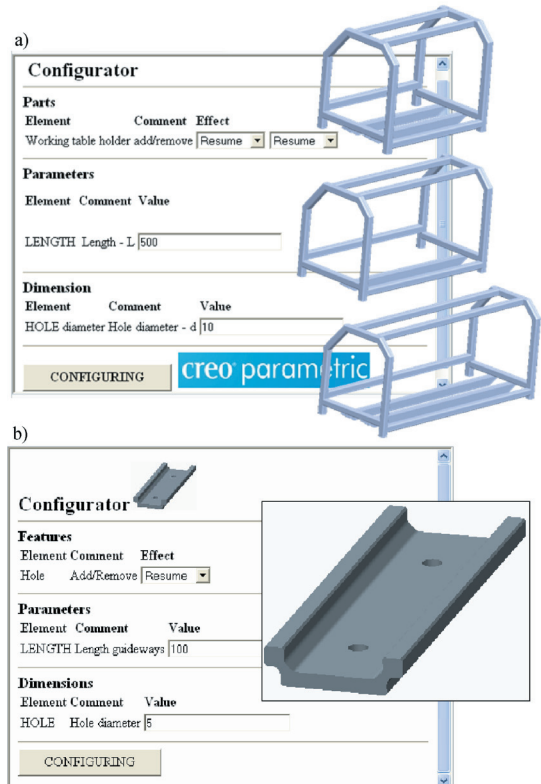
Fig. 9. *CAD configurators in Pro/Web.Link*
a) supporting structure b) Igus guideways

Based on the configurators from Fig. 9, a family of generic modules for configuring the family of machines with different lengths of *x*-axis has been obtained, in which the family parameter is length (*L*).

2.3 Virtual Prototypes

The first low-cost, educational, desktop 3-axis PKMM presented in **[16]** to **[18]** was physically realised and was named pn101_st V1. This paper presents a new version (pn101_st V1.5) with small modifications, which includes the protection cover, as well as a trunk for chips, Fig. 10.

This version is configured from available components for realization of the first prototype. Since this is a mini-laboratory and desktop machine,

its main components (step motors, leadscrews, sliding guideways, joints, etc.) can be easily procured, and all other components can be built in a laboratory.

In addition to the virtual prototype presented in Fig. 10, a virtual prototype of a new version of the machine called pn101_st V2.5, Fig. 11 has been developed and realized. This prototype is configured by using as many standard components as possible, and it is intended for commercial purposes. The pn101_st V1 model is an educational mini-laboratory and desktop 3-axis PKMM whose main components can be purchased commercially; the remaining components can be easily built in the laboratory.

For standard components, some of the common CAD configurators [4] to [6] available on the web have been used; components were downloaded in STEP format, Fig. 1. These components can be easily loaded into any CAD environment and integrated into the required position in the skeleton model.

Upon analysing virtual prototypes from Figs. 10 and 11, the following details can be observed:

- both prototypes have the same built-in parallel mechanism: pn101;
- the first version (V1.5) is configured, so that it can be made of currently available components with a minimum investment, in order to obtain the first prototype;
- the second version (V2.5) is configured with as many standard components as possible, in order to obtain a virtual prototype of a machine that could be easily homemade; the original idea was to use the machine for educational purposes;
- spherical joints in the first prototype are homemade, while in the second standard Igus spherical joints have been used [4];
- guideways of the passive translatory joint are cylindrical in the first prototype, while they are standard square Igus guideways [4] in the second prototype;
- the supporting structure of the first prototype is made of welded steel profiles, while in the second prototype it is made of standard Bosch Rexroth aluminium profiles and connecting elements [6];
- leadscrews in the first prototype are with a common metrical thread, while in the second prototype ball screws were used;
- in both versions, protecting the workspace with transparent Plexiglas on three sides is planned; the front doors are also transparent, and adapted to the form of the supporting structure. Below the machine is a container for the gathering and disposal of chips.

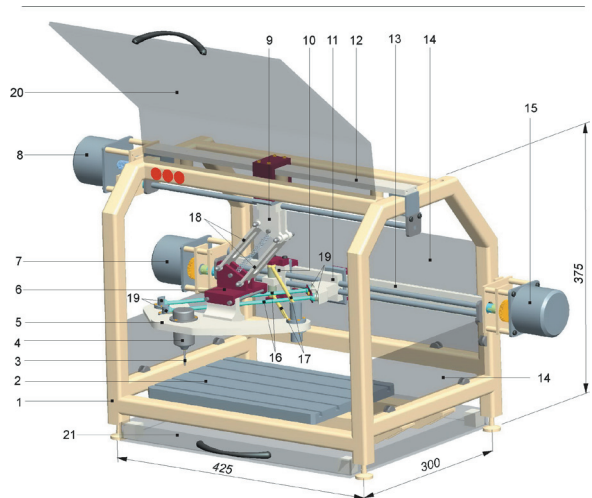Legend: 1- supporting structure, 2-working table, 3-tool, 4-spindle, 5-moving platform, 6- passive translatory-rotating joints, 7-stepper motor axis p1, 8- stepper motor axis p3, 9-slider p3, 10-slider p1, 11-slider p2, 12-guideways p3, 13- guideways p1 and p2, 14- safety cover, 15-stepper motor axis p2, 16- joint parallelograms c2, 17- joint parallelograms c1, 18- joint parallelograms c3, 19-ball joints, 20- protection cover, 21- container for chip

Fig. 10. *CAD model of mini-laboratory and desktop 3-axis PKMM - pn101_st V1.5*
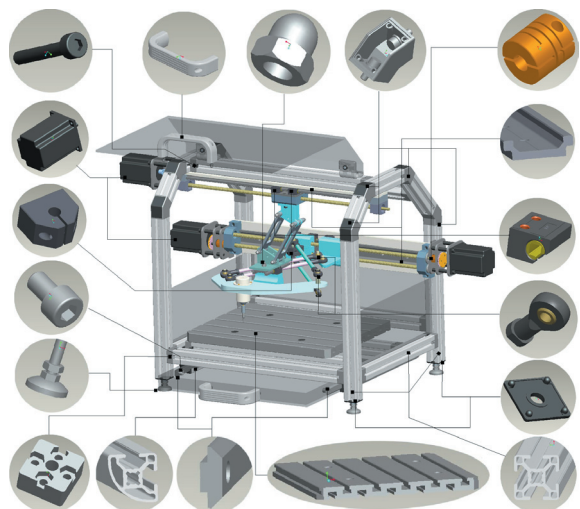
Fig. 11. *Mini-laboratory and desktop 3-axis PKMM - pn101_st V2.5*

Both virtual prototypes have the same parallel mechanism with identical primary parameters designed with different components. The first prototype (pn101_st V1.5) is designed to use available components, while the second prototype (pn101_st V2.5) is designed to use standard components. The second prototype is planned for further commercial development.

3 MACHINING SIMULATION IN THE CAD/CAM SYSTEM

The configured virtual prototypes are used for the verification of the programming system in a CAD/CAM environment by machining simulation based on the generated tool path, which also includes machine simulation. This machining simulation is critical in order to: (i) configure the off-line programming environment, (ii) verify the program before machining, (iii) detect the collision of the parallel mechanism during program execution, and (iv) verify the position of the workpiece within the workspace of a parallel mechanism.

Machining simulation by running the program is possible thanks to the applied modelling of the parallel mechanism with all kinematic connections between the components, which allows the motion of a virtual model as a system of rigid bodies.

Fig. 12 shows a detailed virtual prototype of parallel mechanism with all kinematic relationships defined in the same way as shown in the skeleton model in Fig. 6.
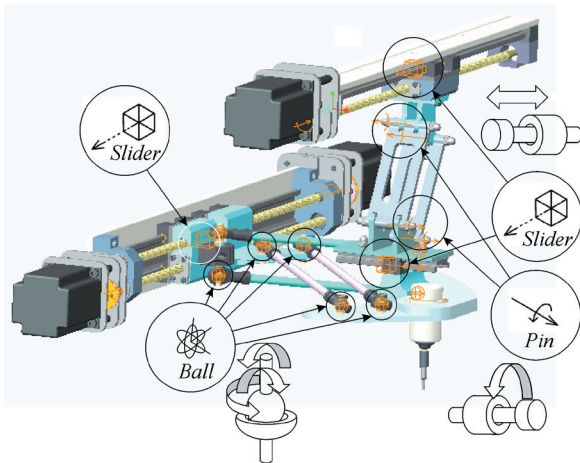
Fig. 12. *CAD model for the simulation of mechanism kinematics*

This assembly enables the motion of models in the range defined for each connection, which is of particular importance for the identification of possible collisions during the work of the parallel mechanism.

Machining simulation of the virtual prototype allows the motion of movable segments with a tool at the end. The tool path is a result of the execution program obtained by programming using the CAD/CAM system. The machine is programmed in the programming format based on the G code.

Although this is a parallel kinematic machine, the same resources are used for its programming as for the machine tool with serial kinematics. Post-processing

is done as for a 3-axis vertical milling machine. The postprocessor is configured using the postprocessor generator in the Creo CAD/CAM system. The equations of direct and inverse kinematics are incorporated into the control system for this machine [16] and [17].

For the first test, a scaled ISO test workpiece whose dimensions are 50×50×12.5 mm is used. Because of the particular shape and size of the workspace of parallel kinematics machines, attention should be paid when setting up a workpiece, which must be within the limits of the workspace of the machine. For the test workpiece shown in Fig. 13a, the zero point in the middle of the underside of the workpiece has been adopted, with the coordinate axes x, y, z as has been used in the vertical 3-axis milling machine, marked as MACH_ZERO. The identical zero point (MACH_ZERO) exists on the machine (on the working table) on which the workpiece is placed, Fig. 13c. Matching these two coordinate systems is accomplished by setting the workpiece on the machine during the machining simulation. Fig. 13b presents the simulated tool path on the scaled ISO test workpiece, based on the generated CL file. The tool coordinate system is defined in the same way as the workpiece coordinate system and marked as a TOOL_POINT (Figs. 13b and d).

During the simulation of tool paths, a complete prototype of the virtual machine can be included into the simulation, with a machine play option. An example of machine simulation for virtual prototype pn101_st V2.5 is shown in Fig. 14 for an ISO test workpiece.
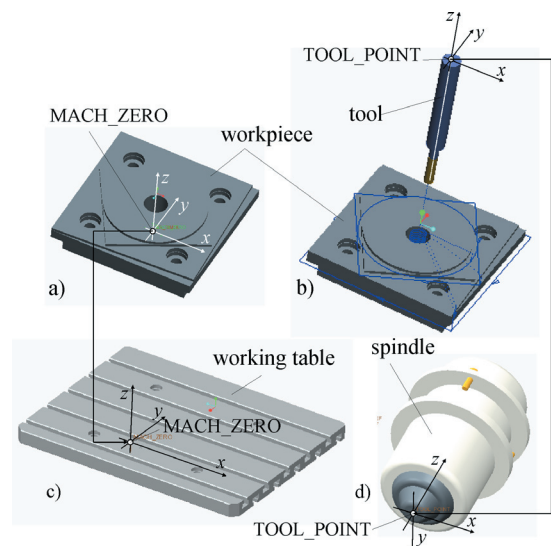
Fig. 13. *Coordinate system of the workpiece and tool with tool path simulation*
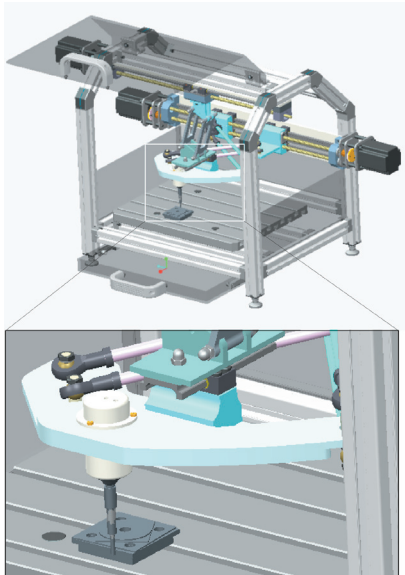
Fig. 14. *Machining simulation in the CAD/CAM system - pn101_st V2.5*

Fig. 15 presents the second test with a machining simulation of the virtual prototype of real world machine pn101_st V1.5. For the machining test and verifying control and programming system, a non-standard test workpiece with a grid of slots was chosen [28].
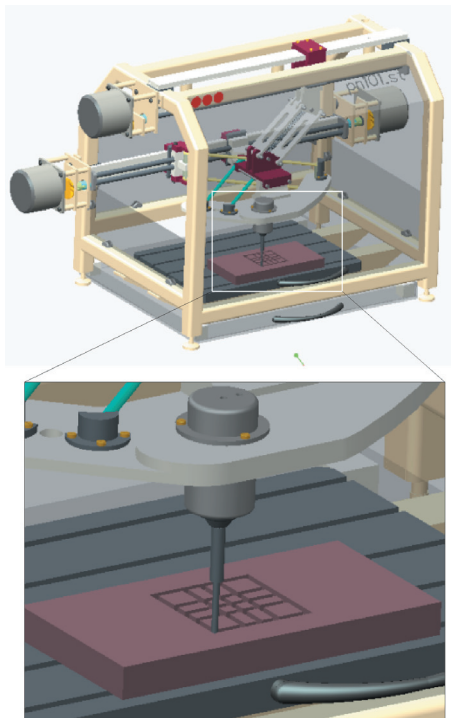
Fig. 15. *Machining simulation in the CAD/CAM system - pn101_st V1.5*

This type of workpiece is used since linear interpolation represents a significant test for the parallel kinematic machine. A linear motion is perhaps one of the most difficult motions that parallel kinematic machines can perform.

Based on the realized simulations of machine virtual prototypes according to the running programs, no collision between the machine elements was observed during program execution. Accordingly, we can state that these tests have successfully verified the programming system and program in G code for both machine virtual prototypes. For the prepared program, the workpiece is set in workspace boundaries correctly and workpiece machining can be performed without collision.

4 MACHINING TEST

The model pn101_st V1.5 mini-laboratory and desktop 3-axis PKMM has been built and tested in our laboratory. While it is educational system with complex kinematics, a virtual machine is included in the control and programming system too [17]. A virtual machine configured in the Python object-oriented programming language is implemented in the control system's enhanced machine controller (EMC2) in an axis graphical users interface (GUI) [29], for program simulation and verification, Fig. 16.
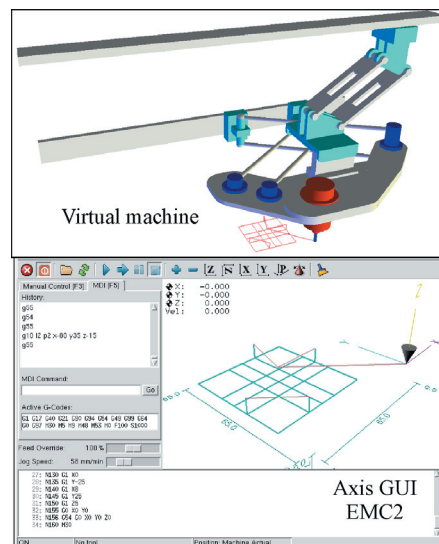
Fig. 16. *Virtual machine - pn101_st V1.5 for program simulation and verification*

A completely realized version of the machine (pn101_V1.5) during a real world machine verification is shown in Fig. 17a. Both test workpieces considered in the machining simulation were used for

verifying control and programming the system. The machined ISO test workpiece is shown in Fig. 17b, and a machined non-standard test workpiece with grid of slots is shown in Fig. 17c.

Dimensions of the workpieces are set according to the dimensions of the machine workspace. These two test workpieces (Figs. 17b and c) were made of Styrofoam. In both cases, a flat end mill tool (diameter 3 mm) was used. These experiments confirmed that it is possible to realize a low-cost mini-laboratory and desktop 3-axis PKMM for workpieces of light materials and lower tolerances, which can be directly used by students, CNC machine tool programmers and operators.
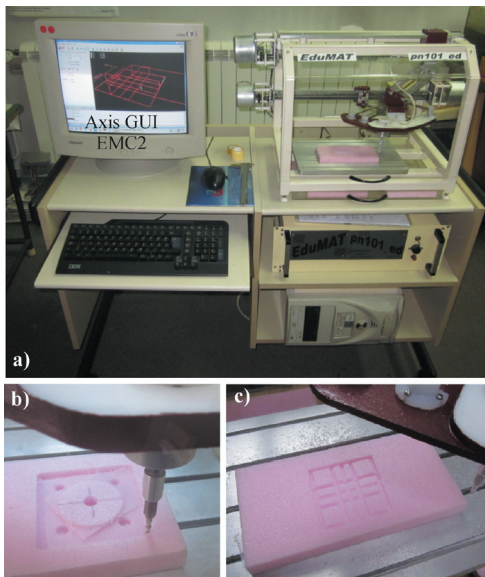
Fig. 17. *Machining tests*

For this machine, in the future we are planning to upgrade the control system, so that it can be utilized for research and application of the new method of programming known as STEP-NC [30]. Furthermore, we will consider the upgrade of the existing parallel mechanism by adding a two-axis serial head on the platform, so that the machine tool can be used for five-axis machining.

5 CONCLUSIONS

In order to contribute towards the acquisition of practical experiences in configuring, design, control, programming, verification and the use of a PKMM, we have developed a mini-laboratory and desktop 3-axis parallel kinematic milling machine.

Two versions of mini-laboratory and desktop 3-axis PKMM have been considered. The first version of the machine was completely carried out, while the second represents a project for possible commercial development for education. Both machines use the same parallel mechanism, which is incorporated into the skeleton model. The difference in machine design is in the components that are built in the skeleton model using specially developed and standard CAD configurators. In its essence, this is a top-down approach, since we start from the basic idea represented by the machine skeleton, which is further developed depending on the available components and desired machine parameters.

The concept of the mini-laboratory and desktop 3-axis PKMM was verified by simulation and by the machining of standardized test pieces. The simulation enabled prior identification of possible collisions between the machine elements during program execution and verification, regardless of whether the parallel mechanism motion is within the boundaries of the machine workspace.

The developed mini-laboratory and desktop 3-axis PKMM represents a comprehensive and sophisticated didactic facility. It can machine soft materials, it is programmable in a conventional way, and it is completely safe for beginners to use.

6 ACKNOWLEDGEMENT

7 REFERENCES

[1] Chen, S., Wang, Y., Tseng, M. (2009). Mass customisation as a collaborative engineering effort, *International Journal of Collaborative Engineering*, vol. 1, no. 1/2, p. 152-167, **DOI:10.1504/IJCE.2009.027444**.

[2] McCarthy, I.P. (2004). Special issue editorial: the what, why and how of mass customization. *Production Planning & Control*, vol. 15, no. 4, p. 347-351, **DOI:10.1080/0953728042000238854**.

[3] Simpson, T.W. (2004). Product platform design and customization: Status and promise. *Artificial Intelligence for Engineering Design, Analysis and Manufacturing*, vol. 18, no. 1, p. 3-20, **DOI:10.1017/S0890060404040028**.

[4] Igus CAD Configuration (2013), from *http://igus.kimweb.de/index.asp*, accessed on 2013-10-17.

[5] NSK Precision America, Solid Components (2013), from *http://www.solidcomponents.com/company/default.asp*, accessed on 2013-10-22.

[6] Bosch Rexroth Corp., CAD Files and Solid Models (2013), from *http://boschrexroth.com*, accessed on 2013-10-27.

[7] Lewis, C. (2004). *Pro/Web.Link Trailer Configurator Demo, Picks & Script - Setup & Reset. Technical Demonstration Development*. Parametric Technology Corporation.

[8] Wang. C.S. (2009). Web-based modular interface geometries with constraints in assembly models. Computers & Industrial Engineering, vol. 56, no. 4, p. 1675-1686, **DOI:10.1016/j.cie.2008.10.018**.

[9] Deciu, E.R., Ostrosi, E., Ferney, M., Gheorghe, M. (2008). Product family modelling in conceptual design based on parallel configuration grammars. *Strojniški vestnik - Journal of Mechanical Engineering*, vol. 54, no. 6, p. 398-412.

[10] Jiao, J., Simpson, T., Siddique, Z. (2007). Product family design and platform-based product development: a state-of-the-art review. *Journal of Intelligent Manufacturing*, vol. 18, no. 1, p. 5-29, **DOI:10.1007/s10845-007-0003-2**.

[11] Simpson, T.W., Maier, J.R.A., Mistree, F. (2001). Product platform design: Method and application. *Research in Engineering Design*, vol. 13, no. 1, p. 2-22, **DOI:10.1007/s001630100002**.

[12] Du, X., Jiao, J., Tseng, M.M. (2001). Architecture of product family: Fundamentals and methodology. *Concurrent Engineering: Research and Application*, vol. 9, no. 4, p. 309-325, **DOI:10.1177/1063293X0100900407**.

[13] Zivanovic, S. (2012). *Development of Educational Parallel Kinematic Machine*. Zaduzbina Andrejevic, Beograd. (in Serbian)

[14] Weck, M., Staimer, D. (2002). Parallel kinematic machine tools-current state and future potentials. *CIRP Annals - Manufacturing Technology*, vol. 51, no. 2, p. 671-683, **DOI:10.1016/S0007-8506(07)61706-5**.

[15] Cheng, G., Xu, P., Yang, D., Li, H., Liu, H. (2013). Analysing kinematics of a novel 3CPS parallel manipulatorm based on rodrigues parameters. *Strojniški vestnik - Journal of Mechanical Engineering*, vol. 59, no. 5, p. 291-300, **DOI:10.5545/sv-jme.2012.727**.

[16] Milutinovic, D., Glavonjic, M., Zivanovic, S., Dimic, Z., Kvrgic, V. (2008). Mini educational 3-axis parallel kinematic milling machine. *Proceedings of 3rd International Conference on Manufacturing Engineering ICMEN and EUREKA Brokerage Event*, Kallithea of Chalkidiki, p. 463-474.

[17] Glavonjic, M., Milutinovic, D., Zivanovic, S., Dimic, Z., Kvrgic, V. (2010). Desktop 3-axis parallel kinematic milling machine. *The International Journal of Advanced Manufacturing Technology*, vol. 46, no. 1-4, p. 51-60, **DOI:10.1007/s00170-009-2070-3**.

[18] Zivanović, S., Glavonjić, M., Dimić, Z. (2009). Methodology for configuring desktop 3-axis parallel kinematic machine. *FME Transactions*, vol. 37, no. 3, p. 107-115.

[19] Milutinovic, D., Glavonjic, M., Kvrgic, V., Zivanovic, S. (2005). A new 3-DOF spatial parallel mechanism for milling machines with long X travel. *Annals of the CIRP*, vol. 54, no. 1, p. 345-348, **DOI:10.1016/S0007-8506(07)60119-X**.

[20] Glavonjic, M, Milutinovic, D. (2008). Parallel structured milling machines with long X travel. *Robotics and Computer-Integrated Manufacturing*, vol. 24, no. 3, p. 310-320, **DOI:10.1016/j.rcim.2006.12.001**.

[21] Vijay Sekar, K.S., Pradeep Kumar, M. (2012). Optimising flow stress input for machining simulations using taguchi methodology. *International Journal of Simulation Modelling*, vol. 11, no. 1, p. 17-28, **DOI:10.2507/IJSIMM11(1)2.195**.

[22] Deng, W.J., Xie, Z.C., Li, Q., Lin, P. (2013). Finite element modelling and simulation of chip breaking with grooved tool. *International Journal of Simulation Modelling*, vol. 12, no. 4, p. 264-275, **DOI:10.2507/IJSIMM12(4)5.250**.

[23] Kopač, J., Kržič, P. (2008). CAM algorithm as important element by achieving of good machined surface quality. *Strojniški vestnik - Journal of Mechanical Engineering,* vol. 54, no. 4, p. 280-287.

[24] Lewis, C. (2008). *A Pro/Engineers Guide to Pro/Web.Link*, Printed on-demand by, www.lulu.com.

[25] Creo Parametric 1.0. (2011). *Pro/Web.LinkUser's Guide*, Parametric Technology Corporation, 140 Kendrick Street, Needham.

[26] Remmers, V. (2006). Top-down design tools-managing complex assemblies, tips & techniques. Parametric Technology Corporation, The way to product first, from *http://www.ptcuser.nl/conf_06/presentations/T%20&%20T%20Top-Down%20Design.ppt*, accessed on 2013-10-30.

[27] *Pro/Engineer: Top-down Design Task Guide: Release 20.0.* (1998). Parametric Technology Corporation.

[28] Powel, N.P., Whittingham, B.D., Gindy, N.N.Z. (1999). *Parallel Link Mechanism Machine Tools: Acceptance Testing and Performance Analysis, Parallel Kinematic Machines – Theoretical Aspects and Industrial Requirements*, Springer-Verlag, London.

[29] Linux CNC: Software for real-time control (2013). from *http://www.linuxcnc.org*, accessed on 2013-04-30.

[30] Kržič, P., Stoic, A., Kopač, J. (2009). STEP-NC: A New Programming Code for the CNC Machines. *Strojniški vestnik - Journal of Mechanical Engineering*, vol. 55, no. 6, p. 406-417.

The Effect of Dynamic Local Self-Preheating in Laser Cladding on Grey Cast Iron

Peng Yi* – Pengyun Xu – Changfeng Fan – Chengkai Li – Yongjun Shi

China University of Petroleum, College of Mechanical and Electrical Engineering, China

In laser cladding, high cooling rates are accompanied by superior mechanical and metallurgical properties. However, these characteristics, along with the additive nature of the process, significantly contribute to the formation of thermal stresses, which are the main cause of any potential delamination and crack formation across the remelted area. To reduce thermal stress and better manage the microstructure, a strategy of dynamic local self-preheating has been designed. Laser-cladding experiments with no preheating, static global preheating, and dynamic local preheating with grey cast iron have been conducted. Parallel to the experimental investigations, numerical models have been established in order to study the temperature distributions and thermal stresses in different processes. The results indicate that dynamic local self-preheating contributes to reducing the transient thermal stress and residual stress compared with other methods. With self-preheating of the substrate, microstructures of the coarse-grained region are well-developed. The self-preheated sample reveals a more compact structure in the fusion area and can exhibit less cracking during the cladding process.

Keywords: laser cladding, grey cast iron, local self-preheating, numerical models, microstructure

Highlights
- *Proposed dynamic local self-preheating process.*
- *Numerical modeling of different heating strategies.*
- *Cracking resistance capacity study.*
- *Research on declination of thermal stress and residual tensile stress.*
- *Representation of temperature gradient influences on grains and phases.*

0 INTRODUCTION

Laser cladding, as one of advanced flexible surface manufacturing techniques, has shown great application potential in different fields, including coating modification, cladding of high-value components, and freeform fabricating. Compared to other conventional techniques, laser cladding has several advantageous technical characteristics, i.e. small heat-affected areas, minimal dilution and specific sizes for raw material procurement [1]. In this technique, a laser beam (as a heat source) strikes the upper surface of a substrate to form a small molten pool. By pre-placing or depositing metallic powder onto the upper surface, a narrow cladding tract is formed, and solid state transformation then occurs during the cooling process [2].

In spite of all the demonstrated advantages of the laser-cladding process, the substrates manufactured by this technique are prone to a number of drawbacks, including porosity, delamination and crack formation. Consequently, the process domain inherently undergoes a high cyclic heating and cooling regime. Many efforts have been made to improve the operating strategy to overcome these drawbacks. Jendrzejewski and Śliwiński [3] studied temperature and stress in the laser-cladding process

of chromium steel; this research indicated that cracks in a single-layer coating decreased with preheating of the substrate. Danlos et al. [4] determined that laser ablation elevated the temperature of the substrate and that this is beneficial to suppress splashing in the thermal-spraying process. Amongst them, substrate preheating has been indicated to be a novel and important method, and can be expected to show better results. Many articles have implemented numerical and experimental approaches to investigate the effect of global substrate preheating in the laser-cladding process. The research of Zhang et al. [5] focused on the laser-cladding process of austenitic stainless steel; the experiments showed that preheating is necessary in order to prevent cracking. Aghasibeig and Fredriksson [6] investigated the laser-cladding process of an iron-based alloy on steel substrate; the results indicated that pre-heating the substrate reduced the number of cracks. Parallel to these, the feasibility of preheating on the reduction of micro-cracks has been demonstrated, and the susceptibility to micro-cracking is smaller for the preheated base. In these studies, the substrate was preheated globally in advance, i.e. static global preheating (SGP); the corresponding temperature field was then considered as an initial condition for the following analysis. The means of placing the work pieces in a furnace for an

extended period as SGP process have been adopted widely but usually accompanied by low cladding efficiency and hostile working environments [7]. From another perspective, during the investigation concerned with the multilayer or overlapping cladding process, the effect of dynamic local preheating (DLP) from preceding tracks to a successive one should be considered, because they tend to increase the dilution of current cladding and improve the thermal stress status, as well as the metallurgical microstructure. Drawing inspiration from this, several research groups have developed different approaches to imitate the effect of DLP. For instance, in works from Zhou, the laser cladding was combined by simultaneously preheating the substrate with an induction heater (coil) (i.e. laser induction hybrid rapid cladding (LIHRC)), and the microstructure characteristics of the coating and interface were investigated [8]. As a result, the temperature gradient decreased, and the dilution of composite coating increased with the increase of the preheated temperature; moreover, the extent of metallurgical reaction can be controlled. This is an effective method of achieving the effect of DLP; however, it is accompanied by disadvantages, such as higher process cost and complexity because an entire set of removable induction heater devices (including the control operation) is additionally needed. Fallah et al. developed a laser DLP strategy, and conducted experimental and numerical measures to investigate the effects on the management of temperature and thermal stress distributions of Stellite 1 laser cladding powder on AISI-SAE 4340 alloy steel [9]. It was confirmed that a crack-free coating layer well-bonded to the substrate with a uniform dendritic structure and well-distributed deposited layer could be obtained. While multi-track and overlap scans made the DLP effects lack definition, the absence studies on the process parameters of a laser DLP strategy resulted in an incomplete investigation.

In this paper, single-track laser cladding experiments of different preheating strategies are conducted, and the microstructures are analysed. Numerical models are established to investigate the temperature and stress distribution under different preheating strategies. The effects of dynamic local preheating with different process parameters are shown.

1 EXPERIMENTAL PART

1.1 Materials

It is well known that the grey cast iron, as a prominent type of ferrous metal, is widely used in the manufacture of machine tool beds, cams, pistons, cylinders, etc., because of its low cost and desirable properties. Laser heat-treatment was successfully employed with cast iron to improve surface microstructures and harden machine parts in the research of Grum and Šturm [10] and [11]. However, few studies have reported research on the laser-cladding processes on grey cast iron since considerable free carbon, in the form of graphite flakes or globules, is present, and cladding on cast iron is difficult [12]. Therefore, for this work, a common grey cast iron, codenamed HT250, is selected as the substrate material. HT250 grey cast iron is denominated by Chinese Standard GB 9439-88. Commercial Fe-based powder, codenamed Fe311, is used as the cladding materials. The Fe311 powdered alloy is one of the product lines of the Beijing General Research Institute of Mining & Metallurgy. The powder size and density are approximately 150 to 250 μm and 2.8 to 4.8 g/cm³, respectively. The chemical compositions of HT250 and Fe311 are given in Table 1.

Table 1. *Chemical composition (wt. %) of HT250 substrate and Fe311 powder*

Material	C	Si	Mn	P	S	Cr	Ni	B	Fe
HT250	3.250	1.570	0.920	0.060	0.059	0.270	-	-	Bal.
Fe311	0.100	1.000	-	-	-	15	10.000	1.000	Bal.

Table 2. *Processing parameters for different test cases*

Case No.	Strategy	T_0 [ºC]	P_p [W]	v_p [mm/min]	d_p [mm]	P [W]	v [mm/min]	d [mm]
1	UNP	22	-	-	-	2500	300	3.2
2	SGP	350	-	-	-	2500	360	3.2
3	DLP	22	800	400	5.5	2500	360	3.2
4			800	600				
5			600	600				

Samples of 50×40×10 mm are cut and mechanically surface polished. As shown in optical micrograph Fig. 1, the HT250 microstructure consists of A-type flaky graphite (G) surrounded by lamellar pearlite (P) and some amount of ferrite (F).
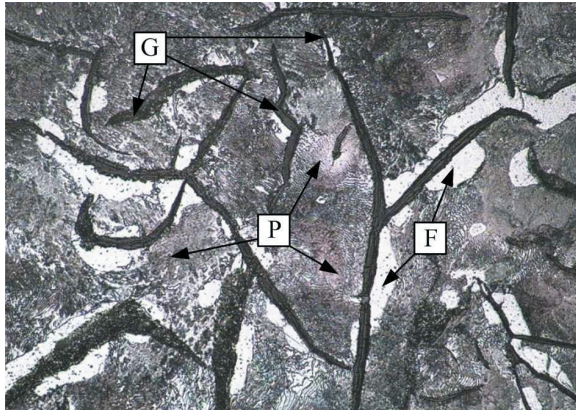

Fig. 1. *Microstructure of HT250 grey cast iron*

1.2 Processing Conditions

A single-track laser DLP strategy is designed and implemented to make the laser-cladding process more effective. Both the macro- and micro- characteristics of coating layers on substrates are processed by this DLP and traditional SGP methods, as well as on un-preheated (UNP) substrate. The process parameters are of vital importance for laser processing, and a great deal of research has been performed to determine the proper parameters to improve laser manufacturing quality [13] and [14]. Considering the lack of studies on the process parameters of the laser DLP strategy, different preheating laser power levels and scan rates are taken into account. To interpret the experimental results, coupled 3D time-dependent numerical models are employed to simulate the process along with the experimental analyses.

For the purpose of discussing the effects of the self-preheating process, six test cases are prepared, and the processing parameters are listed in Table 2. Firstly, numerical models for each case are established, and the results are comparatively analysed. Next, experiments are conducted for Cases 1 and 2 and complex ones for Cases 3 to 5. Furthermore, in the experimental process, three samples are taken to be fused for each case so as to avoid accidental events.In Table 2 T_0 is the initial substrate temperature, P, v and d denote the laser power, scan rate and spot diameter, respectively, and the parameter with subscript p represents the preheating condition.

For Cases 1 to 2, a conventional laser-cladding process without preheating and one with SGP in advance are conducted, respectively. With regard to Cases 3 to 5, laser claddings are separately prepared by using laser DLP with different parameters prior to the cladding process; the schematic is shown in Fig. 1. In DLP cases, cladding powders are always placed on substrates after the preheating process, with an approximate handling time of 40 s due to the processes of laying powders, raising the laser power and reducing the scan rate.
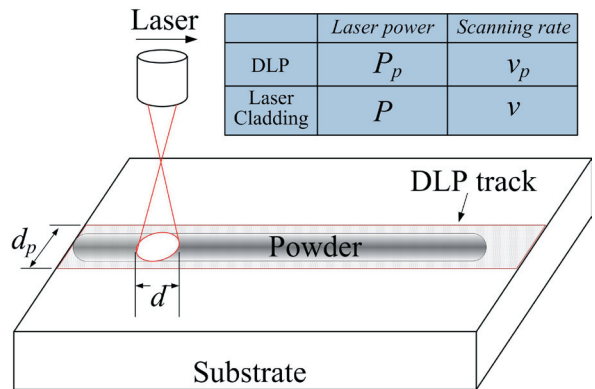
Fig. 2. *Schematic diagram of the laser-cladding process with DLP in advance*

In an experimental procedure, the substrates are cleaned with alcohol and then preset with the Fe311 powders on the surfaces. Laser cladding is carried out using a continuous wave CO_2 laser (HL-10 type). Laser cladding experiments of UNP, SGP and DLP are performed in the course of the study to either verify or interpret the numerical outcomes. The metallographic samples are made with wire-electrode cutting, ground and polished, then etched in 4% Nital for 3 to 4 seconds, and blown dry after being flushed with pure alcohol. The microstructure and morphology are obtained via an MBA-1000 optical microscope.

2 NUMERICAL PROCEDURE

Since with laser cladding the temperature distribution and its evolution throughout the process determine the final mechanical and metallurgical qualities of the outcomes, to study and interpret the experimental results, a 3D numerical approach is developed using ANSYS commercial FEM code and employed to simulate the process [15]. In order to discretize the substrate, eight-node hexahedron elements are used. As shown in Fig. 3, for the appropriate result of a compromise between computing time and accuracy,

a dense mesh is used around the fusion line, and a coarser mesh is adopted for the rest.
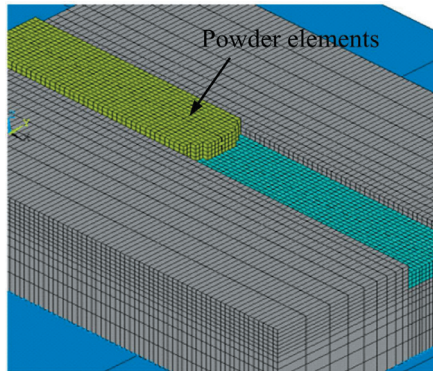
Fig. 3. *FEM model with activation of powder elements*

In this approach, a circular Gaussian TEM_{00} mode is considered for the laser energy distribution, as well as the effects of heat losses through convection and radiation, the latent heat of fusion, and the constraint forces are taken into account [16]. Meanwhile, a finite idle time between preheating and fabricating tracks is considered in the simulation, because it is inevitable in the experiments. For the numerical simulations, all process parameters and specifications are considered to be the same as those in experiments; then, by using this approach, time-dependent temperature and thermal stress fields across the process domain can be predicted. More details regarding the modelling process and its verification have been provided in previous work [17]. Consistent with the experiment process, numerical models (including processes of UNP, SGP and DLP) are established to investigate the effect of pre-heating. The time-dependent temperature, thermal stress and residual tensile stress in different processes are analysed.

In order to better analyse and interpret the effect of different pre-heating impacts, the microstructures of the samples need to be studied further. Therefore, experiments are carried out parallel with numerical models, and the microstructure morphology is analysed with OM.

3 RESULTS

3.1 Numerical Results

As the variation of the molten pool is extremely high and complex, it is difficult to accurately acquire data from this area. Meanwhile, thermal stress in the area at 0.5 mm under the molten pool is larger than that

of other areas [9]. In order to investigate the time-dependent maximum temperature and thermal stress variation, a path that is along the deposition direction and at 0.5mm under the molten pool is selected.
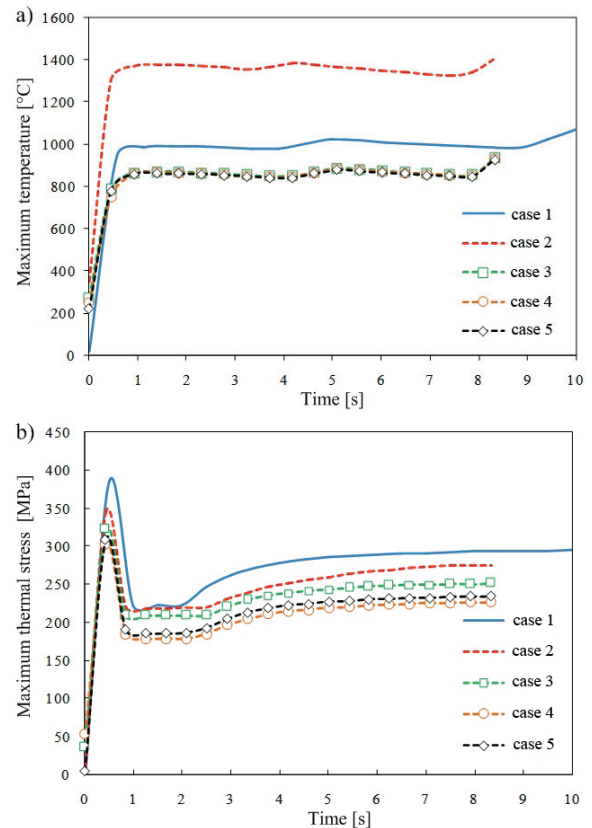
Fig. 4. *a) Maximum temperature; and b) thermal stress of path along the deposition direction and at 0.5 mm under the molten pool in laser cladding in cases 1 to 5*

Fig. 4 illustrates the maximum temperature and thermal stress variation of the path. The cladding time is 10 and 8.33 s in Case 1 and Cases 2 to 5, respectively. As shown in Fig. 4a, the initial temperature of Case 1 is 22 °C while Case 2 is 350 °C as a result of global preheating before the cladding process. The initial temperatures of Cases 3 to 5 are 274, 248 and 220 °C, respectively, due to the different processing parameters of laser self-preheating. At the beginning of the laser-cladding process (0 to 0.8 s), the temperature rises rapidly due to the sudden heat input. Next, the temperature remains steady and, during this period, the maximum temperature in Case 2 is the highest (1350 °C), followed by Case 1 (990 °C) and Cases 3 to 5 (870 °C).

Fig. 4b shows the maximum thermal stress of the path in laser cladding. There is little thermal stress in Cases 1 and 2 at the beginning of cladding process,

while the initial thermal stresses in Cases 3 to 5 are 39, 47 and 6 MPa, respectively. When laser cladding is employed, there is a sharp increase of thermal stress in the initial period (0 to 0.8 s), as shown in Fig. 4b. The thermal stress of Case 1 is the largest (385 MPa) followed by Case 2 (343 MPa) while DLP (Cases 3 to 5) indicates lower stresses: 322, 302 and 308 MPa, respectively. After the initial period, the laser-cladding process enters a stable period, and the temperature of the path remains constant. The maximum thermal stress declines by around 120 MPa and then remains stable, as shown in Fig. 4b. In this period, the maximum thermal stress in Case 1 is the largest (290 MPa), followed by Case 2 (260 MPa). Thermal stresses in Cases 3 to 5 are smaller in comparison to Cases 1 and 2: 245, 220 and 230 MPa, respectively.
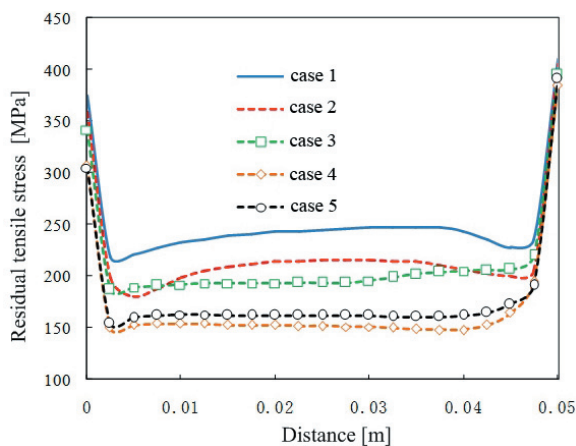
Fig. 5. *Residual tensile stress of the path in the middle of the coating surface in cases 1 to 5*

A path in the middle of the coating surface is selected to study the residual tensile stress, which has a vital impact on cladding quality. As shown in Fig. 5, residual tensile stress is very great at the ends of the coating, while maintaining a small and stable status in the middle. At the start of cladding layer (*Distance* = 0 m), the residual tensile stress of Case 1 (375 MPa) and Case 2 (359 MPa) is larger than that of Cases 3 to 5 (337, 307 and 305 MPa, respectively). The residual stress decreases sharply by about 140 MPa in the 0 to 0.0025 m distance. At the middle part of the coating (*Distance* = 0.0025 to 0.048 m), the residual tensile stress remains at a small and stable value. Case 1 is the largest (245 MPa) followed by Case 2 (215 MPa) and Case 3 (195 MPa). The residual tensile stresses in Cases 4 and 5 are small in comparison to others: 150 and 160 MPa respectively. At the terminal of the coating (*Distance* = 0.048 to 0.05 m), the residual

tensile stresses in Cases 1 to 5 have an acute increase, reaching 400 MPa.

3.2 Microstructure Morphology Characteristics

3.2.1 Microstructure of UNP

Fig. 6 shows a cross-section morphology for a sample of Case 1 without preheating (UNP). The overall morphology, cladding zone and fusion zone microstructure are illustrated in Fig 6 at high magnification. It is demonstrated that the overall cross section of the cladding zone is in a half-moon shape as a result of the uneven energy distribution of circular facula. The quality of the cladding zone is good, with a compacted microstructure and a low level of porosity. The depth of heat-affected zone is small, the maximum depth is approximately 450 μm and the delamination of fusion zone is obvious.

As seen in Fig. 6b, the non-spontaneous nucleation process of the cladding zone is rapid due to the high cooling and temperature gradients. The formative column crystal has a refined structure with an average diameter of 9.6 μm and is not highly directional due to the rapid crystal growth time. The microstructure of the fusion zone is shown in Fig. 6c. The top of the fusion zone is close to the cladding zone, and there is mutual fusion with elements in the cladding zone. This area consists of high amounts of lamellar cementite and some acicular martensite. In the middle of the fusion zone, there is a great deal of acicular martensite, residual austenite and partially-dissolved graphite. The bottom of the cladding zone consists of lamellar pearlite and acicular ferrite, as the heat effect is less than the top and middle area, and the transformation of materials is not obvious. In addition, the molten mass begins to transit with rapid super-cooling below the eutectic temperature of $Fe-Fe_3C$. Meanwhile, cementite, a small amount of austenite and martensite form the hard eutectic phase.

3.2.2 Microstructure of SGP

Fig. 7 shows the cross section morphology for Case 2 (SGP, global preheating temperature of 350 °C). It can be determined from Fig. 7a that the quality of the cladding zone is good, having a refined microstructure and a low level of porosity. The size of the cladding zone, the heat-affected zone and the fusion zone are all widened compared with Fig. 6a, owning to the preheating process prior to laser cladding. As shown in Fig. 7b, the average diameter of crystal is around 13.5 μm, which is obviously coarser than that of
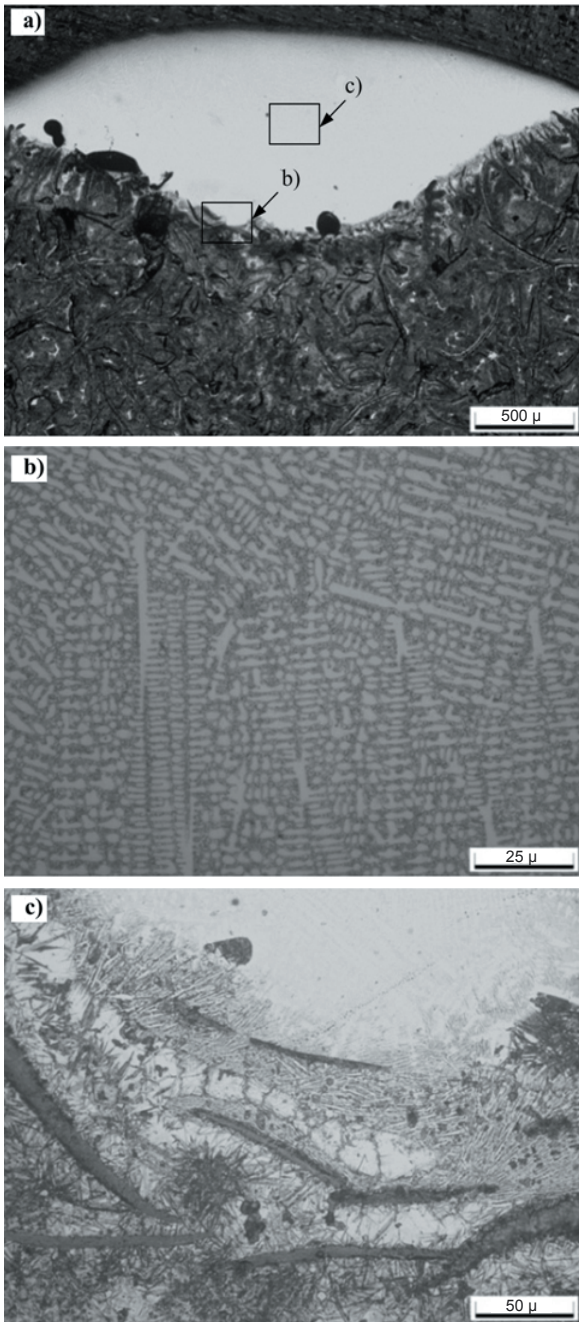
Fig. 6. *Optical images of the clad cross section for case 1 sample in: a) overall section (50×), b) cladding zone (500×), and c) fusion zone (1000×)*
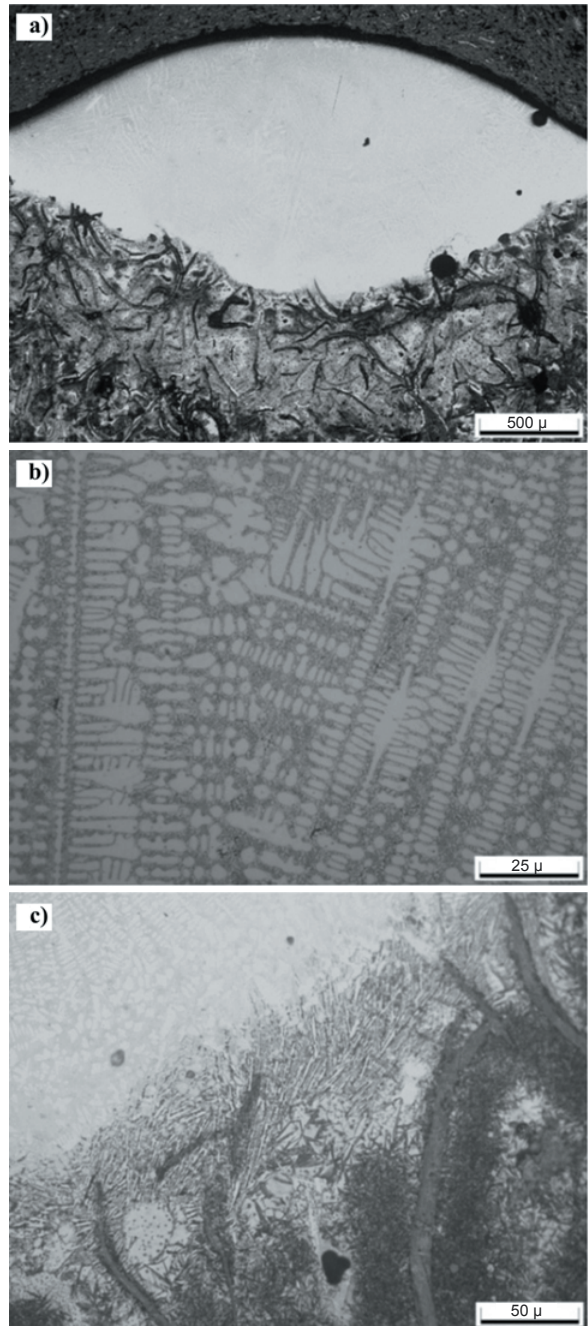
Fig. 7. *Optical images of the clad cross section for case 2 sample in: a) overall section (50×), b) cladding zone (500×), and c) fusion zone (1000×)*

Fig. 6b. As a result of the 350 °C global preheating process, the growth of crystals is better, and the secondary dendrite arms are stronger than that of UNP. Fig. 7c shows the microstructure of the fusion zone. It includes large amounts of lamellar cementite in the top and acicular martensite, residual austenite in the middle, which is similar to the microstructure

distribution of UNP. However due to the decrease of the cooling rate and the degree of super-cooling, the proportions of cementite, martensite and bainite in the fusion zone decline, and the molten mass then begins to transit with the temperature above the eutectic temperature of Fe-Fe3C and below that of Fe-C.

Yi, P.– Xu, P.Y. – Fan, C.F. – Li, C.K. – Shi, Y.J.

White iron structures are replaced by eutectic grey iron structures formed by graphite, austenite and martensite, inducing a decrease of micro-cracks and a decline of micro-hardness. Additionally, the graphite phase gathers in this zone, which mainly contains thick flake graphite with many branches, owning to the sufficient precipitation and rapid growth of graphite, which is not favourable for maintaining the structure integrity.

3.2.3 Microstructure of DLP

The microstructure morphology of the clad cross section for the Case 4 sample is illustrated in Fig. 8. The preheating temperature discipline is similar to the cladding process due to the same laser energy effect, which results in a small heat-affected zone, and the temperature descends to around 220 °C before cladding. Consequently, the maximum heat-affected zone depth achieves about 530 μm between that of UNP and SGP. Local self-preheating raises the temperature to the value between the eutectoid and eutectic points in terms of the iron-carbon phase diagram. The duration is around 0.7 s, which leads to the primary cementite decomposition and ferrite growth because of the eutectoid phase transformation in surface microstructure. At this point, cladding is implemented, and the similarity of the molten mass is high, which induces a large amount of convection and a proliferation and decrease of local segregation. The substrate depth is influenced more obviously as a result of the direction of the laser thermal input. Similar to Fig. 7b, the degree of super-cooling is reduced by local preheating; the columnar crystals in the cladding zone with an average diameter around 11.8 μm shown in Fig. 8b are coarser than that demonstrated in Fig. 6b. As illustrated in Fig. 8c, the amount of cementite or other brittle organization in the fusion zone decreases more in comparison to SGP, while the ferrite increases, which results in a decline of micro-hardness.

3.3 Hardness Distribution of Clad Area

As seen in Fig. 9, the micro-hardness of the clad area under different preheating temperatures is examined from its surface to its bottom in a cross section along the depth direction. The hardness variation tendency of UNP, SGP and DLP is similar, which maintains a high hardness at the cladding zone and declines towards the substrate. The hardness of UNP is the highest, which reaches about 500 HV at the top of the cladding zone, while the hardness of SGP is the
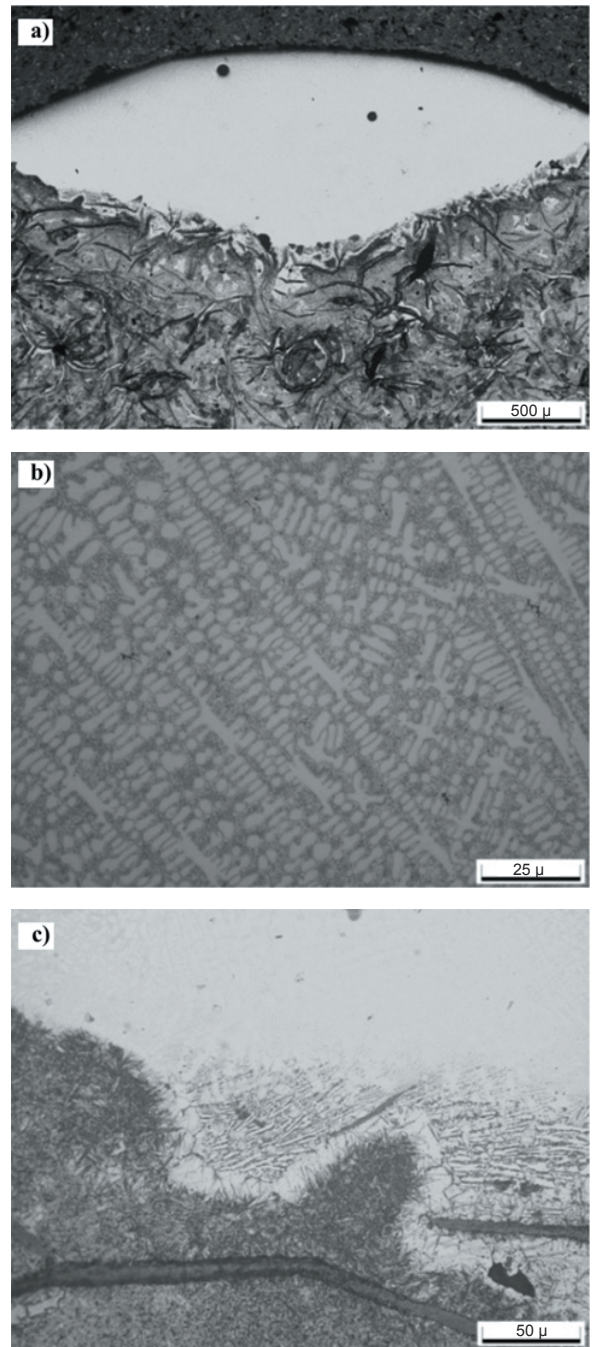
Fig. 8. *Optical images of the clad cross section for Case 5 sample in: a) overall section (50×), b) cladding zone (500×), and c) fusion zone (1000×)*

lowest (425 HV). The hardness of DLP is between that of UNP and SGP, which is around 475 HV. With the increase of distance away from the surface of the cladding zone, the hardness declines gradually. As the effect of laser heat input on the heat-affected zone and substrate is slight, the microstructure has little change.

Therefore, the hardness of the heat-affected zone and the substrate area of UNP, SGP and DLP is quite close, at 230 HV.
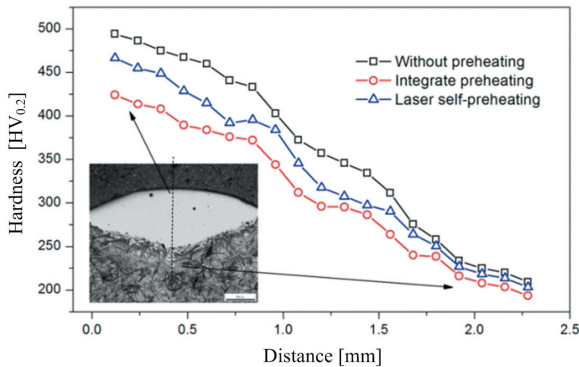
Fig. 9. *Hardness distribution in cross section of the clad area*

4 DISCUSSION

4.1 Analysis of Numerical Models

From the variation of maximum temperature and thermal stress (Fig. 4), it can be determined that, prior to laser-cladding process, the initial temperature for Cases 1 and 2 is 22 °C (ambient temperature) and 350 °C (SGP temperature), respectively. No thermal stress exists in Cases 1 and 2, as there is no external heat effect, and the substrates in Cases 1 and 2 achieve heat balance. For Cases 3 to 5, the substrates underwent a DLP process before cladding, so the initial temperature is higher than the ambient temperature, and there is a small amount of residual stress inside. When the laser-cladding process begins, substrates undergo a sudden massive heat input, and the temperature rises acutely in a short period (0 to 0.8 s). The original stress balance is broken, and the material melts and deforms acutely, which induces a sharp increase of thermal stress at the beginning of the cladding process. Next, the cladding process enters a stable period, and the temperature of the path remains constant. As a result of the stable heat input, the maximum thermal stress declines and then remains stable. It is clearly indicated on Fig. 4b that laser preheating is beneficial in reducing thermal stress. Cases 4 and 5 have the lowest stress (about 220 MPa), which is 70 MPa lower than that of Case 1 and 34 MPa lower than that of Case 2. It can be summarized that DLP has a positive effect on reducing thermal stress, and that a relatively low preheating power is more suitable.

The residual tensile stress distribution in Fig. 5 demonstrates that without preheating (Case 1), the residual thermal stress is very great (375 MPa at ends and 240 MPa at middle) and is highly likely to cause cracks. Cases 2 and 3 reveal a relatively lower stress than Case 1, which is around 200 MPa in the middle coating. As Case 3 has a high preheating power, and the temperature in the preheating process can reach 800 °C, a great deal of stress appears and remains in the coating. Therefore, the accumulated stress is higher than that in Cases 4 and 5. Comparatively dynamic local preheating with low preheating power (Cases 4 and 5) indicates lower and uniform stresses, which are about 150 MPa in the middle coating. It is concluded that residual tensile stress is reduced significantly by dynamic local preheating, due to the decline of temperature gradient and cooling rate. Case 4 exhibits a better performance than Case 5 does, as the preheating temperature is higher, and temperature gradient in Case 4 is smaller.

4.2 Microstructure Changes

From the overall section of microstructure in Cases 1, 2 and 5, it can be determined that the quality of the cladding zone is good, containing compacted and refined microstructures and low porosity. The initial temperature of Case 1 is the lowest (22 °C) as no preheating is applied, while the initial temperature of Case 2 is the highest (350 °C) due to the SGP process. Case 5 undergoes the DLP process prior to laser cladding, and the initial temperature (220 °C) is between Cases 1 and 2. The high initial temperature increases the heat input in the laser-cladding process, and the sizes of the cladding zone, fusion zone and heat-affected zone are widened.

As no preheating is employed in Case 1, the convection time is extremely short, and the diffusion and penetration are incomplete. This results in a very low dilution rate and local composition aliquation of the fusion zone. However, the heat input increase in Case 2 contributes to the expansion of the molten pool and heat-affected area as a result of the constant laser-specific energy. Furthermore, the substrate can reach its melting point in less time, and the convection, diffusion and penetration of the molten mass are better, which result in more uniform composition and less local aliquation. The increasing initial temperature the reduces super-cooling degree and temperature gradient, and the nucleation rate in the molten pool decreases, which leads to better growth of crystals with clearer direction.

As for Case 5, the substrate has a dynamic laser preheating process, and the temperature increases to the point between eutectoid and eutectic. Therefore,

the DLP process helps to decompose the primary cementite and improve the growth of ferrite. Due to the DLP process, the material has more similar characteristics with that in the laser-cladding process. The increase of the similarity of the molten mass improves the convection and proliferation, which dramatically decreases local aliquation.

4.3 Hardness Variation

It can be concluded that micro-hardness distributions are similar if one takes into consideration that in microstructure analysis the overall hardness gently declines after preheating. The hardness of testing points in the clad zone for UNP is highest, because no preheating is applied, and the microstructure after cladding includes many compact and refined grains and a great deal of hard phase. A sample of SGP is heated globally to 350 °C prior to the laser-cladding process, which results in a small super-cooling degree and temperature gradient. The nucleation rate declines and grains grow adequately. The microstructure of the clad area contains many coarse grains and phase with lower hardness, which induces the lowest hardness of the clad zone for SGP. The microstructure property of DLP is between that of UNP and SGP. The grain size of the cladding zone is larger than that of UNP but smaller than that of SGP. The convection and proliferation are better than that of UNP because of the laser preheating process, and the little hard phase. Therefore, the hardness of DLP is lower than that of UNP but higher than that of SGP.

5 CONCLUSIONS

(1) Different heating strategies, which include un-preheated substrate, SGP and DLP, are investigated in this work. Numerical models are established to study the effect of different preheating strategies and preheating parameters on temperature and stress variation. Experiments are employed to investigate the microstructure and micro-hardness. Compared with SGP in [6] and induction preheating in [8], laser DLP provides a flexible and reliable technology to reduce thermal stress and manage microstructure for laser cladding on grey cast iron.

(2) The numerical calculation proves that DLP elevates the initial temperature of the substrate before cladding. The temperature gradient, thermal stress and residual tensile stress decline in the laser-cladding process, which achieves highly consistent results with reference [9]. The analysis

of different processing parameters indicates that laser power of 800 W and a scanning rate of 600 mm/min is suitable for the dynamic preheating process.

(3) Laser DLP improves the convection and proliferation of the molten mass, which effectively helps to control the formation of the hard phase and contributes to the uniform microstructure in the cladding zone. Compared with the un-preheated substrate and static global preheating, laser dynamic local preheating has a more obvious effect on improving cracking resistance capacity.

(4) DLP reduces the super-cooling and temperature gradient, which induces coarse columnar grains and phase with lower hardness and brittleness. This causes the DLP sample to have lower micro-hardness than UNP, but the hardness is still higher than that of the substrate, which guarantees the integral hardness level.

6 ACKNOWLEDGMENTS

7 REFERENCES

[1] Kim, Y.D., Kim, W.S. (2008). A numerical analysis of heat and fluid flow with a deformable curved free surface in a laser melting process. *International Journal of Heat and Fluid Flow*, vol. 29, no. 5, p. 1481-1493, **DOI:10.1016/j.ijheatfluidflow.2008.06.009**.

[2] Zhang, Y.M., Drake, R.P., Glimm, J. (2007). Numerical evaluation of the impact of laser preheat on interface structure and instability. *Physics of Plasmas*, vol. 14, no. 6, p. 62703, **DOI:10.1063/1.2739453**.

[3] Jendrzejewski, R., Śliwiński, G. (2007). Investigation of temperature and stress fields in laser cladded coatings. *Applied Surface Science*, vol. 254, no. 4, p. 921-925, **DOI:10.1016/j.apsusc.2007.08.014**.

[4] Danlos, Y., Costil, S., Liao, H., Coddet, C. (2008). Combining effects of ablation laser and laser preheating on metallic substrates before thermal spraying. *Surface and Coatings Technology*, vol. 202, no. 18, p. 4531-4537, **DOI:10.1016/j.surfcoat.2008.04.038**.

[5] Zhang, H., Shi, Y., Kutsuna, M., Xu, G.J. (2010). Laser cladding of Colmonoy 6 powder on AISI316L austenitic stainless steel.

Nuclear Engineering and Design, vol. 240, no. 10, p. 2691-2696, **DOI:10.1016/j.nucengdes.2010.05.040**.

[6] Aghasibeig, M., Fredriksson, H. (2012). Laser cladding of a featureless iron-based alloy. Surface and Coatings Technology, vol. 209, p. 32-37, **DOI:10.1016/j.surfcoat.2012.08.013**.

[7] Alimardani, M., Toyserkani, E., Huissoon, J.P., Paul, C.P. (2009). On the delamination and crack formation in a thin wall fabricated using laser solid freeform fabrication process: An experimental–numerical investigation. *Optics and Lasers in Engineering*, vol. 47, no. 11, p. 1160-1168, **DOI:10.1016/j. optlaseng.2009.06.010**.

[8] Zhou, S.F., Dai, X.Q. (2010). Microstructure evolution of Fe-based WC composite coating prepared by laser induction hybrid rapid cladding. *Applied Surface Science*, vol. 256, no. 24, p. 7395-7399, **DOI:10.1016/j.apsusc.2010.05.079**.

[9] Fallah, V., Alimardani, M., Stephen, F.C., Khajepour, A. (2010). Impact of localized surface preheating on the microstructure and crack formation in laser direct deposition of Stellite 1 on AISI 4340 steel. *Applied Surface Science*, vol. 257, no. 5, p. 1716-1723, **DOI:10.1016/j.apsusc.2010.09.003**.

[10] Grum, J., Šturm, R. (1997). Laser surface melt-hardening of gray and nodular irons. *Applied Surface Science*, vol. 109-110, p. 128-132, **DOI:10.1016/S0169-4332(96)00648-4**.

[11] Grum, J., Šturm, R. (1996). Microstructure analysis of nodular iron 400-12 after laser surface melt hardening. *Materials Characterization*, vol. 37, no. 2-3, p. 81-88, **DOI:10.1016/ S1044-5803(96)00063-0**.

[12] Gallo, S.C. Alam, N., O'Donnell, R. (2013). In-situ precipitation of TiC upon PTA hardfacing with grey cast iron and titanium for enhanced wear resistance. *Surface and Coatings Technology,* vol. 214, p. 63-68, **DOI:10.1016/j.surfcoat.2012.11.003**.

[13] Petru, J., Zlamal, T., Cep, R., Monkova, K., Monka, P. (2013). Influence of cutting parameters on heat-affected zone after laser cutting. *Tehnički vjesnik – Technical Gazette*, vol. 20, no. 2, p. 225-230.

[14] Šugár, P., Mikoláš, J., Šugárová, J. (2013). Experimental study of Nd:YAG laser machining of Cr-Ni austenitic stainless steel. *Tehnički vjesnik – Technical Gazette*, vol. 20, no. 4, p. 577-580.

[15] Yi, P., Liu, Y.C, Shi, Y.J., Jang, H., Lun, G.D. (2011). Effects analysis of ambient conditions on process of laser surface melting. *Optics and Laser Technology*, vol. 43, no. 8, p. 1411-1419, **DOI:10.1016/j.optlastec.2011.04.010**.

[16] Shi, Y.J., Yi, P., Liu, Y.C. (2011). Numerical investigation of temperature field of different mechanisms in laser forming. *Proceedings of the Institution of Mechanical Engineers, Part C: Journal of Mechanical Engineering Science*, vol. 226, no. 8, p. 2118-2125, **DOI:10.1177/0954406211430884**.

[17] Yi, P., Xu, P.Y., Yin, K.P., Li, C.K., Liu, Y.C. (2013). Laser Thermo-Repairing Process Modeling and Thermal Response Analysis on Gray Cast Iron Surface. *Chinese Journal of Lasers*, vol. 40, no. 3, p. 0303007 (In Chinese), **DOI:10.3788/ CJL201340.0303007**.

Analysis of Energy Efficiency of a Test Rig for Air Springs

Ivan Okorn* – Marko Nagode

University of Ljubljana, Faculty of Mechanical Engineering, Slovenia

During dynamic testing of vehicle air springs, work is required for loading the springs. This work is partially returned by the spring to the driving system during the release phase. Testing is energy-efficient when at least a portion of the returned work can be utilised. This was taken into account in the design of the new inovative test rig for the simultaneous testing of four air springs. There is a phase shift between the phases of loading individual air springs; thus, the work returned to the drive system by a spring during its release is also used for loading another spring. The test rig was constructed and operates in the laboratory of an air spring manufacturer. We developed a computer program to analyse the energy situation in the test rig. The program calculates the work required for loading the springs, power and friction for different sizes of springs and test conditions. In this paper, computational algorithms are deduced and the results of the calculation for the treated spring are presented. The energy situation in the test rig during start-up and operation is discussed, taking into account the energy loss due to the hysteresis of springs and friction losses. The friction losses are evaluated for different implementations of critical elements. The influence of a flywheel on conditions during the start-up and operation of the test rig is analysed.
Keywords: air spring, test rig, energy efficiency, spring hysteresis, friction losses

Highlights
- *The simultaneous testing of four air springs is presented.*
- *The energy situation in the test rig was analysed with developed computer program.*
- *The power required for operation and start-up is calculated.*
- *Energy efficiency is proven by the mesured electric current flowing through the electrical motor.*
- *The effect of the flywheel on the uniformity of the drive is discussed.*

0 INTRODUCTION

Dedicated test rigs are used for the dynamic testing of air springs. These test rigs allow a change of geometry of fixing the springs, which reflects the real spring fixing in a vehicle. Our test rig was constructed for a well-known manufacturer of air springs. It is primarily used for type-approval testing in order to confirm the customer and legislative requirements. The users of springs, who install the springs to their vehicles, define the amplitude and frequency of load, and the minimum number of cycles until the critical damage may appear in a spring. The test rig is also used for research. The paper [1] presents a method for estimating the fatigue life of the air-spring. Experimental data were obtained from several accelerated experiments using constant load amplitude. In [2], the influence of the cord angle on the air-spring fatigue life is presented. Constant amplitude tests were used to make life predictions based on the standardised load spectrum in [3].

Test rigs used for testing air springs can be divided into two major groups: hydraulic and mechanical test rigs. Usually, only one spring is tested at a time on hydraulic test rigs. The work returned by the spring during unloading remains unused. During the test, it is possible to modify the amplitude and frequency of load, which is not possible in mechanical test rigs.

Mechanical test rigs are used mainly for type-approval tests. The amplitude and frequency of the sinusoidal load are set at the start of the test, and they remain the same throughout the test. On the existing mechanical test rigs, two air springs are tested at the same time, being alternatively loaded and released. The new test rig allows the simultaneous testing of four springs. All four springs are loaded under the same conditions (same amplitude and frequency); only the loading is done with a phase shift. During the test, a large part of the work returned by the spring during its release is used for loading the adjacent spring. The energy efficiency of the test rig will be analysed in the following section. The hysteresis of a spring and friction losses in the mechanical elements will also be taken into account.

We developed a computer program that calculates the load of the test rig components and friction losses during the test of any spring. The program calculates the power for start-up and testing. Calculation results for a spring that was tested on the new test rig will be presented. We used a flywheel to ensure the uniformity of the drive. The mass moment of the inertia of the flywheel was determined on the basis of surpluses and deficits of work with respect to the medium work for a load cycle.

1 MOUNTING AND LOADING THE AIR SPRING

When designing the test rig, we took into account the dimensions of the spring and the method of mounting the spring to the vehicle. Methods are presented in [4] and [5]. An example of mounting is shown in Fig. 1.

A lever is fixed on the vehicle's axle and connected to the chassis of the vehicle via a pivot. An air spring is mounted between the lever and the chassis. The spring can be mounted in front of the axle as shown in Fig. 1, directly below the axle or behind the axle of the vehicle.
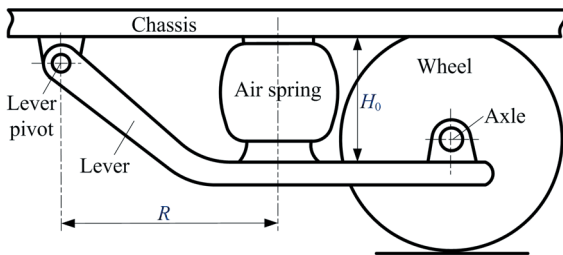
Fig. 1. *Mounting the air springs on a vehicle*

Fig. 2 schematically shows the mounting of springs on the test rig. One side of the spring is fixed on an inclined plate on the lever, and the other side on an inclined plate on the test rig framework. The two inclined plates are parallel in the horizontal position of the lever. Eccentric with a rotation point 3 pushes the lever in point 4 via the slider. The lever oscillates around point 5, loading one spring and releasing the other one via inclined plates.

Two pairs of springs are loaded on the test rig, each pair with its own lever and its corresponding eccentric. In this paper, we will use the terms 'upper' and 'lower' spring, 'left' and 'right' eccentric. The springs are alternately loaded and released during rotation of the eccentrics. While the upper spring is released on the right lever, the lower spring is loaded on the left lever. The spring that is released returns the work to the system, while the spring that is compressed uses the work from the system. The two eccentrics can be rotated to each other by any angle. The shift on an active test rigs is 90°.

With the test rig, it is possible to continuously adjust the distance between the lever rotation point and the centre of the spring R, the eccentricity of the slider r, the inclination of the spring, the distance between the inclined plates and the frequency of loading the springs. When setting the distance R, the rotation point of the lever 5 is moved, both with respect to the test rig framework and lever. Friction joints with pre-stressed screws are used for mounting the lever to the pivot axle and for mounting the pivot housing to the framework. When the pivot position is changed, the lever is fixed with respect to the test rig framework.

The test rig drive is shown schematically in Fig. 3. A three-phase asynchronous electric motor with a power of $P_1 = 11$ kW and a rotational speed of $n_1 = 1450$ rpm drives the shaft 1, on which the flywheel is mounted. The power is transmitted from the shaft 1 to 3 by two belt drives. Eccentrics that
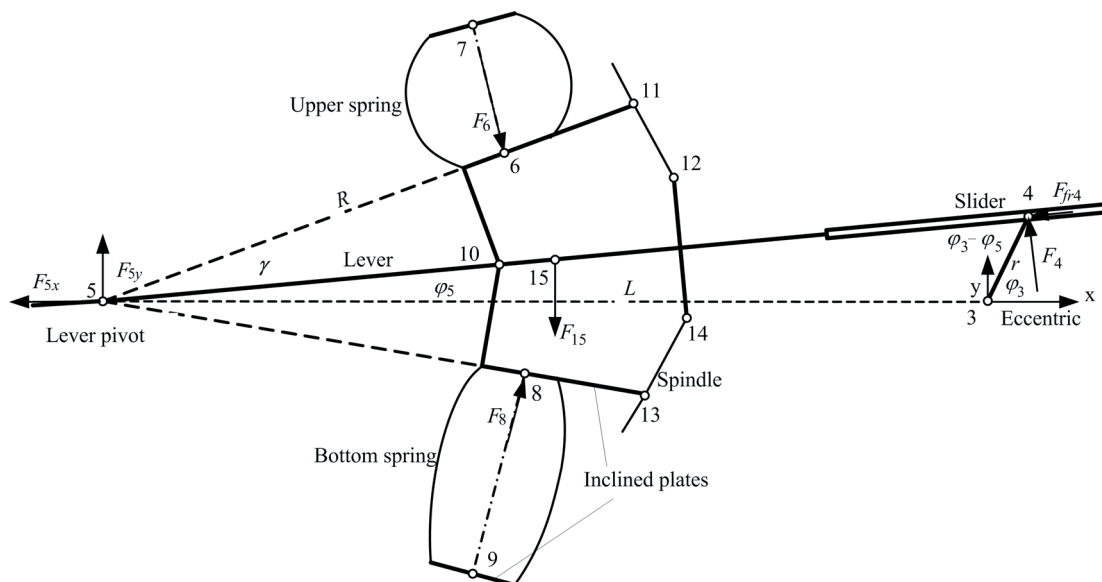
Fig. 2. *Loading the air spring on the test*

push levers are mounted at both ends of the shaft 3. The frequency regulation of the electric motor allows setting the frequency of loading the springs between 0.5 and 3.5 Hz.

The test rig consists of three functional components: mechanical part with a drive, pneumatic part and controller. This article discusses only the mechanical part in detail. The display controller displays air pressure in all four springs, the electric motor current, the rotational speed of shaft 3 (i.e. the testing frequency) and the number of load cycles.

The first indication of a damaged spring is a pressure drop in the spring. The average pressure must be the same in all four springs. The average pressure and the pressure drop when the test rig automatically stops are set on the controller. By monitoring the pressure on the controller screen, the changing working force of the air spring can be monitored indirectly.
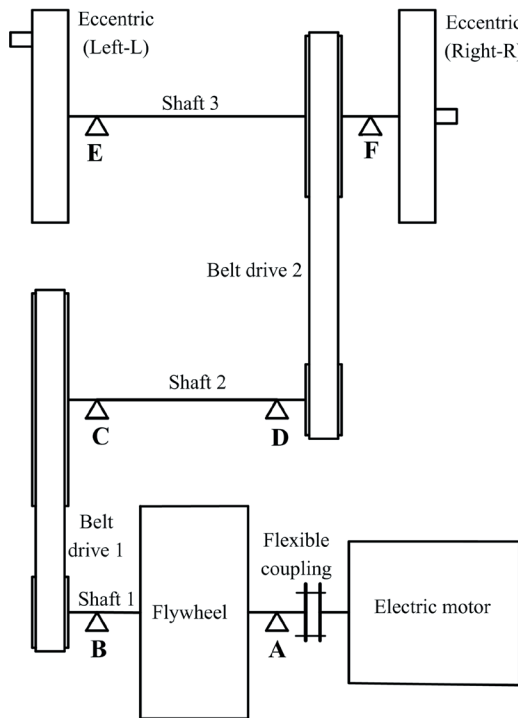
Fig. 3. *Outline of the test rig drive*

The test rig has built-in high-current protection. It stops automatically if the operating current exceeds the velue 60% of rated current.

2 LOAD ON THE ECCENTRIC

Forces in a particular eccentric depend on the work force of the spring, and the weight and inertia of the lever. We shall deal with the load on the right eccentric. The load on the left eccentric is the same; it just occurs with a phase shift. Variables related to the left eccentric are labelled as 'L', while variables for the right eccentric are labelled as 'R'. The height of the springs in the horizontal position of the lever is known as installation height and denoted by 'H_0'.

2.1 Work Force of a Spring

The program calculates the work forces in springs F_6 and F_8 on the basis of the current height of springs and the known characteristics of springs. Geometrical parameters of the lever and characteristic points on it are presented in Fig. 2. The positions of the points are described by vectors with their origin in the rotation point of the eccentric. The vectors that define anchorages of springs depend on the mounting parameters R, L and γ, the mounting height of springs H_0 and the angle of rotation of the lever φ_5.

$$\vec{r}_6 = \begin{pmatrix} R\cos(\varphi_5 + \gamma) - L \\ R\sin(\varphi_5 + \gamma) \end{pmatrix}, \qquad (1)$$

$$\vec{r}_7 = \begin{pmatrix} R\cos\gamma - H_0\sin\gamma - L \\ R\sin\gamma + H_0\cos\gamma \end{pmatrix}. \qquad (2)$$

The lever's angle of rotation changes during the test; it is calculated using the following equation:

$$\varphi_5 = \arctan\frac{r\sin\varphi_3}{L + r\cos\varphi_3}. \qquad (3)$$

The heights of springs at a defined angle of rotation equal the absolute difference of vectors. For the difference of vectors:

$$\vec{r}_7 - \vec{r}_6 = \begin{pmatrix} R(\cos\gamma - \cos(\gamma + \varphi_5)) - H_0\sin\gamma \\ R(\sin\gamma - \sin(\gamma + \varphi_5)) + H_0\cos\gamma \end{pmatrix}, \qquad (4)$$

the absolute value is

$$H = |\vec{r}_7 - \vec{r}_6| =$$
$$= \sqrt{2R^2(1 - \cos\varphi_5) + H_0(H_0 - 2R\sin\varphi_5)}. \qquad (5)$$

An air spring characteristic depends on the type and dimension of the spring, and air pressure in the spring [6]. The influance of the rubber bumpers built into the air-springs is analysed in [7]. Dynamic load-sharing analysis of longitudinal-connected air suspensions is presented in [8]. The pressure in the spring changes during contraction and expansion of

the spring, causing changes in the work force of the spring.

The measured characteristic of the treated air spring is shown in Fig. 4. The installation height of the spring in the horizontal position of the lever is $H_0 = 254$ mm. We used the fourth order polynomials to define the load and release curves. Approximately 30 kW (maximal) is required in hydraulic test rig for loading one spring with a frequency of 3.5 Hz. Losses in the hydraulic system are not included in this value. The load work was determined on the basis of the measured characteristics of the spring (Fig. 4).

Fig. 4. *Measured characteristics of the treated spring*

2.2 Acceleration of the Lever and Force of Inertia

Acceleration of the lever is calculated by deriving Eq. (3) for rotation of the lever twice.

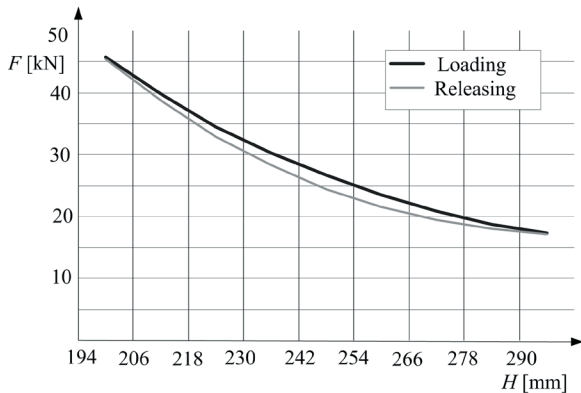$$\ddot{\varphi}_5 = \frac{rL\sin\varphi_3\left(r^2 - L^2\right)}{\left(L + r\cos\varphi_3\right)^4}\cdot\dot{\varphi}_3^2 + \frac{r\left(r + L\cos\varphi_3\right)}{\left(L + r\cos\varphi_3\right)^2}\cdot\ddot{\varphi}_3. \quad (6)$$

Torque becouse of inertia with respect to the rotation point of the lever:

$$M_{ti} = J_5 \cdot \ddot{\varphi}_5 = \left(J_{15} + m_{15}\cdot l_{5,15}^2\right)\cdot\ddot{\varphi}_5. \quad (7)$$

The moment of inertia of the lever with respect to its rotation point J_5 depends on the moment of inertia J_{15} around the centre of mass, mass of the lever m_{15} and the distance between the rotation point and the centre of mass $l_{5,15}$. The mass of the lever together with two tilting plates is $m_{15} = 420$ kg and the centre of mass moment of inertia is $J_{15} = 225$ kgm2. The flywheel is installed into the drive system, so the variation of the angular velocity of the eccentric is negligible. The results of the calculations indicate a negligible influence of the second term in Eq. (6).

2.3 Normal Force on the Slider

The slider of the eccentric presses on the guide with a force F_4, which is perpendicular to the lever. The losses due to friction and thus heating of the slider depend on the size of the force. We have derived the term for a normal force on the eccentric from the moment equilibrium equation for the rotation point of a lever. We assumed that the forces of the springs act perpendicular to the inclined plates of the lever.

$$\sum M_{i5} = 0,$$

$$F_8 \cdot R - F_6 \cdot R - F_{15} \cdot l_{5,15} \cdot \cos\varphi_5 +$$
$$+ F_4 \cdot \left(L + r\cos(\varphi_3 + \varphi_5)\right) - J_5 \cdot \ddot{\varphi}_5 = 0,$$

$$F_4(\varphi_3) = \frac{-\left(F_8 \cdot R - F_6 \cdot R\right)}{L + r\cos(\varphi_3 + \varphi_5)} +$$

$$+ \frac{F_{15} \cdot l_{5,15} \cdot \cos\varphi_5}{L + r\cos(\varphi_3 + \varphi_5)} + \frac{J_5 \cdot \ddot{\varphi}_5}{L + r\cos(\varphi_3 + \varphi_5)}. \quad (8)$$

The first term takes into account the spring forces, the second term the lever's own weight, and the third one the influence of inertia of the lever. Analyses have shown that the inertia of the lever has a significant impact on the load of the slider. We performed special analyses in which we took into account only the weight and inertia of the lever. Work forces of the spring are negligible in the start-up phase because of minimal air pressure in the springs. Only when the shafts rotate at the testing frequency does the pressure in the springs begin to increase gradually to the nominal pressure.

2.4 Circumferential Force on the Eccentric Crank

The circumferential force on the eccentric crank depends on the normal force F_4 and friction force on the slider F_{fr4}. It is calculated with the following equation:

$$F_{t4R}(\varphi_3) = F_4(\varphi_3)\cdot\cos(\varphi_3 - \varphi_5) +$$

$$+ \left|F_{fr4}(\varphi_3)\cdot\cos\left(\frac{\pi}{2} - (\varphi_3 - \varphi_5)\right)\right|, \quad (9)$$

Fig. 5. shows the forces on the eccentric.

When determining the circumferential force on the left eccentric, the phase shift between the eccentric cranks ϕ should be taken into account.

$$F_{t4L}(\varphi_3) = F_{t4R}(\varphi_3 + \phi). \quad (10)$$
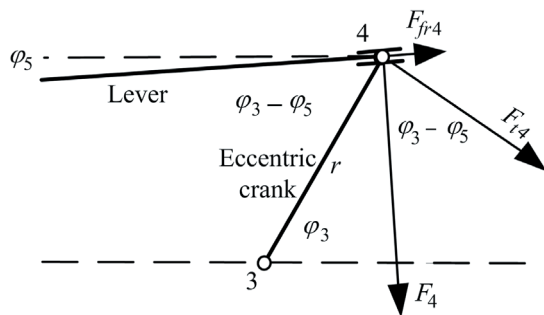
Fig. 5. *Forces on the eccentric crank*

3 ANALYSIS OF FRICTION LOSSES IN THE ECCENTRIC SLIDER

During tests, it has been shown that the main source of friction losses was slider of the eccentric, so we will pay special attention to these losses in this paper.

3.1 Shape of the Slider

In the initial phase of the test rig development, we evaluated two concepts of the transfer of force from the eccentric to the lever. In the first concept, the force is transmitted from the eccentric to the lever via an intermediate connecting rod, and in the second concept it is transmitted directly via the slider. The springs are not loaded under the same conditions in the first concept, so the concept with a slider was selected.

Regarding the type of friction, a rolling or sliding design of the slider is possible. The force is transmitted via rolling elements in the rolling design. The force of friction is small, friction losses are minimal, and heating of elements is negligible. Simplified implementation of the rolling version is presented in Fig. 7a. Pushing the lever is carried out with a roller, which rolls on the rails in the groove of the lever.

The rail and roller wear, so the distance between the rails is continuously adjustable. During the tests, we monitored the wear of the guides and roller. At frequencies up to 2 Hz, the wear of the roller and guide was within acceptable limits. At higher frequencies, we noticed uneven wear along the guide. Maximum wear occurred in the outermost roller positions, while we did not notice wear in the region of the largest rolling pressure. Roller kinematics was recorded with a fast camera. We found that increased wear was caused by the roller slip in extreme positions. Wear of the rail is presented in Fig. 6.

Fig. 6. *Wear of the rail*

Because of uneven wear of the rail and the need for frequent replacement of rails, we switched to the sliding design. We used a square block with replaceable sliding pads (Fig. 7b) instead of a roller. The test rig is currently operating with a sliding version in spite of increased friction force and the increased thermal load of elements. In the next step, we will calculate the friction power on the slider, which is critical for the wear and heat load of sliding pads.
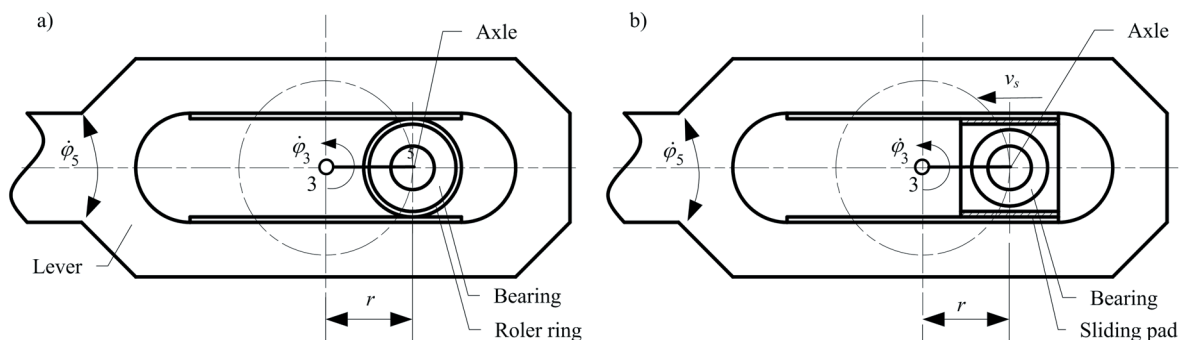
Fig. 7. *Structural designs of slider*

3.2 Friction Power on the Slider

The friction power on the slider depends on the force of friction and sliding velocity. During rotation of the eccentric crank, both the friction force and sliding velocity vary. The maximum sliding velocity is equal to the peripheral velocity of the eccentric. At the frequency of 3.5 Hz and given test rig setup ($R = 0.9$ m, $r = 0.095$ m), the maximum sliding velocity is $v_{s4max} = 2.1$ m/s.

$$P_{fr4}(\varphi_3) = F_{fr4} \cdot v_{s4} = F_4(\varphi_3) \cdot \mu \cdot v_{s4}, \quad (11)$$

$$P_{fr4}(\varphi_3) = M_{fr4} \cdot \dot{\varphi}_3 =$$
$$= F_4(\varphi_3) \cdot \mu \cdot \cos\left(\frac{\pi}{2} - (\varphi_3 - \varphi_5)\right) \cdot r \cdot \dot{\varphi}_3. \quad (12)$$

Fig. 8 shows the power curve if only the working forces of springs are taken into account, without considering the weight of the lever and inertia force. The power curve peaks appear at the extreme positions of the lever. The medium friction power is 0.75 kW. The actual friction power on the slider is shown in Fig. 9. Due to the inertia force, the normal force on the slider is reduced, and so is the frictional force. The average friction power is thus lower: 0.4 kW. The upper side of the slider is more loaded than the lower side due to the weight of the lever, resulting in two different power peaks. Higher peaks correspond to the friction power on the upper slider pad and lower peaks correspond to the situation on the lower pad. By integrating the power curve, the friction work is obtained, which is equal to the heat on the sliding surfaces.

4 ANALYSIS OF FRICTION LOSSES IN BEARINGS

4.1 Friction Losses in the Lever Pivot

Rolling or sliding bearings can be used for the pivot axle. A version with rolling bearings is more favourable in terms of losses, but is less favourable in terms of maintenance costs. Small angles of rotation (in our case $\varphi_{5max} = \pm3.4°$) cause grooves in bearing rings under rolling elements (Fig. 10); the play of the bearings increases and after about three months of operation it is necessary to replace the bearings. The average power of friction is only 3 W and is negligible in comparison with other losses.

4.2 Friction Losses in Shaft Bearings

We took into account constant radial forces on pulleys when we calculated the losses in bearings on Shafts 1 and 2, and we considered forces on both eccentrics and on the pulley for bearings on Shaft 3.
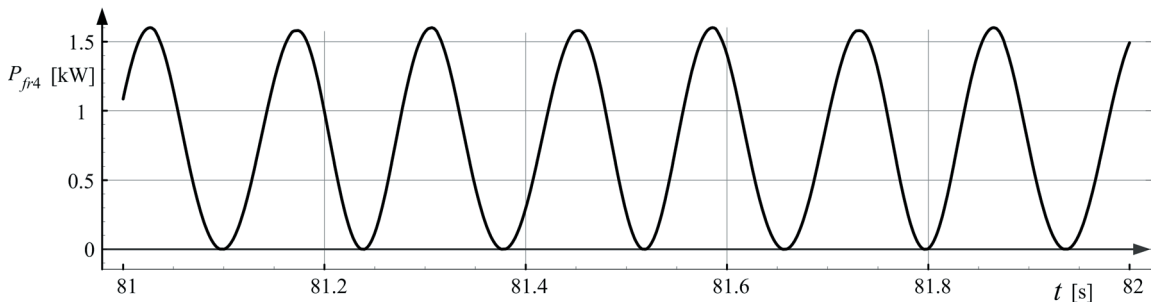
Fig. 8. *Friction power on the slider (only working forces of the spring taken into account, $\mu = 0.05$)*
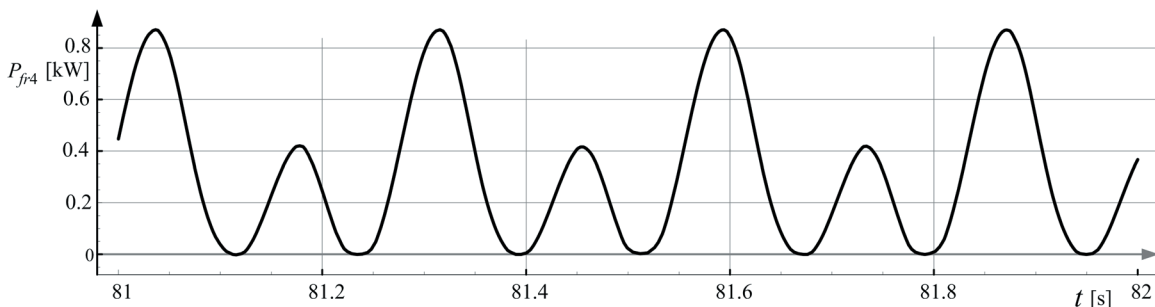
Fig. 9. *Friction power on the slider (inertia and mass of the lever taken into account)*

Fig. 10. *Damaged bearing of lever pivot*

Data on the coefficient of friction were obtained from the manufacturers of bearings. We used the coefficient of friction $\mu_b = 0.0018$ for the selected bearings. The bearings are labelled with capital letters from **A** to **F** on Fig. 3. Radial load was calculated for individual bearings. The results of the calculation are presented in Table 1. Radial forces on bearings **E** and **F** change during rotation. We used medium values of forces.

$$P_{fr,b} = M_{fr,b} \cdot \omega_b = F_b \cdot \frac{d_b}{2} \cdot \mu_b \cdot \omega_b. \qquad (13)$$

It is expected that the total losses of power on all roller bearings and seals are about 0.5 kW.

Table 1. *Energy losses in bearings*

| Bearing	ω_b [s^{-1}]	F_b [N]	d_b [mm]	$P_{fr,b}$ [W]
A	151.8	1990	60	16.3
B	151.8	6400	60	52.5
C	47.3	6450	80	22
D	47.3	10200	80	34.8
E	22	20000	90	35.6
F	22	20000	90	35.6

5 POWER NEEDED FOR OPERATION AND START-UP

Knowing circumferential forces on both eccentrics and friction losses, it is possible to calculate the required power for the drive.

$$P_1 = \left(F_{t4L} + F_{t4R}\right) \cdot r \cdot \dot{\varphi}_3 + P_{fr}. \qquad (14)$$

The medium work for one cycle is obtained by numerical integration of the power curve.

$$W = \int_{t_s}^{t_s + \frac{2\pi}{\omega_1}} P_1(t)dt. \qquad (15)$$

The required power of the electric motor is:

$$W = P_1 \cdot \frac{2\pi}{\omega_1} \Rightarrow P_1 = \frac{W \cdot \omega_1}{2\pi}. \qquad (16)$$

The power curve on the shaft 1 is shown in Fig. 11. The difference between the maximum and minimum power is 13.7 kW. The power needed for the testing (average power) is about 3.8 kW. Fig. 12 shows the power curve during a test of one pair of springs. The work returned by the upper spring during release is partially used for loading the lower spring. The difference between the maximum and minimum power is 18 kW, which is 4.3 kW more than when testing four springs. Medium power is 4.6 kW. When testing one spring, the spring returns the loading work (reduced by hysteresis and friction losses) to the driving system. The difference between the maximum and minimum power is 66 kW. The selected flywheel cannot provide the speed variation within the required limits.

Energy efficiency of the new test rig is proven by the actual current flowing through the electrical motor winding. It depends on the torque load of the electric motor shaft during the test. The rated current at the rated torque is known for the selected electric motor (in our case, the rated power is 11 kW). The actual current reaches about 40% of the rated current during the test of the selected spring. This means that the power of 4.4 kW is needed for testing four springs (1.1 kW per spring). The power on the basis of the measured current is about 0.6 kW higher than the calculated value. This indicates that the friction losses are somewhat higher than predicted.

When starting the test rig, the work forces of springs are negligible. Air pressure in the springs is only gradually increased when the testing frequency is achieved. The RPM of the drive shaft is being steadily increased by the frequency control of the electric motor. The power required for start-up depends on acceleration time t_a, moments of inertia J_1, angular velocity of the shaft ω_1 and losses. Friction losses increase with rotational speed and are the highest at the end of the start-up.

$$P_{1a}(t) = J_1 \cdot \frac{\omega_{1n}}{t_a} \cdot \omega_1(t) + P_{fr}(t). \qquad (17)$$
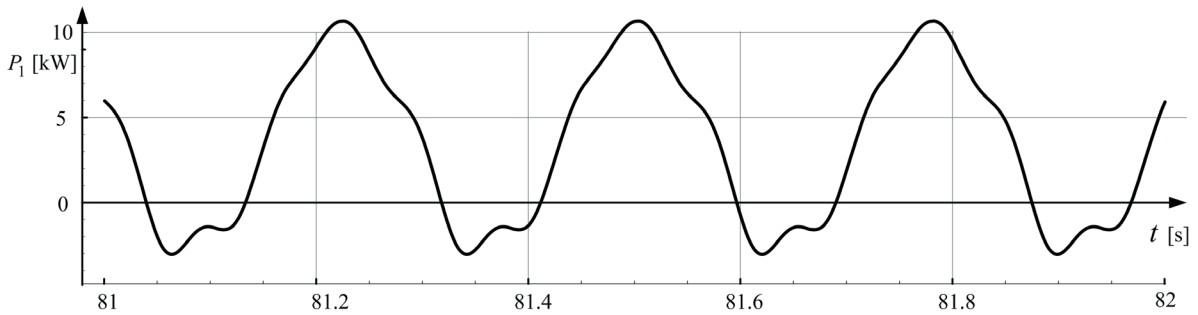
Fig. 11. *Power on Shaft 1 (four springs, R = 900 mm, μ = 0.05)*
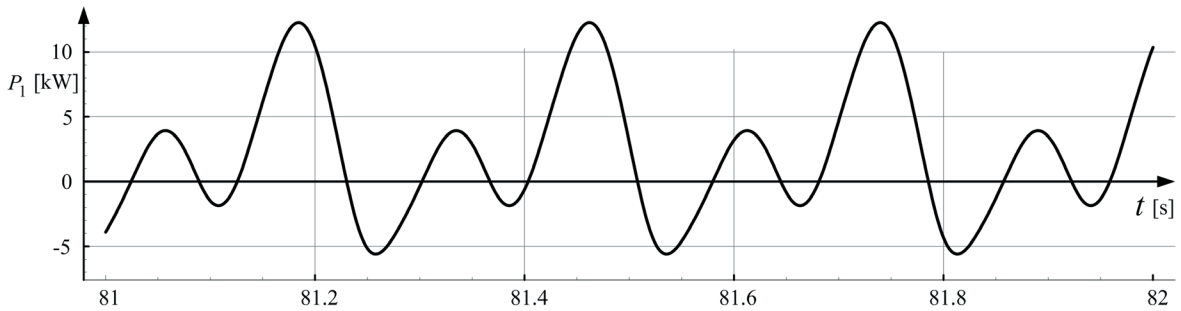
Fig. 12. *Power on Shaft 1 (one pair of springs)*
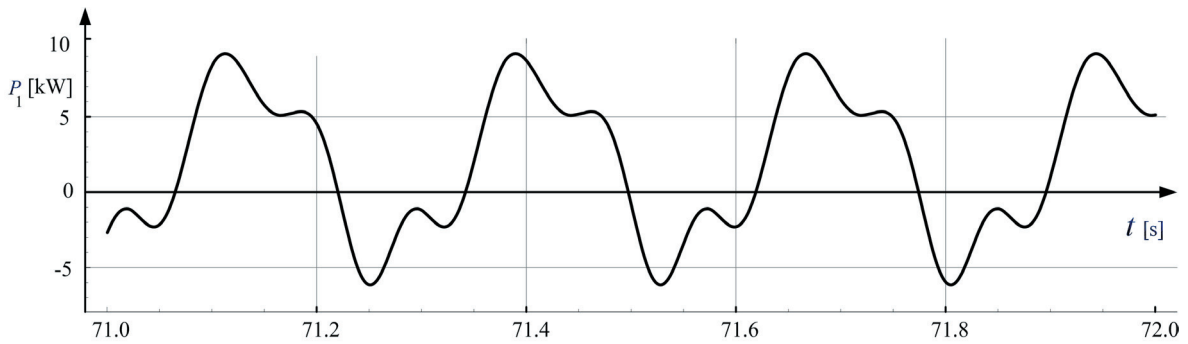
Fig. 13. *Power on Shaft 1 at the end of acceleration (behind the flywheel)*

Start-up power increases linearly as a function of rotational speed. If the start-up time is 60 s and the testing frequency is 3.5 Hz (ω_{1n} = 153 min^{-1}), then 15.5 kW of power is needed at the end of start-up. Fig. 13 presents the power curve on Shaft 1 after start-up. The fluctuation of power occurs due to the acceleration (deceleration) of the lever and the lifting (lowering) the lever. By gradually increasing the pressure in springs, work forces increase. When medium pressure reaches its final value, the need for power varies as shown in Fig. 11.

6 EFFECT OF FLYWHEEL ON THE ENERGY SITUATION

A flywheel was installed on Shaft 1, which rotates at the rotational frequency of the electric motor ω_n.

Calculation of the moment of inertia of the flywheel was based on the equation of motion for Shaft 1 presented in [9]. The moment of the load M_{t1L} affects the shaft behind the flywheel and moment of the drive M_{t1D} affects the shaft before the flywheel.

$$M_{t1D} + M_{t1L} = J_1 \cdot \frac{d}{dt}\left(\frac{d\varphi_1}{dt}\right) =$$

$$= J_1 \cdot \frac{d\varphi_1}{dt} \cdot \frac{d}{d\varphi_1}\left(\frac{d\varphi_1}{dt}\right) = J_1 \cdot \omega_1 \cdot \frac{d\omega_1}{d\varphi_1},$$

$$\left(M_{t1D} + M_{t1L}\right) \cdot d\varphi_1 = J_1 \cdot \omega_1 \cdot d\omega_1. \qquad (18)$$

By integrating both sides of the equation we obtain:

$$\int_{\varphi_{1,1}}^{\varphi_{1,2}} \left(M_{t1D} + M_{t1L} \right) \cdot d\varphi_1 = \int_{\omega_{1,1}}^{\omega_{1,2}} J_1 \cdot \omega_1 \cdot d\omega_1 =$$

$$= \frac{1}{2} \cdot J_1 \cdot \left(\omega_{1,2}^2 - \omega_{1,1}^2 \right). \qquad (19)$$

The left side of the equation represents the work, and the right side represents the change in kinetic energy of the flywheel. We are interested in the largest change within a single cycle.

$$\Delta E_{\max} = \frac{1}{2} \cdot J_1 \cdot \left(\omega_{1\max}^2 - \omega_{1\min}^2 \right) =$$

$$= \frac{1}{2} \cdot J_1 \cdot \left(\omega_{1\max} - \omega_{1\min} \right) \cdot \left(\omega_{1\max} + \omega_{1\min} \right). \qquad (20)$$

With the introduction of the medium angular velocity:

$$\omega_{1n} = \frac{\left(\omega_{1\max} + \omega_{1\min} \right)}{2}, \qquad (21)$$

and coefficient of variation of velocity:

$$C_S = \frac{\left(\omega_{1\max} - \omega_{1\min} \right)}{\omega_{1n}}, \qquad (22)$$

the equation takes the form:

$$\Delta E_{\max} = J_1 \cdot \omega_{1n}^2 \cdot C_S. \qquad (23)$$

The difference between the largest surplus and shortage of power with respect to the medium work for one cycle (one revolution of the eccentric) and thus the maximum change in kinetic energy of the flywheel is obtained from the power diagram (Fig. 11). The degree of non-uniformity in our case is:

$$C_S = \frac{\Delta E_{\max}}{J_1 \cdot \omega_{1n}^2} = \frac{1120}{35 \cdot 153^2} = 0.0054. \qquad (24)$$

Variation of rotational speed is minimal. Results have also been confirmed by measuring the rotational speeds on the test rig. Identical results have been achieved by solving the differential equation of the drive in [10].

7 CONCLUSIONS

Tests of endurance of air springs require significant amounts of time. The test rig discussed in this paper operates seven days a week, 24 hours a day. Testing costs were an important criterion that had to be considered during the design process. The costs consist of the costs of building the test rig, maintenance costs

and energy costs. The test rig allows the use of work returned by the spring during unloading. In this way, we achieved a significant reduction of energy costs and simultaneously increased the number of tests.

The energy conditions change by changing the geometrical settings and load frequency on the test rig. We developed a computer program to calculate the power and work. The geometrical settings of the test rig, measured spring characteristics, and test frequency are entered into the program. The program allows us to quickly assess the risk of thermal overload of critical elements and to calculate the actual energy losses. The power required for testing is calculated by taking into account the working forces of a spring, inertia forces, spring hysteresis and friction losses. The analyses prove that the output energy in a single air spring can with only very limited loses be transferred into the input energy of other three air springs.

Energy efficiency of the new test rig is proven by the mesured current flowing through the electrical motor winding. The actual current reaches 40% of the rated current during the test of the selected spring. This means that the power of about 4.4 kW is needed for testing four springs (1.1 kW per spring). A hydraulic test rig and mechanical test rig for simultaneous testing of two springs also operate in the laboratory of the manufacturer, for which we developed the new test rig. Approximately 30 kW (maximal) is required in hydraulic test rig for loading one spring with a frequency of 3.5 Hz. 5.5 kW (2.75 kW per spring) is needed for testing two springs on the existing mechanical test rig.

Variations of the actual current and testing frequency are negligible (less than 1%). This proves the effect of the flywheel on the uniformity of the drive.

On the basis of the friction power, suitability of the solution is determined with respect to the heat load. Springs that are larger than the one described, cannot be tested with a frequency above 2 Hz due to excessive heat load of the slider. The largest springs from the set of springs can be tested at a frequency of 3.5 Hz only if a rolling version of the slider is used.

8 REFERENCES

[1] Oman, S., Nagode, M., Fajdiga, M. (2010). Estimation of air-spring life based on accelerated experiments. *Materials & Design*, vol. 31, no. 8, p. 3859-3868, **DOI:10.1016/j.matdes.2010.03.044**.

[2] Oman, S., Nagode, M. (2013). On the influence of the cord angle on air-spring fatigue life. *Engineering Failure Analysis*, vol. 27, p. 61-73, **DOI:10.1016/j.engfailanal.2012.09.002**.

[3] Bešter, T., Fajdiga, M., Nagode, M. (2014). Application of constant amplitude dynamic test for life prediction of air springs at various control parameters. *Strojniški vestnik - Journal of Mechanical Engineering*, vol. 60, no. 4, p. 241-248, **DOI:10.5545/sv-jme.2013.1348**.

[4] Harris, C.M. (1988). *Shock and Vibration Handbook-Air Suspension and Active Vibration-Isolation Systems*. chap. 33, McGraw-Hill, London.

[5] Bank, T.A. (1980). Some ABC's of air spring suspensions for commercial road vehicles, *SAE*, SAE Technical paper 800482, **DOI:10.4271/800482**.

[6] Hirtreiter, A.B. (1973). Principles and applications of pneumatic springs. *SAE*. SAE technical paper 730273, **DOI:10.4271/730273**.

[7] Chen, Y., He, I., King, M., Chen, W., Wang, C., Zhang, W. (2013). Model development and dynamic load-sharing analysis of longitudinal-connected air suspensions. *Strojniški vestnik - Journal of Mechanical Engineering*, vol. 59, no. 1, p. 14-24, **DOI:10.5545/sv-jme.2012.755**.

[8] Mankovits, T., Szabo, T., Kocsis, I., Paczelt, I. (2014). Optimisation of the shape of axi-symmetric rubber bumpers. *Strojniški vestnik - Journal of Mechanical Engineering*, vol. 60, no. 1, p. 61-71, **DOI:10.5545/sv-jme.2013.1315**.

[9] Cleghorn, W.L. (2010). *Mechanics of Machines*, Oxford University Press, Oxford.

[10] Okorn, I., Fajdiga, M., Nagode, M. (2010). Analysis of test rig drive for air springs. *Proceedings of the Institution of Mechanical Engineers Part C: Journal of Mechanical Engineering Science*, vol. 224, no. 1, p. 263-271, **DOI:10.1243/09544062JMES1602**.

Crack Fault Detection for a Gearbox Using Discrete Wavelet Transform and an Adaptive Resonance Theory Neural Network

Zhuang Li* – Zhiyong Ma – Yibing Liu – Wei Teng – Rui Jiang

North China Electric Power University, School of Energy Power and Mechanical Engineering, China

In this paper, a new approach using discrete wavelet transform and an adaptive resonance theory neural network for crack fault detection of a gearbox is proposed. With the use of a multi-resolution analytical property of the discrete wavelet transform, the signals are decomposed into a series of sub-bands. The changes of sub-band energy are thought to be caused by the crack fault. Therefore, the relative wavelet energy is proposed as a feature. An artificial neural network is introduced for the detection of crack faults. Due to differences in operating environments, it is difficult to acquire typical, known samples of such faults. An adaptive resonance theory neural network is proposed in order to recognize the changing trend of crack faults without known samples on the basis of extracting the relative wavelet energy as an input eigenvector. The proposed method is applied to the vibration signals collected from a gearbox to diagnose a gear crack fault. The results show that the relative wavelet energy can effectively extract the signal feature and that the adaptive resonance theory neural network can recognize the changing trend from the normal state to a crack fault before the occurrence of a broken tooth fault.

Keywords: relative wavelet energy, pattern recognition, gearbox, fault detection, adaptive resonance theory, neural network

Highlights
- *Early fault diagnosis of a gearbox.*
- *Proposed relative wavelet energy for feature extraction.*
- *Proposed an adaptive resonance theory neural network for recognizing crack faults.*
- *Recognized the changing trend from the normal state to a crack fault without known samples.*

0 INTRODUCTION

A gearbox is a core component in rotating machinery and has been widely employed in various industrial equipment. The meshing of gear teeth is a dynamic process that generates dynamic excitation forces, i.e. elastic variable forces and collision forces, but also forces due to the sliding and rolling of tooth flanks [1]. The gear of a gearbox in operation bears alternating friction and impact loads, which easily lead to variable defects and faults. Detecting gearbox faults as early as possible is essential in order to avoid fatal breakdowns of machines and loss of production and casualties.

Vibration signal analysis is the main technique for monitoring the condition and detecting faults in a gearbox. By employing appropriate signal processing methods, changes in vibration signals caused by faults can be detected to aid in evaluating the gearbox's health status. The development process from the normal state to a fault in the gearbox is a slow one. With the limitation of the mechanical structure and its working environment, it is difficult to directly measure the changes of state for a gearbox, e.g. gear wear and cracking. Generally, the changes of state are estimated by observing the changes of features extracted from vibration signals. Although a great variety of features provides information about different aspects of the

working condition, it remains difficult to identify the condition only with a visual estimation. To solve this problem, pattern recognition is employed on the basis of feature extraction. With pattern recognition, the working condition of a gearbox can be classified, and faults can be detected automatically. Therefore, gearbox fault detection consists of feature extraction and pattern recognition [2].

New types of signal-processing techniques for feature extraction have emerged with different theoretical bases. Due to different working environments, not all the signal processing techniques work well for a specific system. Because the nonlinear factors (loads, friction, impact, etc.) have influence on gearbox vibration signals, choosing suitable signal processing techniques to acquire features for accurate and reliable fault detection should be considered. The main feature extraction methods include: time-domain methods, frequency-domain method and time-frequency methods. Time-domain and frequency-domain methods are the basic methods of signal processing. Features extracted with time-domain methods include peak amplitude, root-mean-square amplitude, kurtosis, crest factor, etc. [3]. Frequency-domain methods, including power spectrum, cepstrum analysis, and an envelope spectra technique, have been successfully applied to gear fault diagnosis [4]

*Corr. Author's Address: North China Electric Power University, School of Energy Power and Mechanical Engineering, Beijing, China, 102206, lizhuang@ncepu.edu.cn

63

to [5]. As the gearbox vibration signals possess non-stationary and non-linear characteristics, it is difficult to diagnose the fault only by using traditional time-domain or frequency-domain methods. To solve this problem, time-frequency methods have been proposed, e.g. short-time Fourier transform (STFT), Wigner-Ville distribution (WVD) and wavelet transform, and have been widely used [6] to [8]. In the abovementioned methods, the wavelet transform that has the capability to offer good frequency resolution for low-frequency components and good time resolution for high-frequency components provides an efficient method for non-stationary signals [9]. Furthermore, discrete wavelet transform (DWT) based on a Mallat algorithm has received widespread attention in recent years. The DWT can be represented as a filtering process in which the signal is separated into a series of sub-bands and wavelet coefficients that are distributed on different frequency bands to reflect the signal feature at each of sub-band [10]. The DWT has been acknowledged to be a successful tool for fault detection [11].

In recent years, many studies on artificial neural networks have been carried out with the aim of determining intelligent fault diagnosis to investigate the potential applications in pattern recognition. It is common to train a neural network by using samples so that it can recognize the required input-output characteristics and classify the unknown input patterns [12]. This type of neural network is based on supervised learning, including back-propagation (BP) neural networks, fuzzy networks, probability neural network, etc.; they are commonly used in fault diagnosis [13] to [15]. However, only the patterns that occur in the training samples can be classified. If a new pattern is classified by the neural network, an incorrect result will be given. Both new patterns with original training samples as well as renewal training are needed in order to enable the neural network to recognize new patterns. Therefore, a neural network based on supervised learning cannot function without training samples. To overcome this issue, some unsupervised neural networks have been developed, including self-organizing competitive neural networks, self-organizing feature map neural networks, and adaptive resonance theory networks. They are all used for implementing pattern recognition without training samples [16] to [18]. Regarding this matter, an adaptive resonance theory (ART) neural network can not only recognize objects in a way similar to a brain learning autonomously, but also can solve the plasticity-stability dilemma [18]. Its algorithm can accept new input patterns

adaptively without modifying the trained neural network and/or increasing memory capacity with the species of samples. The process of learning, memory and training of an ART neural network proceed synchronously. ART was presented by Carpenter in 1976, and an ART neural network was presented in 1987 [19]. The type of ART neural network presented then was an ART-1 [19]. However, while an ART-1 neural network is appropriate for binary input, it is not appropriate in practical application. For adapting any types of input, an ART-2 neural network was presented [20], and it has been widely used in pattern recognition and fault detection. Lee et al. transferred the estimated parameters by using the ART-2 neural network with uneven vigilance parameters for fault isolation, which showed the effectiveness of the ART-2 neural network-based fault diagnosis method [21]. Lee et al. combined DWT and an ART-2 neural network for fault diagnosis of a dynamic system [22]. Obikawa and Shinozuka developed a monitoring system for classifying the levels of the tool flank wear of coated tools into some categories using an ART-2 neural network [23].

In this study, a new method for crack fault detection is proposed. Considering the non-stationary and non-linear characteristics of the signals, DWT is applied for feature extraction. The current situation of gearbox fault detection is time-consuming, and it is costly (or even impossible) to collect all kinds of known fault samples. Furthermore, an operating gearbox is influenced by its working environment. The samples obtained from a specific gearbox may not be suitable for other gearboxes with different working environments. There is a lack of known samplesfor the training of supervised neural networks. Therefore, an ART-2 neural network is proposed for state recognition and classification. Through the unsupervised classification of the samples via an ART-2 neural network, the changing trend from the normal state to a crack fault before a broken tooth fault occurs can be determined. Meanwhile, to verify the effectiveness of the ART-2 neural network, it is compared with a self-organizing competitive neural network and a self-organizing feature map neural network.

This paper is organized as follows: in Section 1, the relative wavelet energy is proposed as a feature and an ART-2 neural network is presented for pattern recognition. In Section 2, the gearbox experiment is introduced. The relative wavelet energy of the signal samples are extracted and compared with the analysis in time and frequency domain, after which the ART-2 neural network is used for recognizing the changing

trend of the crack fault before a broken tooth fault happens. The conclusion is given in Section 3.

1 THEORETICAL BACKGROUND OF DWT AND ART-2 NEURAL NETWORK

1.1 Fundamental of Wavelet Transform

1.1.1 Discrete Wavelet Transform (DWT)

The basic analysis wavelet $\psi(t)$ is a square integrable function, and it meets the following relationship:

$$C_\psi = \int_R \frac{\left|\hat{\psi}(\omega)\right|^2}{|\omega|} d\omega < \infty, \qquad (1)$$

where $\psi(\omega)$ is the Fourier transform of $\psi(t)$. Through translation and dilation, a member of the function can be derived from the $\psi(t)$. The equation can be described as follows:

$$\psi_{a,b}(t) = |a|^{-\frac{1}{2}} \psi(\frac{t-b}{a}), \qquad (2)$$

where $\psi_{a,b}(t)$ is a member of the wavelet basis, a and b represent the scale parameter and translation parameter, respectively. The continuous wavelet transform of a finite-energy signal $x(t)$ is defined as follows:

$$W_\psi(a,b) = \int_{-\infty}^{+\infty} x(t)\psi_{a,b}^*(t)dt =$$
$$= |a|^{-\frac{1}{2}} \int_{-\infty}^{+\infty} x(t)\psi^*(\frac{t-b}{a})dt, \qquad (3)$$

where * denotes complex conjugation and $W_\psi(a,b)$ is wavelet coefficients. As seen in Eqs. (2) and (3), $\psi_{a,b}(t)$ can be regarded as a window function. a and b are used to adjust the frequency and time location of the wavelet. A small a offers high-frequency resolution and is useful in extracting high-frequency components of signals. a increases in response to the decrease in frequency resolution but the increase in time resolution and low-frequency components is easily extracted.

The DWT is derived from the CWT through the discretization of the parameters a and b. Generally, a is replaced by 2^j and b is replaced by $k2^j$ ($j, k \in Z$). $W_\psi(a,b)$ can be shown as:

$$W_\psi(j,k) = \int x(t)\psi_{j,k}^*(t)dt, \qquad (4)$$

where $\psi_{j,k}(t) = 2^{-\frac{j}{2}}\psi(2^{-j}t - k)$.

The Mallat algorithm is a breakthrough of the DWT, providing a fast algorithm and achieves multi-resolution analysis of signals. Wavelet filters are used for decomposition and re-construction. It is shown in Eqs. (5) to (7).

$$A_0[x(t)] = x(t), \qquad (5)$$

$$A_j[x(t)] = \sum_k H(2t-k)A_{j-1}[x(t)], \qquad (6)$$

$$D_j[x(t)] = \sum_k G(2t-k)A_{j-1}[x(t)], \qquad (7)$$

where $x(t)$ is the original signal, j is the decomposition level ($j = 1, 2, \ldots, J$). H and G are wavelet decomposition filters for low-pass filtering and high-pass filtering, respectively. A_j and D_j are the low frequency wavelet coefficients (Approximations) and the high frequency wavelet coefficients (Details) of signal $x(t)$ at the jth level, respectively. The decomposition procedure of a J-level DWT is shown in Fig.1. It can be seen that D_j and A_j are obtained through high-pass filtering and low-pass filtering with down-sampling at each level. After the signal $x(t)$ is decomposed by the J-level DWT, D_j at each level and A_J at the Jth level are obtained. Therefore, the DWT based on Mallat algorithm can be represented as a filtering process that the signal is decomposed into a series of sub-bands.
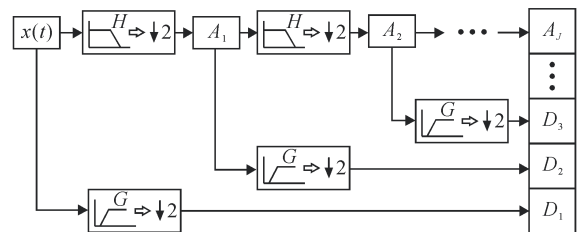
Fig. 1. *Decomposition procedure of J-level DWT*

D_j and D_J can be used to reconstruct the signal branch separately, which represents the signal component in each sub-band through up-sampling and reconstruction filter h and g. The reconstruction process is shown in Fig. 2. $\tilde{D}_j(t)$ and $\tilde{A}_J(t)$ are represented as the signal branch reconstruction of D_j and A_J, respectively. The original signal $x(t)$ can be regarded as the sum of each component. It can be described as:

$$x(t) = \tilde{A}_J(t) + \sum_{j=1}^{J} \tilde{D}_j(t). \qquad (8)$$
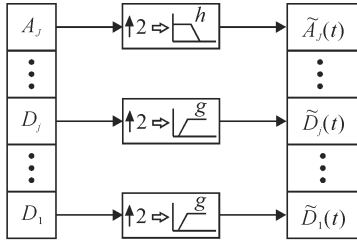
Fig. 2. *Reconstruction for the component of the signal in each sub-band*

1.1.2 Relative Wavelet Energy

The signal components derived through decomposition and reconstruction of DWT are distributed into independent sub-bands, and the component energy in each sub-band contains information available for fault detection. When a gear fault occurs, non-stationary and non-linear vibration energy is generated, which leads to a change of signal energy in some sub-bands. As the DWT has the characteristic of multi-resolution analysis, which makes it suitable for the analysis of non-stationary and non-linear signals, the DWT is used for feature extraction and the relative wavelet energy is proposed and calculated as the feature. The procedure is as follows:

(1) Decomposition by J-level DWT for the N-point signal $x(t)$ to obtained D_j ($j = 1, 2, …, J$) and A_J.

(2) Reconstruction for D_j and A_J to obtain the signal components $\tilde{D}_j(t)$ and $\tilde{A}_J(t)$ in each sub-band. The length of $\tilde{D}_j(t)$ and $\tilde{A}_J(t)$ are the same as that of $x(t)$.

(3) Let $\tilde{A}_J(t) = \tilde{D}_{J+1}(t)$ and the wavelet sub-band energy in each sub-band is calculated as:

$$E_j = \left\| \tilde{D}_j(t) \right\|^2 = \sum_{k=1}^{N} \left| d_j(k) \right|^2, \qquad (9)$$

where N is the number of the data samples of $\tilde{D}_j(t)$, k represents the time-series of data samples, and $d_j(k)$ is the data sample of $\tilde{D}_j(t)$ (i.e. $d_j(k) \in \tilde{D}_j(t)$, $j = 1, 2, …, J+1$).

(4) The relative wavelet energy σ_j in each sub-band is shown as:

$$\sigma_j = E_j / E_{total}, \qquad (10)$$

where $E_{total} = \sum_{j=1}^{J+1} \sum_{k=1}^{N} \left| d_j(k) \right|^2 = \sum_{j=1}^{J+1} E_j$.

According to the above analysis, it can be seen that the DWT has a multi-resolution analytical property and that the relative wavelet energy can reflect the energy distribution of signals in different sub-bands. Thus, the relative wavelet energy is chosen as the

feature of signals and used for future work in pattern recognition.

1.2 Fundamental of ART-2 Neural Network

1.2.1 Structure of ART-2 Neural Network

The structure of an ART-2 neural network is shown in Fig. 3. It consists of two subsystems: the attentional subsystem and the orienting subsystem. The attentional subsystem consists of two layers: the comparison layer (F_1) and the recognition layer (F_2). The orienting subsystem is the reset system, which is represented as the trigonal part R. The F1 layer that contains n groups of neurons is used to accept an n-dimension input pattern $(x_1, x_2, …, x_n)$. The F_2 layer has m neurons, each of which represents a type of pattern or category. The neurons in the two layers form the short-term memory of the neural network. The F_1 layer and F_2 layer are connected by weights that form the long-term memory. With the processing of the F_1 layer and weights, the input pattern is transferred to the F_2 layer, and the output of the F_2 layer $(y_1, y_2, …, y_m)$ is obtained. The maximum value of output is chosen, and the corresponding neuron is activated as the winning neuron. If the degree of match between the feedback of the F_2 layer and the output of the F_1 layer is less than the threshold value, the orienting subsystem will reset the F_2 layer, and the activated neuron will be restrained. Next, the winning neuron is again chosen from the F_2 layer until the degree of match meets the requirements, and the weights connected to the activated neuron are modified at the same time.
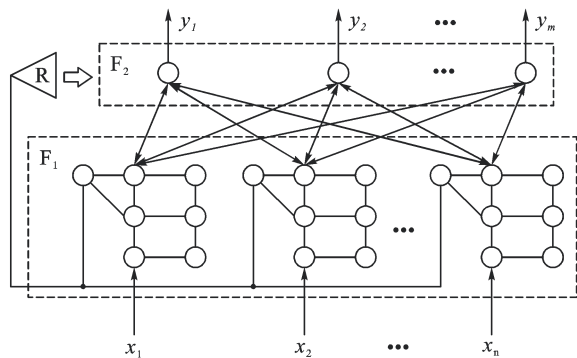

Fig. 3. *Structure of ART-2 neural network*

1.2.2 Algorithm of ART-2 Neural Network

A topological structure is shown in Fig. 4 that describes the connection between the ith group of

neurons in the F_1 layer and the jth neuron in the F_2 layer. It can be seen that the F_1 layer includes three levels. Two types of neurons exist in each level. The neurons represented by hollow circles are used to calculate the module of the input vector and transfer the inhibitive incentive; the neurons represented by filled circles are used to transfer excited incentives.
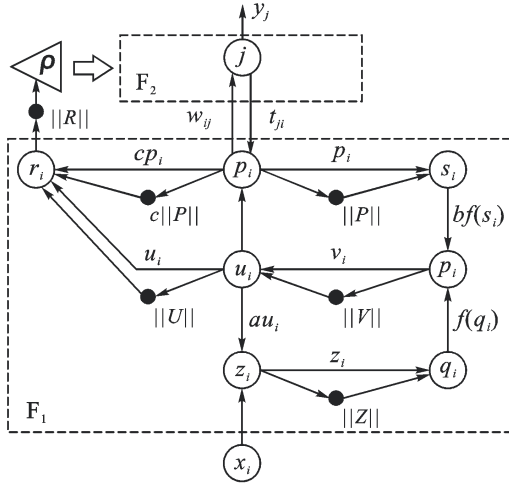
Fig. 4. *Topological of ART-2 neural network*

The algorithm process of an ART-2 neural network is shown as follows:

(1) Calculation in the F_1 layer

The lower level of F_1 layer receives the input x_i, and the upper level receives the feedback of the F_2 layer. These two levels are combined with the middle level separately, and positive feedback loops are formed. The algorithms in each level are shown in Eqs. (11) to (16).

$$z_i = x_i + au_i, \qquad (11)$$

$$q_i = z_i / (e + \|Z\|), \qquad (12)$$

$$v_i = f(q_i) + bf(s_i), \qquad (13)$$

$$u_i = v_i / (e + \|V\|), \qquad (14)$$

$$s_i = p_i / (e + \|P\|), \qquad (15)$$

$$p_i = u_i + \sum_{j=1}^{m} g(y_j) t_{ji}, \qquad (16)$$

where a and b are the coefficients of positive feedback ($a > 1$, $b > 1$), e is far less than 1. t_{ji} refers to the connected weight from the jth neuron in

F_2 layer to the neuron p_i in F_1 layer and $g(y_j)$ is the feedback of the jth neuron in F_2 layer. $f(x)$ is a non-linear transformation function, which is shown in Eq. (17).

$$f(x) = \begin{cases} 2\theta x^2 / (x^2 + \theta^2) & 0 \le x \le \theta \\ x & x \ge \theta \end{cases}, \qquad (17)$$

where θ is the anti-noise coefficient ($\theta = 1/\sqrt{n}$).

(2) Calculation in the F_2 layer

The jth neuron in F_2 level receives the output of neuron p_i which can be described as:

$$T_j = \sum_{i=1}^{n} p_i w_{ij} \qquad j = 1, 2, ..., m, \qquad (18)$$

where w_{ij} is the connected weight from the neuron p_i in F_1 layer to the jth neuron in F_2 layer. The activated neuron is determined by Eq. (19):

$$T_{j^*} = \max\{T_j\} \qquad j = 1, 2, ..., m \qquad (19)$$

where j^* refers to the serial number of activated neuron. The feedback of each neuron in F_2 layer is calculated as:

$$g(y_j) = \begin{cases} d & j = j^* \\ 0 & j \ne j^* \end{cases}, \qquad (20)$$

where d is the learning rate ($0 < d < 1$). According to Eq. (20), Eq. (16) can be described as:

$$p_i = \begin{cases} u_i + dt_{ji} & j = j^* \\ u_i & j \ne j^* \end{cases}. \qquad (21)$$

(3) Calculation of the orienting subsystem

According to Eqs. (11) to (16), it can be seen that the vector $U = (u_1, u_2, ..., u_i, ..., u_n)$ contains the features of input vector X, and the feedback features of F_2 layer are included in the vector $P = (p_1, p_2, ..., p_i, ..., p_n)$. Through comparing the degree of match between the vectors U and P, the orienting subsystem can determine whether the F_2 layer should be reset. The degree of match $\|R\|$ can be calculated as:

$$\|R\| = \left\| \frac{u_i + cp_i}{e + \|U\| + \|cP\|} \right\|, \qquad (22)$$

where c is the weighting coefficient ($c \le 1/d - 1$). The greater $\|R\|$ is, the more similar the vectors U and P are. Define parameter ρ as the threshold

value ($0 < \rho < 1$). When $\|R\| > \rho$, the F_2 layer need not be reset, and the weights are modified directly. Otherwise, the orienting subsystem will reset the F_2 layer. The activated neuron is restrained and chosen again from the F_2 layer. Furthermore, the degree of match is repeatedly calculated until it meets the requirements, i.e. $\|R\| > \rho$.

(4) Modification of the weights

After the winning neuron $j*$ is determined, the weights connected to the activated neuron are modified according to Eqs. (23) and (24).

$$w_{ij^*}(k+1) = w_{ij^*}(k) + d(1-d)[\frac{u_i(k)}{1-d} - w_{ij^*}(k)], \quad (23)$$

$$t_{j^*i}(k+1) = t_{j^*i}(k) + d(1-d)[\frac{u_i(k)}{1-d} - t_{j^*i}(k)]. \quad (24)$$

2 FEATURE EXTRACTION AND PATTERN RECOGNITION OF GEARBOX VIBRATION SIGNAL

2.1 Method for Crack Fault Detection

A schematic representation of the proposed method is shown in Fig. 5. First, the sample series of the gearbox is acquired, and the relative wavelet energy features are extracted by DWT. Next, an ART-2 neural network is used for the recognition and classification of the sample series. Through the unsupervised classification, the samples of the same state are classified into the same category, and those of different states are classified into separate categories. Finally, the recognition result is output, and the changing trend from the normal state to the crack fault can be recognized from the classification of the samples.
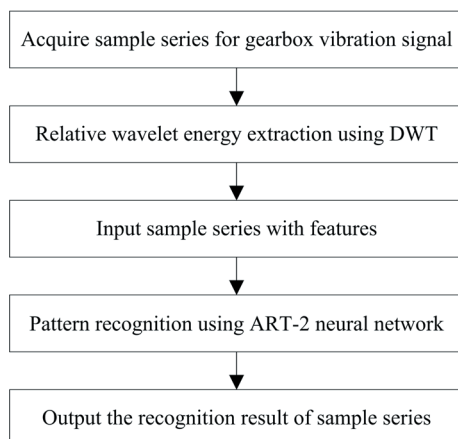
Fig. 5. *Scheme of the proposed method*

2.2 Experiment Specification

Fig. 6 shows a diagram of the experimental system used for analysing the changing trend of the crack fault. The gearbox is single-stage with helical cylindrical gears. Table 1 lists the parameters of the experimental system.
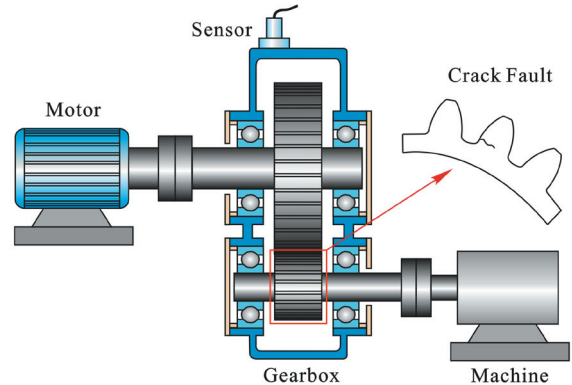
Fig. 6. *Structure of experiment gearbox*

Table 1. *Parameters of the experimental system*

Motor	Rated speed	1120 rpm
Gearbox	Number of teeth of driving gear	75
	Number of teeth of driven gear	17
	Mesh frequency	1400 Hz

The vibration signal of the gearbox was collected with a piezoelectric accelerometer, and the sampling frequency was 8000 Hz. The process of the driven gear from the normal state to a broken tooth fault was recorded with a monitoring system. The entire measuring time was 8 minutes, during which it took approximately 90 seconds for the motor to reach its rated speed. The rated speed was maintained for 290 seconds with constant load, after which a broken tooth fault occurred on the driven gear. The collected vibration signal contained the information of the change of state for the driven gear changes: normal state, crack formation, crack expansion and broken tooth fault.

2.3 Analysis of Time and Frequency Domain

The time vibration signal is shown in Fig. 7a. In the first 90 seconds, the vibration amplitude increases with the rotational speed. The amplitude changes to steady in the following 290 seconds in which rotational speed of the motor reaches the rated speed, and the system enters a normal working state. At 380 s, the amplitude increases noticeably, and a broken tooth fault occurs.
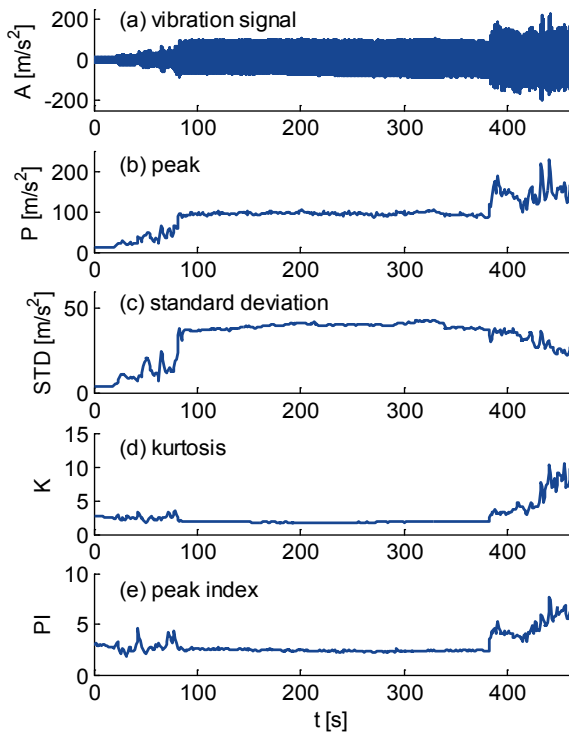
Fig. 7. *Gearbox vibration signal and the time-domain features*

During the normal working state (90 to 380 s), the vibration amplitude remains steady, and no abnormal condition that suggests a symptom of a broken tooth fault can be observed. The vibration signal is analysed using time-domain analysis. Four types of time-domain features are employed: peak, standard deviation, kurtosis, and peak index. The changing process of the features is shown in Fig. 7b to d. The features change noticeably only in the stage of increasing speed (0 to 90 s) and that of a broken tooth fault (380 to 480 s). However, the features do not change significantly during the normal working state (90 to 380 s). Neither the symptom of a broken tooth fault nor the information of crack formation and expansion can be acquired. Early fault detection via time-domain analysis only is difficult to obtain.

Four signal sections are extracted from the vibration signal at 90, 200, 310 and 390 s; the length of each signal section is 0.25 s. They are represented as the four states of the operating gearbox including initial, middle, later and faulted. These signal sections are analysed using a logarithmic power spectrum, and the logarithmic power spectrum density (PSD) are shown in Fig. 8. The faulted state can be clearly identified, but the rest overlap each other. The initial period, the middle period and later period cannot be distinguished clearly. The integral for the logarithmic

power spectrum density of the four signal sections is calculated, and the results are shown in Fig. 9. The value of the integral for the faulted logarithmic power spectrum density is higher than the others; there is no obvious changing trend from initial to later period. Therefore, the crack changing process before the broken tooth fault occurs cannot be identified by using frequency-domain analysis.
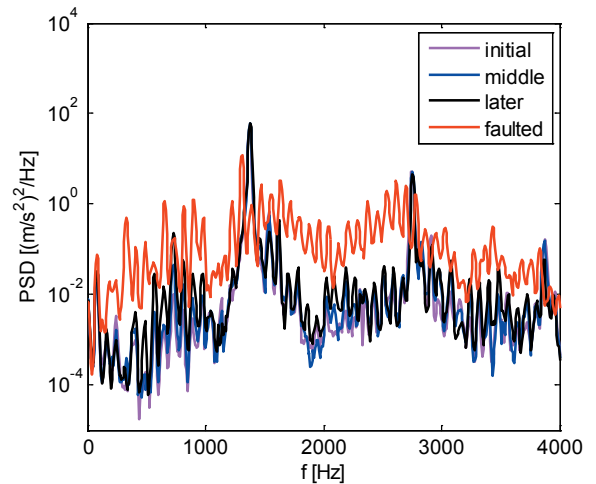
Fig. 8. *Logarithmic power spectrum density of the four signal section*
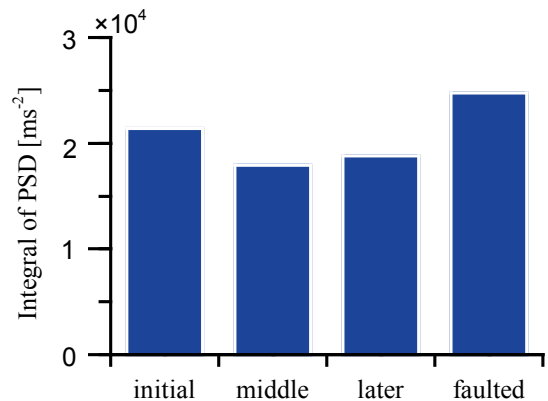
Fig. 9. *Integral of logarithmic power spectrum density of the four signal section*

2.4 Analysis Based on the Relative Wavelet Energy

According to the above analysis, the broken tooth fault can be diagnosed by using traditional methods of time and frequency domain analysis, but neither obvious symptoms nor changing trend of the fault can be obtained before the broken tooth fault occurs. When the crack occurred on the gear and expanded gradually, non-linear vibration energy was generated that led to a change of signal energy in the sub-bands.

Therefore, the vibration signal from 90 to 380 s (i.e. the normal working state before the broken tooth fault happens) is analysed here and divided into 130 sections. In each section, 1 second of data with 8000 points is extracted and analysed via the 4-level DWT. The relative wavelet energy of the five sub-bands is calculated according to Eqs. (9) and (10), as shown in Fig. 10. A slight decrease and increase of the relative wavelet energy are found in d1 and d2, respectively. However, in the sub-bands of d3, d4 and a5, the relative wavelet energy shows an obviously increasing trend. Thus, the relative wavelet energy in different sub-bands can be used as the features for reflecting the changing trend of operating state of the gear.

It can be seen from the above analysis that the relative wavelet energy based on DWT can essentially reflect the changing trend of the crack. However, the development process of the gear crack fault cannot be recognized, which makes early fault diagnosis difficult. Therefore, it is essential to introduce a method of pattern recognition for crack fault detection.
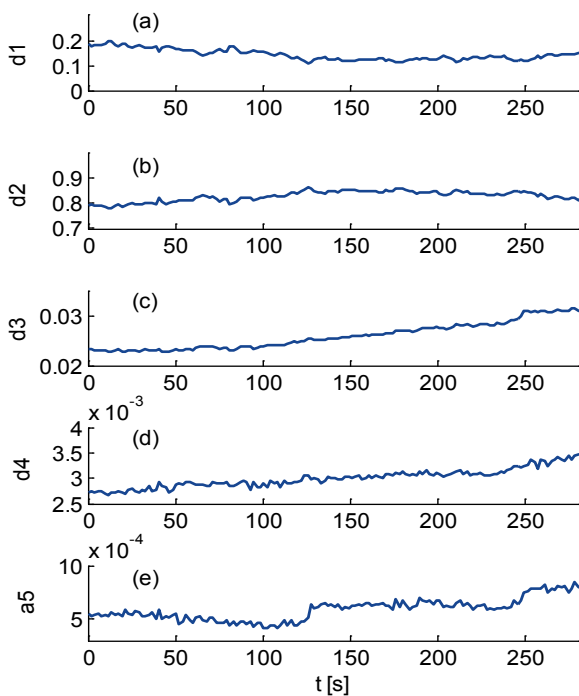
Fig. 10. *Relative wavelet energy of the vibration signal*

2.5 Pattern Recognition for Crack Fault Detection Based on an ART-2 Neural Network

On the basis of extracting the relative wavelet energy as an input eigenvector, an ART-2 neural network is proposed in order to recognize the changing trend

of crack faults for early fault diagnosis. The process is mainly divided into four parts: normal state, mild wear, micro-crack and crack expansion. The analysed signal and the extracted features mentioned in Section 2.4 are used here for the pattern recognition of an ART-2 neural network. A sample matrix is acquired with 130 samples and 5 features.

The neural network is designed as follows: The number of neurons in the F_1 layer is 5 ($n = 5$), which are used to receive the features of each sample. The number of neurons in the F_2 layer is 130 ($m = 130$) which are the same as the number of samples. The connected weights are initialized according to Eq. (25).

$$w_{ij} = \frac{1}{(1-d)\sqrt{n}}, \quad t_{ji} = 0, \qquad (25)$$

where $i = 1, 2, ..., n$ and $j = 1, 2, ..., m$. To obtain better classification results, many experiments have been performed to set the parameters mentioned in Section 1.2, which are shown as follows: $a = 10$, $b = 10$, $c = 0.1$, $d = 0.9$, $e = 10^{-8}$. θ is 0.4472, according to Section 1.2.

Next, the sample matrix is classified with the ART-2 neural network. The threshold value ρ affects the number of categories. The bigger the threshold value is, the more precise the classification result is; the number of categories increases with the threshold value. Fig. 11 shows the relationship between the number of categories and the threshold value.
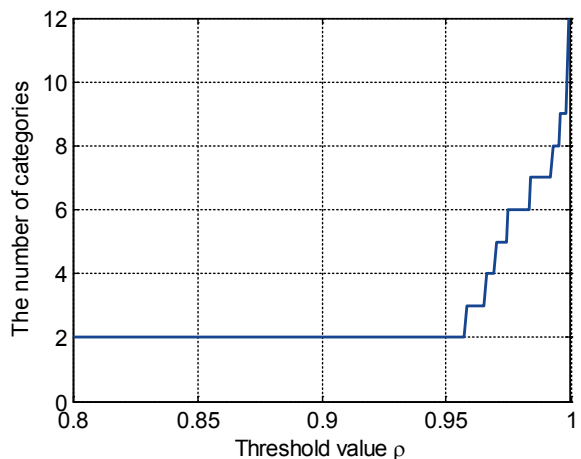
Fig. 11. *Changes in the number of categories with the threshold value*

The classification results with the different number of categories are shown in Fig. 12. In Fig. 12a, 130 samples are almost classified into the 1st category; only a few of samples belongs to the 2nd category,

which is because the threshold value is low, and the degree of match is not high. In this case, the changing trend of crack faults cannot be identified. When the threshold value is increased, three and four categories can be obtained, shown in Figs. 12b and c. The stage change can be reflected briefly from the classification categories, but identifying the changing trend of crack faults remains difficult. A high threshold value causes the number of categories to be excessive, as is seen in Fig. 12d. The stage change is so confusing that the changing trend cannot be analysed. Therefore, neither too high nor too low a threshold value is suitable for the pattern recognition of the crack fault.
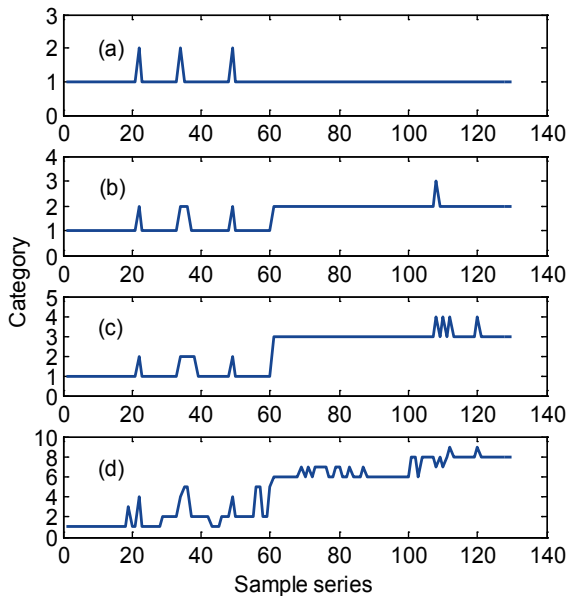
Fig. 12. *The classification results with the different number of categories; a) $\rho = 0.9$, b) $\rho = 0.96$, c) $\rho = 0.967$, and d) $\rho = 0.996$*

Through many experiments, the best pattern recognition can be acquired when the threshold value ρ is set 0.97 to 0.974, following which five categories are classified, according to Fig. 10. The classification result with five categories is shown in Fig. 13a. According to the distribution of samples, the entire operating process can be divided into four stages to represent the development process of a crack fault from the normal state to crack expansion. In the first stage (samples 1 to 21), the gearbox enters into a normal working state, and the gear is in a healthy state. Therefore, the classification result is steady. The first stage can be regarded as the normal state. In the second stage (samples 22 to 60), a new category (i.e. the 2nd category) occurs. The sample category switches between the 1st and the 2nd categories. This stage is different from the first stage but has the characteristics

of the first category. It indicates that the mild wear has just been formed, and the vibration increases slightly but not significantly. In the third stage (samples 61 to 100), the samples are classified into the 3rd category. The category in this stage is clearly distinct from the first two stages. It indicates that the micro-crack may occur on the gear that makes the vibration greater than that of the second stage. Under the influence of the alternating load, the micro-crack will gradually expand, while the vibration clearly and simultaneously increases. In the fourth stage (samples 101 to 130), new categories occur (i.e. the 4th category and the 5th category). Most of the samples in this stage are classified into the 4th category and a few samples are classified into the 5th category. According to the above analysis, the crack expansion exists in the fourth stage until the broken tooth fault occurs. It can be inferred that the crack fault has been serious from the start of 101st sample. Shutdown and maintenance are needed for the gearbox. Therefore, early fault detection is achieved.
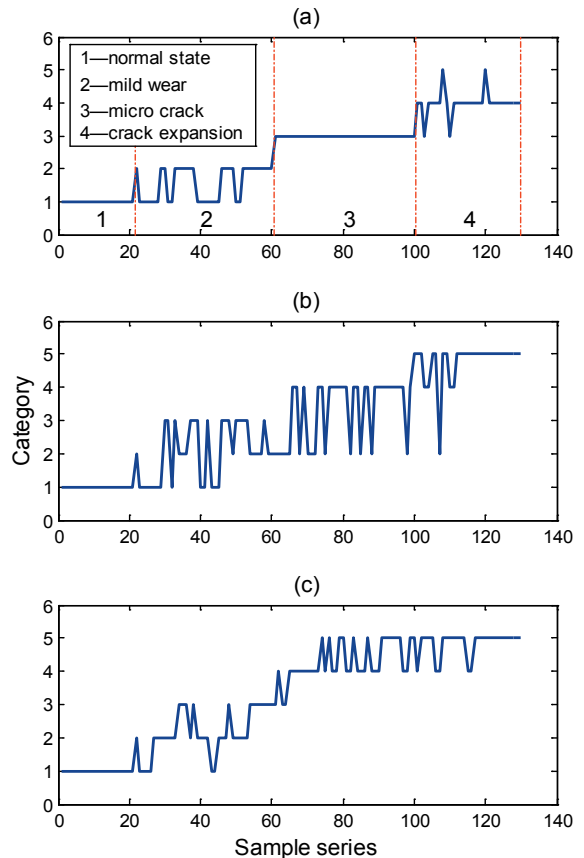
Fig. 13. *The classification result by using: a) ART-2 neural network proposed in this paper, b) self-organizing competitive neural network, and c) self-organizing feature map neural network*

The effectiveness of the ART-2 neural network is verified through comparisons with a self-organizing competitive neural network and a self-organizing feature map neural network. The same data are used for these networks, and the recognition results are shown in Figs. 13b and c. Through a comparison with the result shown in Fig. 13a, it can be seen that the recognition result is not obvious. The state of the sample series cannot be classified effectively by these two networks. Furthermore, the changing trend is also complex. Therefore, the crack fault cannot be detected effectively, which demonstrates the effectiveness of the DWT and the ART-2 neural networks in this paper.

3 CONCLUSIONS

(1) For the detection of crack faults in a gearbox, a new approach using the discrete wavelet transform, and an adaptive resonance theory neural network is proposed in this paper.

(2) The signal can be decomposed into a series of sub-bands based on the discrete wavelet transform; the relative wavelet energy is proposed to reflect the energy distribution of signals in different sub-bands. An adaptive resonance theory neural network based on unsupervised learning is proposed and designed for recognizing the changing trend of crack faults without known samples.

(3) An experiment with a crack fault in the gearbox is implemented and analysed, using the proposed method. The results show that the relative wavelet energy extracted by discrete wavelet transform can extract the fault feature effectively. Through comparison with different unsupervised neural networks, it is verified that an adaptive resonance theory neural network can clearly recognize the changing trend from the normal state to a crack fault via crack fault detection with an appropriate threshold value. It provides a new tool for condition monitoring and early fault diagnosis of gearboxes.

4 ACKNOWLEDGEMENTS

5 REFERENCES

[1] Ognjanović, M.B., Ristić, M., Vasin, S. (2013). BWE traction units failures caused by structural elasticity and gear resonances. *Tehnički Vjesnik – Technical Gazette*, vol. 20, no. 4, p. 599-604.

[2] Wenyi, L., Zhenfeng, W., Jiguang, H., Guangfeng, W. (2013). Wind turbine fault diagnosis method based on diagonal spectrum and clustering binary tree SVM. *Renewable Energy*, vol. 50, p. 1-6, DOI:10.1016/j.renene.2012.06.013.

[3] Bin, G.F., Gao, J.J., Li, X.J., Dhillon, B.S. (2012). Early fault diagnosis of rotating machinery based on wavelet packets— Empirical mode decomposition feature extraction and neural network. *Mechanical Systems and Signal Processing*, vol. 27, p. 696-711, DOI:10.1016/j.ymssp.2011.08.002.

[4] Mark, W.D., Lee, H., Patrick, R., Coker, J.D. (2010). A simple frequency-domain algorithm for early detection of damaged gear teeth. *Mechanical Systems and Signal Processing*, vol. 24, no. 8, p. 2807-2823, DOI:10.1016/j.ymssp.2010.04.004.

[5] Badaoui, M.E., Guillet, F., Daniere, J. (2004). New applications of the real cepstrum to gear signals, including definition of a robust fault indicator. *Mechanical Systems and Signal Processing*, vol. 18, no. 5, p. 1031-1046, DOI:10.1016/j.ymssp.2004.01.005.

[6] Sharma, G.K., Kumar, A., Babu Rao, C., Jayakumar, T., Raj, B. (2013). Short time Fourier transform analysis for understanding frequency dependent attenuation in austenitic stainless steel. *NDT & E International*, vol. 53, p. 1-7, DOI:10.1016/j.ndteint.2012.09.001.

[7] Peng, Z.K., Tse, P.W., Chu, F.L. (2005). A comparison study of improved Hilbert–Huang transform and wavelet transform: application to fault diagnosis for rolling bearing. *Mechanical systems and signal processing*, vol. 19, no. 5, p. 974-988, DOI:10.1016/j.ymssp.2004.01.006.

[8] Fang, N., Pai, P.S., Edwards, N. (2012). Tool-edge wear and wavelet packet transform analysis in high-speed machining of Inconel 718. *Strojniski vestnik – Journal of Mechanical Engineering*, vol. 58, no. 3, p. 191-202, DOI:10.5545/sv-jme.2011.063.

[9] Al-Badour, F., Sunar, M., Cheded, L. (2011). Vibration analysis of rotating machinery using time–frequency analysis and wavelet techniques. *Mechanical Systems and Signal Processing*, vol. 25, no. 6, p. 2083-2101, DOI:10.1016/j.ymssp.2011.01.017.

[10] Rosso, O.A., Martin, M.T., Figliola, A., Keller, K., Plastino, A. (2006). EEG analysis using wavelet-based information tools. *Journal of Neuroscience Methods*, vol. 153, no. 2, p. 163-182, DOI:10.1016/j.jneumeth.2005.10.009.

[11] Saravanan, N., Ramachandran, K.I. (2010). Incipient gear box fault diagnosis using discrete wavelet transform (DWT) for feature extraction and classification using artificial neural network (ANN). *Expert Systems with Applications*, vol. 37, no. 6, p. 4168-4181, DOI:10.1016/j.eswa.2009.11.006.

[12] Fan, J., Song, Y., Fei, M. (2008). ART2 neural network interacting with environment. *Neurocomputing*, vol. 72, no. 1-3, p. 170-176, DOI:10.1016/j.neucom.2008.02.026.

[13] Sun, Y.J., Zhang, S., Miao, C.X., Li, J.M. (2007). Improved BP neural network for transformer fault diagnosis. *Journal of China University of Mining and Technology*, vol. 17, no. 1, p. 138-142, DOI:10.1016/S1006-1266(07)60029-7.

[14] Čuš, F., Župerl, U. (2011). Real-time cutting tool condition monitoring in milling. *Strojniski vestnik – Journal of Mechanical*

Engineering, vol. 57, no. 2, p. 142-150, **DOI:10.5545/sv-jme.2010.079**.

[15] Wang, C., Zhou, J., Qin, H., Li, C., Zhang, Y. (2011). Fault diagnosis based on pulse coupled neural network and probability neural network. *Expert Systems with Applications*, vol. 38, no. 11, p. 14307-14313, **DOI:10.1016/j.eswa.2011.05.095**.

[16] Xu, P., Xu, S., Yin, H. (2007). Application of self-organizing competitive neural network in fault diagnosis of suck rod pumping system. *Journal of Petroleum Science and Engineering*, vol. 58, no. 1-2, p. 43-48, **DOI:10.1016/j.petrol.2006.11.008**.

[17] Ghosh, S., Patra, S., Ghosh, A. (2009). An unsupervised context-sensitive change detection technique based on modified self-organizing feature map neural network. *International Journal of Approximate Reasoning*, vol. 50, no. 1, p. 37-50, **DOI:10.1016/j.ijar.2008.01.008**.

[18] Grossberg, S. (2013). Adaptive Resonance Theory: How a brain learns to consciously attend, learn, and recognize a changing world. *Neural Networks*, vol. 37, p. 1-47, **DOI:10.1016/j.neunet.2012.09.017**.

[19] Carpenter, G.A., Grossberg, S. (1987). A massively parallel architecture for a self-organizing neural pattern recognition machine. *Computer Vision, Graphics, and Image Processing*, vol. 37, no. 1, p. 54-115, **DOI:10.1016/S0734-189X(87)80014-2**.

[20] Carpenter, G.A., Grossberg, S. (1987). ART 2: Self-organization of stable category recognition codes for analog input patterns. *Applied Optics*, vol. 26, no. 23, p. 4919-4930, **DOI:10.1364/AO.26.004919**.

[21] Lee, I.S., Kim, J.T., Lee, J.W., Lee, D.Y., Kim, K.Y. (2003). Model-based fault detection and isolation method using ART2 neural network. *International Journal of Intelligent Systems*, vol. 18, no. 10, p. 1087-1100, **DOI:10.1002/int.10134**.

[22] Lee, I.S., Lee, S.J., Kim, Y.W. (2010). Fault diagnosis based on discrete wavelet transform and ART2 neural network. *SICE Annual Conference Proceedings*, p. 3365-3370.

[23] Obikawa, T., Shinozuka, J. (2004). Monitoring of flank wear of coated tools in high speed machining with a neural network ART2. *International Journal of Machine Tools and Manufacture*, vol. 44, no. 12-13, p. 1311-1318, **DOI:10.1016/j.ijmachtools.2004. 04.021**.

Mechanical Failure Mode Causes of In-Wheel Motors

Matej Biček[1,*] – Gorazd Gotovac[1] – Damijan Miljavec[2] – Samo Zupan[3]

[1] Elaphe Propulsion Technologies, Slovenia
[2] University of Ljubljana, Faculty of Electrical Engineering, Slovenia
[3] University of Ljubljana, Faculty of Mechanical Engineering, Slovenia

The presented survey includes a comprehensive overview of mechanical failure mode causes for direct driven electric in-wheel motors. As electric vehicles evolve and develop, in-wheel motor driven vehicles gain acknowledgement, more and more papers are published in order to show individual design challenges and overcoming solutions for failure causes and effects. Obtainable literature is mainly concerned with integral electrical failure modes, neglecting structural causes and effects which in some cases interact. The presented paper inspects the most likely potential mechanical causes of failure modes for in-wheel motors and shows related paper's results for comparison and reference. As several mechanical and electromagnetic layouts and construction topologies exist, only the most promising and generally used one has been studied within this work in order to emphasize sensible directions of further development. Failure mode and effects analysis (FMEA) has been made with severity rating which present mechanical failure potential for permanent magnet synchronous motors intended for in-wheel motor application.
Keywords: in-wheel, failure mode and effects analysis, unsprung mass, excessive vibrations, eccentricity, bearing faults

Highlights
- *Novel propulsion architecture for vehicles.*
- *Permanent magnet synchronous motors.*
- *Benchmark of papers discussing in-wheel motor's pros and cons.*
- *Acoustic emissions of PMSM motors and related effects to user's comfort.*
- *Mechanical construction optimization of in-wheel motor design.*
- *Risk priority number estimation for mechanical failure mode causes.*

0 INTRODUCTION

The International Energy Agency (IEA) has announced that at the end of 2012 about 0.02% of world's registered vehicles had electric propulsion, including battery electric vehicle (BEV), plug in hybrid electric vehicles (PHEV) and hybrid electric vehicle (HEV). Several scenarios can be obtained for future electric vehicle (EV) global market predictions, mostly dependent on battery's performance to cost ratio. Without any speculations, an objective estimation can be placed where global EV market will reach between 4 and 20 million vehicles, which by then will be equivalent to 0.5% and respectively 2% of the global vehicle share [1] to [4].

The future EV should combine the knowledge gained from current vehicles combining passenger safety and comfort aspects, vehicle aerodynamics, weight reduction, low energy consumption and reduced ecological footprint. Electric vehicles meet these requirements at ease, as they have less moving parts and consequently require less maintenance, have much higher efficiency than internal combustion engine (ICE) propulsion, can run on electricity from renewable resources and have no CO emissions, provide quiet operation and with batteries normally placed under the floor enable better handling characteristics [5] to [7]. The propulsion system architecture within the current EVs does not exploit the versatility of electric motors as they are implemented centrally and maintain the propulsion's transmission and consequently its losses [8]. An in-wheel motor placed inside the rim of two or four wheels exceeds current designs with its holistic approach placing the propulsion system where it is needed, inside the wheel [9]. Direct driven wheels have no losses due to transmission and require no additional space inside the vehicle providing the designers with complete flexibility and freedom to improve passenger's safety, vehicle performance and space. The vehicle's center of gravity becomes lower which in combination with a true torque vectored four-wheel drive significantly improves the drivability of the vehicle [10] and [11].

Consequently, in-wheel motor propulsion systems have a scalable market potential in personal transportation as well as in public usage, ranging from smaller urban vehicles to larger buses and trains [10]. Direct driven vehicles require high specific torque, wide speed range and should be free from maintenance. Permanent magnet synchronous motors (PMSM) with outer rotor and radial electromagnetic flux are among top candidates for such applications

[12] to [14]. In-wheel motor's electric faults can be found in several surveys and studies. However, a much lesser extent of papers deals with mechanical faults and no paper exists describing interacting impacts of different mechanical faults. The present survey shows a comprehensive overview of permanent magnet synchronous motors (PMSM) motor failure modes with an emphasis on mechanical failures. The scope of this paper covers all potential mechanical fault causes and evaluates their severity objectively, based on measurements and tests performed by different institutions and companies.

1 GENERAL OVERVIEW OF POTENTIAL IN-WHEEL MOTOR FAILURE MODES

Safety aspects with fault tolerant control are of major interest in automotive industry [15]. All potential failures should be carefully analyzed and evaluated in the pre-design stage in order to meet automotive standards [16]. It is important to note that the importance of each fault differs, as they have variable probability of occurrence [17]. Safety is largely determined by the ability to cope with unexpected component's overloads without total failure [18]. The failure mode and effects analysis (FMEA) is a procedure in product development, which evaluates risk priority numbers (RPN) for each potential fault. RPN consists of three evaluation parameters: S (severity rating), O (occurrence rating) and D (detection rating) as stated in Eq. (1) [17].

$$RPN = S \times O \times D, \qquad (1)$$

Severity rating is only partly subjective evaluation, since the standard severity scale from 1 to 10 can be used for evaluation (Table 1).

Table 1. *Severity rating* [19]

Rating	Meaning
S1	No effect
S2	Very minor (only noticed by discriminating customers)
S3	Minor (affects very little of the system, noticed by average customer)
S4; S5; S6	Moderate (most customers are annoyed)
S7; S8	High (causes a loss of primary function; customers are dissatisfied)
S9; S10	Very high and hazardous (product becomes inoperative; customers angered; the failure may result in unsafe operation and possible injury)

Occurrence rating is also scaled from 1 to 10.

Table 2. *Occurrence rating* [19]

Rating	Meaning
O1	No failure
O2; O3	Low (relatively few failures)
O4; O5; O6	Moderate (occasional failures)
O7; O8	High (repeated failures)
O9; O10	Very high (failure is almost inevitable)

And detection rating is also scaled from 1 to 10.

Table 3. *Detection rating* [19]

Rating	Meaning
D1	Almost certain
D2	High
D3	Moderate – noticeable
D4; D5; D6	Moderate – disagreeable or unwanted
D7; D8	Low
D9; D10	Very remote to absolute uncertain

A comprehensive overview and objective result evaluation can be a good basis for subjective FMEA evaluation.

The most critical direct drive system failure mode causes include:

Electrical nature of the failure [13], [17] and [20] to [26]:
- Motor winding open circuit, short circuit to housing (ground fault), winding terminal short circuit and internal turn-turn short circuit;
- Power device failures (inverter shuts down, open or short circuit);
- Capacitor failures (open or short circuit);
- Direct current (DC) bus open or short circuit;
- Magnetization faults (uneven magnetization would cause higher torque ripple, lost current in the field weakening range);
- High impedance (broken strand, loose connection);
- Thermal effects (sufficient cooling necessary in order to sustain magnetization and winding insulation.

Mechanical nature of failure:
- Deteriorated driving dynamics when higher unsprung mass is applied [27] to [38];
- Thermomechanical effects (different expansions of materials in assembly and consequential stress – strain state) [13], [30] and [39] to [45];
- Structural elastic deformation due to sudden and unexpected external impacts [15] and [46] to [52];
- Torque pulsation induced vibrations and their impact on acoustics and structure fatigue [53] to [65];

- Mechanical failures due to bearing system failure [66] to [68];
- Mechanical failures due to static or dynamic eccentricity [22], [69] and [70];
- Challenges for sealing on high diameter [30] and [71].

Obtainable literature [13], [17] and [20] to [25] has shown in-wheel motor faults in detail from the electrical point of view, in order to understand potential hazards for designing and preventing potential motor malfunction when in operation. Markedly less literature is obtainable regarding potential mechanical malfunctions, irrespective of the fact that some of them are directly connected with electric motors for other applications. As the in-wheel motor is integrated inside the vehicle's rim and usually uses a standard hub bearing from automotive industry, several potential threats need to be envisioned. Fig. 1 shows a simple layout of an in-wheel motor with interchangeable brake elements in exploded view.
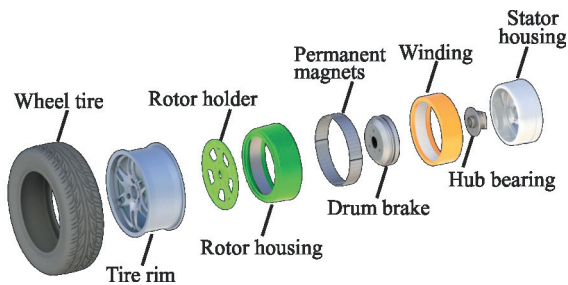

Fig. 1. *Elaphe Smart2Gen in exploded view*

2 REVIEW OF MECHANICAL FAULT CAUSES

As in-wheel motors gain acknowledgement, research papers from commercial and academic literature are frequently published. However, papers and theses consider only the electromagnetic construction design as in [72]. Mechanical fault surveys are mainly oriented to in-wheel motor's effects on driving dynamics via higher unsprung mass, sealing challenges and acoustic emissions and vibrations. The following chapters evaluate published topics, based on their approach, measurements and concluding remarks.

2.1 Higher Unsprung Mass and Its Impact on Driving Dynamics

A frequently cited drawback for in-wheel motors is the potential detrimental effect of higher unsprung mass on driving dynamics [12], [27], [30] to [33] and [36]. In the survey [33], different driving scenarios have been investigated by on road experiments with VW Lupo 3L. The analysis envisioned that two in-wheel motors, each weighting 15 kg, have sufficient performance and can be integrated in front or rear wheels. As the battery pack has been included, the total vehicle mass has been enhanced and also the center of mass has lowered, the ride comfort has actually been improved. The comfort has been measured via the intensity of accelerations of the sprung body and relating them to sensitivity of a human body via ISO 2631-1:1997 [34], [57], [73] and [74]. Even though the ride comfort was allegedly improved, the dynamic wheel load was increased by up to 40% and the suspension travel up to 16%. Reduction of the tire pressure or usage of an additional vibration absorber is found to be inefficient. In addition, a semi-active and fully active skyhook and hybrid control have been investigated, which both result in final 9% reduction of dynamic wheel load.

In [27], numerical models and real physical vehicles have been studied for degrading performance and ride comfort. Vehicle performance was divided into ride (ability to absorb disturbances), refinement (ability to attenuate noise and vibration), active safety (stop and steer in emergency cases), driveability (response of the vehicle to steering, braking and drive in normal situations). Each category was subjectively assessed by experts for vehicle dynamics and also objectively assessed via measurements and tests of steering, handling and ride behavior. With subjective results assessment, conclusions were made that the additional unsprung mass equal to 30 kg in each of the four wheels of Ford Focus 2007 results most notably in heavier steering under a wide circumstance specter. Objective measurements were made with accelerometers applied on different parts of the vehicle and driving over typical UK roads referred to as shake roads. The wheel-hop mode of vibration where the unsprung mass is in motion was reduced from 14 Hz (conventional vehicle) to 10 Hz (vehicle with additional unsprung mass in each wheel equivalent to 30 kg). This is somewhat reasonable as the additional mass is connected with higher inertias and results in response with less contact and vibration when driving over a barrier. The measured overall ride resulted in perceptible differences with increased unsprung mass. However, they are unlikely to be apparent to an average driver, since they are all within normal boundaries, as noted in the paper. Authors also suggest that the changes can be overcome with standard engineering capabilities and processes which could substantially enhance the vehicle behavior at the final stage [30].

In **[36]**, effects on stability, safety and ride comfort of the vehicle were analyzed using a quarter vehicle suspension model. During all simulations, the occurrence of wheel hop phenomena was monitored, which is a function of the unsprung mass and tire stiffness and results in unsprung mass motion relative to vehicle chassis. The survey concludes that the wheel hop is present with in-wheel motors and results with tire needing more time to get back into contact with the surface. The results show potential handling problems at higher vehicle velocities. Despite wheel hop results, the authors conclude that standard suspension of a conventional car can be used for in-wheel motor drive vehicles without loss of comfort and safety.

In undergraduate thesis **[32]**, a quarter car model recorded with measured characteristics was simulated. The dynamic system is shown in Fig. 2 with parameters m_v being sprung mass, k_v spring coefficient with linear characteristics, d_d damper relative to speed (measured characteristics), m_s stator mass, m_r rotor mass (motor rotor + rim + tire), d_p tire damping coefficient, k_p tire stiffness coefficient.
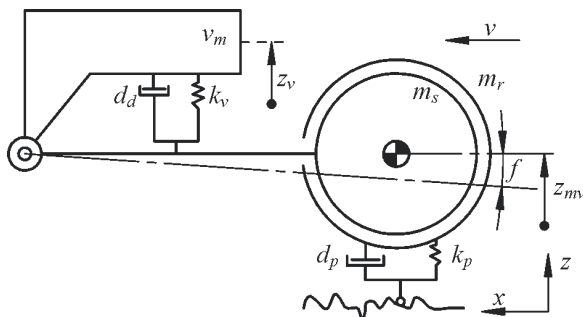

Fig. 2. *Quarter car model based on* **[32]**

The entire mechanical system is moving with velocity *v* and the advantage compared to other quarter vehicle models is that due to the unchanged chassis geometry there is no need for adding corrected spring and damper values and mass can be applied to the rear axle, which is not negligible for the whole system. Different driving scenarios have been considered using multibody dynamics with emphasis on different driving performance and loads for a conventional car and a car with additional 37 kg of unsprung mass in each rear wheel. Simulations have been carried out for driving over curb-sides with different heights (100 and 120 mm) at different speeds (2, 4 and 8 km/h), driving over a standard speed bump at different speeds (15, 30 and 45 km/h) and over a road pothole (500 mm long and 100 mm deep) at different speeds (30, 50, 70 and 90 km/h). Additional studies have been

made for vibration isolation and suspension travel ratio, which can be connected with vehicle safety and comfort. Conclusions within this work combine negligible differences for loads on hub bearing when driving over a speed bump and lower accelerations on unsuspended parts, when driving over a curb for all speeds and heights. This can be explained with higher inertias due to higher mass.

Simulating driving over a road pot-hole results also in smaller accelerations when higher unsprung mass is applied and driving with different frequency excitations results in the same way. Accelerations are however higher when the excitation amplitudes and frequencies reach the system's resonant frequencies. Regarding to vibration isolation and the suspension travel ratio, an inconsiderable effect was noticed which shows deterioration. Especially vibration isolation results in lower second eigenfrequency by a factor of two. Eigenfrequency is the motor system's characteristic frequency, at which the system tends to oscillate in the absence of damping. These reductions are closely connected with vehicle suspensions and could be, as noted by the author, largely increased with suspension optimization, such as in **[75]**, where active suspension has been analyzed.

The survey **[31]** introduces the requirements and stages which were carried out in order to design their electric in-wheel motor, with a brief presentation of the required goals. One crucial in-wheel motor design conflict presented in this survey is the motor weight which must be limited as much as possible to have a small influence of the unsprung mass on dynamic loads and optimized vehicle performance. On the other hand, a motor with a higher mass of active material will have better properties and also passive elements need high stiffness to reduce deformations in the air-gap region and maintain motor's electromagnetic performance. Since stiffness and mass are directly connected, a reasonable inflection point should be defined. As noted by the authors, the main concerns with higher unsprung mass being accelerated, are the increased dynamic forces and negative influence towards vehicle dynamics. In order to evaluate these effects, several test drives have been performed with a conventional propulsion and added equivalent to motor masses into rear wheels of a sports car Artega. The complete mass (two motors with 44.2 kg) has been divided to static and rotating part in the same way as it is done when the functional motors are mounted on the vehicle. Drive tests have been performed on a test track, which has route sections with different durability relevant sections and maneuvers have been made on all of them. Extensive equipment for

measuring accelerations, strain gauges and GPS sensors have been implemented on the vehicle and rear wheels. To eliminate the drivers influence on test results, each of the tests has been made with five different drivers with different driving skills. The authors conclude the survey with an increased force amplitude from 0 to 15% for chassis components and 0 to 25% for wheel components, decreased wheel hop frequency from 16 to 10 Hz, higher noise when driving over rough road (yet not disturbing) and a more tail-heavy driving characteristic, noticeable as over-steering. As noted in the paper, this is manageable. From the structural durability point of view, however, many other durability tests should be made before a series product can be released.

All surveys conclude that higher dynamic loads are present when additional unsprung mass is incorporated. Although by installing battery packs and setting the vehicle's center of mass lower to the ground, a non-professional driver would most probably not notice any difference in handling, comfort or safety, in fact with true four wheel drive via torque vectoring, the driving experience should even be improved [76]. Three most comprehensive papers [27], [31] and [33] conclude that the negative effects of feeling a tail-heavy rear should be resolved with suspension balancing, the ride comfort should not be reduced and the dynamic loads are increased from 15 to 40%.

2.2 Eccentricity

For rotary dynamics, eccentricity is an important durability factor and, as such, should be discussed in detail. Static and dynamic eccentricity result in different ways and due to finite tolerances within production technologies, eccentricity is present in every mechanical design [22] and [70]. Static radial eccentricity can be described with shifted axes of rotor to stator, as a consequence of mounting errors or inaccuracies when producing positioning flanges. Radial dynamic eccentricity can be described as rotor's center misaligned with the axis of rotation [77]. Both eccentricities mainly result from dimensional and geometrical inaccuracies when producing elements and are always present to some extent as is the accuracy of production. As shown in Fig. 3, eccentricities deform the air gap in different ways and both have an additional impact on induced radial forces due to motor's changed magnetic flux.

Static axial eccentricity is present when a rotor rotates around its natural axis that is inclined compared to the stator one and dynamic axial

eccentricity is present when rotor's natural axis is inclined to its rotational [22]. Both axial eccentricities can be achieved with inaccurate machining operations and positioning accuracy when assembling parts. As shown in Fig. 4, axial eccentricities have similar effects on the deformed air gap and are mainly dependent on inclination angle and axial motor length.
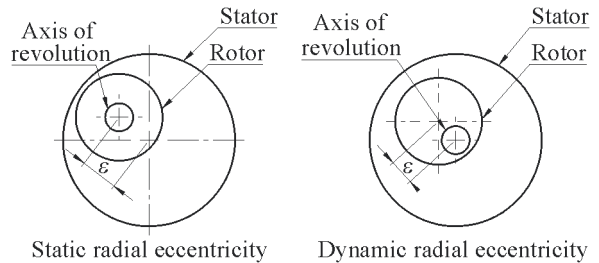
Fig. 3. *Static and dynamic radial eccentricity* [77]
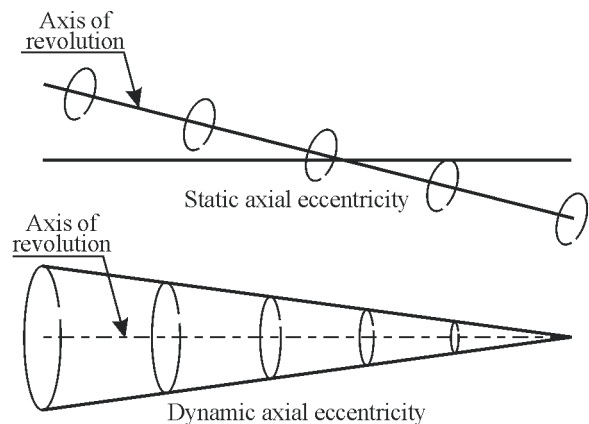
Fig.4. *Static and dynamic axial eccentricity* [22]

All eccentricities result in higher radial forces due to uneven magnetic fields, which was analyzed in [38] and [68]. It can also have an impact on winding failure, induced vibrations or consequently lead to premature bearing failure [70].

In-wheel motors are designed with a nominal air gap, between stator lamination and rotor magnets, normally dimensioned to 1 mm in order to minimize reluctance in the magnetic flux path [12]. When eccentricity of the motor is present, a non-uniform air gap occurs, consequently leading to uneven electromagnetic force distribution around the circumference. As discussed in the survey [68], the force due to eccentricity can be calculated via the electromagnetic energy in the magnetic air gap, which is directly connected to its thickness [65]. Results of analytical calculations were verified numerically using finite element based software for a 450 Nm direct drive in-wheel motor. The whole machine was modeled, including the appropriate materials. The

force was calculated for a stationary case, where there is no current in the winding. The numerical calculation was performed for discrete values of eccentricity ε ranging from 0 to 0.7 mm. The results and comparison to the analytical calculation are shown in Fig. 5.
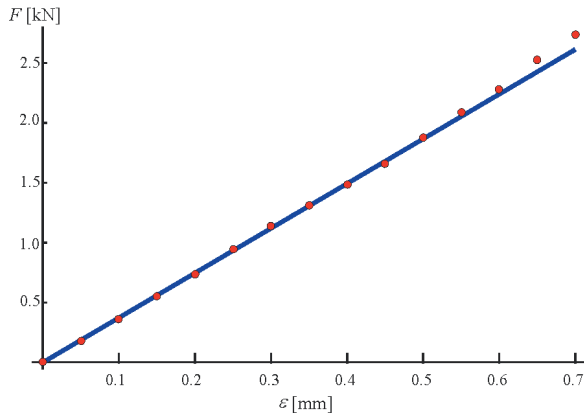
Fig. 5. *Comparison of values for the analytical force calculation (solid line) and the FEM based calculations (points)* **[68]**

The calculation was also made for a fully electromagnetically loaded motor, but no relevant increase of radial force occurs. The analysis of the additional radial forces shows that although the eccentricity of 0.1 mm is deemed within acceptable limits, it yields an additional radial force of 350 N. If the eccentricity is larger, due to an unexpected fault, the value of the force rises to 1.1 kN for 0.3 mm and 1.9 kN for 0.5 mm of eccentricity. Survey **[38]** used a similar approach for calculating the additional radial force, due to electromagnetism when eccentricity is applied. The conclusion of this survey shows that 0.1 mm of eccentricity corresponds to 500 N of additional radial force and at 0.5 mm the additional force is 550 N. Calculations from different surveys vary as the motor electromagnetic topologies differs and results in different electromagnetic fluxes. Eccentricity and bearing faults are connected via vibrations in both directions. When one occurs, the other is a consequence **[23]**. Based on **[38]** and **[68]**, 0.1 mm of eccentricity can result in approximately 350 to 500 N of additional radial force for PMSM outer rotor motors, due to changed electromagnetic flux density.

Dynamic eccentricity is normally eliminated with balancing, while static needs to be envisioned when designing static and rotating components **[77]**. However, in case balancing has not been resolved as required, an additional centrifugal force should be expected as shown on Fig. 6. Applied centrifugal force

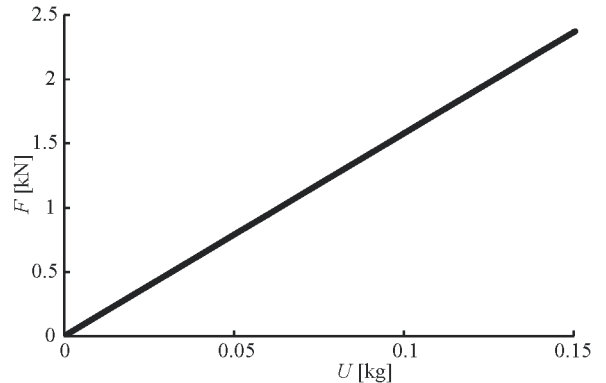has been calculated for rotor diameter from Table 4 and maximum velocity.

Fig. 6. *Additional radial centrifugal force due to eccentricity*

Figs. 5 and 6 show additional radial forces which need to be taken into account with PMSM motors when eccentricity (ε) and unbalance (U) is applied. Resulting forces have been calculated for in-wheel motor with specifications shown in Table 4.

Table 4. *In-wheel motor specifications*

Peak torque	[Nm]	700
Continuous torque	[Nm]	450
Peak power	[kW]	75
Constant power	[kW]	50
DC supply voltage	[V]	96
DC supply current	[A]	500
Axial width	[mm]	130
Radial diameter	[mm]	360
Maximum speed	[rpm]	1500
Motor mass – electromagnetic active (magnets, iron, steel blades, copper winding) parts	[kg]	13
Motor mass – electromagnetic passive (Al housing for rotor and stator, cooling system) parts	[kg]	11
Parts from the original propulsion (hub bearing, drum brake with anchor plate)	[kg]	7

Eccentricity is one of the most common mechanical fault causes within rotational devices and should be resolved with caution **[23]**. As described above, PMSM devices have two side effects when eccentricity occurs, one is additional radial force due to changed magnet flux and the other is additional force due to inertia.

2.3 Sealing of In-Wheel Motors

Sealing failure is not a direct motor-failure mode cause, but its design must be considered carefully in order to avoid inducing other mechanical faults. In-

wheel motor's layout can have internal or external rotor, both layouts have its own pros and cons. Internal rotor motors can have simmering sealing, which is reliable, cost efficient and generates low braking torque. External rotor motors have a higher diameter of air gap and consequently higher specific torque, which makes them a better choice for vehicle propulsion application. On the other hand, they require seals of higher diameter, which can generate higher braking torques or result in unreliable sealing **[12]**, **[31]** and **[76]**. As noted in **[30]**, sealing for in-wheel motors was resolved with a combination of different materials, offering complete protection against water and particle ingress, with the possibility of allowing condensation and moisture release. A V lip is used in this design for water and particle ingress protection, while all electronic parts are potted with epoxy resin providing IP 68 rating. Additional hydrophobic gel is applied on electronics to avoid damage during any submerging situations. It is apparent from **[76]** that a successful sealing unit was developed, which can withstand high circumferential velocities (30 m/s) and prevents ingress of contaminants during operation and standstill.

24 Vibration and Noise

Permanent magnet synchronous motors are known for emitting low noise in comparison with other types of motors for similar applications **[55]**. Noise of operation originates from vibrations due to mechanical (bearing defects and mounting accuracy, loads, rotor and shaft misalignment), electromagnetic (excited magnetic flux density waves in the air gap, caused by the slot geometry, distribution of winding in slots, input current waveform distortion, air gap permeance fluctuations, rotor eccentricity, phase unbalance all resulting in torque pulsation) and aerodynamic sources (obstacles placed in the air stream **[53]** and **[55]**. Vibrations arising from the above causes can vary from an almost soundless to unwanted loud noise, which indicates a certain motor failure. With predictive design and FEM based modal analyses, it is possible to identify the root cause of vibration problems, caused by motor's geometry and more significantly eliminate or reduce most problems in the design stage **[78]**. With a rational electromagnetic design of a PMSM motor, the torque pulsation can be minimized and designing a rotor with proper stiffness results in low noise when operating. Torque pulsation sources can be divided to cogging effects, distortion of sinusoidal distribution of the magnetic flux inside the air gap and as the difference between permeance of the air gap. Cogging frequency,

which is in most literature represented as the most problematic, can be calculated using Eq. (2) **[12]**, **[65]** and **[72]**. When designing rotor elements, geometry eigenfrequencies should be taken into consideration, controlled and if possible, any overlapping cogging and eigen-frequencies should be avoided **[53]**.

$$f_c = s_1 n_s = s_1 \frac{f}{p}, \qquad (2)$$

where s_1 is the number of stator slots, $n_s = f/p$ is the synchronous speed, p is the number of pole pairs and f is the input electrical frequency. Since direct driven vehicles have no gears, n_s is normally in the range 0 to 1200 rpm, relative to tire size selection and desired vehicle top speed. Consequential cogging frequency depends on the EM motor design, such as the number of slots and their geometry. If the first eigenmodes are designed to have a higher value than cogging frequency, less vibration should occur when operating **[56]**.

Further development should integrate vibrational fatigue tests for random loads the motor is subjected to during operation, such as stated in **[60]** where a numerical fatigue prediction model has been compared to experimental tests in order to verify its accuracy. The damping loss factor percent has been defined within this survey for proper high cycle fatigue life estimations of dynamic structures.

2.5 Bearing Related Faults

According to **[21]**, **[25]** and **[70]**, 40 to 50 % of all motor failures are bearing related and they are certainly more likely to occur when higher than normal loads are applied. Automotive hub bearings are one of the most important elements for vehicle dynamics, sustaining performance and maintaining safety. Bearings are designed to withstand various sets of loads, while providing minimal rotational resistance in a long lifespan. The latter is dependent on several factors, such as sealing, lubrication, cleanliness, material properties, machining and mounting accuracy, system stiffness and axial/radial load quantities **[79]**. Hub bearing loads are successfully managed in mass produced vehicles, but should be considered when integrated into an in-wheel motor, due to possible impacts from higher wheel mass **[76]**.

Motor's internal vibrations, eccentricity and premature bearing failure are in relation with each other and simultaneously open new categories of potential motor failures if not resolved in time.

Hypothetical combinations of static eccentricities and unsprung mass effects are discussed in **[68]**, where

a reasonable eccentricity equal to 0.1 mm and 40 % increase in dynamic loads due to higher unsprung mass result in 31% life reduction for a standard hub bearing used in a urban vehicle.

3 FAILURE MODE CAUSES

Failure mode and effects analysis is normally held as several meetings of highly skilled individuals who mostly participate in the design or process stage of a project in several iterations. The highest possible result objectiveness is sought-after and in this way the impact of an individual opinion is reduced [17]. FMEA is a subjective assessment tool, which uses a qualitative approach to identify potential failure modes, their causes and effects for design, manufacture and operation stages [23]. Table 5 shows the results of the analysis made corresponding to the studied and cited obtainable literature. In general, high severity was rated only for faults which are presented as continuous or problematic in obtainable literature. Severity of failure modes can easily be extrapolated from the obtained analyses. However, occurrence and detection can only be previsioned, since in wheel motors exist only for testing and showcase purposes.

In relation to the known parameters of permanent magnet motors with high pole numbers used for other applications, analogies have been made. Mechanical faults such as vibrations and eccentricity have described the occurrence rating in [23]. Detection rating was envisioned based on findings in review articles such as [87] to [89].

4 CONCLUSION

The presented survey examines mechanical failure mode causes for electric in-wheel motors intended for propulsion systems of purely electric or hybrid vehicles. Within the scope of research, emphasis was made on frequently cited topics, such as application of higher unsprung mass and its effects on potentially deteriorated driving dynamics. In addition, failure mode causes such as static and dynamic eccentricity, excessive vibrations and consequential noise, reduced hub bearing lifetime and sealing challenges have also been examined in obtainable literature in order to be addressed with severity. This was used to establish an overview failure mode and effects analysis covering all the mechanical failure mode causes known for rotational devices, with emphasis on direct driven

Table 5. *Mechanical failure mode causes for PMSM in-wheel motors*

Functions/ requirements	Failure modes	Failure mode causes	Potential failure mode effect	Severity based on literature	Previsioned occurrence and detection ratings	RPN rate	Ref.
Rotational motion with limited rolling resistance providing safety and sufficient handling	Rolling resistance is too high, too little traction with surface, unexpected breaking torque, rotor locking,	Higher unsprung mass	Deteriorated driving comfort	Very minor (S2)	High occurrence (O7) Moderate detection (D3)	42	[27] to [38]
			Induced dynamic loads	Minor (S3)	Low occurrence (O3) Low detection (D6)	54	
			Tail-heavy effect	Moderate (S5)	Moderate occurrence (O4) High detection (D2)	40	
		Eccentricity	Reduced durability	Very minor (S2)	High occurrence (O7) Low detection (D6)	84	[22], [23], [53], [69], [70]
			High noise	Moderate (S6)	High occurrence (O7) Moderate detection (D3)	126	[77]
		Excessive vibrations	Reduced durability	Very minor (S2)	High occurrence (O7) Low detection (D6)	84	[59], [60], [80], [81]
			High noise	Moderate (S6)	High occurrence (O7) Moderate detection (D3)	126	[55], [82], [83], [84]
		Insufficient sealing	Unexpected braking torque due to mechanical contaminants	High (S7)	Remote occurrence (O1) Low detection (D6)	42	[30], [31], [76]
			High voltage on chassis due to conductive liquid in the air gap	High (S7)	Remote occurrence (O1) Low detection D(6)	42	
			Reduced durability	Minor (S3)	Low occurrence (2) Low detection (6)	36	
		Bearing failure	Vehicle stability reduction	High (S8)	High occurrence (O8) Moderate detection (D3)	192	[54], [68], [69], [85], [86]

outer rotor PMSM in-wheel motors. Within the FMEA, a comprehensive benchmark of risk potentials for individual mechanical failure mode causes has been determined via risk priority numbers.

4.1 Main Surveys's Findings

Surprisingly, the most cited mechanical fault, higher unsprung mass effects on deteriorated driving dynamics, achieves one of the lowest risk potentials, based on all objective surveys. Sealing challenges, which are also frequently cited as very problematic, seem to be solved and do not present a high risk potential. Vibrations with consequential acoustic emissions and static/dynamic eccentricity result in highest risk potential as their interactions with other failure mode causes were taken into account. Within mature applications, rotational device designs have been successfully managed towards eliminating vibrations and eccentricity. As PMSM motors for in-wheel propulsion application are currently under testing and development, all of the presented mechanical faults should be considered in a novel design.

4.2 Evaluation of RPN Ratings for Mechanical Mode Causes

Since individual failure mode causes have a different number of failure effects, they should be summed up in order to show the most problematic mechanical ones. Based on the existing literature and analyses made for motors for another applications, extrapolation was made for determining the most problematic mechanical causes.

They are presented in Table 6 in relation to the achieved maximum rating priority numbers.

Table 6. *RPN ratings for most likely mechanical failure causes*

Mechanical failure mode case	Evaluated RPN ratings
Higher unsprung mass	126
Eccentricity	210
Excessive vibrations	210
Insufficient sealing	120
Bearing failure	192

As evident from the results obtained, the mainly cited failure causes do not represent threats and are manageable, based on the obtained literature. Standard design faults for rotational devices reach higher risk ratings and should be considered, e.g. hub bearing

deflection angle should be reduced in comparison to standard original equipment manufacturer's (OEM) products for current automotive industry. Similar examples are eccentricity and vibrations, which interact with motor's electromagnetic properties and have a more significant effect on the product's safety, durability and overall performance.

5 FURTHER WORK

The authors have made a complete review of published literature regarding in-wheel motor's electromagnetic and mechanical design. Within the research, several deficiencies have been observed from the mechanical design perspective as no FMEA analysis for mechanical faults is obtainable, neither is a structural optimization methodology for a stochastically loaded construction, which should preserve low mass and high stiffness. Further work should be aimed at thermo-mechanical analyses and structural deformations due to sudden impacts, which are much more complex, yet necessary for complete failure mode evaluation of a product that could reach series production in automotive industry.

6 REFERENCES

[1] International Energy Agency - Electric Vehicle Initiative and Clean Eenergy Ministerial. Global EV Outlook - Understanding the Electric Vehicle Landscape to 2020, from *http://www.iea. org/publications*, accessed on 2014-10-05.

[2] Frost & Sullivan. Global EV market by 2020, from *http://www. thegreenautomotivecompany.com*, accessed on 2014-10-05.

[3] Nemry, F., Brons, M. (2011). *Market Penetration Scenarios of Electric Drive Vehicles*. Institute for Prospective Technological Studies, Seville.

[4] Balducci, P.J. (2010). *Plug-in Hybrid Electric Vehicle Market Penetration Scenarios*. US Department of Energy – Pacific National Laboratory, Springfield.

[5] Khusid, M. (2010). *Potential of Electric Propulsion Systems to Reduce Petroleum Use and Greenhouse Gas Emissions in the U. S. Light-Duty Vehicle Fleet*. Massachusets Institute of Technology, Massachusets

[6] Geissinger, J.M. (2012). The future powertrain – challenge between internal combustion engine and electric mobility. *33rd International Vienna Motor Symposium*, p. 22-37.

[7] Kulkarni, A., Kapoor, A., Ektesabi, M., Lovatt, H. (2012). Electric vehicle propulsion system design. *Sustainable Automotive Technologies*, vol. 61, no. 03, p. 199-206, **DOI:10.1007/978-3-642-24145-1_26**.

[8] Lampič, G., Slivnik, T., Detela, A. (2005). Holistic approach in developing propulsion system for urban electric vehicles. *Vehicle Power and Propulsion Conference Proceedings*, p. 268-272, **DOI:10.1109/VPPC.2005.1554569**.

[9] Lampič, G. (2006). *Analysis of the Deployment of Electric Drives in Various Types of Vehicles and Drive Design for the*

Modern Urban Electric Hybrid Car. University of Ljubljana, Faculty of Electrical Engineering, Ljubljana. (in Slovene)

[10] Heim, R., El Dsoki, C. Hanselka. H. (2012). Technical potential of in-wheel motors, *ATZ*, vol. 114, no. 10, p. 4-9.

[11] Fraser, A. (2011). In-wheel electric motors. *10th International CTI Symposium*, p. 12-23.

[12] Hooper, I. (2011). *Development of In-Wheel Motor Systems for Formula SAE Electric Vehicles*. University of Western Australia, Perth.

[13] Pérez, S.R. (2011). *Analysis of a Light Permanent Magnet In-Wheel Motor for an Electric Vehicle With Autonomous Corner Modules*. Royal Institute of Technology, Stockholm.

[14] Rasmussen, P.O., Matzen, T.N. (2009). *Torque Control in Field Weakening Mode*. Institute of Energy Technology, Aalborg.

[15] Heyes, A.M. (1998). Automotive component failures. *Engineering Failure Analysis*, vol. 5, no. 2, p. 129-144, DOI:10.1016/S1350-6307(98)00010-7.

[16] ISO 6469-2:2009 (2009). *Electric Road Vehicles - Safety Specifications - Part 2: Functional Safety Means and Protection Against Failures*. International Organization for Standardization, Geneva.

[17] Liao, Y. (2011). *Analysis of Fault Conditions in Permanent-Magnet In-Wheel Motors*. Royal Institute of Technology, Stockholm.

[18] Grubišić, V., Fischer, G. (1997). Methodology for effective design evaluation and durability approval of car suspension components. *SAE*. SAE technical paper 970094, DOI:10.4271/970094.

[19] Jonas, P., Karlberg, M. (1997). Variation mode and effect analysis compared to FTA and FMEA in product development. *ASME Design Engineering Technical Conference*, p. 252-260.

[20] Ifedi, C.J., Mecrow, B.C., Brockway, S.T.M., Boast, G.S., Atkinson, G.J., Kostic-Perovic, D. (2011). Fault tolerant in-wheel motor topologies for high performance electric vehicles. *IEEE Electric Machines & Drives Conference*, p. 1310-1315, DOI:10.1109/IEMDC.2011.5994794.

[21] Wang, R., Wang, J. (2011). Fault-tolerant control with active fault diagnosis for four-wheel independently driven electric ground vehicles. *IEEE Transactions on Vehicular Technology*, vol. 60, no. 9, p. 4276-4287, DOI:10.1109/TVT.2011.2172822.

[22] Ghoggal, A., Zouzou, E.S., Razik, R., Sahraoui, M., Khezzar, A. (2009). An improved model of induction motors for diagnosis purposes – slot skewing effect and air–gap eccentricity faults. *Energy Conversion Management*, vol. 50, no. 5, p. 1336-1347, DOI:10.1016/j.enconman.2009.01.003.

[23] Tavner, J.P., Ran, L., Sedding, H. (2008). *Review of Condition Monitoring of Rotating Electrical Machines*. The Institution of Engineering and Technology, London, DOI:10.1049/iet-epa:20070280.

[24] Jonasson, M., Wallmark, O. (2007). Stability of an electric vehicle with permanent-magnet in-wheel motors during electrical faults. *World Electric Vehicle Association Journal*, vol. 1, no. 4, p. 100-107.

[25] Muenchof, M., Beck, M., Isermann, R. (2009). Fault -tolerant actuators and drives-structures, fault detection principles and applications. A*nnual Reviews in Control*, vol. 33, no. 2, p. 136-148, DOI:10.1016/j.arcontrol.2009.08.002.

[26] Liu, X., He, H., Xiong, R., Qian, T. (2012). Study on the fault tolerance control strategy of the distributed driving electric vehicle running in straight line with failure motor(s). *2nd International Conference on Electronic & Mechanical Engineering and Information Technology*, p. 1627-1632.

[27] Anderson, M., Harty, D. (2010). Unsprung mass with in-wheel motors - myths and realities. *AVEC 2010*, p. 261-266.

[28] Purdy, D.J., Simner, D. (2004). A brief investigation into the effect on suspension motions of high unsprung mass. *Journal of Battlefield Technology*, vol. 7, no. 1, p. 15-20.

[29] Nagaya, G., Wakao, Y., Abe, A. (2003). Development of an in-wheel drive with advanced dynamic-damper mechanism. *JSAE Review*, vol. 24, no. 4, p. 477-481, DOI:10.1016/S0389-4304(03)00077-8.

[30] Perovic, D.K. (2012). Making the impossible, possible – overcoming the design challenges of in wheel motors. *EVS 26*, p. 48-58.

[31] Kasgen, J., Heim, R. (2013). *Product Development & Testing Requirements for Fraunhofer E-Concept Car - Frecc0*. Fraunhofer LBF, Darmstadt.

[32] Trček, T. (2013). *The Impact of the Increased Weight of the Wheel Assembly on the Vertical Dynamics of a Vehicle and on the Forces of the Wheel Bearing*. University of Ljubljana – Faculty of Mechanical Engineering, Ljubljana. (in Slovene)

[33] Vos, R. (2010). *Influence of In-Wheel Motors on the Ride Comfort Of Electric Vehicles*. Eindhoven University of Technology, Eindhoven.

[34] Wong, J.Y. (2001). *Theory of Ground Vehicle*. John Wiley & sons, New York.

[35] Siddiqui, O.M. (2002). *Dynamic Analysis of a Modern Urban Bus for Assessment of Ride Quality and Dynamic Wheel Loads*. Concordia University, Concordia.

[36] van Schalkwyk, D.J., Kamper, M.J. (2006). Effect of hub motor mass on stability and comfort of electric vehicles. *IEEE Vehicular Power Propulsion Conference*, vol. 4, no. 1, p. 1-6, DOI:10.1109/VPPC.2006.364297.

[37] Bruder, T. (2011). *An Insight into Fraunhofer System Research for Electromobility*. German - American Chambers of Commerce, p. 1-24.

[38] Luo, Y., Tan, D. (2012). Study on the dynamics of the in-wheel motor system. *IEEE Transactions on Vehicular Technology*, vol. 61, no. 8, p. 3510-3518, DOI:10.1109/TVT.2012.2207414.

[39] Belhocine, A., Bouchetara, M. (2013). Investigation of temperature and thermal stress in ventialted disc brake based on 3D thermomechanical coupling model. *Ain Shams Engineering Journal*, vol. 4, no. 1 p. 475-483, DOI:10.1016/j.asej.2012.08.005.

[40] Jayaprakash, G., Sivakumar, K., Thilak, M. (2011). Integration of thermo mechanical strains into optimal tolerance design of mechanical assembly using NSGA II and FE simulations. *Journal of Mechanical Engineering Research*, vol. 3, no. 6, p. 168-180.

[41] Kuria, J., Hwang, P. (2011). Optimizing heat sink geometry for electric vehicle BLDC motor using CFD. *Sustainable Research and Innovation Proceedings*, vol. 3, p. 122-146.

[42] Camilleri, R., Howey, D.A., McCulloch, M.D. (2012). Thermal limitations in air-cooled in-wheel motors for urban mobility

vehicles. *Electrical Systems for Aircraft, Railway and Ship Propulsion*, p. 48-60, DOI:10.1109/ESARS.2012.6387494.

[43] Bennion, K. (2011). *Electric Motor Thermal Management*. US Department of Energy, Washington, D.C.

[44] Yanhua, S., Chun, J. (2011). Thermal behavior of pm in-wheel motor used in off-road motor driven truck. *Procedia Engineering Conference*, vol. 23, p. 222-228, DOI:10.1016/j.proeng.2011.11.2493.

[45] Markovic, M., Muller, V., Hodder, A., Perriard, Y. (2010). Optimal design of an in-wheel BLDC motor for a kick scooter. *2010 IEEE Energy Conversion Congress and Exposition*, p. 292-296, DOI:10.1109/ECCE.2010.5618023.

[46] Cebon, D., Winkler, C. (1991). *A Study of Road Damage Due to Dynamic Wheel Loads Using a Load Measuring Material*. University of Cambridge, Department of Engineering, Cambridge.

[47] Gallagher, R.H. (1973). *Optimum Structural Design: Theory and Applications*. John Wiley & Sons, New York.

[48] Zienkiewicz, O.C., Campbell, J.S. (1973). *Shape Optimization and Sequential Linear Programming - Optimum Structural Design Theory and Applications*. John Wiley & Sons, New York.

[49] Kirsch, U. (1993). *Structural Optimization: Fundamentals and Applications*. Springer, Berlin, DOI:10.1007/978-3-642-84845-2.

[50] Gajewski, A., Zyczkowski, M. (1988). *Problems of Optimal Structural Design*. Springer Science+Business Media B.V., Dordrecht.

[51] Cakir, K., Sabanovic, A. (2006). In-wheel motor design for electric vehicles. *9th IEEE International Workshop on Advanced Motion Control*, p. 613-618, DOI:10.1109/AMC.2006.1631730.

[52] Triche, E.J.J., Beno, J.H., Tims, H.E., Worthington, M.T., Mock, J.R. (2005). Shock Loading experiments and requirements for electric wheel motors on military vehicles, *SAE World Congress & Exhibition*, DOI:10.4271/2005-01-0278.

[53] Gieras, J.F., Wang, C., Lai, J.C. (2006). *Noise of Polyphase Electric Motors*. Taylor & Francis Group, Columbus.

[54] Rubio, E., Jáuregui, J.C. (2012). Experimental characterization of mechanical vibrations and acoustical noise generated by defective automotive wheel hub bearings. *Procedia Engineering Conference*, vol. 35, p. 176-181, DOI:10.1016/j.proeng.2012.04.178.

[55] Lakshmikanth, S., Natraj, K.R., Rekha, K.R. (2012). Noise and vibration reduction in PMSMs. *International Journal of Electrical and Computer Engineering*, vol. 2, no. 3, p. 405-416.

[56] Lee, S., Hong, J., Member, S., Hwang, S., Lee, W., Lee, J., Kim, Y. (2006). Optimal design for noise reduction in interior permanent-magnet motor. *41st IAS Annual Meeting*, p. 1954-1960.

[57] Griffin, M.J. (2007). Discomfort from feeling vehicle vibration. *International Journal of Vehicle Mechanics and Mobility*, vol. 45, no. 7-8, p. 679-698, DOI:10.1080/00423110701422426.

[58] Hostettler, R. (2012). *Vehicle Parameter Estimation Using Road Surface Vibrations*. Lulea University of Technology, Lulea.

[59] Kelly, S. G. (2012). *Mechanical Vibration - Theroy and Applications*. Cengage Learning, Stamford.

[60] Česnik, M., Slavič, J. (2014). Vibrational fatigue and structural dynamics for harmonic and random loads. *Strojniški vestnik - Journal of. Mechanical Engineering*, vol. 60, no. 5, p. 339-348, DOI:10.5545/sv-jme.2014.1831.

[61] Gobbi, M., Mastinu, G. (1998). Expected fatigue damage of road vehicles due to road excitation. Vehicular. *System Dynamics: International Journal of Vehicular Mechanical Mobility*, vol. 29, suppl. 1, p. 778-788, DOI:10.1080/00423119808969608.

[62] SAE J 2562 (2005). *Biaxial Wheel Fatigue Test*. Society of Automotive Engineers International, Warrendale.

[63] Fatemi, A., Vangt, L. (1998). Cumulative fatigue damage and life prediction theories: a survey of the state of the art for homogeneous materials. *International Journal of Fatigue*, vol. 20, no. 1, p. 9-34, DOI:10.1016/S0142-1123(97)00081-9.

[64] Sonsino, C. (2007). Fatigue testing under variable amplitude loading. *International Journal of Fatigue*, vol. 29, no. 6, p. 1080-1089, DOI:10.1016/j.ijfatigue.2006.10.011.

[65] Abbaszadeh, K., Rezaee Alam, F., Saied, S.A. (2011). Cogging torque optimization in surface-mounted permanent-magnet motors by using design of experiment. *Energy Conversation Management*, vol. 52, no. 10, p. 3075-3082, DOI:10.1016/j.enconman.2011.04.009.

[66] Harris, T.A., Kotzalas, M.N. (2007). *Essential Concepts of Bearing Technology*. Taylor & Francis, Boca Raton.

[67] Heim, R., Zinke, R., Klock, J. (2006). *Experimental Testing of Wheel Bearings - Operating Load Simulation in the Biaxial Wheel / Hub Bench*, VDI-Verlag, Düsseldorf, p. 249-264. (in German)

[68] Biček, M., Gotovac, G., Miljavec, D., Zupan, S. (2013). Hub bearing loading and lifetime for in-wheel motors. *DVM Tag 2013: Sicherheit im Elektromobilitat,* p. 79-88. (in German)

[69] Weng, Z.Y., Fang, L.K., Huang, D.J., Lu, B. (2011). Study on life estimation of car hub bearing. *Applied Mechanics and Materials*, vol. 58-60, p. 319-325, DOI:10.4028/www.scientific.net/AMM.58-60.319.

[70] Seker, S. (2000). Determination of air-gap eccentricity in electric motors using coherence analysis. *IEEE Power Engineering Review*, vol. 20, no. 7, p. 48-50, DOI:10.1109/39.850436.

[71] Murotani. C. (2005). Bearing & seal technologies for electric vehicle eliica project. Koyo Engineering Journal English Edition, No. 168E, p. 35-38.

[72] Chaithongsuk, S. (2006). *Design and Construction of Permanent Magnet Synchronous Motor*. King Mongkut's Institute of Technology, Bangkok.

[73] ISO 2631-1:1997. (1997). *Mechanical Vibration and Shock – Evaluation of Human Exposure to Whole-Body Vibration - Part 1: General requirements*. International Organization for Standardization, Geneva.

[74] Johansson, A., Nilsson, L. (2006). *Evaluation of Discomfort Using Real-Time Measurements of Whole Body Vibration and Seat Pressure Distribution While Driving Trucks*. Lulea University of Technology, Lulea.

[75] Krishnasamy, P., Jayaraj, J., Dennie. J. (2013). Experimental investigation on road vehicle active suspension. *Strojniški vestnik - Journal of Mechanical Engineering*, vol. 59, no. 10, p. 620-625, DOI:10.5545/sv-jme.2012.925.

[76] Fraunhofer Institute for manufacturing Technology and Advanced Materials IFAM (2012). *Fraunhofer IFAM - Annual Report 2011/2012*. Fraunhofer IFAM, Bremen.

[77] Rezig, A., Mekideche, M.R., Djerdir, A. (2010). Effect of rotor eccentricity faults on noise generation in PMSM. *Progress in Electromagnetics Research C*, vol. 15, p. 117-132, **DOI:10.2528/PIERC10071001**.

[78] Nasser, M.A. (2004). Modal based predictive design and analysis of electric motors. *IMAC-XXII Conference & Exposition on Structural Dynamics*, p. 142-166.

[79] ISO 281:2007(E). *Bearing Life Standard*. International Organization for Standardization. Geneva.

[80] Inman, D.J. (2006). *Vibration with Control*. John Wiley & Sons, New York, **DOI:10.1002/0470010533**.

[81] Palmer, B., Lee, Y.L., Polehna, D. (2009). Fatigue damage spectrum calculation based on vibration specifications, *International Auto Body Congress*, p. 1-33.

[82] Sakashita, Y. (2002). Noise and vibration analysis technology of electric motors. *JMAG Users Conference*, p. 34-56.

[83] Choi, K.K., Kim, N.-H. (2005). *Structural Sensitivity Analysis and Optimization 1: Linear Systems*. Springer, New York.

[84] Choi, K.K., Kim, N.-H. (2006). *Structural Sensitivity Analysis and Optimization 2: Nonlinear Systems and Applications*. Springer, New York.

[85] Yin, D. (2010). Method research of establishing load spectrum on durability test of the car hub bearing. *International Conference of Mechanical Automation and Control Engineering*, vol. 2, no. 1, p. 3132-3136.

[86] Weissner, G. (2013). Wheel hub drive: system testing on test rig in vehicle. *DVM Tag 2013: Sicherheit im Elektromobilitat*, p. 69-77. (in German)

[87] Bhowmik, P.S., Pradhan, S., Prakash, M. (2013). Fault diagnostics and monitoring methods of induction motors. *International Journal of Applied Control, Electrical and Electronics Engineering*, vol. 1, no. 1, p. 1-18.

[88] Ergin, S., Uzuntas, A., Gulmezoglu, M.B. (2012). Detection of stator, bearing and rotor faults in induction motors. *Procedia Engineering*, vol. 30, p. 1103-1109, **DOI:10.1016/j.proeng.2012.01.969**.

[89] Heyes, A.M. (1998). Automotive component failures. Engineering Failure Analysis, vol. 5, no. 2, p. 129-144, **DOI:10.1016/S1350-6307(98)00010-7**.

List of reviewers in 2014

Bojan Ačko, Slovenia

Ahmad Al Hanbali,
   The Netherlands

Angelo Algieri, Italy

Luis F. Almeida, Brazil

Abdullah Altin, Turkey

Cláudio Alves, Portugal

Miha Ambrož, Slovenia

S. Aravindan, India

Yuriy Aristov, Russian Federation

Ciril Arkar, Slovenia

Gianmario Arnulfi, Italy

Kamil Arslan, Turkey

Viktor P. Astakhov, USA

Evelyne Aubry, France

Erin Elizabeth Bachynski,
   Norway

Jeffrey Allen Badger, USA

Ivan Bajsić, Slovenia

Jani Barle, Slovenia

Cemal Baykara, Turkey

Mostefa Bendouba, Algeria

Josep M. Bergada, Spain

Anton Bergant, Slovenia

Tomaž Berlec, Slovenia

Andre Boehman, USA

Miha Boltežar, Slovenia

David Bombač, Slovenia

Éd Claudio Bordinassi, Brazil

Przemyslaw Borkowski, Poland

Drago Bračun, Slovenia

Boštjan Brank, Slovenia

Charles-Henri Bruneau, France

Hrvoje Cajner, Croatia

Erasmo Carrera, Italy

Paolo Casoli, Italy

Ramón Barber Castaño, Spain

Marco Ceccarelli, Italy

K. Chandrashekhara, USA

Yikai Chen, China

Mario Costa, Portugal

Pieter Coulier, Belgium

Dario Croccolo, Italy

Robert Čep, Czech Republic

Gregor Čepon, Slovenia

Martin Česnik, Slovenia

Mirko Čudina, Slovenia

Franci Čuš, Slovenia

Joanna Daaboul, France

Jos Darling, UK

J. Paulo Davim, Portugal

Victor Juliano De Negri, Brazil

Marta Cristina Cardoso de
   Oliveira, Morocco

Mihael Debevec, Slovenia

Antonio Del Prete, Italy

Guilherme DeSouza, USA

Ferdinand Deželak, Slovenia

Francesca Di Puccio, Italy

Janez Diaci, Slovenia

Burak Dikici, Turkey

Anselmo Eduardo Diniz, Brazil

Janez Dolenšek, Slovenia

Željko Domazet, Croatia

Rosario Domingo, Spain

Božin Donevski, FYROM

Giorgio Donzella, Italy

Matevž Dular, Slovenia

Andreas Echtermeyer, Norway

Manar Abd Elhakim Eltantawie,
   Egypt

Igor Emri, Slovenia

Ahmet Erklig, Turkey

Hakan Ersoy, Turkey

Gorazd Fajdiga, Slovenia

Darinka Fakin, Slovenia

Mingjing Fang, China

Imre Felde, Hungary

Cuneyt Fetvaci, Turkey

Tomasz Figlus, Poland

Bogdan Filipič, Slovenia

Miha Finžgar, Slovenia

Rastko Fišer, Slovenia

Livan Fratini, Italy

Alessandro Freddi, Italy

Matjaz Gams, Slovenia

Andrés Gabriel García, Argentina

Alessandro Gasparetto, Italy

Rok Gašperšič, Slovenia

Marina Gergesova, Slovenia

Jacek F. Gieras, Poland

Hiwa Golpira, Iran

Darko Goričanec, Slovenia

Aleš Gosar, Slovenia

Karl Gotlih, Slovenia

Kursad Gov, Turkey

John R. Grace, Canada

Janez Grum, Slovenia

Junjie Gu, Canada

Leo Gusel, Slovenia

Jiří Hájek, Czech Republic

Niels Hansen, Denmark

Boštjan Harl, Slovenia

Mario Hirz, Austria

Marko Hočevar, Slovenia
Imre Horvath, The Netherlands
Aleš Hribernik, Slovenia
Matjaz Hribersek, Slovenia
Soichi Ibaraki, Japan
Clara Mihaela Ionescu, Belgium
Juan Carlos Jauregui, Mexico
Boris Jerman, Slovenia
Matija Jezeršek, Slovenia
Libin Jia, USA
Xin Jin, China
Dragica Jošt, Slovenia
Đani Juričić, Slovenia
Marek Kacmar, Slovakia
Roman Kamnik, Slovenia
Uroš Karadžić, Montenegro
Tomaž Katrašnik, Slovenia
John Kechagias, Greece
Tomaž Kek, Slovenia
Fouad Khaldi, Algeria
Kadir Kiran, Turkey
Simon Klančnik, Slovenia
Jernej Klemenc, Slovenia
Milan Kljajin, Croatia
Damjan Klobčar, Slovenia
Fritz Klocke, Germany
David Koblar, Slovenia
Pino Koc, Slovenia
Davorin Kofjač, Slovenia
Janez Kogovšek, Slovenia
Filip Kokalj, Slovenia
Janez Kopač, Slovenia
Kari Koskinen, Finland
Martin Kovač, Slovenia
Peter Krajnik, Slovenia
Davorin Kramar, Slovenia
Alicja Krella, Poland
Gorazd Krese, Slovenia
Boris Kržan, Slovenia
Jeetender Singh Kushawaha,
    India
Janez Kušar, Slovenia
Karl Kuzman, Slovenia

Hamid Lankarani, USA
Jay Lee, USA
Hirpa G. Lemu, Norway
Zsófia Lendek, Romania
S. V. Levyakov,
    Russian Federation
Zili Li, The Netherlands
Božidar Liščić, Croatia
Xiang Liu, USA
Gorazd Lojen, Slovenia
Andrew Peter Longstaff, UK
Michael R. Lovell, USA
Darko Lovrec, Slovenia
Željan Lozina, Croatia
Thomas Lübben, Germany
Balázs Magyar, Germany
Franc Majdič, Slovenia
Julio César Gómez Mancilla,
    Mexico
Tamás Mankovits, Hungary
Milan Marčič, Slovenia
Anton Mavretič, USA
Sašo Medved, Slovenia
Giovanni Meneghetti, Italy
Florian Menter, Germany
Gyula Mešter, Hungary
Masaaki Mochimaru, Japan
Paulo José Modenesi, Brazil
Nikolaj Mole, Slovenia
Swarnajay Mukherjee, USA
Domenico Mundo, Italy
Hubertus Josef Murrenhoff,
    Germany
Marko Nagode, Slovenia
Janusz Narkiewicz, Poland
Kanthavelkumaran Natesan, India
George K. Nikas, UK
Saša S. Nikolić, Serbia
Anatolij Nikonov, Slovenia
Antti Nurmikolu, Finland
Ivan Okorn, Slovenia
Mireia Olave, Spain
Simon Oman, Slovenia

Aljaž Osterman, Slovenia
Giovanni Battista Palmerini, Italy
Detlef Pape, Switzerland
Larry D. Peel, USA
Stanislav Pehan, Slovenia
Ettore Pennestri, Italy
Tomaž Pepelnjak, Slovenia
Matjaž Perpar, Slovenia
Miha Pevec, Slovenia
Damian Pietrusiak, Poland
Miroslav Plančak, Serbia
Bojan Podgornik, Slovenia
Pavel Polach, Czech Republic
Milton Luiz Polli, Brazil
Vladimir Popović, Serbia
Primož Potočnik, Slovenia
Iztok Potrč, Slovenia
Ivan Prebil, Slovenia
Radu-Emil Precup, Romania
Andrej Predin, Slovenia
Franci Pušavec, Slovenia
Rudolf Pušenjak, Slovenia
José Ragot, France
Homer Rahnejat, UK
Matjaž Ramšak, Slovenia
Sudheer D. Rani, USA
Dag Raudberget, Sweden
Zlatko Rek, Slovenia
Roger R. Riehl, Brazil
Mihailo Ristić, UK
Robert Christopher Roberts,
    China
Samuel Rodman Oprešnik,
    Slovenia
Liane Roldo, Brazil
Yiming Kevin Rong, USA
Valery Rudnev, USA
Izidor Sabotin, Slovenia
Mohammad Reza Safaei,
    Malaysia
Tadeusz Salacinski, Poland
Yahya Ahmad Saleh, Palestinian
    Territory

Tonio Sant, Malta

Rafael M. Santos, Belgium

Tomislav Saric, Croatia

Bernd Sauer, Germany

Rudolph J. Scavuzzo, USA

Tony L. Schmitz, USA

Stephan Schuschnigg, Austria

Marko Sedlaček, Slovenia

Andrej Senegačnik, Slovenia

Terry Sheppard, UK

Silvio Simani, Italy

Rok Simič, Slovenia

Wolfgang Sinz, Austria

Anže Sitar, Slovenia

Gunilla Sivard, Sweden

Janko Slavič, Slovenia

Shengli Song, China

Marco Sortino, Italy

Roman Staniek, Poland

Tino Stanković, Switzerland

Uroš Stritih, Slovenia

Ian A. Stroud, Switzerland

Rashed A. Abdelsalam Sultan, Egypt

Domen Šeruga, Slovenia

Marko Šimic, Slovenia

Brane Širok, Slovenia

Željko Šitum, Croatia

Leopold Škerget, Slovenia

Radislav Šmíd, Czech Republic

Boris Štok, Slovenia

Roman Šturm, Slovenia

Mohd Nasir Tamin, Malaysia

Jože Tavčar, Slovenia

Erman Tekkaya, Germany

Iztok Tiselj, Slovenia

Zdenko Tonković, Croatia

Eloisa Torres-Jimenez, Spain

Gabrielle J.M. Tuijthof, The Netherlands

Miran Ulbin, Slovenia

Nicolae Ungureanu, Romania

Erdem Uzunsoy, Turkey

Joško Valentinčič, Slovenia

Jožef Vižintin, Slovenia

Arkady Voloshin, USA

Rok Vrabič, Slovenia

Jasper A. Vrugt, USA

Natasa Vujica Herzog, Slovenia

Nikola Vukašinović, Slovenia

Željko Vukelič, Slovenia

Chao Wang, USA

Gerhard-Wilhelm Weber, Turkey

Ursula Weidig, Germany

Walter Lindolfo Weingaertner, Brazil

Jerzy Adam Winczek, Poland

Xi Wu, USA

Xinping Yan, China

Murat Yazici, Turkey

Rong-Hua Yeh, Taiwan

Jiangang Yi, China

Andrzej Zbrowski, Poland

Iman Zohourkari, Iran

Dejan Zupan, Slovenia

Franc Zupanič, Slovenia

Vesna Žegarac Leskovar, Slovenia

Janez Žerovnik, Slovenia

Leon Žlajpah, Slovenia

Uroš Župerl, Slovenia

Vsebina

Strojniški vestnik - Journal of Mechanical Engineering

Uvodnik

Zahvala članom Mednarodnega Uredniškega odbora

Glavni in odgovorni urednik *Strojniškega vestnika – Journal of Mechanical Engineering* se zahvaljuje članom mednarodnega Uredniškega odbora, ki v letu 2014 zaključujejo večletno članstvo v mednarodnem Uredniškem odboru, za cenjeno delo pri recenzijskem procesu. Vaše recenzije člankov predstavljajo pomemben temelj za dvig kakovosti revije. Obenem so avtorji pridobili pomembne povratne informacije ter na podlagi recenzijskih komentarjev izboljšali svoja dela. Cenimo vaš čas in napor pri soustvarjanju revije:

Koshi Adachi, Tohoku univerza,Visoka šola za inženirstvo, Japonska
Bikramjit Basu, Indijski inštitut za tehnologijo, Indija
Narendra B. Dahotre, Univerza v Tennesseeju, ZDA
Matija Fajdiga, Univerza v Ljubljani, Fakulteta za strojništvo, Slovenija
Jože Flašker, Univerza v Mariboru, Fakulteta za strojništvo, Slovenija
Bernard Franković, Fakulteta za inženirstvo, Hrvaška
Janez Kopač, Univerza v Ljubljani, Fakulteta za strojništvo, Slovenija
Franc Kosel, Univerza v Ljubljani, Fakulteta za strojništvo, Slovenija
Brian Prasad, Inštitut za tehnologijo v Kaliforniji, ZDA
Brane Širok, Univerza v Ljubljani, Fakulteta za strojništvo, Slovenija
Leopold Škerget, Univerza v Mariboru, Fakulteta za strojništvo, Slovenija
George E. Totten, Portland zvezna univerza, ZDA
Nikos C. Tsourveloudis, Tehnična univerza na Kreti, Grčija
Toma Udiljak, Univerza v Zagrebu, Hrvaška

Urednik prav tako že pozdravlja nove člane mednarodnega Uredniškega odbora *Strojniškega vestnik – Journal of Mechanical Engineering*, ki so v preteklih letih kakovostno prispevali k recenzijskemu procesu:

Kamil Arslan, Univerza v Karabuku, Turčija
Josep M. Bergada, Politehnična univerza v Kataloniji, Španija
Miha Boltežar, Univerza v Ljubljani, Fakulteta za strojništvo, Slovenija
Anselmo Eduardo Diniz, Državna univerza v Campinasu, Brazilija
Igor Emri, Univerza v Ljubljani, Fakulteta za strojništvo, Slovenija
Aleš Hribernik, Univerza v Mariboru, Fakulteta za strojništvo, Slovenija
Iyas Khader, Fraunhofer Inštitut za strojništvo, Nemčija
Jernej Klemenc, Univerza v Ljubljani, Fakulteta za strojništvo, Slovenija
Janez Kušar, Univerza v Ljubljani, Fakulteta za strojništvo, Slovenija
Gorazd Lojen, Univerza v Maribor, Fakulteta za strojništvo, Slovenija
George K. Nikas, KADMOS inženirstvo, Velika Britanija
José L. Ocaña, Tehnična univerza v Madridu, Španija
Vladimir Popovič, Univerza v Beogradu, Fakulteta za strojništvo, Srbija
Franci Pušavec, Univerza v Ljubljani, Fakulteta za strojništvo, Slovenija
Rudolph J. Scavuzzo, Univerza v Akronu, ZDA

Vincenc Butala,
glavni in odgovorni urednik

Uporaba termomehanske analogije za določitev zaostalega napetostnega stanja arterij

Janez Urevc[1,*] – Milan Brumen[2, 3] – Vojko Flis[4] – Boris Štok[1]

[1]Univerza v Ljubljani, Fakulteta za strojništvo, Slovenija
[2]Univerza v Mariboru, Medicinska fakulteta, Slovenija
[3]Institut "Jožef Stefan", Slovenija
[4]Univerzitetni klinični center Maribor, Oddelek za žilno kirurgijo, Slovenija

Določitev breznapetostnega stanja arterij predstavlja še vedno nerazrešen problem na področju numeričnega modeliranja mehanskega odziva realnih arterij. Breznapetostno stanje arterije, ki ima v splošnem obliko krožnega sektorja, je namreč eksperimentalno nemogoče določiti. Oblika breznapetostnega stanja (oziroma temu pripadajoče zaostalo napetostno stanje) pa je pomembno zato, ker predstavlja začetno stanje in tako ključen podatek sleherne numerične analize.

Arterije se za karakterizacijo njihovega mehanskega odziva običajno obravnava kot idealno krožne cevi, to pomeni idealno krožne in ravne. Takšna poenostavitev omogoča določitev zaostalih napetosti arterije brez poznavanja njihovega breznapetostnega stanja. Prisotnost zaostalih napetosti je posledica homogenizacije odziva arterij *in vivo*. Napetostno stanje arterije *in vivo* bi bilo namreč izrazito nehomogeno z velikim transmuralnim gradientom brez upoštevanja zaostalih napetosti. Zaradi njihove porazdelitve skozi debelino žilne stene se jih običajno asociira z upogibnimi napetostmi. Na notranji površini kolobarja so zaostale napetosti tlačne, medtem ko so na zunanji površini natezne.

Zaradi kompleksnosti problematike določitve mehanskega stanja realnih arterij na osnovi podatkov in vivo so v literaturi v splošnem privzete številne poenostavitve. Te se večinoma nanašajo na poenostavitev določitve breznapetostnega stanja arterij. Najbolj splošen pristop je, da je za začetno breznapetostno stanje upoštevana neobremenjena geometrija arterije, zaostale napetosti pa se zanemari.

V tem delu smo določili mehanski odziv prednapete, tlačno obremenjene hiperelastične cevi, ki predstavlja in vivo stanje arterije, brez poznavanja njene začetne breznapetostne oblike. To smo dosegli z vpeljavo termomehanskega pristopa, ki ga kot prvič predstavljamo v tem delu. Kot prikažemo v delu, lahko zaostalo napetostno stanje arterij (ki vsebuje upogibne in vzdolžne napetosti) določimo ekvivalentno s termičnim obremenjevanjem ustrezno definirane zaprte cevi, katere začetna breznapetostna oblika predstavlja obliko arterije v obremenjenem stanju. Na osnovi zaostalega napetostnega stanja arterij, pridobljenega s pomočjo termomehanskega modela arterije, pa nadalje lahko določimo stanje arterije in vivo. Ustreznost razvite metodologije smo prikazali z določitvijo breznapetostnega stanja arterije. Izračunano ravnotežno stanje arterije, ki je pridobljeno z vzdolžnim in prečnim rezom njenega zaostalega napetostnega stanja, zasede obliko odprte cevi, katere napetostno stanje predstavlja le majhen delež zaostalega napetostnega stanja. Ti rezultati kažejo, da imajo zaostale napetosti, ki smo jih določili s pomočjo pripadajočega termomehanskega modela, porazdelitev upogibnih napetosti, kar potrjuje ustreznost metodologije.

Mehanski odziv karotidne arterije je v tem delu obravnavan kot nelinearno-elastičen, izotropen in nestisljiv. Vpliv okoliškega tkiva arterije je zanemarjen, arterija pa je obravnavana kot enoplastna snov. Arterije so v splošnem sestavljene iz treh različnih plasti, intime, medije in adventicije, katerih mehanski odziv je v splošnem anizotropen. Upoštevanje teh lastnosti arterij v predstavljeni termomehanski metodologiji je ena izmed smernic za naše nadaljnje delo.

Ključne besede: biomehanika, zaostale napetosti, breznapetostno stanje arterij, metoda končnih elementov, termomehanika

---

Zaznavanje površinskih napak na optičnih napravah s pomočjo mikroskopije v temnem polju

Yingjie Yin – De Xu – Zhengtao Zhang* – Mingran Bai – Feng Zhang – Xian Tao – Xingang Wang

Kitajska akademija znanosti, Institut za avtomatizacijo, Raziskovalno središče za natančne meritve in krmiljenje, Kitajska

Optične naprave so pomemben del ojačevalnika moči in končnega optičnega sestava pri laserskih sistemih za inercijsko zadrževanje plazme (ICF). Točkovne in linijske napake na površini optičnih naprav močno vplivajo na učinkovitost laserskih sistemov za ICF in članek predstavlja predlog metode za zaznavanje površinskih napak na optičnih napravah. Na tej podlagi je bil tudi zasnovan in zgrajen sistem za zaznavanje napak na površini optičnih naprav.

Gibanje vrstične kamere po načrtovani poti je upravljano z visokonatančno motorizirano linearno in vertikalno mizico. Vrstična kamera zajame vrsto posnetkov, narejenih z mikroskopijo v temnem polju. Prekrivanje sosednjih posnetkov, narejenih z mikroskopijo v temnem polju, je mogoče opisati s posebno transformacijo. Podan je predlog algoritma za zlaganje posnetkov na osnovi SIFT, ki daje transformacijsko matriko prekrivanja dveh sosednjih posnetkov v temnem polju. S predlaganim algoritmom zlaganja posnetkov so bili izluščeni ujemajoči pari točk značilnosti SIFT na področjih zanimanja sosednjih posnetkov v temnem polju. Najboljša množica ujemajočih parov točk značilnosti SIFT je bila pridobljena z algoritmi vzporednih grozdov. Transformacijska matrika dveh posnetkov je bila izračunana s to množico parov točk z najboljšim ujemanjem in z matriko so bili nato sestavljeni sosednji posnetki v temnem polju. Svetlost slikovnih točk na mestu napak na posnetkih v temnem polju je bistveno večja od svetlosti ozadja, zato so bili s tehniko mejne segmentacije vzorčevanja segmentirani posnetki, združeni z algoritmom za sestavljanje posnetkov.

Napake na površini optičnih naprav se delijo na točkovne in linijske napake. Opisati jih je mogoče s šestimi glavnimi značilnostmi: površina napake, površina pravokotnika, ki obdaja napako, dolžina obrisa napake, razmerje med dolžino obrisa in površino napake, razmerje med površino napake in površino pravokotnika, ki obdaja napako, ter razmerje stranic pravokotnika, ki obdaja napako. Za učinkovito identifikacijo vrst napak so bili primerjani štirje kandidati za klasifikatorje: linearna diskriminantna funkcija (LDF), metoda podpornih vektorjev (SVM), metoda k najbližjih sosedov (KNN) in metoda radialne bazne funkcije (RBF).

Pri 15 sestavljenih slikah je bila največja absolutna napaka vodoravnega odmika prekrivanj sosednjih posnetkov v temnem polju 3 slikovne točke in največja absolutna napaka navpičnega odmika 2 slikovni točki; izhodiščna situacija je bila ugotovljena z ročno analizo. Natančnost klasifikatorja LDF je 92,7 %, klasifikatorja SVM 86,7 %, klasifikatorja KNN 86,0 % in omrežja RBF 81,0 %. Natančnost klasifikatorja LDF presega natančnost ostalih klasifikatorjev, zato je najprimernejši za razvrščanje napak, ki jih predstavlja šestrazsežnostni vektor značilnosti.

Članek predstavlja novo metodo zaznavanja napak na površini optičnih naprav. Transformacija med prekritji sosednjih posnetkov, narejenih z mikroskopijo v temnem polju, je posledica načina snemanja in gibanja vrstičnega fotoaparata. Predlagan je algoritem zlaganja slik na podlagi značilnosti SIFT za sestavljanje sosednjih posnetkov v temnem polju, ki jih zajame vrstična kamera. Za segmentacijo sestavljenih posnetkov v temnem polju z ozirom na njihove lastnosti je bila uporabljena tehnika mejne segmentacije vzorčevanja. Klasifikator LDF je najprimernejši za razvrščanje napak, ki jih predstavlja predlagani šestrazsežnostni vektor značilnosti.

Rezultati eksperimentov kažejo, da je predlagana metoda primerna za učinkovito zaznavanje napak na optičnih napravah.

Ključne besede: SIFT, LDF, algoritem grozdov, segmentacija posnetka, zlaganje posnetkov, snemanje v temnem polju, optične naprave

*Naslov avtorja za dopisovanje: Kitajska akademija znanosti, Institut za avtomatizacijo, Raziskovalno središče za natančne meritve in krmiljenje, 95 Zhongguancun East Road, Peking, Kitajska, zhengtao.zhang@ia.ac.cn

Konfiguriranje mini laboratorijskega in namiznega triosnega rezkalnega stroja s paralelno kinematiko

Sasa Zivanovic* – Milos Glavonjic – Dragan Milutinovic

Univerza v Beogradu, Fakulteta za strojništvo, Srbija

Konfiguriranje novih obdelovalnih strojev je zahtevna naloga, ki vključuje uporabo cele vrste konceptov, metod, modelov, virtualnih prototipov in simulacij. V članku je predstavljena metodologija za konfiguriranje novega obdelovalnega stroja do ravni virtualnega prototipa s pomočjo CAD konfiguratorja, vmesnika Pro/WEB.Link in pristopa »od zgoraj navzdol«. Članek opisuje uporabo CAD-konfiguratorjev s spletnim vmesnikom za izbiro komponent in sestavov mini laboratorijskega in namiznega triosnega rezkalnega stroja s paralelno kinematiko (RSPK) v okolju CAD/CAM. V raziskovalni študiji je bil uporabljen spletni konfigurator za izbiro standardnih komponent, iz katerih so bili nato sestavljeni CAD-modeli. Za družino posebnih komponent smo uporabili Pro/Web.Link kot programski spletni vmesnik za konfiguriranje posameznih komponent v CAD/CAM-sistemu Creo. Metodologija je preučena na primeru razvoja mini laboratorijskega in namiznega triosnega rezkalnega stroja s paralelno kinematiko (RSPK). Predlagani stroj je pripomoček za pridobivanje osnovnih izkušenj na področju RSPK. Pri pristopu od zgoraj navzdol se med konfiguriranjem uporabi model skeleta paralelnega mehanizma za opredelitev načrta za integracijo delov/podsestavov v končni sestav stroja.

Rezultat sta dve različici virtualnega prototipa in en fizični prototip. Konfigurirani virtualni prototipi se uporabljajo za verifikacijo sistema za programiranje v okolju CAD/CAM s simulacijo obdelave na osnovi generirane poti orodja, ki vključuje tudi simulacijo stroja. Simulacija obdelave je pomembna za: oblikovanje okolja za programiranje zunaj stroja, verifikacijo programov pred izvedbo, preprečevanje trkov paralelnega mehanizma med izvajanjem programa ter preverjanje položaja obdelovanca v delovnem prostoru paralelnega mehanizma. Simulacija obdelave z izvedbo programa je možna zahvaljujoč modelu paralelnega mehanizma, ki vključuje vse kinematične povezave med komponentami za gibanje virtualnega modela kot sistema togih teles. Omogoča gibanje modelov znotraj območja, ki je opredeljeno za vsako povezavo, in je še posebej pomembna za preprečevanje morebitnih trkov med delom paralelnega mehanizma.

Mini laboratorijski in namizni triosni RSPK je bil zgrajen in preskušen v našem laboratoriju. Gre za šolski sistem s kompleksno kinematiko in v sistem za krmiljenje in programiranje je vključen tudi virtualni stroj. Mini laboratorijski in namizni triosni RSPK je bil uspešno preizkušen z obdelavo dveh testnih obdelovancev. Eksperimenti so potrdili, da je možno zgraditi poceni mini laboratorijski in namizni triosni RSPK za obdelovance iz lahkih materialov in z enostavnejšimi tolerancami, ki ga bodo lahko neposredno uporabljali študentje, programerji in operaterji CNC-obdelovalnih strojev.

Razviti mini laboratorijski in namizni triosni RSPK je lahko poglobljen in dovršen didaktični pripomoček, ki obdeluje mehke materiale, se programira na običajen način in je varen tudi za uporabnike začetnike.

V prihodnje načrtujemo nadgradnjo krmilnega sistema stroja, ki ga bo mogoče uporabiti pri raziskavah in uporabi nove metode programiranja STEP-NC. Obstoječi paralelni mehanizem nameravamo nadgraditi z dvoosno serijsko glavo na platformi, tako da bo lahko stroj izvajal tudi petosne obdelave.

Ključne besede: CAD konfigurator, Pro/Web.Link, pristop od zgoraj navzdol, CAD/CAM, konfiguriranje, obdelovalni stroj, simulacija obdelave

---

*Naslov avtorja za dopisovanje: Univerza v Beogradu, Fakulteta za strojništvo, Kraljice Marije 16, 11120 Beograd 35, Srbija, szivanovic@mas.bg.ac.rs

Vpliv dinamičnega lokalnega samopredgrevanja sive litine pri laserskem navarjanju

Peng Yi* – Pengyun Xu – Changfeng Fan – Chengkai Li – Yongjun Shi

Kitajska univerza za nafto, Kolidž za strojništvo in elektrotehniko, Quingdao, Kitajska

Temperatura se med postopkom laserskega navarjanja nenehno povečuje in zmanjšuje, to pa povzroča velike toplotne napetosti in pride lahko do delaminacije ter do nastanka razpok v pretaljenem delu. Reševanju tega problema je bilo posvečeno že veliko pozornosti, med ukrepi pa je predvsem predgrevanje osnovnega materiala v peči ali z induktivno tuljavo. Problem takšnega pristopa je predvsem v zahtevnosti in nepriklandosti. Članek podaja strategijo dinamičnega lokalnega samopredgrevanja za zmanjšanje toplotnih napetosti in boljši nadzor nad mikrostrukturo. Opravljeni so bili eksperimenti in numerični preračuni za preučitev procesa dinamičnega lokalnega samopredgrevanja in različnih parametrov predgrevanja.

Opravljeni so bili eksperimenti laserskega navarjanja brez predgrevanja, s statičnim globalnim predgrevanjem in z dinamičnim lokalnim predgrevanjem. Preučena je bila mikrostruktura in mikrotrdota pri različnih strategijah predgrevanja. Vzporedno z eksperimentalnimi preiskavami so bili uveljavljeni numerični modeli za preučevanje temperaturne porazdelitve in toplotnih napetosti pri različnih procesih.

Članek obravnava postopek laserskega navarjanja sive litine. Za zmanjšanje toplotnih napetosti in izboljšanje kakovosti navarjanja je bil zasnovan pristop dinamičnega lokalnega predgrevanja. Opravljeni so bili eksperimenti laserskega navarjanja sive litine z nepredgretim osnovnim materialom, s statičnim globalnim predgrevanjem in z dinamičnim lokalnim predgrevanjem. Za dodajni material je bila uporabljena železova zlitina v prahu. Analiziran je tudi vpliv različnih parametrov obdelave na dinamično lokalno predgrevanje. Preučena je bila mikrostruktura v coni navarjanja ter v coni taljenja in preizkušena je bila porazdelitev trdote po prerezu navarjenega območja. Postavljeni so bili tudi numerični modeli v paketu ANSYS za simulacijo različnih strategij predgrevanja. Spremembe temperature, variabilnost toplotnih napetosti in preostale napetosti so bili analizirani s simulacijo.

Lasersko lokalno dinamično predgrevanje je v primerjavi z globalnim statičnim predgrevanjem in z induktivnim predgrevanjem fleksibilna in zanesljiva tehnologija za zmanjšanje toplotnih napetosti in upravljanje z mikrostrukturo. Dinamično lokalno predgrevanje dvigne začetno temperaturo osnovnega materiala pred navarjanjem. Temperaturni gradient, toplotne napetosti in preostale natezne napetosti med procesom laserskega navarjanja se zmanjšajo. Lasersko lokalno dinamično predgrevanje izboljša konvekcijo in širjenje raztaljene mase za učinkovit nadzor nad oblikovanjem trde faze in prispevek k enakomerni mikrostrukturi v coni navarjanja. Lokalno dinamično predgrevanje zmanjša stopnjo podhlajevanja in temperaturni gradient, s tem pa nastanejo groba stolpčasta zrna ter manj trda in krhka faza. Mikrotrdota vzorcev dinamičnega lokalnega predgrevanja je manjša kot pri nepredgretih vzorcih, vendar večja kot pri osnovnem materialu, zato je zagotovljena integralna trdota.

Članek obravnava eksperimentalno enosledno lasersko navarjanje z različnimi strategijami predgrevanja. Prihodnje raziskave bodo morale biti usmerjene v večsledne in večslojne postopke laserskega navarjanja z dinamičnim lokalnim predgrevanjem.

Objavljeni članki poročajo o postopkih laserskega navarjanja z različnimi metodami predgrevanja in različnimi materiali, pri večini pa gre za predgrevanje v peči ali za hibridno predgrevanje. Ti postopki predgrevanja pa zahtevajo dodatno opremo in delovni postopki so zahtevni. Dinamično lokalno predgrevanje, ki je predstavljeno v članku, je v primerjavi z omenjenimi postopki prilagodljivejše in bolj praktično. Obravnavan je tudi vpliv parametrov dinamičnega lokalnega predgrevanja, ki zaokrožujejo raziskavo laserskega lokalnega predgrevanja.

Ključne besede: lasersko navarjanje, siva litina, lokalno predgrevanje, numerični modeli, mikrostruktura

---

*Naslov avtorja za dopisovanje: Kitajska univerza za nafto, Kolidž za strojništvo in elektrotehniko, Quingdao, Changjiang West ul., Qingdao, Kitajska, yipupc@gmail.com

Analiza energijske učinkovitosti preizkuševališča za zračne vzmeti

Ivan Okorn* – Marko Nagode

Univerza v Ljubljani, Fakulteta za strojništvo, Slovenija

Namen raziskave je bil analizirati energijsko učinkovitost novega preizkuševališča za zračne vzmeti in jo primerjati z energijsko učinkovitostjo obstoječih preizkuševališč. Za dinamično preizkuševanje se uporabljajo namenska preizkuševališča, ki omogočajo spreminjanje geometrije vpetja vzmeti, ki odraža realno vpetje vzmeti na vozilu. Za obremenjevanje vzmeti je potrebno delo, ki ga vzmet v fazi razbremenjevanja delno vrne v pogonski sistem. Količina vrnjenega dela je odvisna od histereze vzmeti in izgub zaradi trenja med pogonom in vzmetjo. Preizkušanje je energijsko učinkovito, če se vsaj del vrnjenega dela koristno izrabi. To dejstvo je bilo upoštevano pri zasnovi novega preizkuševališča. Preizkuševališče je bilo izdelano in obratuje v laboratoriju proizvajalca zračnih vzmeti. Uporablja se za homologacijske preizkuse in za raziskovalno delo.

V prvem delu prispevka sta predstavljena način obremenjevanja vzmeti in izvedba pogona. Na novem preizkuševališču se preizkušajo štiri zračne vzmeti istočasno. Sestavljajo ga trije funkcijski sklopi in sicer mehanski del s pogonom, pnevmatski del in krmilnik. Za pogon preizkuševališča se uporablja trifazni asinhronski elektromotor, ki poganja gred, na kateri sta dva fazno zamaknjena ekscentra. Ekscentra obremenjujeta in razbremenjujeta vzmeti preko dveh vzvodov. Vse štiri vzmeti so obremenjene pod enakimi pogoji (enaka amplituda in frekvenca obremenitve), le obremenjevanje poteka s faznim zamikom. Med preizkusom se velik del dela, ki ga vzmet vrne pri razbremenjevanju, izkoristi za obremenjevanje sosednje vzmeti. Enakomernost pogona zagotavlja vztrajnik. Vztrajnostni moment vztrajnika je določen na podlagi presežkov in primankljajev dela glede na srednje delo za en cikel.

Za analizo energijskih razmer na preizkuševališču je bil izdelan računalniški program. Omogoča izračun dela za obremenjevanje vzmeti, moči in dela trenja za različne velikosti vzmeti in pogoje preizkušanja. V prispevku so izpeljani računski algoritmi in podani rezultati izračuna za obravnavano vzmet. V program se vnese geometrijske nastavitve preizkuševališča, karakteristiko vzmeti in frekvenco preizkušanja. Omogoča hitro oceno nevarnosti toplotne preobremenitve kritičnih elementov in izračun dejanskih izgub energije. Posebej je analizirano trenje na drsniku ekscentra in v vsah ležajih. Za izbrano vzmet so v diagramih prikazani poteki moči. Določena je potrebna moč za preizkušanje, ki za obravnavano vzmet znaša 3,8 kW. Upoštevane so delovne sil vzmeti, vztrajnostne sile, histereza vzmeti in torne izgube.

Rezultate teoretičnih analiz potrjujejo meritve tokov skozi navitje elektromotorja in vrtilnih frekvenc. Na zaslonu krmilnika spremljamo tlak zraka v vseh štirih vzmeteh, tok na elektromotorju, frekvenco preizkušanja in število obremenitvenih ciklov. Dokaz energijske učinkovitosti preizkuševališča je dejanski tok skozi navitje elektromotorja. Odvisen je od vrtilnega momenta, ki med preizkusom obremenjuje gred. Na podlagi merjenja dejanskega toka je bilo ugotovljeno, da za preizkušanje štirih obravnavanih vzmeti potrebujemo 4,4 kW (1,1 kW/vzmet). Vrednost moči na podlagi izmerjenega toka je za 0,6 kW večja od analitičnih vrednosti. To kaže, da so torne izgube nekoliko večje od predpostavljenih. Spreminjanje toka in frekvence preizkušanja je zanemarljivo (pod 1 %). S tem je dokazan učinek vztrajnika na enakomernost pogona. Potrebe po moči na novem preizkuševališču so bistveno manjše kot pri hidravličnem in obstoječem mehanskem preizkuševališču. Pri hidravličnem preizkuševališču je potrebna maksimalna moč za obremenjevanje ene vzmeti okoli 30 kW, na mehanskem preizkuševališču pa za preizkušanje dveh vzmeti okoli 5,5 kW (2,75 kW/vzmet).

Na novem preizkuševališču je mogoče opraviti v istem času štirikrat več preizkusov kot na hidravličnemi in dvakrat več preizkusov kot na obstoječem mehanskem preizkuševališču. Na obstoječih mehanskih preizkuševališčih je navečja frekvenca preizkušanja 2 Hz, pri novem pa 3,5 Hz. Do rezultatov raziskovalnega dela, na področju zdržljivosti zračnih vzmeti, je mogoče priti v krajšem času in z nižjimi stroški.

Ključne besede: preizkuševališče, zračna vzmet, energijska učinkovitost, vztrajnik, histereza vzmeti, torne izgube

---

Zaznavanje razpok na prenosnikih moči s pomočjo diskretne valčne transformacije in nevronske mreže s teorijo adaptivne resonance

Zhuang Li* – Zhiyong Ma – Yibing Liu – Wei Teng – Rui Jiang
Severnokitajska univerza za elektroenergetiko, Fakulteta za energetiko in strojništvo, Kitajska

Zgodnje zaznavanje napak na prenosnikih moči je pogoj za preprečitev usodnih okvar strojev, izgub v proizvodnji in telesnih poškodb. Proces prehoda prenosnika iz normalnega stanja v stanje napake poteka počasi. Zaradi omejitev, ki jih postavljata mehanska zgradba in delovno okolje, je težko meriti spremembe stanj pri oblikovanju razpoke zgolj na osnovi vizualne ocene značilnosti, izluščenih iz signala vibracij. Zato potekajo raziskave nove metode zaznavanja razpok, ki omogoča zgodnjo diagnostiko napak na prenosnikih.

Signali vibracij iz prenosnikov so nestacionarni in nelinearni, diskretna valčna transformacija (DWT) pa je učinkovito orodje za obdelavo takšnih nestacionarnih in nelinearnih signalov. V praksi pri zaznavanju napak na prenosnikih manjkajo primerki znanih napak, ki bi jih bilo mogoče uporabiti za učenje nadzorovane nevronske mreže. Nevronska mreža z adaptivno resonančno teorijo (ART) je metoda prepoznavanja vzorcev brez znanih primerkov za učenje. Članek združuje transformacijo DWT in nevronsko mrežo ART za zaznavanje razpok na prenosniku.

Za izločitev relativnih značilnosti energije valčkov iz vzorčne vrste signalov vibracij prenosnika je bila uporabljena transformacija DWT. Nato je bila uporabljena nevronska mreža ART za prepoznavanje in razvrščanje vrste primerkov. Primerki v istem stanju se pri nenadzorovanem razvrščanju dodelijo v isto kategorijo, primerki različnih stanj pa v različne kategorije. Nato se opredeli rezultat prepoznave in trend prehoda iz normalnega stanja v stanje z razpoko je mogoče prepoznati na podlagi klasifikacije primerkov. Učinkovitost nevronske mreže ART je bila preverjena v primerjavi s samoorganizirajočo kompetitivno nevronsko mrežo in s samoorganizirajočo karto.

Signal se lahko s transformacijo DWT razstavi na vrsto podpasov. Relativna energija valčkov, določena z diskretno valčno transformacijo, lahko učinkovito opredeli značilnosti napake. Primerjava z drugačno nenadzorovano nevronsko mrežo je potrdila, da je mogoče z nevronsko mrežo ART jasno prepoznati trend prehoda iz normalnega stanja v stanje napake (razpoke), z ustrezno določljivo vrednostjo praga za ugotovitev razpoke.

Članek podaja predlog metode zaznavanja razpok na osnovi transformacije DWT in nevronske mreže ART, katere zmožnosti so bile potrjene tudi na preizkuševališču. Testni pogoji pa se razlikujejo od realnih situacij, npr. pri prenosnikih v vetrnih turbinah, ki so zaradi turbulenc vetra podvrženi kompleksnim izmeničnim obremenitvam. Prihodnje študije bodo zato usmerjene v praktično uporabo predlagane metode ter v analizo njene učinkovitosti. Naša ekipa preučuje omenjene teme, ki bodo obravnavane v prihodnjih člankih.

Umetne nevronske mreže za prepoznavanje vzorcev, o katerih poročajo objavljeni članki, so predvsem nadzorovane nevronske mreže, ki se učijo na znanih primerkih. Pri realni diagnostiki napak pa ne razpolagamo z znanimi primerki za učenje. V članku je predstavljen pristop, kjer je na podlagi izločitve relativne energije valčkov s transformacijo DWT uporabljena nevronska mreža ART za razvrščanje in prepoznavanje vzorcev brez znanih primerkov za učenje. Pristop je novo orodje za nadzorovanje stanja prenosnikov moči in zgodnje diagnosticiranje napak.

Ključne besede: relativna energija valčkov, prepoznavanje vzorcev, prenosnik, zaznavanje napak, teorija adaptivne resonance, nevronska mreža

*Naslov avtorja za dopisovanje: Severnokitajska univerza za elektroenergetiko, Fakulteta za energetiko in strojništvo, Peking, Kitajska, 102206, lizhuang@ncepu.edu.cn

Mehanski vzroki za okvare kolesnih motorjev

Matej Biček[1,*] – Gorazd Gotovac[1] – Damijan Miljavec[2] – Samo Zupan[3]

[1] Elaphe Propulsion Technologies Slovenija
[2] Univerza v Ljubljani, Fakulteta za elektrotehniko, Slovenija
[3] Univerza v Ljubljani, Fakulteta za strojništvo, Slovenija

Izzivi sodobnih električnih vozil so tehnološko osveščeni javnosti že v precejšni meri znani. Skalabilnost tehnologije je možna ob predpostavki, da je poskrbljeno za nizko cenovni energijski vir in s tem povezano infrastrukturo, ki končnemu odjemalcu omogoča nemoteno uporabo ob enakih ali nižjih stroških kot z obstoječimi vozili z motorji na notranje izgorevanje. Iniciativa Evropske Unije je v zadnjih letih usmerjena v povečanje deleža električnih vozil, ki znižujejo stopnjo emisij CO_2. in zmanjšujejo akustične emisije, ki posebej za večja mesta predstavljajo že aktualne probleme pri kakovosti življenja. Vzporedno z razvojem energijskih virov se vedno več podjetij in akademskih ustanov ukvarja z razvojem pogonskih arhitektur, ki bi izboljšale obstoječe energijske in prostorske izkoristke ob hkratnem zmanjševanju proizvodnih in vzdrževalnih stroškov.

Pogon na mestu kjer je ta potreben, z bistveno manjšim številom sestavnih komponent in neposrednim pogonom, omogočajo kolesni elektromotorji, ki v zadnjih letih pridobivajo priznavanje strokovne javnosti, s tem pa tudi narašča število objavljenih strokovnih prispevkov na temo razvoja konstrukcije kolesnih elektromotorjev. Ti večinoma omenjajo posamezne inkrementalne izboljšave konstrukcije elektromagnetno aktivnih sklopov motorja, medtem ko se optimizacija mehanske konstrukcije v strokovnih krogih zapostavlja, oz. ne prihaja do objav razvoja in raziskav na tem področju. Z namenom izdelave kompleksnega modela za optimizacijo mehanske konstrukcije je v prvem koraku potrebno popisati vse znane vzroke za potencialne mehanske okvare kolesnih elektromotorjev, jih znanstveno okarakterizirati in kasneje v skladu z omenjenim modelom optimirati.

Pričujoča študija vključuje celovit pregled mehanskih vzrokov za potencialne okvare kolesnih elektromotorjev, namenjenih za neposredni pogon vozil. Pri tem so bili strokovni prispevki, ki govorijo o posameznem mehanskem vzroku za okvaro, primerjani s sorodno literaturo in njenimi izsledki. V splošnem laična javnost povezuje kolesne elektromotorje s slabšo vozno dinamiko zaradi povečane mere nevzmetene mase in nezmožnost tesnjenja motorja z zunanjim rotorjem zaradi razmeroma velikega premera in hkrati želenega nizkega zavornega navora. Poleg omenjenih mehanskih vzrokov za okvare so v prispevku analizirani tudi vplivi ekscentričnosti, povečanih vibracij in odpovedi ležaja.

Znanstveni doprinos dela je pregled in primerjava dosegljive literature iz omenjenega področja, praktični pa povezava omenjenih mehanskih vzrokov za okvare s statističnimi podatki glede okvar iz podobnih aplikacij in končna tabela, kjer so vse potencialne okvare definirane in okarakterizirane z vrednostjo stopnje resnosti, odkrivanja in ponovitve. S tem je opravljen prvi potreben korak za vso nadaljnjo optimizacijo kritičnih delov mehanske konstrukcije. V skladu z definiranimi stopnjami so bile za posamezno okvaro izračunane skupne ocene tveganosti za delovanje celotnega pogonskega sklopa, ki predstavlja edinstven vpogled na problematiko in hkrati objektivno oceno najbolj kritičnega mehanskega vzroka za okvare, ter hkratne ovržbe manj tveganih dejavnikov.

Pri pregledu obstoječe literature so izsledki različnih neodvisnih raziskav pokazali slabše vozne lastnosti pri povečani nevzmeteni masi za neopazne. Izzivi s tesnjenjem motorjev so glede na literaturo za dotično aplikacijo rešeni do stopnje IP68 in tako v nasprotju z laičnim prepričanjem ne dosegajo visoke stopnje tveganja oz. potencialne okvare sklopa motorja. Najvišjo stopnjo tveganja, glede na obstoječo literaturo, predstavljajo vibracije in s tem povezane akustične emisije, ter ekscentričnost elementov motorja, ki pri stohastičnih obremenitvah lahko prispevajo k zmanjšanim zmogljivostim motorja, saj imajo neposreden vpliv na deformacijo zračne reže med permanentnimi magneti na rotorju in statorskim navitjem, oz. na gostoto elektromagnetnega polja in s tem povezanim generiranim navorom.

Ključne besede: kolesni elektromotor, analiza potencialnih okvar in njihovih učinkov, povečana nevzmetena masa, povečane vibracije, ekscentričnost, odpoved ležaja

*Naslov avtorja za dopisovanje: Elaphe Propulsion Technologies, Ltd., Teslova 30, SI-1000 Ljubljana, Slovenija, matej@elaphe-ev.com

Doktorske disertacije, diplomske naloge

DOKTORSKE DISERTACIJE

Na Fakulteti za strojništvo Univerze v Ljubljani so obranili svojo doktorsko disertacijo:

● dne *1. decembra 2014* **Joamin GONZALEZ GUTIERREZ** z naslovom: »Časovno odvisne lastnosti polimerno-kovinskih kompozitov za uporabo v tehnologiji brizganja (Time-dependent Characteristics of Polymer-Metal Composites for the Use in Injection Moulding Technology)« (mentor: akad. prof. dr. Igor Emri);

Injekcijsko brizganje prahu (PIM) je vsestranska tehnika za proizvodnjo kovinskih ali keramičnih izdelkov kompleksnih oblik. PIM postopek sestavljajo štirje glavni koraki, pri čemer je odstranjevanje veziva najbolj zamuden korak. V prizadevanjih po skrajšanju časa, potrebnega za odstranjevanje veziva, je bila v surovino vpeljana uporaba polioksimetilena. Poglaviten problem surovine na osnovi POM veziva je njihova visoka viskoznost, ki lahko predstavlja probleme pri injekcijskem brizganju majhnih kosov, kompleksnih geometrij.

V sklopu dizertacije sta bili preizkušeni dve strategiji za zmanjšanje viskoznosti surovine na osnovi POM veziva. Prva strategija temelji na izboru prave porazdelitve molekularne teže polimernega veziva, medtem ko druga sloni na izboru pravilne porazdelitve velikosti delcev prahu. Z uporabo obeh strategij je bila razvita nova surovina, ki izkazuje sedem kratno zmanjšanje viskoznosti in 2 % povečanje masnega deleža prahu v primerjavi s komercialno dostopno surovino na osnovi POM veziva;

● dne *5. decembra 2014* **Benjamin BIZJAN** z naslovom: »Razvlaknjenje mineralne volne na vrtečih kolesih centrifuge« (mentor: prof. dr. Branko Širok, somentor: doc.dr. Alen Orbanić);

Doktorsko delo obravnava proces nastanka vlaken mineralne volne iz taline, natekajoče na kolo centrifuge. Zaradi omejenih možnosti opazovanja realnega procesa je razvlaknjenje modelirano na enokolesni centrifugi z natokom hladnih Newtonskih kapljevin. Kot merilna metoda se uporablja vizualizacija procesa s hitro kamero v različnih obratovalnih točkah, dobljenih s spreminjanjem vrtilne hitrosti kolesa ter volumskega toka in fizikalnih lastnosti kapljevin. Kot rezultat analize fotografij procesa so ugotovljeni značilni obratovalni režimi centrifug in oblikovani regresijski modeli za karakteristične integralne parametre razvlaknjenja, kot so število, dolžina in premer ligamentov ter spremljajočih tokovnih struktur. Predmet študije je tudi kinematika rasti ligamentov v povezavi s hidrodinamsko stabilnostjo razvlaknjenja. Na podlagi rezultatov kvalitativne in kvantitativne analize procesa je izvedena primerjava obratovalnih karakteristik z ostalimi izvedbami rotacijskih naprav za razvlaknjenje in z znanimi teoretičnimi modeli relevantnih hidrodinamskih pojavov. V povezavi z neželenima pojavoma abrazije površine kolesa industrijske centrifuge in nastanka nerazvlaknjenega materiala sta kot možna mehanizma preučena hitrostni zdrs filma kapljevine po kolesu oziroma trganje vodilnih kapljic z ligamentov;

● dne *17. decembra 2014* **Tilen THALER** z naslovom: »Karakterizacija procesa odrezavanja na horizontalni dvosteberni tračni žagi« (mentor: prof. dr. Edvard Govekar, somentor: prof. dr. Janez Kopač);

V doktorskem delu obravnavamo proces odrezovanja na dvosteberni horizontalni tračni žagi. Pri tem smo se osredotočili na karakterizacijo in zaznavanje nastopa drdranja ter obrabe orodja. Proces odrezovanja smo okarakterizirali na osnovi statistične, spektralne in rekurenčne analize izmerjenih signalov rezalnih sil, vibracij stroja ter zvočnega tlaka. Izbrani statistični momenti ter karakteristike frekvenčne in rekurenčne analize v povprečju z več kot 95 % uspešnostjo zaznavajo prisotnost drdranja pri odrezovanju s tračno žago. Pri tem so najinformativnejše značilke signalov pospeškov in zvočnega tlaka. Na osnovi analize stabilnosti odrezovalnega procesa smo izdelali stabilnostne diagrame tračnega žaganja v prostoru procesnih parametrov razdalje med podporama orodja ter rezalne in podajalne hitrosti. Zaznali smo nelinearno in nemonotono odvisnost drdranja od rezalne hitrosti ter histerezo drdranja. Nelinearnost in nemonotonost stabilnostnega diagrama omogočata izogib drdranja s spreminjanjem rezalne hitrosti, kar smo pokazali z dodatnim nizom preizkusov za izogib drdranja. V okviru obravnave obrabe orodja smo pokazali, da ima geometrija orodja lahko velik vpliv na rezalne sile, predvsem najvišje vrednosti, ki lahko od povprečja rezalnih sil odstopajo tudi preko 90 %. Slednje se odraža na izraziti lokalni obrabi orodja;

● dne *22. decembra 2014* **Jure JERINA** z naslovom: »Tribološke lastnosti trdih prevlek pri povišanih temperaturah« (mentor: prof. dr. Mitjan Kalin, somentor: izr.prof.dr. Bojan Podgornik);

Doktorska naloga obravnava inženiring kontaktnih površin primernih za preoblikovanje aluminija in njegovih zlitin v temperaturnem območju med 20 in 500 °C. Uporabili smo dve trdi prevleki

CrN in TiAlN ter konvencionalno orodno jeklo za delo v vročem in ovrednotili njihove tribološke lastnosti v drsnem kontaktu z aluminijevo zlitino EN AW-6060. V ta namen razvitem tribološkem preizkuševališču in ob uporabi naprednih površinskih analiznih tehnik smo dokazali, da je z uporabo trdih prevlek mogoče znižati trenje, kot tudi povečati odpornost površin na nastanek prenosnega filma aluminijeve zlitine. Raziskali in določili smo mehanizme prenosa aluminijeve zlitine na raziskovanih površinah v odvisnosti od temperature in drsne razdalje, ter preverili učinek trdnih maziv na tribološki kontakt prevlek in aluminijeve zlitine;

● dne *22. decembra 2014* **Drago KOVAČIČ** z naslovom: »Neposredna laserska izdelava tiskanih vezij visoke gostote« (mentor: prof. dr. Janez Možina);

Cilj doktorske naloge je razvoj metode neposredne laserske izdelave mikroelektronskih tiskanih vezij visoke gostote, ki omogoča izdelavo mikroelektronskega tiskanega vezja visoke gostote v celoti z enim samim postopkom. Osnovo metode predstavlja postopek selektivnega laserskega strukturiranja prevodniškega sloja, s katerim se izdela kontura vezja ter večje površine prevodniškega sloja razdeli na manjše segmente. Slednji se v nato s pomočjo snopa laserske svetlobe ter usmerjenega pretoka medija v celoti odstranijo brez poškodbe nosilnega substrata. Parametri laserskega procesa, kot so moč in hitrost gibanja snopa laserske svetlobe, frekvenca proženja ter stopnja prekrivanja bliskov, trajanje bliskov laserske svetlobe ter energija, dimenzija snopa laserske svetlobe v gorišču, so medsebojno povezani in imajo direkten vpliv na hitrost in kakovost procesa, saj določajo dimenzije strukturiranega izolacijskega kanala, intenzivnost termične obremenitve materiala ter velikost toplotno obremenjenega področja. Postopek izdelave mikroelektronskih tiskanih vezij visoke gostote z uporabo nove metode je zaradi enostavnosti postopka ter izredne fleksibilnosti primeren za razvoj in izdelavo prototipov ter manjših serij mikroelektronskih tiskanih vezij večini laminatnih materialov.

*

Na Fakulteti za strojništvo Univerze v Mariboru je obranil svojo doktorsko disertacijo:

● dne *1. decembra 2014* **Boštjan RAJH** z naslovom: »Model zgorevanja trdnih odpadkov na rešetki« (mentor: prof. dr. Niko Samec);

V doktorskem delu je predstavljen model za zgorevanje trdnih odpadkov na rešetki. Modeliranje trdnih odpadkov na rešetki je sestavljeno iz dveh delov: modeliranje pretvorbe trdnega goriva v plinasto fazo na rešetki s pomočjo ustreznega ravnotežnega modela in numerična simulacija plinaste faze zgorevanja nad plastjo trdnega goriva s pomočjo računalniške dinamike tekočin (RDT). Oba dela sta med seboj neposredno povezana preko sestave sinteznega plina in sevalnega toplotnega toka. Predstavljen pristop modeliranja zahteva medsebojno izmenjavo podatkov med obema modeloma, dokler se podatki obeh modelov ne uskladijo oz. ni bistvene spremembe, t.j. med sinteznim plinom, ki zapušča plast trdnega goriva in sevalnim toplotnim tokom, ki prihaja na samo plast.

Pretvorba trdnih odpadkov v plinasto fazo na rešetki je bila modelirana s pomočjo lastno razvitega empiričnega 1D ravnotežnega modela, ki temelji na vhodnih podatkih kot so: količina in sestava trdnih odpadkov, količina primarnega zraka, ki se dodatno pomeša še z recirkuliranimi dimnimi plini pod rešetko in sevalnim toplotnim tokom na vrhu plasti trdnega goriva.

Ravnotežni model na podlagi vhodnih podatkov predvidi ustrezne robne pogoje na medfazni površini trdnega goriva in plinaste faze kot je sestava (O_2, H_2O, CO, volatili) temperatura in hitrost sinteznega plina vzdolž rešetke. Pridobljeni robni pogoji v okviru ravnotežnega modela predstavljajo vstopne robne pogoje za izvedbo simulacije plinaste faze zgorevanja. Numerična simulacija je bila narejena s pomočjo komercialnega paketa RDT ANSYS CFX z uporabo ustreznih numeričnih modelov zgorevanja.

Z vidika validacije numeričnega modela je bila na različnih mestih znotraj kurišča narejena primerjava temperature z eksperimentalno pridobljenimi podatki. Narejena analiza s pomočjo RDT razkriva detaljno mešanje in karakteristike zgorevanja v realni kurilni napravi z rešetko in nudi možnost poiskati ustrezne rešitve na kakšen način jo optimizirati kot tudi kako izboljšati obratovanje takšnih naprav za energijsko izrabo odpadkov (EIO) z namenom doseganja boljšega izkoristka. Rezultati so pokazali, da neupoštevanje učinka vzgona lahko povzroči bistvene napake v numeričnih rezultatih. Izkazalo se je, da je v industriji mogoče uporabiti RDT kot osnovno orodje za optimizacijo takšnih objektov za EIO glede na številne kritične faktorje kot tudi, na kakšen način učinkovito optimizirati takšen sistem za namen boljšega obratovanja.

DIPLOMSKE NALOGE

Na Fakulteti za strojništvo Univerze v Ljubljani je zagovarjal svoje diplomsko delo univerzitetnega študija (Erasmus izmenjava):

dne 17. decembra 2014:

Antonio LOPEZ LOPEZ z naslovom: »Razvoj simulatorja hidroelektrarne za potrebe raziskovanja

krmilnih algoritmov / The development of hydro power plant simulator for control related research« (mentor: doc. dr. Primož Podržaj, somentor: izr. prof. dr. Anton Bergant);

*

Na Fakulteti za strojništvo Univerze v Ljubljani je so pridobili naziv univerzitetni diplomirani inženir strojništva:

dne 18. decembra 2014:

Miha JERAJ z naslovom: »Vpliv prevleke izpušnih cevi motorjev z notranjim zgorevanjem na prenos toplote« (mentor: izr. prof. dr. Tomaž Katrašnik);

Gašper MRAK z naslovom: »Razvoj izolatorja za ciostatike« (mentor: prof. dr. Iztok Golobič).

*

Na Fakulteti za strojništvo Univerze v Ljubljani so pridobili naziv magister inženir strojništva:

dne 1. decembra 2014:

Taja CERAR z naslovom: »Posodobitev pralno-sušilne linije v obratu predelave debele jeklene pločevine« (mentor: prof. dr. Janez Diaci, somentor: prof. dr. Iztok Golobič);

Matej KOS z naslovom: »Nadgradnja sistema za načrtovanje in vodenje proizvodnje« (mentor: prof. dr. Marko Starbek, somentor: izr. prof. dr. Janez Kušar);

Matjaž NERED z naslovom: »Termografska analiza dogajanj pri mehurčkastem vrenju vode na tankih grelnikih« (mentor: prof. dr. Iztok Golobič);

Peter PANJAN z naslovom: »Membransko čiščenje s topili in solmi onesnažene vode« (mentor: prof. dr. Iztok Golobič);

dne 18. decembra 2014:

Rok DOLINAR z naslovom: »Vpliv samoomočljivosti fluida na proces vrenja v mikrokanalih« (mentor: prof. dr. Iztok Golobič);

Andrej LUKŠIČ z naslovom: »Eksperimentalno raziskovanje izboljšanih površin za prenos toplote pri mehurčkastem vrenju« (mentor: prof. dr. Iztok Golobič);

Ervin STRMČNIK z naslovom: »Raziskava in razvoj empiričnih modelov za napovedovanje odjema toplote v vročevodnem sistemu« (mentor: prof. dr. Edvard Govekar, somentor: doc. dr. Primož Potočnik);

Matej KRANJEC z naslovom: »Numerična deformacijsko-napetostna analiza odziva ahilove tetive« (mentor: izr. prof. dr. Robert Kunc, somentor: prof. dr. Ivan Prebil);

Tim OREŠNIK z naslovom: »Optimizacija CNC-obdelave pri serijski obdelavi ohišja ventila« (mentor:

doc. dr. Franci Pušavec, somentor: prof. dr. Janez Kopač);

Aleš TRKOV z naslovom: »Določitev tehnoloških oken struženja Inconela 718 z visokotlačnim dovodom rezalnega olja« (mentor: doc. dr. Davorin Kramar, somentor: prof. dr. Janez Kopač).

*

Na Fakulteti za strojništvo Univerze v Mariboru so pridobili naziv magister inženir strojništva:

dne 17. decembra 2014:

Žiga CAPL z naslovom: »Simulacija in analiza globokega vleka zadnje stene potniške kabine tovornega vozila« (mentor: doc. dr. Mirko Ficko);

Nejc GORINŠEK z naslovom: »Projekt vpenjalnih priprav za varjenje karoserijskih delov v naročniški proizvodnji podjetja Oprema Ravne« (mentor: doc. dr. Iztok Palčič, somentor: doc. dr. Mirko Ficko);

Matej KUŠER z naslovom: »Hlajenje stanovanjske hiše z absorpcijsko hladilno napravo« (mentor: prof. dr. Milan Marčič, somentor: prof. dr. Jurij Avsec);

Niko SRT z naslovom: »Zasnova in konstruiranje komore za merjenje hrupa« (mentor: doc. dr. Aleš Belšak).

*

Na Fakulteti za strojništvo Univerze v Mariboru so pridobili naziv magister gospodarski inženir:

dne 17. decembra 2014:

Nika KOPŠE z naslovom: »Napredno načrtovanje materialnih potreb v proizvodnem podjetju« (mentor: prof. dr. Borut Buchmeister, somentor: prof. dr. Majda Bastič);

dne 19. decembra 2014:

Boštjan HORJAK z naslovom: »Predlog strategij invalidskega podjetja« (mentorja: doc. dr. Marjan Leber, izr. prof. dr. Mojca Duh);

Aleš KREL z naslovom: »Vključevanje dobaviteljev v procese razvoja izdelkov« (mentorja: doc. dr. Marjan Leber, doc. dr. Aleksandra Pisnik).

*

Na Fakulteti za strojništvo Univerze v Mariboru je pridobil naziv magister inženir mehatronike:

dne 17. decembra 2014:

Mitja FILIPIČ z naslovom: »Posredno programiranje robota ACMA XR701« (izr. prof. dr. Karl Gotlih, somentorja: dr. Simon Brezovnik, doc. dr. Miran Rodič);

*

Na Fakulteti za strojništvo Univerze v Ljubljani sta pridobila naziv diplomirani inženir strojništva:

dne 3. decembra 2014:

Tomaž KOS z naslovom: »Analiza pojava slabega naleganja pri procesu uporovnega točkovnega varjenja« (mentor: doc. dr. Primož Podržaj, somentor: doc. dr. Damjan Klobčar);

Gašper TUŠEK z naslovom: »Izdelava puhala za srednje volumske pretoke« (mentor: izr. prof. dr. Marko Hočevar, somentor: prof. dr. Branko Širok).

*

Na Fakulteti za strojništvo Univerze v Ljubljani so pridobili naziv diplomirani inženir strojništva (VS):

dne 3. decembra 2014:

Uroš ADAMLJE z naslovom: »Hidrostatični pogon v zaprtem tokokrogu« (mentor: doc. dr. Franc Majdič);

Vid KOŽELJ z naslovom: »Eksperimentalna določitev energijske učinkovitosti prezračevanja z rekuperatorjem« (mentor: doc. dr. Matjaž Prek, somentor: prof. dr. Vincenc Butala);

dne 5. decembra 2014:

Gašper JALŠOVEC z naslovom: »Sistem za pozicioniranje obdelovanca pri selektivnem odlaganju lasersko tvorjenih kovinskih kapljic« (mentor: doc. dr. Drago Bračun, somentor: prof. dr. Edvard Govekar);

Nace MATIČIČ z naslovom: »Induktivno kaljenje materiala za velike ležajne obroče« (mentor: izr. prof. dr. Roman Šturm);

Ambrož MIKELJ z naslovom: »Analiza zgorevalnega procesa piroliznega olja iz odpadnih pnevmatik v tlačno polnjenem dizelskem motorju« (mentor: izr. prof. dr. Tomaž Katrašnik);

Miha SIMETINGER z naslovom: »Vizualna analiza curka alternativnih goriv vbrizganih iz dvotokovne šobe za uporabo v turbinskih motorjih« (mentor: izr. prof. dr. Tomaž Katrašnik).

Information for Authors

All manuscripts must be in English. Pages should be numbered sequentially. The manuscript should be composed in accordance with the Article Template given above. The maximum length of contributions is 10 pages. Longer contributions will only be accepted if authors provide juastification in a cover letter. For full instructions see the Information for Authors section on the journal's website: http://en.sv-jme.eu .

SUBMISSION:

Submission to SV-JME is made with the implicit understanding that neither the manuscript nor the essence of its content has been published previously either in whole or in part and that it is not being considered for publication elsewhere. All the listed authors should have agreed on the content and the corresponding (submitting) author is responsible for having ensured that this agreement has been reached. The acceptance of an article is based entirely on its scientific merit, as judged by peer review. Scientific articles comprising simulations only will not be accepted for publication; simulations must be accompanied by experimental results carried out to confirm or deny the accuracy of the simulation. Every manuscript submitted to the SV-JME undergoes a peer-review process.

The authors are kindly invited to submit the paper through our web site: http://ojs.sv-jme.eu. The Author is able to track the submission through the editorial process - as well as participate in the copyediting and proofreading of submissions accepted for publication - by logging in, and using the username and password provided.

SUBMISSION CONTENT:

The typical submission material consists of:
- A **manuscript** (A PDF file with title, all authors with affiliations, abstract, keywords, highlights, inserted figures and tables and references),
- Supplementary files:
  - a **manuscript** in a WORD file format
  - a **cover letter** (please see instructions for composing the cover letter)
  - a ZIP file containing **figures** in high resolution in one of the graphical formats (please see instructions for preparing the figure files)
  - possible **appendicies** (optional), cover materials, video materials, etc.

Incomplete or improperly prepared submissions will be rejected with explanatory comments provided. In this case we will kindly ask the authors to carefully read the Information for Authors and to resubmit their manuscripts taking into consideration our comments.

COVER LETTER INSTRUCTIONS:

Please add a **cover letter** stating the following information about the submitted paper:
1. Paper **title**, list of **authors** and their **affiliations**.
2. **Type of paper**: original scientific paper (1.01), review scientific paper (1.02) or short scientific paper (1.03).
3. A **declaration** that neither the manuscript nor the essence of its content has been published in whole or in part previously and that it is not being considered for publication elsewhere.
4. State the **value of the paper** or its practical, theoretical and scientific implications. What is new in the paper with respect to the state-of-the-art in the published papers? Do not repeat the content of your abstract for this purpose.
5. We kindly ask you to suggest at least two **reviewers** for your paper and give us their names, their full affiliation and contact information, and their scientific research interest. The suggested reviewers should have at least two relevant references (with an impact factor) to the scientific field concerned; they should not be from the same country as the authors and should have no close connection with the authors.

FORMAT OF THE MANUSCRIPT:

The manuscript should be composed in accordance with the Article Template. The manuscript should be written in the following format:
- A **Title** that adequately describes the content of the manuscript.
- A list of **Authors** and their **affiliations**.
- An **Abstract** that should not exceed 250 words. The Abstract should state the principal objectives and the scope of the investigation, as well as the methodology employed. It should summarize the results and state the principal conclusions.
- 4 to 6 significant **key words** should follow the abstract to aid indexing.
- 4 to 6 **highlights;** a short collection of bullet points that convey the core findings and provide readers with a quick textual overview of the article. These four to six bullet points should describe the essence of the research (e.g. results or conclusions) and highlight what is distinctive about it.
- An **Introduction** that should provide a review of recent literature and sufficient background information to allow the results of the article to be understood and evaluated.
- A **Methods** section detailing the theoretical or experimental methods used.
- An **Experimental section** that should provide details of the experimental set-up and the methods used to obtain the results.
- A **Results** section that should clearly and concisely present the data, using figures and tables where appropriate.
- A **Discussion** section that should describe the relationships and generalizations shown by the results and discuss the significance of the results, making comparisons with previously published work. (It may be appropriate to combine the Results and Discussion sections into a single section to improve clarity.)
- A **Conclusions** section that should present one or more conclusions drawn from the results and subsequent discussion and should not duplicate the Abstract.
- **Acknowledgement** (optional) of collaboration or preparation assistance may be included. Please note the source of funding for the research.
- **Nomenclature** (optional). Papers with many symbols should have a nomenclature that defines all symbols with units, inserted above the references. If one is used, it must contain all the symbols used in the manuscript and the definitions should not be repeated in the text. In all cases, identify the symbols used if they are not widely recognized in the profession. Define acronyms in the text, not in the nomenclature.
- **References** must be cited consecutively in the text using square brackets [1] and collected together in a reference list at the end of the manuscript.
- **Appendix(-icies)** if any.

SPECIAL NOTES

Units: The SI system of units for nomenclature, symbols and abbreviations should be followed closely. Symbols for physical quantities in the text should be written in italics (e.g. v, T, n, etc.). Symbols for units that consist of letters should be in plain text (e.g. ms^{-1}, K, min, mm, etc.). Please also see: http://physics.nist.gov/cuu/pdf/sp811.pdf .

Abbreviations should be spelt out in full on first appearance followed by the abbreviation in parentheses, e.g. variable time geometry (VTG). The meaning of symbols and units belonging to symbols should be explained in each case or cited in a **nomenclature** section at the end of the manuscript before the References.

Figures (figures, graphs, illustrations digital images, photographs) must be cited in consecutive numerical order in the text and referred to in both the text and the captions as Fig. 1, Fig. 2, etc. Figures should be prepared without borders and on white grounding and should be sent separately in their original formats. If a figure is composed of several parts, please mark each part with a), b), c), etc. and provide an explanation for each part in Figure caption. The caption should be self-explanatory. Letters and numbers should be readable (Arial or Times New Roman, min 6 pt with equal sizes and fonts in all figures). Graphics (submitted as supplementary files) may be exported in resolution good enough for printing (min. 300 dpi) in any common format, e.g. TIFF, BMP or JPG, PDF and should be named Fig1.jpg, Fig2.tif, etc. However, graphs and line drawings should be prepared as vector images, e.g. CDR, AI. Multi-curve graphs should have individual curves marked with a symbol or otherwise provide distinguishing differences using, for example, different thicknesses or dashing.

Tables should carry separate titles and must be numbered in consecutive numerical order in the text and referred to in both the text and the captions as Table 1, Table 2, etc. In addition to the physical quantities, such as t (in italics), the units [s] (normal text) should be added in square brackets. Tables should not duplicate data found elsewhere in the manuscript. Tables should be prepared using a table editor and not inserted as a graphic.

REFERENCES:

A reference list must be included using the following information as a guide. Only cited text references are to be included. Each reference is to be referred to in the text by a number enclosed in a square bracket (i.e. [3] or [2] to [4] for more references; do not combine more than 3 references, explain each). No reference to the author is necessary.

References must be numbered and ordered according to where they are first mentioned in the paper, not alphabetically. All references must be complete and accurate. Please add DOI code when available. Examples follow.

Journal Papers:
Surname 1, Initials, Surname 2, Initials (year). Title. Journal, volume, number, pages, DOI code.
[1] Hackenschmidt, R., Alber-Laukant, B., Rieg, F. (2010). Simulating nonlinear materials under centrifugal forces by using intelligent cross-linked simulations. *Strojniški vestnik - Journal of Mechanical Engineering,* vol. 57, no. 7-8, p. 531-538, DOI:10.5545/sv-jme.2011.013.
Journal titles should not be abbreviated. Note that journal title is set in italics.

Books:
Surname 1, Initials, Surname 2, Initials (year). Title. Publisher, place of publication.
[2] Groover, M.P. (2007). *Fundamentals of Modern Manufacturing*. John Wiley & Sons, Hoboken.
Note that the title of the book is italicized.

Chapters in Books:
Surname 1, Initials, Surname 2, Initials (year). Chapter title. Editor(s) of book, book title. Publisher, place of publication, pages.
[3] Carbone, G., Ceccarelli, M. (2005). Legged robotic systems. Kordić, V., Lazinica, A., Merdan, M. (Eds.), Cutting Edge Robotics. Pro literatur Verlag, Mammendorf, p. 553-576.

Proceedings Papers:
Surname 1, Initials, Surname 2, Initials (year). Paper title. Proceedings title, pages.
[4] Štefanić, N., Martinčević-Mikić, S., Tošanović, N. (2009). Applied lean system in process industry. *MOTSP Conference Proceedings*, p. 422-427.

Standards:
Standard-Code (year). Title. Organisation. Place.
[5] ISO/DIS 16000-6.2:2002. *Indoor Air – Part 6: Determination of Volatile Organic Compounds in Indoor and Chamber Air by Active Sampling on TENAX TA Sorbent, Thermal Desorption and Gas Chromatography using MSD/FID*. International Organization for Standardization. Geneva.

WWW pages:
Surname, Initials or Company name. Title, from http://address, date of access.
[6] Rockwell Automation. Arena, from *http://www.arenasimulation.com,* accessed on 2009-09-07.

EXTENDED ABSTRACT:

When the paper is accepted for publishing, the authors will be requested to send an **extended abstract** (approx. one A4 page or 3500 to 4000 characters). The instruction for composing the extended abstract are published on-line: http://www.sv-jme.eu/information-for-authors/ .

COPYRIGHT:

Authors submitting a manuscript do so on the understanding that the work has not been published before, is not being considered for publication elsewhere and has been read and approved by all authors. The submission of the manuscript by the authors means that the authors automatically agree to transfer copyright to SV-JME when the manuscript is accepted for publication. All accepted manuscripts must be accompanied by a Copyright Transfer Agreement, which should be sent to the editor. The work should be original work by the authors and not be published elsewhere in any language without the written consent of the publisher. The proof will be sent to the author showing the final layout of the article. Proof correction must be minimal and executed quickly. Thus it is essential that manuscripts are accurate when submitted. Authors can track the status of their accepted articles on http://en.sv-jme.eu/.

PUBLICATION FEE:

Authors will be asked to pay a publication fee for each article prior to the article appearing in the journal. However, this fee only needs to be paid after the article has been accepted for publishing. The fee is 240.00 EUR (for articles with maximum of 6 pages), 300.00 EUR (for articles with maximum of 10 pages), plus 30.00 EUR for each additional page. The additional cost for a color page is 90.00 EUR. These fees do not include tax.

Contents

Papers